DOE/NV/25946--1162

NEVADA NATIONAL SECURITY SITE–DIRECTED RESEARCH AND DEVELOPMENT

FY 2010 REPORT

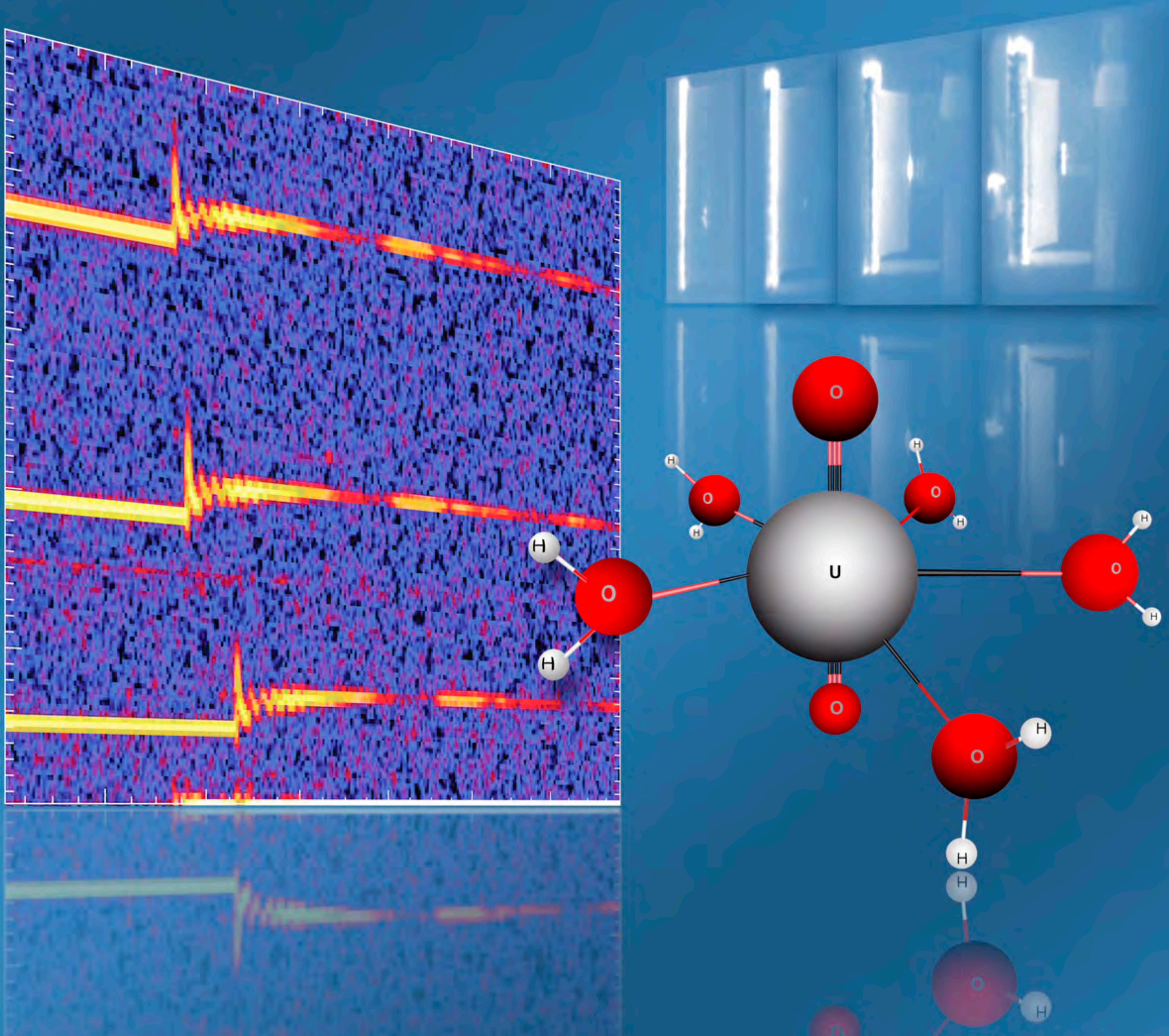

Site Directed R & D SDRD

This work was supported by the U.S. Department of Energy, National Nuclear Security Administration, Nevada Site Office, under Contract No. DE-AC52-06NA25946.

Report Date: April 2011

Availability Statement

Available for sale to the public from—

U.S. Department of Commerce
National Technical Information Service
5301 Shawnee Road
Alexandria, VA 22312
Telephone: 800.553.6847
Fax: 703.605.6900
E-mail: orders@ntis.gov
Online Ordering: http://www.ntis.gov/help/ordermethods.aspx

Available electronically at http://www.osti.gov/bridge

Available for a processing fee to U.S. Department of Energy and its contractors in paper, from—

U.S. Department of Energy
Office of Scientific and Technical Information
P.O. Box 62
Oak Ridge, TN 37831-0062
Telephone: 865.576.6401
Fax: 865.576.5728
E-mail: reports@adonis.osti.gov

DOE/NV/25946--1162

Nevada National Security Site–Directed Research and Development

FY 2010 Report

This work was supported by the U.S. Department of Energy, National Nuclear Security Administration Nevada Site Office, under Contract No. DE-AC52-06NA25946.

Report Date: April 2011

Material Studies and Techniques

Instruments, Detectors, and Sensors

Computational Sciences

Photonics

SDRD FY 2010 PROGRAM SUMMARY

An Historical Year

This annual report of the Site-Directed Research and Development (SDRD) program represents the highly significant R&D accomplishments conducted during fiscal year 2010. This year was noteworthy historically, as the Nevada Test Site was renamed to the Nevada National Security Site (NNSS). This change not only recognizes how the site's mission has evolved, but also heralds a future of new challenges and opportunities for the NNSS. In many ways, since its inception in 2002, the SDRD program has helped shape that evolving mission. As we approach 2012, SDRD will also mark a milestone, having completed its first full decade of innovative R&D in support of the site and national security. The program continues to fund advanced science and technology development across traditional Department of Energy (DOE) nuclear security areas such as stockpile stewardship and non-proliferation while also supporting Department of Homeland Security (DHS) needs, and specialized work for government agencies like the Department of Defense (DoD) and others. The NNSS will also contribute technologies in the areas of treaty verification and monitoring, two areas of increasing importance to national security. Keyed to the NNSS's broadened scope, the SDRD program will continue to anticipate and advance R&D projects that will help the NNSS meet forthcoming challenges.

SDRD FY 2010 People and Successes

NSTec principal investigator M. Manard with mini mass spectrometer, which was recently described in an invited paper in *International Journal of Mass Spectroscopy*

Investments made with SDRD in the areas of spectroscopy and modeling are garnering attention by being recognized as significant contributions. New chemical detection spectroscopy techniques developed by principal investigator M. Manard were featured in a special-issue invited article in the *International Journal of Mass Spectroscopy*. A book chapter in an upcoming publication was written by M. Wu and C. Kruschwitz describing new Monte Carlo techniques in modeling of specialized detectors that have far-reaching use in many fields. These examples highlight the positive impact and contribution that SDRD investment makes to our understanding of complicated issues relevant to national security.

In addition to the above examples, many other program highlights contributed to a very successful 2010. Nine new invention disclosures were submitted on activities related to this year's work and multiple peer-reviewed articles were published along with many of our principal investigators contributing presentations to national technical conferences. The program also generated R&D 100 award entries on technologies representing solutions to national security issues. Four projects were highlighted at the annual Laboratory Directed Research and Development Symposium in Washington, D.C. The featured projects covered a range of areas from nuclear forensics to specialized nuclear radiation detection and were well received by an audience that included NNSA, the National Weapons Laboratories (NWL), DHS, and DoD. The symposium theme was reducing the global danger of weapons of mass destruction, and was particularly relevant to the NNSS mission. Steven Younger, President of National Security Technologies, gave an important talk describing challenges posed by future arms control and nonproliferation agreements.

Applications of Monte Carlo Method in Science and Engineering

INTECH

NSTec principal investigators M. Wu and C. Kruschwitz have written a book chapter based on their Monte Carlo work

A Growing, Effective Program

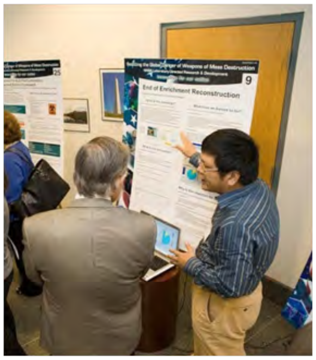

NSTec principal investigator D. Yuan describes a nuclear forensics R&D project at the 2010 LDRD symposium

In FY 2010 we incorporated funding from non-DOE sources into the base funding of SDRD for the first time. This allowed for an enhanced program with more resources and flexibility to address needs across the full mission scope. The overall effect has been hugely positive for the program and NNSS. Proposals were solicited in many new areas such as intelligence, surveillance, and cyber security. In fact, the 2011 proposal call saw an 18% increase in submissions from our staff over the previous year. Selection of actual projects remains highly competitive with about 1 in 6 receiving funding. A strong peer-review system that underpins selection and criteria such as technical innovation value, probability of success balanced with technical risk, potential for mission benefit, and alignment with mission goals and key challenges, provides for robust evaluation. In addition, our *NNSS Technology Needs Assessment* provides a roadmap and guidance for proposal submitters and reviewers in developing ideas to suit critical needs. The needs assessment benefits from a broad base of input from the national security complex including laboratories, NNSA, and other external agencies. Significant revisions to the needs assessment, released in April 2010, included adding emerging areas such as the new National Center for Nuclear Security (NCNS), established to support treaty efforts; the assessment's overall usefulness is enhanced by these annual updates. Total funds expended for the FY 2010 program were $6.8 million, a nearly 25% increase over FY 2009. Average per project cost remains nearly constant at about $225,000. This relatively small investment yields considerable return based on the achievements and benefit earned by our mission and programs.

The effectiveness of an R&D program is often gauged by metrics such as intellectual property and technology transfer. This tangible output is a key indicator of innovation productivity and provides a direct measure of investment return. Figure 1 shows the number of inventions disclosed as a function of the total number of projects from FY 2003 to present. SDRD provides a rich environment for creative exploration and this is evidenced by the fact that over half of all inventions disclosed company-wide have been generated from this program. Multiple patent applications are in process based on these disclosures.

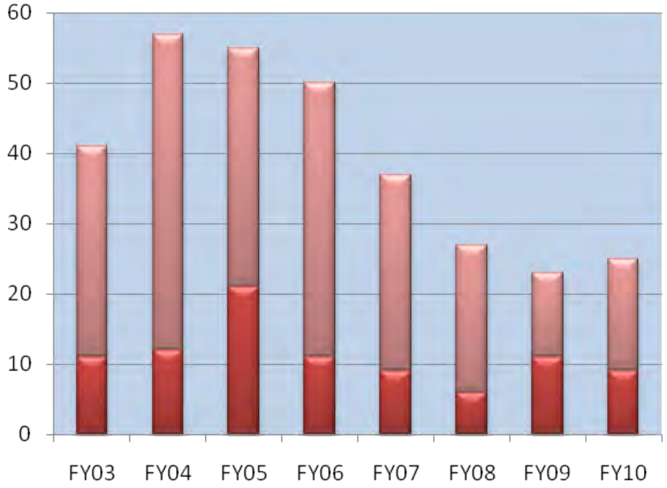

Figure 1. Inventions disclosed (dark red bars) plotted as a function of the total number of SDRD projects (light red bars) in a given fiscal year

Figure 2 shows a chart of the number of projects for which technology was subsequently adopted by NNSS programs per fiscal year. Typically some time is required for technologies to mature and migrate, and SDRD advancements often integrate into programmatic efforts after projects have completed. A concerted effort has been developed to include technologies in NNSS roadmaps to encourage this natural transfer. In addition, many SDRD efforts lend solutions to programmatic needs when evolving requirements mandate them. By staying "ahead of our time by design," we fully expect SDRD–developed technologies will continue to be deployed and grow in number well into the future and impact new mission areas.

Another measure of program effectiveness and alignment with missions is how well projects address technology needs as identified in our *NNSS Technology Needs Assessment* analysis. This needs assessment is updated annually with the most current requirements as foretold by NNSA strategic plans and management, NNSS management and technical staff, and NWL management and staff. The number of projects that have directly addressed a technology "gap" or requirement outlined in the assessment is shown plotted in Figure 3 against the total number of projects. The percentage of needs addressed to total projects is also indicative of a trend that aligns efforts strategically with the NNSS mission.

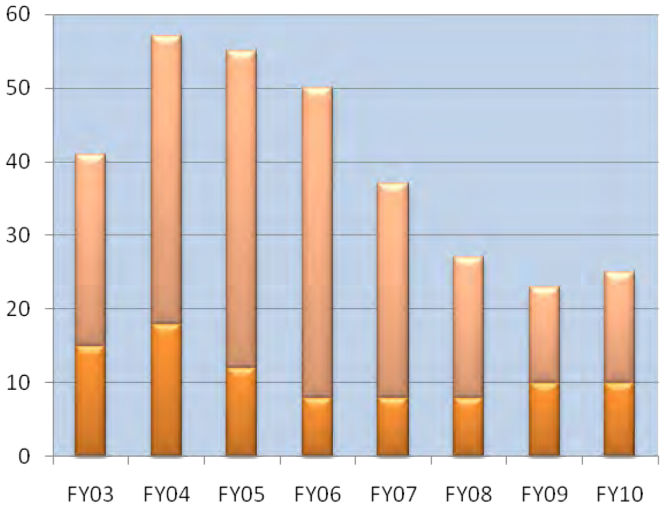

Figure 2. SDRD projects contributing technologies to programs (dark gold bars) compared to the total number of projects (light gold bars) in a given fiscal year

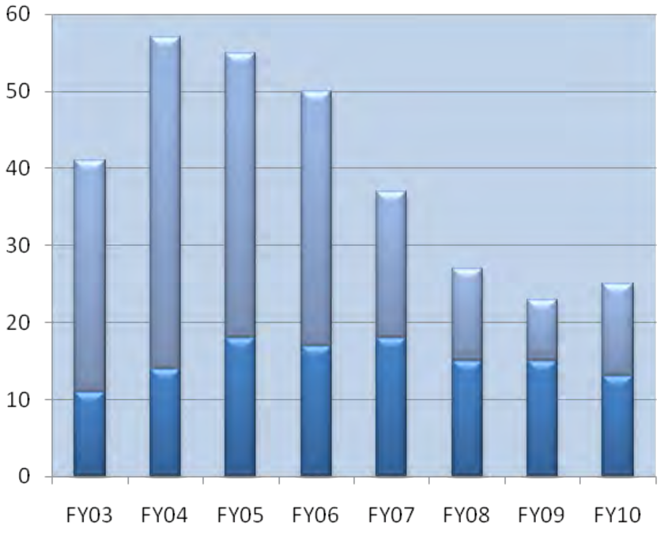

Figure 3. SDRD projects (dark blue bars) that directly address a technology requirement as identified in the yearly *NNSS Technology Needs Assessment* compared to total number of projects (light blue bars) in a given fiscal year

The project reports contained herein are for activities that occurred from October 2009 through September 2010. The numerous achievements described are a tribute to the talent and enthusiasm principal investigators brought to their individual projects. Many of the reports that follow illustrate R&D efforts that resulted in successful conclusions and positive discovery. A desired outcome of SDRD is to develop and/or refine technologies that can ultimately be utilized by programs. SDRD also provides the unique environment for embracing “high-risk” research; and thus, in some cases, finds that a particular technology is currently impractical or an idea is beyond reach. Both types of results advance knowledge and increase our agility by identifying solutions that can be applied appropriately.

In summary, the SDRD program continues to provide a valuable mechanism for innovation and development that returns multifold to the NNSS mission. Overall, the program has been strengthened by enhanced mission, resources, and increased competitiveness to yield maximum benefit. The 25 projects described herein exemplify the creativity and ability of a diverse scientific and engineering talent base. The efforts also showcase an impressive capability and resource that can be brought to find solutions to a broad array of technology needs and applications relevant to the NNSS mission and national security.

Last, I want to acknowledge the tremendous program support by our administrative and technical teams that make SDRD successful. My sincere gratitude goes out to Michele Vochosky, Sierra Cory, and Katharine Kelly Streeton for compiling, editing, and publishing this report; to Nancie Nickels for her contributions to the cover and divider graphics; to Project Controls Engineer Linda Flaugher for her valuable efforts in cost accounting; to Cathy Cooper and Cindy McIntosh for financial planning and data compiling for reporting requirements; to Lynn Veeser and Larry Franks for highly valuable scientific and technical guidance; and to the SDRD site representatives and proposal review committee, Rob Buckles, Frank Cverna, Paul Guss, Steve Iversen, Amy Lewis, Tim Meehan, Sanjoy Mukhopadhyay, Bob Okagawa, and Jerry Stevens. Again, my sincerest appreciation for your dedication in implementing and managing another highly productive year of R&D!

Howard Bender
SDRD Program Manager

this page intentionally left blank

Los Alamos Operations (LAO)
P.O. Box 809
Los Alamos, New Mexico 87544-0809

Livermore Operations (LO)
P.O. Box 2710
Livermore, California 94551-2710

North Las Vegas (NLV)
P.O. Box 98521
Las Vegas, Nevada 89193-8521

Nevada National Security Site (NNSS)
P.O. Box 98521
Las Vegas, Nevada 89193-8521

Remote Sensing Laboratory–Andrews Operations (RSL–A)
P.O. Box 380
Suitland, Maryland 20752-0380
(Andrews Air Force Base)

Remote Sensing Laboratory–Nellis Operations (RSL–N)
P.O. Box 98521
Las Vegas, Nevada 89193-8521
(Nellis Air Force Base)

Sandia Operations (SO)
Sandia National Laboratories
P.O. Box 5800
Mail Stop 1193
Albuquerque, New Mexico 87185

Special Technologies Laboratory (STL)
5520 Ekwill Street
Santa Barbara, California 93111-2352

this page intentionally left blank

A

AChE	acetylcholinesterase
ACR	absorption-contrast radiography
A/D	analog to digital
ADC	analog-to-digital converter
AFM	atomic force microscopy
AFSA	acceleration/focusing/steering assembly
AGL	above ground level
Al	aluminum
AlGaN	aluminum gallium nitride
Al-NP	aluminum nanoparticle
AMS	aerial measurement system
ASE	amplified spontaneous emission

B

^{10}B	boron-10, enriched boron
Be	beryllium
BiMOSFET	bipolar metal oxide semiconductor field effect transistor
BN	boron nitride
BP	boron phosphide

C

CAD	computer-aided design
CARS	coherent anti-Stokes Raman spectroscopy
CCD	charge-coupled device
Cd	cadmium
CDA	characterization data acquisition
$CeBr_3$	cerium bromide
CNP	colloidal nanoparticle
COTS	commercial off the shelf

D

DC	direct current
demux	demultiplex
DFT	density functional theory
DHS	U.S. Department of Homeland Security
DIVA	Decay Interaction Visualization and Analysis
DoD	U.S. Department of Defense

DOE	U.S. Department of Energy
DPF	dense plasma focus
DU	depleted uranium
DWDM	dense wavelength division multiplexing

E

EDFA	erbium-doped fiber amplifier
EDM	electrical discharge machining
EJSM	Europa Jupiter System Mission
EOE	end of enrichment
EOS	equation of state
EPM	embedded piezoresistive microcantilever

F

fcc	face-centered cubic
FDTD	finite-difference time-domain
FFT	fast Fourier transform
FIFO	first-in first-out
FM	fission meter
FMSU	fission meter simulator unit
FPGA	field-programmable gate array
FTIR	Fourier transform infrared (spectrometer)
FTP	Fourier transform pyrometer
FTS	Fourier transform spectrometer

G

GaAs	gallium arsenide
GaN	gallium nitride
GPS	global positioning system

H

HDPE	high-density polyethylene
HE	high explosive
HEDP	high-energy density physics
HEX	high energy x-ray [source]
HPGe	high-purity germanium

I

ID	inner/inside/internal diameter
IDL	Interactive data language
IF	intermediate frequency
In	indium
In-NP	indium nanoparticles
IMU	inertial measurement unit
INU	inertial navigation unit
IR	infrared
ISO	International Standards Organization
ITU	International Telecommunication Union
I-V	current-voltage

L

LANL	Los Alamos National Laboratory
LAO	Los Alamos Operations [NSTec]
$LaCl_3$:Ce	cerium-doped lanthanum halide
LaF_3:Ce	cerium-doped lanthanum fluoride
LBNL	Lawrence Berkeley National Laboratory
LCLS	Linac Coherent Light Source
LED	light-emitting diode
LiF	lithium fluoride
LLNL	Lawrence Livermore National Laboratory
LO	Livermore Operations [NSTec]
LT	low temperature

M

m/z	mass-to-charge (ratio)
MAC	media access control
MC	microsecond counter
MCA	multichannel analyzer
MCNP	Monte Carlo n-Particle [transport code]
MCNPX	Monte Carlo n-Particle eXtended [transport code]
MCP	microchannel plate
MDA	minimum detectable activity
MEF	metal-enhanced fluorescence
MM	multiplet matrix
MNP	metal nanoparticle
MPDV	many-point PDV

MS	mass spectrometer
MSM	metal-semiconductor-metal
mux	multiplex
MWIR	mid-wavelength infrared (spectrometer)

N

NaI	sodium iodide
NASA	National Aeronautics and Space Administration
NCNS	National Center for Nuclear Security
NIF	National Ignition Facility
NMAC	Neutron Multiplicity Analysis Package
NNSA	National Nuclear Security Administration
NNSS	Nevada National Security Site
NP	nanoparticle
NRAT	Nuclear Radiological Advisory Team
NSLS	National Synchrotron Light Source
NSTec	National Security Technologies, LLC
NWL	National Weapons Laboratories

O

OpenCV	Open Source Computer Vision

P

PARC	Palo Alto Research Center
PC	pseudocumene, 1,2,4-trimethylbenzene
PCB	printed circuit board
PCR	phase-contrast radiography
PD	photodiode
PDMS	polydimethylsiloxane
PDV	photonic Doppler velocimetry
PM	polarization maintaining (fiber)
PMC	piezoresistive microcantilevers
PMT	photomultiplier tube
PPO	2,5-diphenyloxazole
PSL	polystyrene latex (spheres)
PTI	Proportional Technologies, Inc.
PuO_2	plutonium oxide
PVA	polyvinyl alcohol
PVT	polyvinyltoluene (detector)

R

R&D	research and development
RAM	random access memory
RDA	real-time data acquisition
RF	radio frequency
RMD	Radiation Monitoring Devices, Inc.
RIO	Redfern Integrated Optics, Inc.
RPI	Rensselaer Polytechnic Institute
RPM	revolutions per minute
RSL	Remote Sensing Laboratory [NSTec]
RSL–A	Remote Sensing Laboratory–Andrews Operations [NSTec]
RSL–N	Remote Sensing Laboratory–Nellis Operations [NSTec]
RSSI	receive signal strength indicator

S

SDRD	(Nevada National Security) Site–Directed Research and Development
SETI	Sensor Electronics Technology, Inc.
SFG	sum-frequency generation
Si	silicon
SI	system initialization
SiO	silicon oxide
SIFT	scale-invariant feature transform (algorithm)
S/N	signal to noise (ratio)
SNM	special nuclear material
SO	Sandia Operations [NSTec]
SRIM	stopping and range of ions in matter (code)
STL	Special Technologies Laboratory [NSTec]
SURF	speeded-up robust features (algorithm)

T

3-D	three-dimensional
THz	terahertz
TOF	time-of-flight
TRIM	transport of ions in matter (code)

U

UAV	unmanned aerial vehicle
UC	University of California

UCSB	University of California, Santa Barbara
UMBI	University of Maryland Biotechnology Institute
USB	universal serial bus
UV	ultraviolet

V

VISAR	velocity interferometer system for any reflector
VISED	MCNPX Visual Editor

X

XML	extensible markup language
XRD	x-ray diffraction

Z

ZnO	zinc oxide

MATERIAL STUDIES AND TECHNIQUES

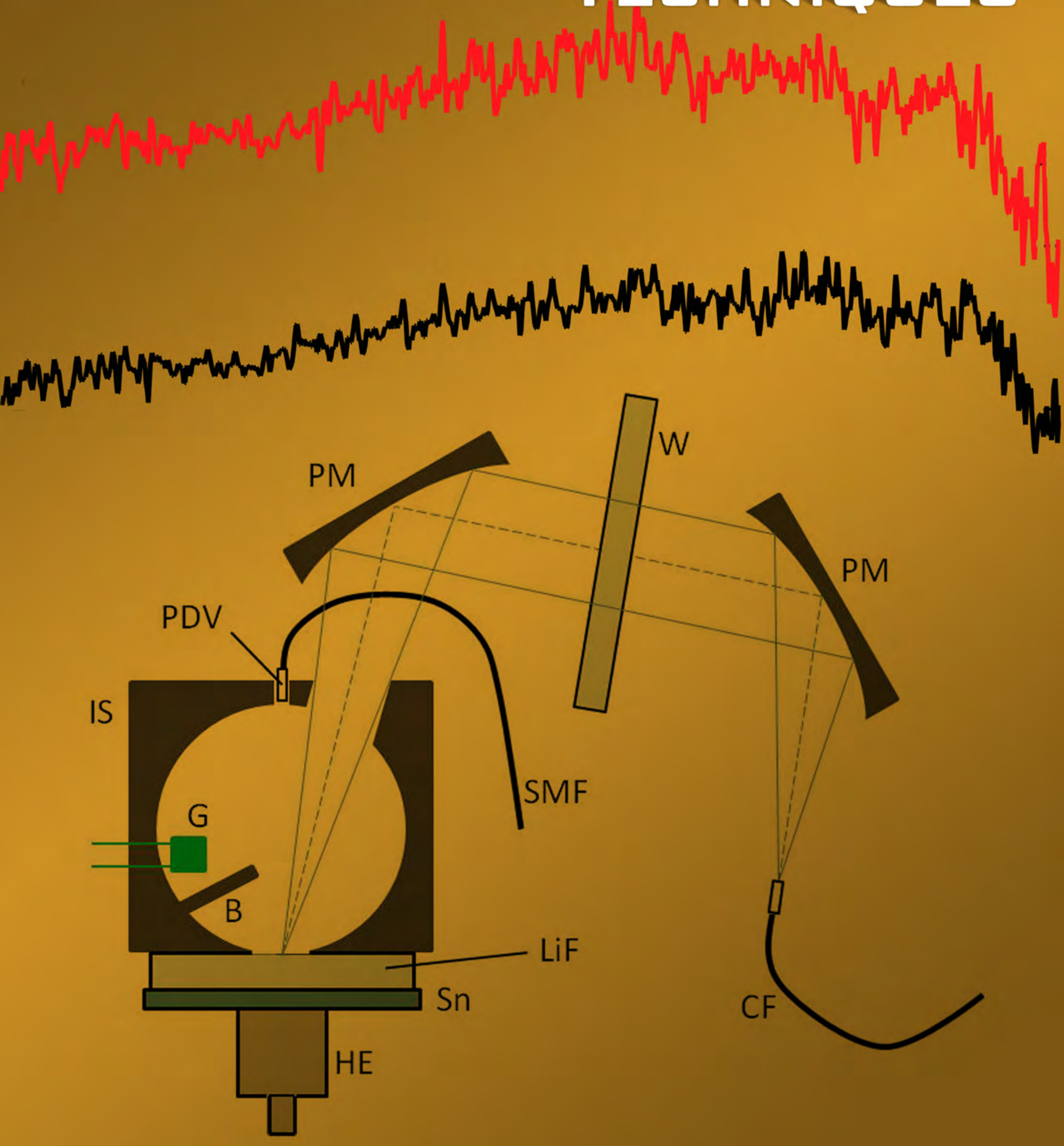

DEBYE-WALLER DYNAMIC TEMPERATURE MEASUREMENTS

Dane Morgan,[1,a] Mike Grover,[b] Don Macy,[a] and Gerald D. Stevens[b]

Studies of shocked aluminum 6061-T6 and silver alloy free surfaces were conducted on the nanosecond time scale with single-pulse x-ray diffraction (XRD). Experiments were performed on 1 mm thick disks of aluminum 6061-T6 and silver-copper alloy (92.5% silver, 7.5% copper) free surfaces, which were shocked to pressures in the range of 30–40 GPa using PBX-9501 high explosives. Bragg-reflected single-pulse XRD line intensity, line broadening, and line shift measurements were obtained to investigate the dynamic properties of these samples immediately after shock-and-release.

Background

We have undertaken an investigation to determine the shocked properties of aluminum and silver alloys with single-pulse x-ray diffraction (XRD). This diagnostic is uniquely capable of nanosecond XRD studies of polycrystalline materials, and has been used previously to study the solid-solid phase transitions that are observed for both shocked tin (Morgan, 2008) and zirconium (Morgan, 2010). For XRD studies of shocked materials, it is important to precisely measure the line shift, line broadening, and changes in line intensity in the dynamic XRD data, because rapid changes in the shocked material properties will affect each of these observable parameters.

Two developments were implemented for FY 2010 experiments to improve the dynamic XRD measurement capabilities. The separation between the tungsten pinhole and the anode was increased to reduce the beam divergence and the spot size, resulting in improved angular resolution of the XRD pattern. Also, we have developed a new single-crystal beam-splitter intensity monitor to provide an intensity reference for the on-axis line emission that forms the XRD pattern. Despite the improvements, monitoring of the x-ray beam line intensity remains an ongoing challenge, because shot-to-shot intensity and source spectrum vary, and the comparatively large amounts of bremsstrahlung create inconsistent background levels.

As the *d*-spacing of the polycrystalline lattices are changed, either by plastic deformation or thermal expansion, the corresponding shift in the Bragg angle is closely approximated by the first derivative of Bragg's Law,

$$\Delta\theta \approx -(\Delta d / d) tan\theta, \tag{1}$$

where the scattering angle is twice the Bragg angle θ, and $\Delta d/d$ is the fractional change in the lattice *d*-spacing. Measurement of the shifts of individual diffraction lines allows us to distinguish line

---

[1] morgandv@nv.doe.gov, 505-663-2047

[a] Los Alamos Operations; [b] Special Technologies Laboratory

shifts caused by changes in the *d*-spacing from systematic effects such as sample translation. Earlier experiments with aluminum 6061-T6 under shock-loaded compression with vitreous carbon back windows to pressures of 6.4–7.3 GPa clearly showed angular increase of the XRD lines consistent with Equation 1. Conversely, shock-induced strain hardening has been shown to increase *d*-spacings in single-crystal copper and aluminum shock-and-release experiments using synchrotron radiation (Turneaure, 2009).

Broadening of the diffraction lines is also quite useful for examining specific dynamic properties of shocked samples, including grain-size broadening and variations in localized strains, which also have been reported in previous dynamic XRD experiments (Turneaure, 2009). A single-pulse XRD system is capable of distinguishing between the different material effects and systematic effects because of the dependence of the effect on the scattering angle. The angular dependence of size-broadening for a cubic grain is given by Scherrer's equation,

$$B\left(2\theta\right) = 0.94\lambda / Lcos\theta, \tag{2}$$

where λ is the x-ray wavelength and L is the edge dimension of a diffracting cubic grain element. If a shock-induced reduction in the grain size occurs, the line-broadening angular dependence is given by Equation 2. However, a distribution of microscopic strains would have the line-broadening angular dependence given in Equation 1. Furthermore, line broadening may also be caused by sample dissociation (spall) and systematic effects, such as velocity broadening, which must be considered.

According to the theory of Debye and Waller, XRD lines decrease in intensity as the temperature of the sample increases, with the effect becoming stronger at greater scattering angles. This effect is caused by the increase in the random displacement of the individual atoms from their exact geometric lattice site, which also results in an increase in the observed incoherently scattered background (James, 1982). Single-pulse XRD bench-top laboratory measurements of this effect have been reported (Morgan, 2007), leading to the possibility that single-pulse XRD could be useful as a dynamic temperature diagnostic. Coherent scattering from atomic centers in a solid-state lattice results in diffraction lines, which are observed at angles for which the difference in path lengths is an integral number of wavelengths. As the temperature of a solid rises, the mean-square displacement of the atoms from their exact geometric lattice position increases. This causes an increased phase shift in the scattered wavefront from adjacent scattering atoms. Therefore, the intensity of the diffraction lines decreases as the temperature increases, which is known as the Debye-Waller effect (Warren, 1990). Instead of scattering into the coherent diffraction lines, there is an increased probability of elastic scattering into the diffuse background. Recently, the possibility of observing and measuring the Debye-Waller effect in shocked copper using laser-plasma x-ray sources has been discussed (Murphy, 2008), emphasizing the importance of the volumetric dependence of the Debye temperature and the required corrections to the data. Therefore, if the intensity of the diffraction lines can be measured precisely, together with the volumetric changes in the lattice, the sample temperature may be measured through the Debye-Waller effect.

Equation-of-state computations predict a temperature increase of 232 K upon adiabatic release for a similar aluminum alloy when shocked to a peak pressure of 35 GPa (Walsh, 1955). Walsh also calculated the shock Hugoniot and release adiabat for aluminum, which show a volume increase of about 1.5% upon release; this volume increase could possibly be measured as a shift of the diffraction lines by our single-pulse XRD system. Recently, calculations for aluminum have been performed for the peak pressures of 300 kbar, consistent with pressures observed in previous aluminum shock experiments with PBX-9501, and these calculations show a temperature increase of about 160 K.

For sample materials driven by uniaxial shock above the elastic limit, plastic deformation and grain size reduction cause an increase in the strength of the material, a process known as work (or strain) hardening. After shock-and-release, the lattice structure has been shown to become elongated in the shock in single-crystal experiments. The observed macroscopic strain in the released state has been shown to be directly related to the materials strength, which has been shown to increase with increasing shock pressure (Turneaure, 2009). Single-pulse XRD probes a macroscopic volume, hence the observed XRD pattern will be composed of microscopic lattice responses from the grain distribution within the sample probe volume, and strain-distribution hardening may be observed.

Project

The results of a series of single-pulse XRD experiments for studying high explosives–driven, shock-and-release aluminum 6061-T6 and 92.5% silver (by weight) silver-copper alloy (sterling silver) are reported here. The shock-and-release experiments described in this report were conducted at the Special Technologies Laboratory (STL) Boom Box using PBX-9501 high explosives. A total of 17 experimental data sets were successfully obtained in FY 2010, having both high-quality images and proper x-ray timing with respect to surface shock breakout; these experiments are listed in Table 1. The input angles ranged from 12.2 degrees to 20 degrees, and XRD wavelengths of 0.71 Å and 0.56 Å were produced by anodes of molybdenum and silver, respectively.

Figure 1 shows the single-pulse XRD system for these experiments, including a flat image plate holder with a 16-degree x-ray beam input angle. The 40 ns x-ray pulse was generated by a 350 kV Marx bank coupled to a needle-and-washer diode through a DS-2158 coaxial cable. The x-ray firing time was measured with an electromagnetic pickup on the DS-2158 cable near the x-ray diode, and the x-ray signal timing with respect to the cable electromagnetic pickup time was measured in the laboratory prior to these experiments. A PDV diagnostic measured the free-surface shock breakout time and the free-surface velocity to determine the surface translation, which was used as an image correction for the dynamic images. The PDV measurements were inserted in the WONDY code to obtain the peak pressure. A reflectometry diagnostic was included in the diagnostic suite for the gold-coated aluminum experiments to determine the temperature of gold-coated aluminum targets via shifts in the visible reflected spectrum. The experimental setup at the STL Boom Box is shown in Figures 2a and 2b.

Table 1. Summary of single-pulse XRD Debye-Waller free-surface experiments on aluminum 6061-T6 and sterling silver

Experiment No.	Target Material	Peak Pressure (GPa)	λ (Å)	Input Angle (degrees)	X-ray Delay from Breakout (ns)	Surface Motion (µm)
100106-1	Al(1)	30.1	0.71	12.2	149	434
100106-2	Al(1)	29.9	0.71	12.2	148	431
100106-3	Al(1)	30.0	0.71	12.2	145	444
100107-1	Al(1)	30.5	0.71	12.2	132	392
100830-1	Ag(2)	41.3	0.71	16	72	116
100901-1	Al(3)	31.0	0.71	16	165	484
100901-2	Al(3)	31.4	0.71	16	108	313
100902-1	Al(3)	31.0	0.71	20	104	311
100902-2	Al(3)	31.1	0.71	20	110	330
100903-1	Ag(2)	39.6	0.71	16	207	320
100907-1	Ag(2)	39.1	0.56	20	268	402
100907-2	Ag(2)	39.6	0.56	20	175	289
100908-1	Ag(2)	40.3	0.71	20	56	86
100908-2	Ag(2)	40.0	0.71	20	142	224
100909-1	Ag(2)	40.0	0.71	20	124	207
100909-2	Al(3):LiF(100)	30.0	0.56	20	109	164
100909-3	Ag(2):LiF(100)	—	0.56	20	125	150

(1) Plate aluminum 6061-T651 per ASTM-B209

(2) 92.5–7.5 silver-copper alloy

(3) Sheet aluminum 6061-T6 with 0.1 µm gold coating

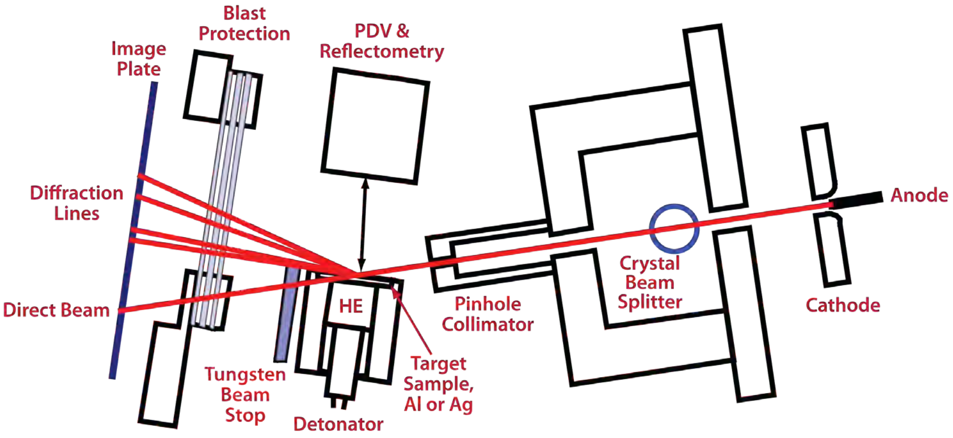

Figure 1. Diagram for single-pulse XRD experiments with aluminum and silver shocked free surfaces

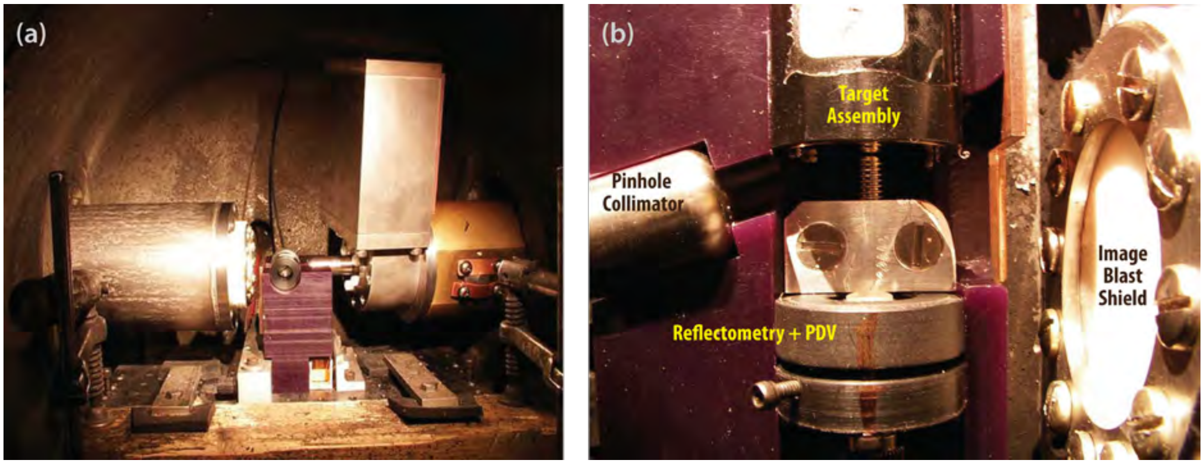

Figure 2 (a) View of the experimental setup at the STL Boom Box High Explosives Facility; (b) top view of the experimental setup showing the diagnostic suite including XRD, reflectometry, and PDV

The most recent version of the single-pulse XRD system includes a single-crystal beam splitter subassembly for the purpose of monitoring the line emission from the output; this subassembly is shown in Figure 3. This is of critical importance for compensating for shot-to-shot variations in the source's production of line emission. The LiF (800) beam-splitter reflection was used for experiments using 0.71 Å x-ray, whereas Si (911) reflections were used for experiments at 0.56 Å. The beam splitter and XRD image were both recorded on image plates and were processed simultaneously for each static and dynamic x-ray pulse. The image plates were calibrated using a radioactive test strip. By recording and measuring the reflection of the line emission, the hard bremsstrahlung x-ray production is removed, providing a wavelength-sensitive measurement.

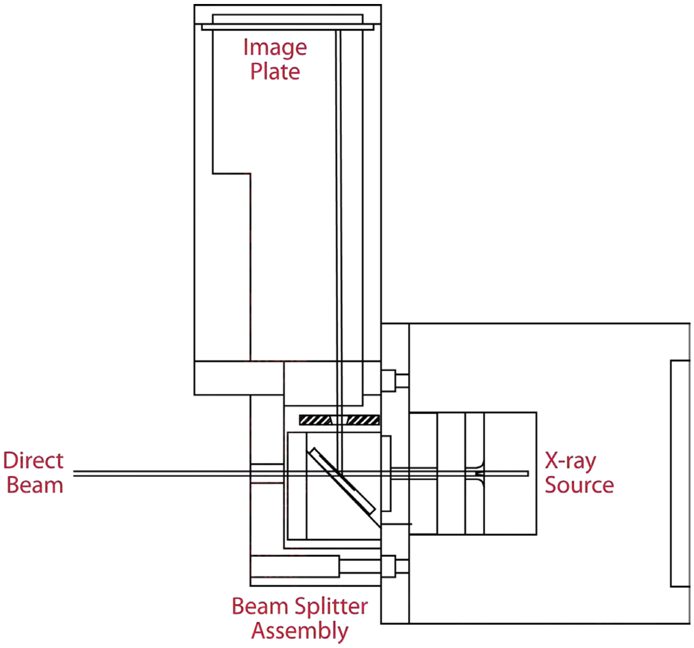

Figure 3. LiF (800) beam splitter intensity monitor shown for 0.71 Å x-rays

Figure 4 shows the static and dynamic XRD images from Experiment No. 100107-1 in which the 1 mm target disk was cut from plate aluminum 6061-T651 in accordance with ASTM-B209. With the typical grain size being greater than 100 µm, it was possible to observe individual grain reflections. The dynamic image shows broadening of the individual reflections along the Debye-Scherrer ring, which is indicative of dynamic mosaic crystal behavior observed in single-crystal aluminum by Turneaure (2009). The dynamic mosaic process is characterized by the fracture of larger grains whose remnants undergo small random rotations. This process, together with the microscopic residual strains, is thought to be responsible for work hardening of the material.

The XRD patterns in Figure 5 were obtained from a 1 mm thick disk of 6061-T6 sheet aluminum alloy fabricated from a 1/16 in. sheet. The typical grain size of this sample is clearly much smaller compared with the 6061-T651 plate aluminum alloy shown in Figure 4. A 0.1 µm gold layer was placed on one surface of the disk in Figure 5 for the reflectometry diagnostic. The gold (222) reflection is observed close to the plane of dispersion, indicating the deposition was highly oriented with (111) planes parallel to the surface.

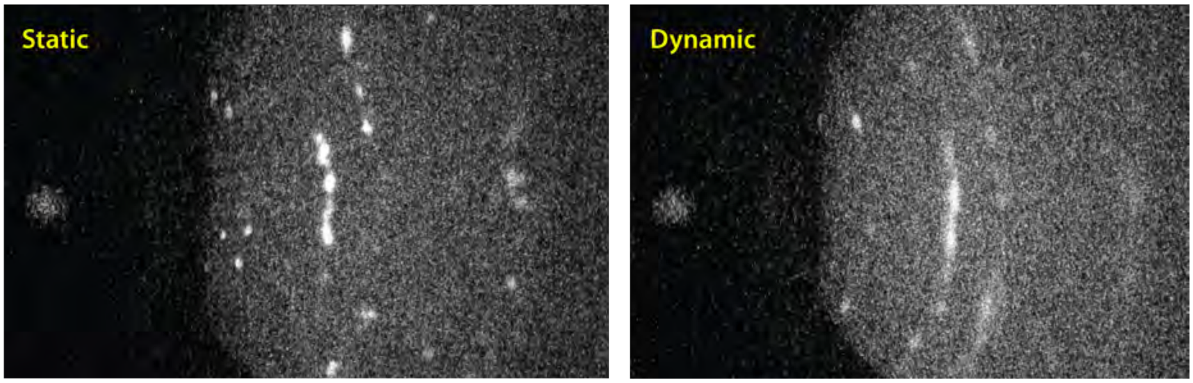

Figure 4. Static and dynamic 0.71 Å XRD images of the shocked free surface of plate aluminum 6061-T651 from Experiment No. 100107-1. The blurring of the reflections around the Debye-Scherrer ring is attributed to fracture and slight disorientation of grain fragments upon shock and release.

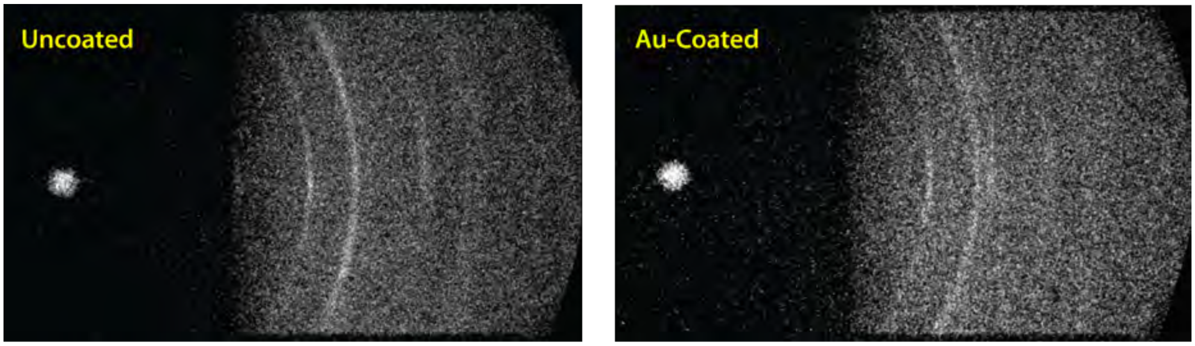

Figure 5. Static and dynamic line-outs from Experiment No. 100830-1 showing the XRD line shift to lower scattering angles caused by increased *d*-spacing

Figure 6 shows the integration of the static and dynamic XRD images near the plane of dispersion obtained using IDL software developed for this project. The inward shift of the XRD lines is shown to increase with increasing scattering angle, consistent with Equation (1). A least-squares fit of the diffraction lines was obtained with Jade 9.0 software from Materials Data Inc., generating output files containing the individual line intensities, mean scattering angle, and line widths. The shift in the Bragg angle versus the scattering angle is plotted in Figure 7 for the lowest-order reflections, along Equation (1) for $\Delta d/d = 1.21\%$. This value for strain is about an order of magnitude higher than what would be expected from thermal expansion for $\Delta T \sim 150$ K. The elongation of the crystal lattice in the direction of the uniaxial shock has been observed by Turneaure (2009), which has been shown to be indicative of work hardening.

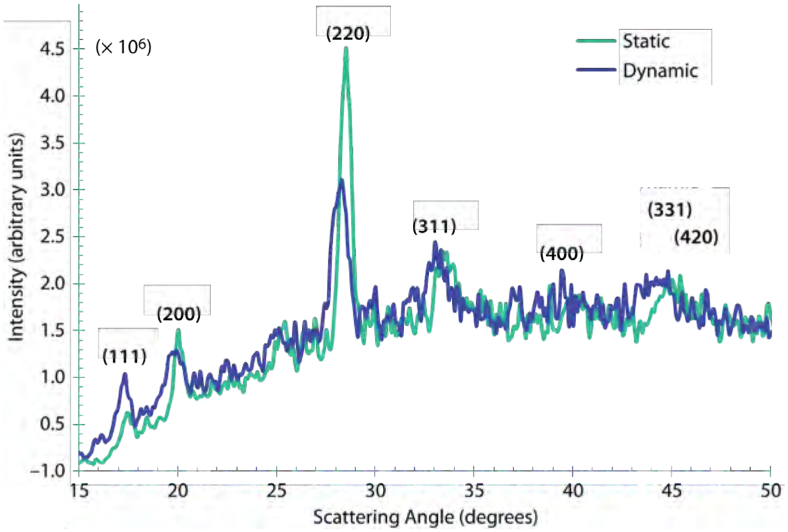

Figure 6. Plot of line shift vs scattering angle for shocked silver free-surface Experiment No. 100830-1 shows the shift to lower scattering angle associated with work-hardened lattice expansion in the shock direction

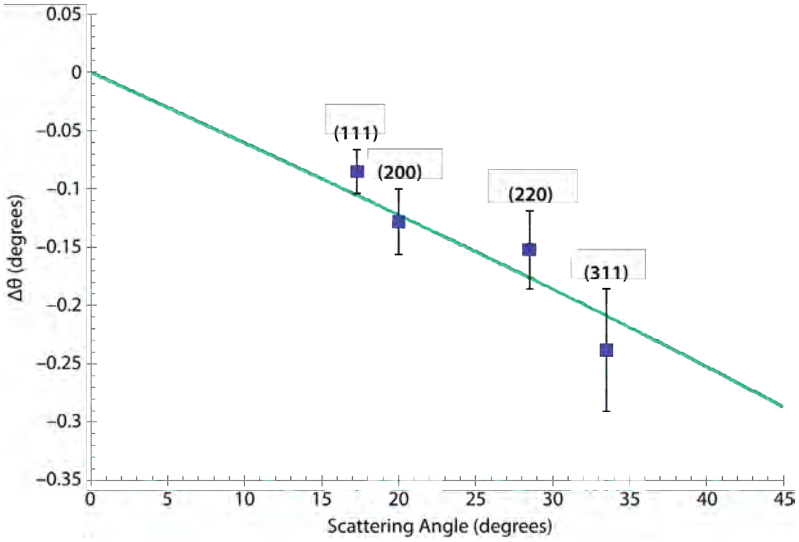

Figure 7. Plot of angular line shift vs scattering angle for Experiment No. 100830-1, showing the stretching of the microscopic lattice dimension in the direction of the shock. The solid line is the least-squares fit to the data, with $\Delta d/d$ = 1.21%.

Conclusion

We have demonstrated that single-pulse XRD can be used to measure the macroscopic strain and strain-broadening of shocked aluminum 6061-T6 and sterling silver free surfaces. Dynamic behavior of individual grains within the plate aluminum 6061-T6 was also observed. Although dynamic line intensity qualitatively was observed to decrease in dynamic experiments, the uncertainty of the beam splitter measurements made temperature measurements problematic. Analysis is continuing for the remainder of the single-pulse XRD experiments performed in FY 2010.

References

James, R. W., *The Optical Principles of the Diffraction of X-Rays*, Ox Bow Press, Woodbridge, Connecticut, 1982, 20–25.

Morgan, D. V., D. R. Macy, M. J. Madlener, J. G. Morgan, "Flash x-ray diffraction system for fast, single-pulse temperature and phase transition measurements," *IEEE Pulsed Power Conference Proceedings* (2007) 209–212.

Morgan, D. V., M. Grover, D. Macy, M. Madlener, G. Stevens, W. D. Turley, "Observations of shock-loaded tin and zirconium surfaces with single-pulse x-ray diffraction," *Powder Diffraction* **25** (June 2010) 138–143.

Morgan, D. V., D. Macy, G. Stevens, "Real time x-ray diffraction measurements of shocked polycrystalline tin and aluminum," *Rev. Sci. Instrum.* **79**, 11 (November 2008) 113904.

Murphy, W. J., A. Higginbotham, J. S. Wark, N. Park, "Molecular dynamics simulations of the Debye-Waller effect in shocked copper," *Phys. Rev. B* **78** (July 2008) 014109.

Turneaure, S. J., Y. M. Gupta, "Real time synchrotron x-ray diffraction measurements to determine material strength of shocked single crystals following compression and release," *J. Appl. Phys.* **106**, 3 (August 2009) 033513.

Walsh, J. M., R. H. Christian, "Equation of state of metals from shock wave measurements," *Phys. Rev.* **97** (March 1955) 1544–1556.

Warren, B. E., *X-ray Diffraction*, Dover Publications Inc., New York, 1990, 189–191.

this page intentionally left blank

IMPROVED UNDERSTANDING OF WINDOWS FOR OPTICAL SHOCK-WAVE DIAGNOSTICS

Dale Turley,[1,a] *David Holtkamp,*[b] *Gerald D. Stevens,*[a] *and Lynn Veeser*[a]

In shock wave equation-of-state experiments, a lack of understanding of the physical and thermodynamic behavior of optical windows and sample-to-window attachment methods can limit the accuracy and precision of dynamic pyrometry, radiance, and reflectivity measurements. In an attempt to understand the thermal conduction contribution of a glue layer, we studied the time-dependent radiance of a set of shocked tin samples, varied the glue thickness from 0 to 29 microns, and evaluated the effect of adding a 100–200 nm thick chromium film to the surface of the tin target. We also captured high-speed images and measured the spectral output (350–750 nm) of light generated by a lithium fluoride (LiF) window during a dynamic experiment. The light spectrum was broad and featureless and could have been generated from fracturing caused by shock waves reflecting from the window edges. We also measured the change in emissivity in the infrared spectral range (1.6 to 4.9 microns) of a tin sample at its interface with a LiF window upon release of a 25 GPa shock wave from the tin into the window. Emissivity changes for the sample, which was initially nearly specular, were small except for the longest wavelength band, where uncertainties were high because of poor signal-to-noise ratio at that wavelength.

Background

Optical reflectivity and radiance diagnostics for equation-of-state (EOS) temperature measurements and detection of phase transitions typically occur under a transparent window. This prevents the sample from expanding when the shock decays, keeping the sample near its shocked conditions long enough to do the measurement. Presently, such measurements suffer from problems related to the window attachment. A gap or glue surface between the optically emitting or reflecting surface and the window can affect the optical transmission and apparent emissivity, and unwanted light generated in the attached window can interfere with reflectivity and pyrometry measurements. These issues can raise uncertainty in absolute temperature measurements to greater than 10%, a value well outside the 1% uncertainty desired for EOS measurements. Although radiance is still viewed as the preferred diagnostic for dynamic temperature measurements, these uncertainties have eroded confidence in this method. In this study we investigated a number of these issues to determine the scientific basis of these effects and quantify their contribution to overall uncertainties in radiance-based temperature measurements.

---

[1] turleywd@nv.doe.gov, 805-681-2239

[a] Special Technologies Laboratory; [b] Los Alamos National Laboratory

Project

Glue Layer Effects between a Shocked Metal Sample and Window

Using time-resolved pyrometry we studied the heating effects of different window attachment methods, such as gaps, glues, and sputtered metal layers with glue. We studied a set of samples including no glue in the gap, thin glue layers (1–2 microns), and moderately thick glue layers (30 microns). The window and sample are at different temperatures after passage of a shock. This temperature difference begins to equilibrate quickly, making the temperature of the emitting surface differ from that of the sample region of interest. We executed a set of experiments that began to determine the magnitude of the effects of thermal diffusivity and conductivity of metals and windows in dynamic experiments.

The samples for this experiment were fabricated from highly pure tin. They were 1 mm thick and 40 mm in diameter. The tin was diamond turned on both sides to obtain highly specular reflectance. Above the tin a 10 mm thick, 38 mm diameter lithium fluoride (LiF) window was attached with a thin layer of Loctite 326 glue. Beneath the tin a PBX-9501 high-explosive (HE) charge (12.7 mm diameter by 12.7 mm high) was initiated at the bottom with an RP80 detonator and drove a shock into the sample.

Table 1 lists sample configurations and results of experiments executed to evaluate thermal equilibrium and the effect of glue and other layers on the temperature response of a shocked tin target. The optical velocimetry and radiance signals were relayed to their respective detectors from the experiment using a fiber-optic probe. Peak interface velocity was measured using PDV. Peak stress after the shock has passed through the interface was calculated from the velocimetry data using the energy conservation equations. Time-resolved radiance measurements were made using a three-channel photomultiplier-based pyrometer with optical band pass filters centered at 677, 830, and 1277 nm. The peak temperature and associated time profiles were calculated from the time-resolved radiance data. The radiometry data were converted to temperature using calibration curves and the literature value for the metal emissivity. The temperature rise time was estimated from the time required for the temperature to rise from the 10% to the 90% amplitude of the peak value. In the course of assembly and characterization of these samples, a new measurement method was developed that allowed measurement of glue layers with accuracy to ±0.5 µm (Marshall, 2010).

Figure 1 shows the measured temperature of the tin/LiF interface for the samples described in Table 1. The vacuum experiment shows the highest peak temperature, while the thick glue the lowest. The vacuum and thin glue show comparable rise times, while the thick glue has the slowest response. The chromium coatings show a slight increase in the rise time and are comparable in peak temperature to the vacuum experiment. The thick glue and 200 nm chromium coating show the largest departure from the nominal thin glue sample. Surprisingly, the peak temperature variations within this set of experiments are very low—within the 10% shot-to-shot uncertainty of typical dynamic pyrometry experiments.

Table 1. Summary of shock conditions and results

Sample	Glue Thickness (μm)	Experiment No.	Peak Interface Velocity (mm/μs)	Peak Stress (kbar)	Peak Temperature (K)	Temperature Rise Time (ns)
Thin glue	4.5	100531-1	1.313	240	1286	7.5
Vacuum	None	100601-1	1.367	252	1383	7.5
100 nm chromium	5.7	100531-2	1.291	235	1291	10
200 nm chromium	2.8	100602-3	1.342	246	1324	15
Thick glue	28.6	100602-1	1.405	261	1198	15

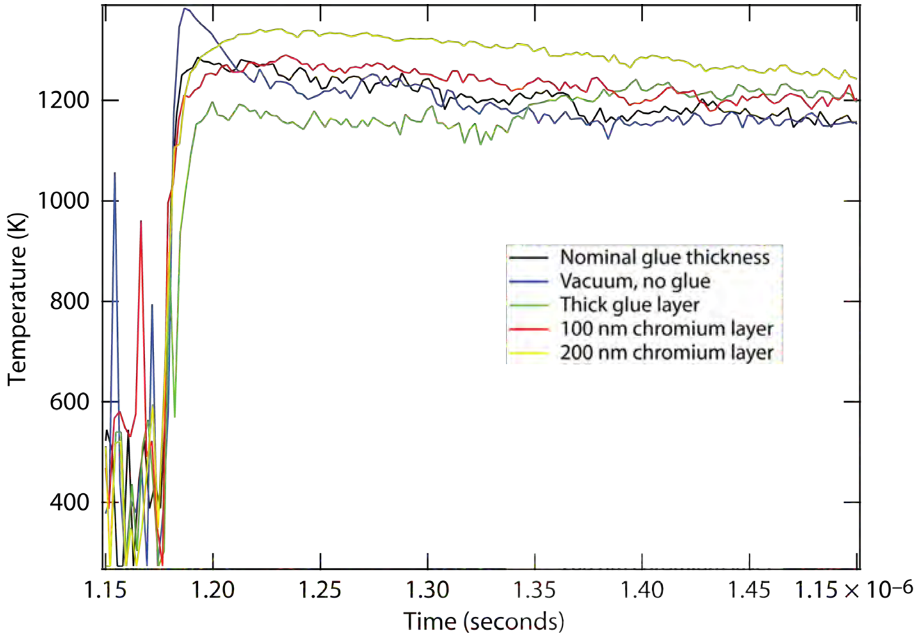

Figure 1. Shock-induced interface temperature vs time measured for the glue and metal film configurations described in Table 1. Shock arrival is at approximately 1.18 microseconds. Rise time and peak temperature data for Table 1 were derived from these data.

Tentative conclusions based on beginning modeling studies include the following. A vacuum in the gap may cause the interface temperature to increase because tin (released from the surface) is compressed in the gap. Filling the gap with a thin layer of glue appears to reduce this temperature increase. Making the glue layer thicker slows the temperature rise, as the compression takes longer, and further reduces the compression heating. The 100 nm chromium layer has little effect relative to the thin glue sample, while the thicker 200 nm coating appears to cause an increase in temperature. This may signal an optimum chromium thickness.

Shock-Induced Light Production in a LiF Window

As described in the background section, shock-induced light emitted from a LiF window is a key noise source for various optical diagnostics. Understanding the nature of this signal is an important step to designing methods to mitigate the problem. We performed experiments to determine the spectral content of this light and its physical origin. In both types of experiments, we selected an experimental package from previous studies known to generate significant light when shocked. This package (Figure 2) was composed of a 40 mm diameter and 1 mm thick aluminum cylinder with a 100 µm foil of tin attached to the surface. A LiF window (25 mm diameter and 10 mm thick) was attached to the top of the tin foil. This package was shock loaded using a 25 mm diameter by 8.8 mm high cylinder of PBX-9501.

Figure 3 shows the velocity profile of the tin/LiF interface measured using PDV. Also shown is the gate time for the optical spectrometer fitted with a gated, MCP (2 µsec width)–intensified linear array. Signals from photomuliplier tubes (PMTs) filtered at different wavelengths (355 nm, 450 nm, and 700 nm) showing the time history of light production are also shown. All signals were relayed

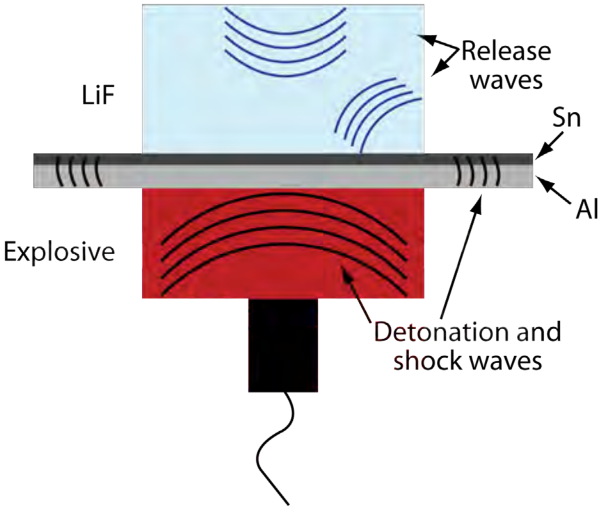

Figure 2. Sketch of explosive package used for the study of shock-induced light from a LiF window 25 mm in diameter and 10 mm thick. The metal target is 40 mm in diameter with a 100 µm tin foil attached to a 1 mm thick aluminum substrate. The explosive is a 25 mm diameter, 8.8 mm thick PBX-9501 cylinder.

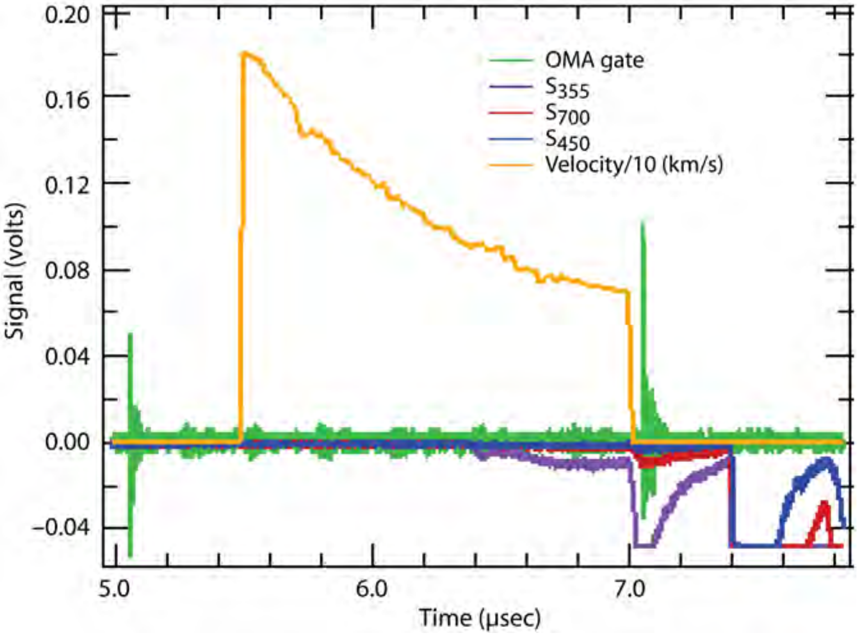

Figure 3. Velocity profile of the tin/LiF interface measured using PDV. Also shown is the gate time for the optical spectrometer fitted with a gated, MCP (2 µsec width marked by two green spikes)–intensified linear array. Signals from PMTs filtered at different wavelengths (355 nm, 450 nm, and 700 nm) showing the time history of light production are also shown.

from the experiment to the recording systems using a compact fiber-optic probe developed from previous shock experiments. A standard lamp was used to determine the system response and to allow correction of the collected spectra. Figure 4 shows spectra collected at two times during shock loading of this package. In both experiments the intensifier gate was opened before the shock wave arrived at the tin surface and then closed just prior to (black spectrum) or just after (red spectrum) shock arrival at the top surface of the LiF window. The spectra are nearly identical, broad, and featureless. These results are similar to those from a previous study evaluating the nature of light produced from fractured quartz (Hare, 2002).

In a supporting experiment a framing camera was assembled to determine the physical origin of this light, and selected results are shown in Figure 5. The experiment captured time-resolved images of a side view of the LiF window under shock load. In Figure 5, time increases from left to right. At the far left, the shock wave arrives at the edge of the window and light is generated. In the next frame, the shock wave has reflected from the window edge and a tension wave forms and begins to propagate inward and toward the window top. In the third frame, the shock has reached the window top and has collided with the PDV probe (bright spot at center of window top).

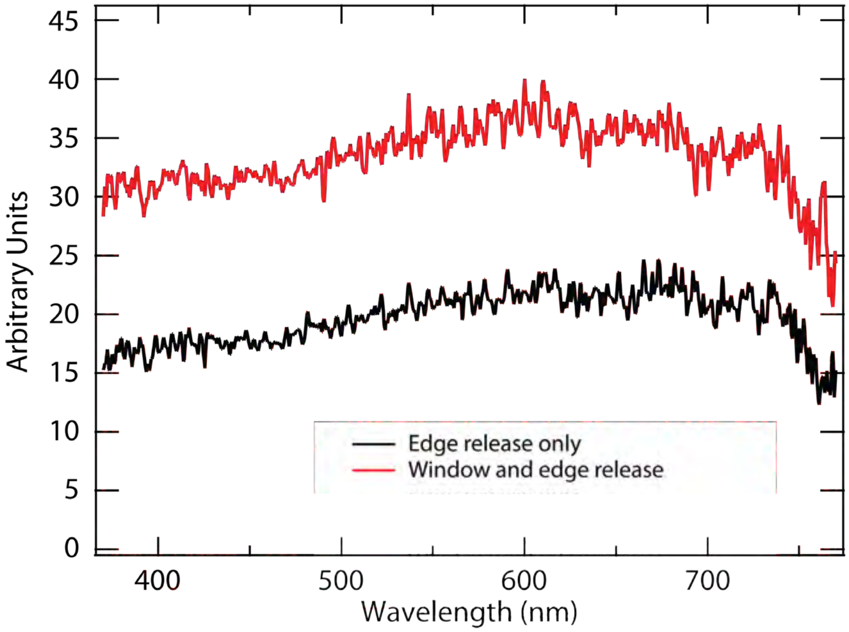

Figure 4. Optical emission from LiF light generated during a dynamic experiment. In both experiments the intensifier gate was opened before the shock wave arrived at the tin surface and then closed just prior to (black spectrum) or just after (red spectrum) shock arrival at the top surface of the LiF window. The spectra are nearly identical, broad, and featureless.

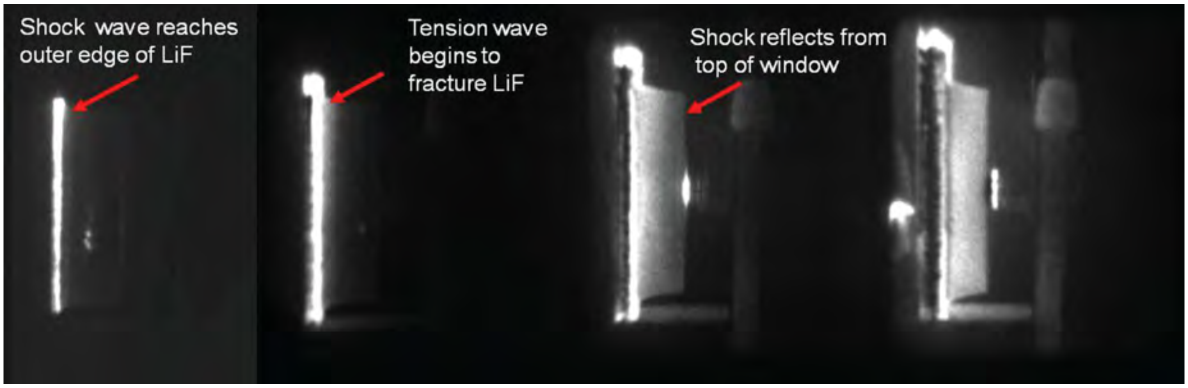

Figure 5. Framing camera images captured during dynamic experiment showing origin and development of light emitted from shocked LiF window. The experimental package in Figure 3 is viewed from the side and the shock wave propagates from left to right. The unshocked window is 25 mm in diameter and 10 mm thick. The integration time per frame is 100 ns and the interframe time is 500 ns.

This effort established a baseline for understanding the nature of this optical noise and will allow a mitigation effort to begin. Follow-on experiments would target solutions such as polishing the LiF edges and surrounding the window with black epoxy and impedance-matched buffers to reduce the magnitude of the tension wave.

Emissivity of Shocked Tin under a LiF Window

Another series of experiments aimed to measure the change in emissivity of a metal sample under a window at the time of shock release at the interface. Even with relatively large uncertainties, an emissivity measurement can greatly reduce the errors in deriving the temperature from the measured radiance. Relative to the shock-induced change in free surface emissivity, the emissivity under a window is not likely to change as much from a shock wave release because the window tamps the release, generally keeping the surface from roughening. We used tin samples, which we have studied in the past, and LiF windows, which impedance match well to tin and remain transparent at relatively high shock stress. The shock waves were explosively driven. Under these conditions tin changes from the beta phase to body-centered tetragonal when shocked and remains in that phase as the shock releases into the LiF.

The samples for this experiment, 3.5 mm thick and 40 mm in diameter, were fabricated from highly pure tin. The tin was diamond turned on both sides to obtain highly specular reflectance. A 5 mm thick, 38 mm diameter LiF window was attached to the tin with a thin layer of Loctite 326 glue. A PBX-9501 HE charge (12.7 mm diameter by 12.7 mm high) was initiated beneath the tin with an RP80 detonator and drove a shock into the sample.

Above the sample and window was a 30 mm diameter integrating sphere, which is highly reflective inside and has apertures for light to enter and exit. The upper surface of the LiF window sat flush to the outer surface of the integrating sphere, and the experiment was complete when the shock wave reached this surface. Inside the sphere was a glower (a small resistive coil) that was pulse-heated to a temperature of 1800–2000 K during the experiment and illuminated the sample indirectly when its thermal light scattered from the inside of the sphere onto the sample. This setup is illustrated in Figure 6.

The integrating sphere and the techniques for using it to measure an emissivity are described in more detail in Seifter (in preparation) and Turley (in preparation). The sphere was machined from aluminum and sandblasted to obtain a rough, high-emissivity inner surface. This inside surface is coated with gold, which has especially high IR reflectance. At the bottom of the sphere was an 8 mm diameter hole to allow light to reach the sample and also light reflected from the sample to go back into the sphere. The sample was illuminated with light from the hot glower inside the sphere. This light scatters several times, losing its directionality, before coming out through the bottom aperture and hitting the sample. A baffle below the glower keeps it from illuminating the sample directly. Near the top of the sphere, 12 degrees from the normal to the sample, is a 10 mm diameter hole through

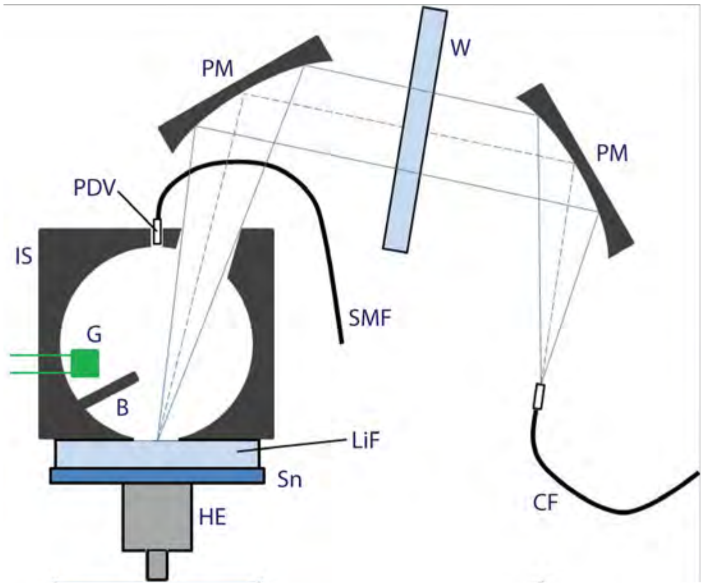

PM: Off-axis parabolic mirrors
W: Sapphire containment chamber window
PDV: PDV probe
IS: Integrating sphere
G: Glower
B: Baffle
SMF: Single-mode optical fiber for PDV
CF: Chalcogenide IR optical fiber
LiF: Window
Sn: Tin sample attached to window with thin glue film
HE: PBX-9501 high-explosive charge with detonator

Figure 6. Schematic of the experimental layout

which passed light that was reflected from the sample but not rescattered within the sphere. This light was collected by a pair of off-axis parabolic mirrors, one of which is outside the explosive containment chamber, and focused into a 1 mm diameter C2 chalcogenide optical fiber. The fiber runs to the detector housing, where the light is divided by mirrors and passes through optical bandpass filters into the detectors.

The detectors, which have been used in the past for pyrometry measurements, were liquid-nitrogen–cooled InSb IR photodiodes (PDs). They are DC–coupled and have linear response to >2 V output. Their response is not especially fast; a short pulse of light into a detector gives a signal with a rise time of about 100 ns. The bandpass filters restrict the detector input wavelengths to known limits. Nominally the centers of the bands are 1.6, 2.4, 3.4, and 4.9 µm.

A PDV probe was mounted in a 1.2 mm hole at the top of the sphere. The PDV measured the velocity of the tin/LiF interface to allow determination of the shock breakout time and the shock stress. In the case of the shortest wavelength pyrometer PD, the accepted band included the PDV laser wavelength. A narrow-band filter was used to block this light from the detector, and tests with the laser on and off confirm that there was no detectable laser signal in the in-band pyrometry detector.

Using this technique we measured the change in reflectivity and emissivity of a tin sample at its interface with a LiF window upon release of a 25 GPa shock wave from the tin into the window. Measurements were made over four wavelength bands between 1.2 and 5.4 µm (see Figure 7). Thermal emission backgrounds from the tin, glue, and LiF were successfully removed from the reflectance signals. Emissivity changes for the sample, which was initially nearly specular, were small except for the longest wavelength band, where uncertainties were high because of poor signal-to-noise ratio at that wavelength. A thin glue layer, which bonds the sample to the window, was found to heat from reverberations of the shock wave during its transition from the tin to the LiF. Around 3.4 μm the thermal emission from the glue is large compared to the tin, allowing a good estimate of the glue temperature from the thermal radiance. The glue appears to remain slightly colder than the tin, thereby minimizing heat conduction into or out of the tin immediately after the shock passage.

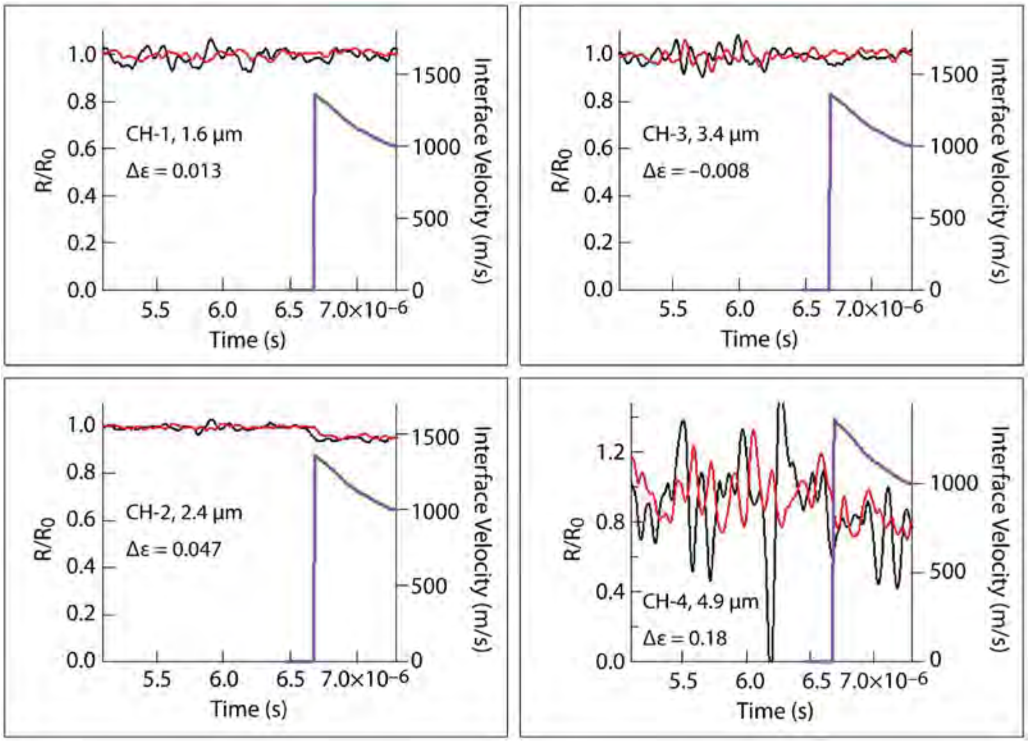

Figure 7. Relative reflectance signals R/R_0 for two experiments (red and black) and measured interface velocities (purple). Each graph shows data from one detector. R_0 is the initial reflectance of the tin sample, nearly 100%. Thermal backgrounds have been removed. The emissivity, ε, is determined from ε = 1 – R. Signal-to-noise ratio on the 4.9 μm channel, Channel 4, is low because of absorption in optical windows.

Conclusion

We have investigated radiance and emissivity of the interface between shocked tin, a LiF window, and the glue used to attach the two. We have established a baseline study of the effect of gaps, including glue of various thicknesses and sputtered chromium films on shock-induced thermal heating. We investigated the shock-induced visible light signature in a LiF window and determined it to be broad and structureless. Also, we found that the light originates at the outer edge of the window and may be associated with release waves and tension that cause the window to fracture. Finally, we measured the emissivity change of a diamond-turned tin sample during release of the shock wave into a LiF window. As anticipated, the emissivity remains relatively unchanged compared to a similar shock release into air because the window tamps the release and greatly reduces distortion of the metal surface. Knowing the emissivity of the metal takes us another step toward the goal of measuring the bulk temperature of a metal sample using optical pyrometry.

Three manuscripts summarizing these results have been written, and a follow-on SDRD project in FY 2011 will further these studies. All of these results, including the development of a new method to measure glue thickness, have caused strong interest from the stockpile stewardship program, and we anticipate these results will readily enhance the radiance-based EOS temperature experiments to be conducted at the Nevada National Security Site and other NNSA shock facilities.

Acknowledgments

We sincerely thank the following people who contributed greatly to the success of these experiments: Benjie Stone for sample preparation, Mike Grover for execution of the explosive experiments and sample preparation, Bob Corrow and Jason Young for operation of the radiometry systems, Stuart Baker and Josh Tybo for set up and operation of the MCP–intensified framing camera, and Gene Capelle for operation of the MCP–intensified, gated spectrometer.

References

Hare, D. E., N. C. Holmes, D. J. Webb, "Shock-wave-induced optical emission from sapphire in the stress range 12 to 45 GPa: Images and spectra," *Phys. Rev. B* **66**, 1 (2002) 014108.

Marshall, B. R., "Glue film thickness measurements by spectral reflectance," National Security Technologies, LLC, Las Vegas, Nevada, September 2010.

Seifter, A., A. J. Iverson, W. D. Turley, J. A. Young, M. Grover, D. B. Holtkamp, G. D. Stevens, L. R. Veeser, "Emissivity measurements of shocked tin using a multi-wavelength integrating-sphere," in preparation.

Turley, W. D., D. B. Holtkamp, B. R. Marshall, G. D. Stevens, L. R. Veeser, "IR emissivity change of a tin surface upon release of a 26-GPa shock into a LiF window," in preparation.

FOURIER TRANSFORM AND REFLECTIVE IMAGING PYROMETRY

Gerald D. Stevens[1,a]

A stationary Fourier transform pyrometer was used to record mid-wavelength IR spectra in dynamic shock experiments. The gated IR camera used with this system was also used to record images of light produced and light reflected from shocked metals in order to constrain the dynamic emissivity and provide temperature estimates. This technique will be referred to as reflective imaging pyrometry.

Background

Traditional dynamic (fast, ns time-resolved) pyrometry is performed using multiband photomultiplier sets. Multiband techniques suffer from poor spectral resolution, making it difficult to discriminate between the desired thermal radiance of a shocked sample and unwanted light sources such as triboluminescence, fractoluminescence, and high-explosive burn-product light. In addition, light is emitted from the glue layer that typically binds the shock-anvil (window) to the metal. In order to provide discrimination against these unwanted light sources, we designed a dynamic Fourier transform pyrometer (FTP) that would record the spectrum from 1.5 to 5.5 µm with greatly improved resolution.

A typical dynamic spectrometer (optical multichannel analyzer, spectral-streak) disperses a broad-spectrum source over an array of detectors using diffraction gratings, prisms, or other dispersive elements. Light at a given wavelength in such a spectrometer is incident on a single (or few) pixels. In order to improve resolution, one must restrict the input aperture of the spectrometer, thereby creating a trade-off between strong signal and high resolution. A stationary Fourier transform spectrometer (FTS) is an interferometer that does not suffer from this signal/resolution trade-off, since its resolution is determined by a maximum path-length difference in an interferometric cavity, not by a slit-width. An FTS is capable of efficiently collecting light from a large-area, divergent light source while maintaining good spectral resolution. In dynamic shock physics experiments, the shocked metal is typically large and emits light into 2π. A mid-wavelength infrared (MWIR) FTS (which we are calling a Fourier transform pyrometer for our applications) is ideally suited for such experiments. Also, in our design, light from a given wavelength creates a spatial interference pattern across an entire two-dimensional array. For an array with N pixels, this causes a factor of $N^{1/2}$ improvement to the signal-to-noise ratio and is known as the multiplex, or Fellgett's, advantage.

---

[1] stevengd@nv.doe.gov, 805-681-2219

[a] Special Technologies Laboratory

Project

FTP Design

One of the simplest and most versatile stationary FTS designs is based on the Sagnac interferometer (see Figure 1), with the mirror farthest from the beam splitter (lower right corner of Figure 1) tilted slightly to produce an interference pattern (Barnes, 1985). We chose to use this design along with a liquid nitrogen–cooled Santa Barbara Focalplane 191E camera with an InSb detector array sensitive from 1 to 6 µm (Stevens, 2010). The camera has 20-micron pixels and a minimum exposure time of 460 ns. The FTP cavity has gold mirrors, a CaF_2 beam splitter, and a Janos NYCTEA 1.5–5.5 µm, 100 mm focal length F2.3 imaging lens. Thermal light was collected and sent through the interferometer with an off-axis parabolic collimator with a 12.7 mm focal length.

Light enters the interferometer and is split into two components that interfere at the mirror (see lower right corner of Figure 1). The two interferometer path lengths are equal at the center of this mirror, and the path-length difference (or retardation) increases to each side of the axis of rotation. The periodic pattern that results is imaged onto a detector (inset, Figure 1); for a simple monochromatic source, the periodicity of the interference pattern is directly proportional to the wavelength of the input light. Taking an FFT of a collapsed line-out of this pattern gives a single frequency that may be calibrated using the alignment laser's wavelength.

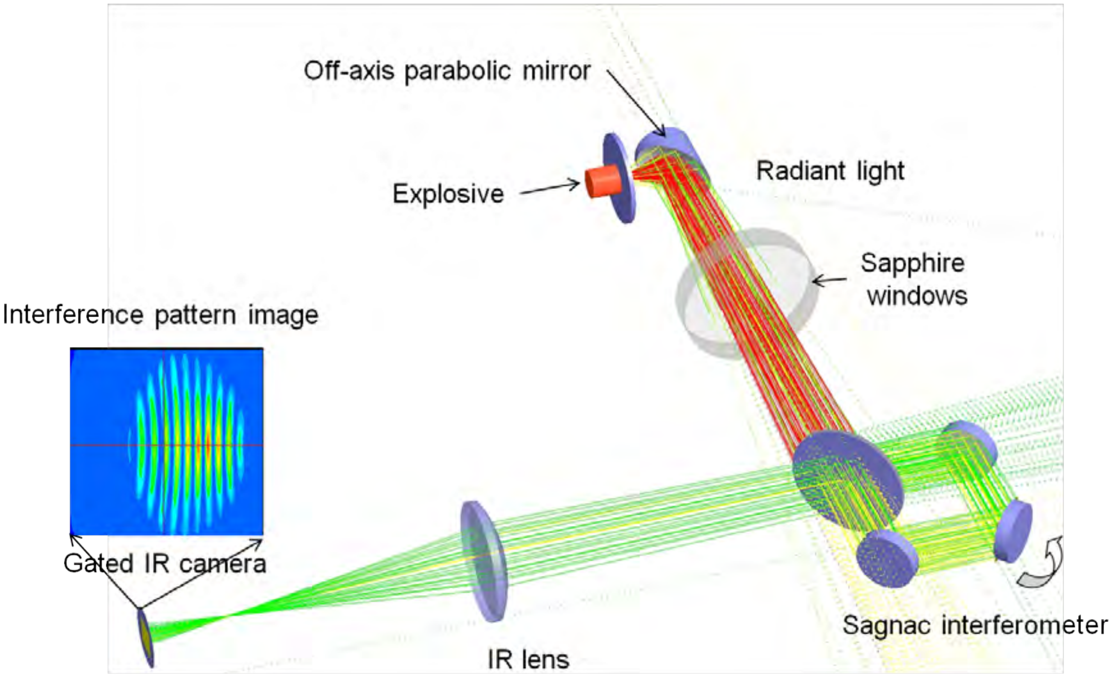

Figure 1. Sagnac interferometer–based stationary FTP. The inset shows a representative relayed image of the interference pattern that forms at the rotated mirror.

For an imaging array with N = 640 pixels, each of width w = 20 µm, an FFT gives 320 frequency bins, each separated by $1/(320w)$ cm^{-1}. Because the spectrum of interest (1.5–5.5 µm) spans only about half of the total range of frequencies observable by an FFT (but not observable by the detector), we effectively have 160 frequency bins over the detector spectrum. For our input spectrum, the resolution ranges from about 1 nm at 1500 nm to about 10 nm at 5500 nm.

The shape of the spectrum recorded by the FTP is dominated by the sensitivity of the camera array and the transmission properties of the mirrors, windows, air, glue, and lenses used in the setup. In order to correct recorded spectra for the system response, measurements were made of a high-temperature blackbody with the same optical components that were present in the dynamic experiment. At 1000°C, the blackbody emission spectrum has an adequate amount of 1.5–5.5 µm light to measure and determine a correction for the system response over the full range. This high-temperature correction is then applied to dynamic spectra and also lower-temperature blackbody spectra.

Figure 2 shows collapsed blackbody interference patterns (2a) and their corresponding uncorrected raw (2b) and corrected (2c) spectra. A fit to each spectrum using a blackbody distribution with a variable fit temperature was performed, and the results are shown in Figure 2d. Note that Figure 2a shows the interpolated and collapsed interference patterns that were reduced using a technique described in our FY 2009 SDRD project (Stevens, 2010).

A corrected spectrum is shown in Figure 3 for a dynamic experiment, Number 100715-1, which consisted of PBX-9501 driving 2 mm of tin, with 3.9 µm of Loctite 326 glue, and a 5 mm lithium fluoride (LiF) window. This figure shows the corrected spectrum (green) along with an estimated combined spectrum (red) of 1050°C tin with an emissivity of 0.08, with an arbitrary glue contribution at the same temperature. The polyurethane methacrylate–based Loctite glue has absorption and emission bands that are apparent in the fit at 3 and 3.5 µm. While there are similarities between the "educated-guess" estimated spectrum and the measured spectrum, it is not clear that the signal-to-noise ratio for this experiment would allow for independent determination of the glue and tin temperatures, despite their very different spectral characteristics. Nevertheless it is apparent that this method has the potential to show spectral information, which can help identify the individual glue and metal emissions that cannot be obtained in a normal pyrometric experiment.

Reflective Imaging Pyrometry

Our work measuring dynamic reflectivity (Turley, 2011) indicates that highly polished or diamond-turned metals beneath transparent shock-anvil "windows" remain very smooth and reflect light in a primarily specular manner after being shocked. We have also found from previous IR imaging experiments that there is a good degree of spatial uniformity in the radiance of a diamond-turned metal sample across its shocked region. These two observations suggested that imaging pyrometry might be possible with a configuration somewhat simpler than the reverse-illumination integrating sphere geometry previously applied (Turley, 2011). We tested such a configuration and technique, which we came to call reflective imaging pyrometry.

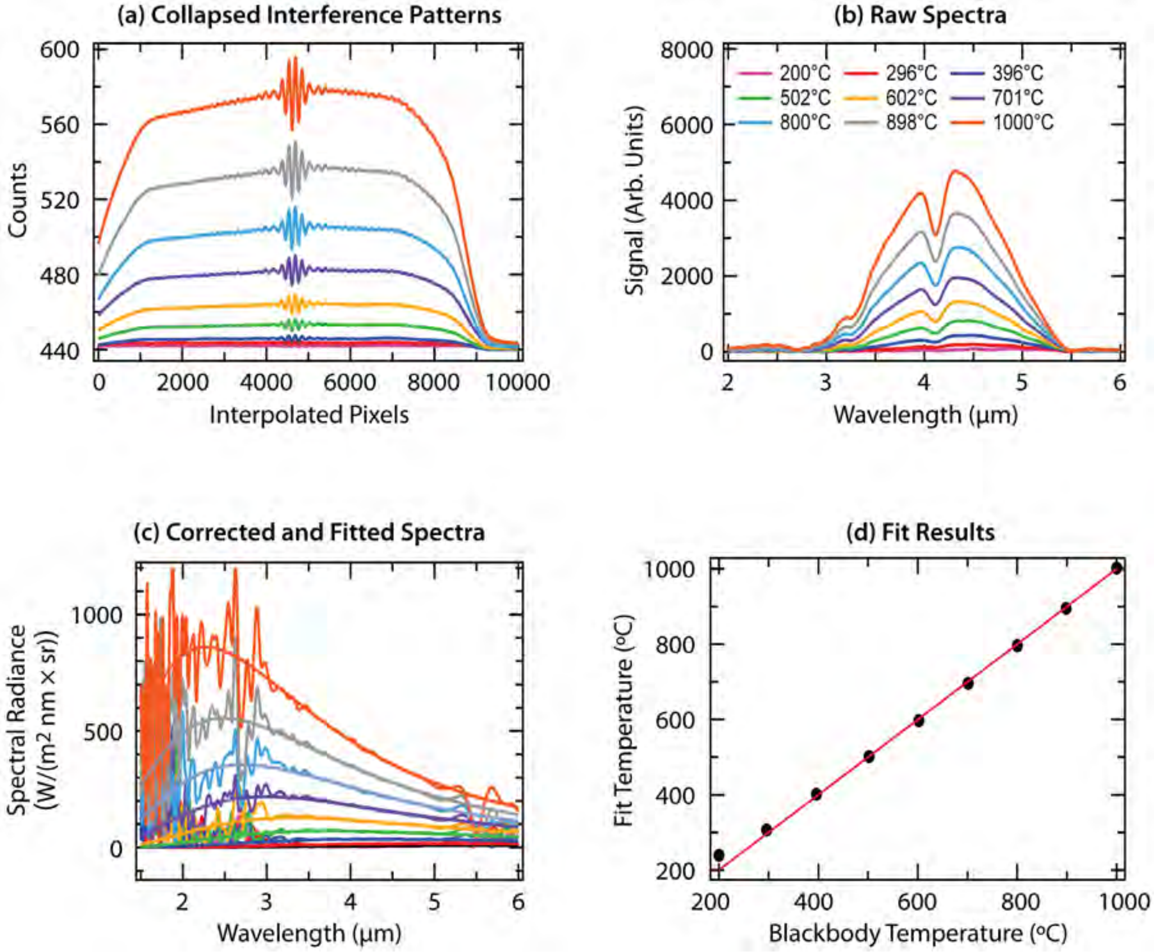

Figure 2. (a) Blackbody interference patterns, (b) corresponding raw spectra, (c) corrected and fitted spectra, and (d) comparison of blackbody fit and measured temperatures. The red line in (d) shows perfect agreement for reference.

For polished, mirror-like surfaces, the simplest way to measure reflectivity is to measure the intensity of a light source and the intensity of the same source reflected from the surface. Setting an extended source (a hot, 200°–300°C black block of aluminum) with high emissivity ($\varepsilon_{\text{paint}}$ ~ 1.0) next to the reflective sample and recording an IR image of both the source and its reflection, one may determine the sample's reflectance by simply dividing the two recorded light levels. Upon shock arrival, a material may experience a change in reflectivity and an increase in emitted thermal light. Measuring the emitted light level and knowing the sample's initial and dynamic reflectivities, one may determine the temperature of the shocked material. Placing a cold block of aluminum beneath the heated block allows determination of the emission from a shocked region without significant contributions from room-temperature background light.

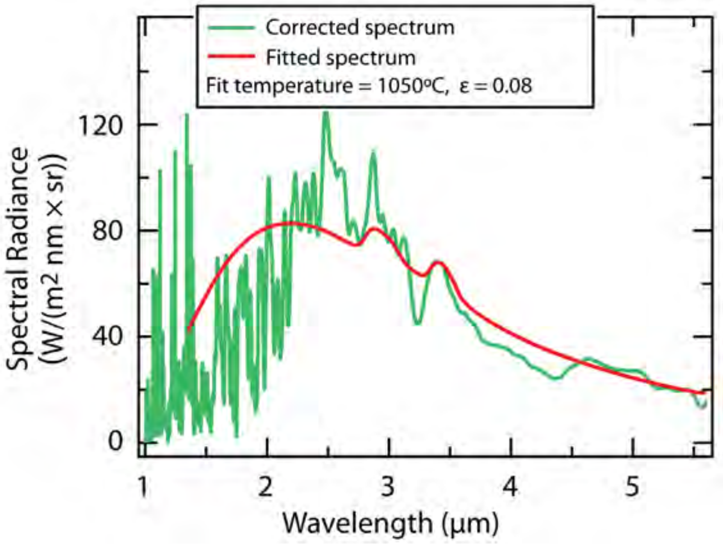

Figure 3. Experiment 100715-1 data plot, showing the corrected (green) and fitted (red) spectra. A small contribution from glue (bumps at 2.9 and 3.3 µm), assumed to be at the temperature of the tin, was included in the fit.

Figure 4 shows a sample and light-source geometry that (with a few caveats) provides enough information to deduce the static and dynamic reflectivity, and temperature of a shocked sample. There are five signal levels of interest in the image (labeled $S_1 - S_5$). $S_1 - S_4$ represent signals reflected off of the tin sample, where S_2 and S_4 both contain additional radiance from the shocked tin area. S_5 is the initial signal from the heated block. These are, to first order (neglecting the 2% surface reflection of LiF and ~2% absorption of LiF), related as follows:

$$S_1 \sim 0 \tag{1}$$

$$S_2 = \varepsilon'_{Sn}\,\Lambda_{Sn} \times \tau'_{glue} + \varepsilon'_{glue}\,\Lambda_{glue} + S_1 \tag{2}$$

$$S_3 = S_5 \times (1 - \varepsilon_{Sn}) \times \tau_{glue}^{2} \tag{3}$$

$$S_4 = S_5 \times (1 - \varepsilon'_{Sn}) \times \tau'^{2}_{glue} + S_2 \tag{4}$$

$$S_5 = \varepsilon_{paint}\,\Lambda_{hot\text{-}block} \sim \Lambda_{hot\text{-}block}. \tag{5}$$

Prime values such as τ'_{glue} refer to post-shock arrival. $\tau_{glue} = (1 - \varepsilon_{glue})$ is the transmission through the glue, $\varepsilon_{Sn} = 0.07$ is the initial emissivity of the tin, Λ_{Sn} is the shocked-metal blackbody radiance, and Λ_{glue} is the shocked-glue blackbody radiance. One may determine the initial transmission of the glue, τ_{glue}, by solving Equation 3. Because we started with a diamond-turned, low-emissivity tin sample, the contribution from the glue cannot be neglected. Either removing the glue from the experiment or using the technique for metals with ε closer to 1 would be desirable.

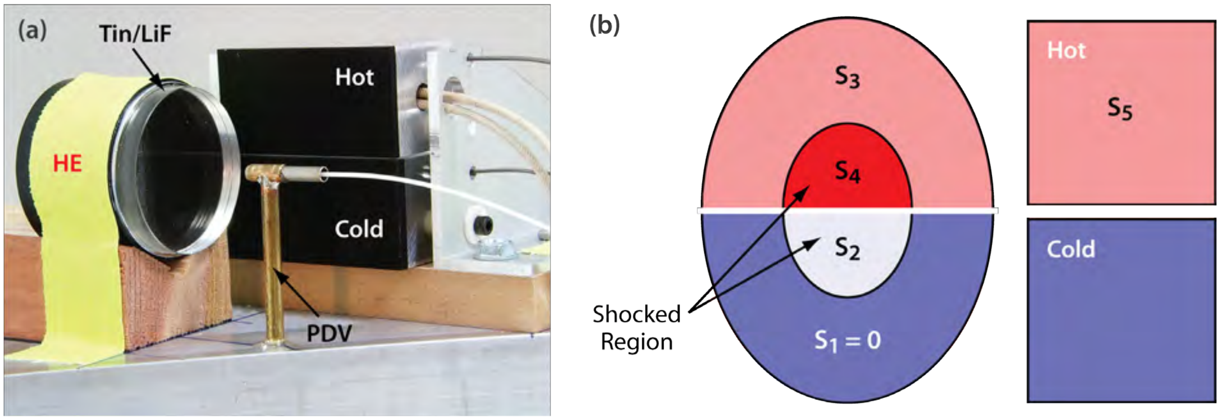

Figure 4. (a) Experimental setup of hot and cold, high-emissivity surfaces and reflective tin and LiF shot assembly. Surface velocity was measured by the PDV probe. (b) The regions of interest and signals recorded (S_1–S_5) from a dynamic IR image.

Notice that non-negligible glue absorption and transmission τ_{glue} complicates the equations considerably, and this pyrometric technique, like most other techniques, does not have any means of differentiating between glue and tin radiance. From the FTP work we did, we can estimate the radiance contribution from the glue to be about 20% of the net signal level.

Figure 5 shows a dynamic recorded thermal image for the geometry shown in Figure 4. This image was recorded for a 2 mm thick tin sample with a 5 mm thick LiF window shocked with PBX-9501 high explosive. The image was taken with a SBFP-134 IR camera, and had a 156 ns total exposure that began about 60 ns after the shock reached the tin surface. The radiance from the two shocked

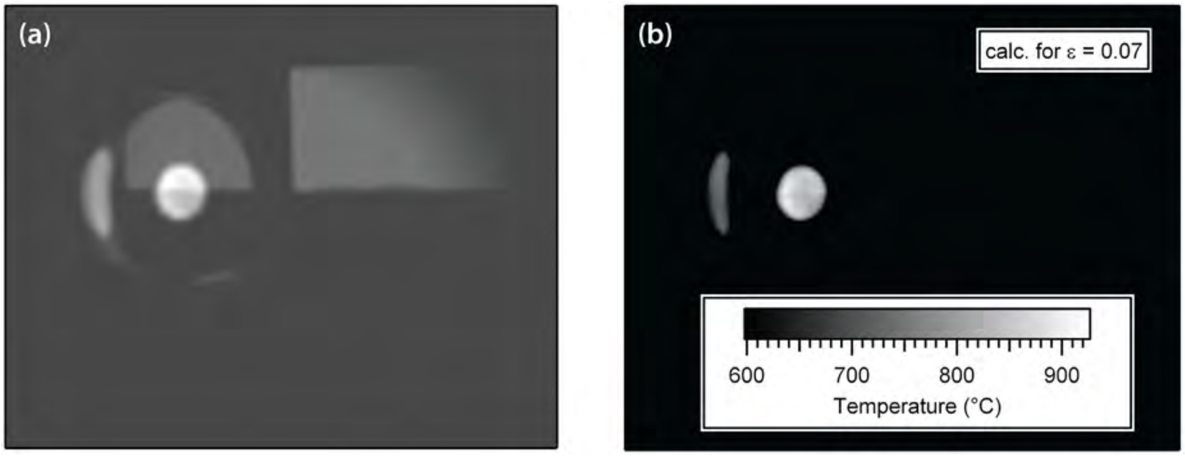

Figure 5. (a) Experimental thermal image of hot and cold, high-emissivity surfaces and reflective tin and LiF shot assembly; and (b) the same image after subtraction of a preshot image and calibration

regions (S_2 and S_4) are comparable to each other once one subtracts the baseline reflected light S_3. This indicated little detectable change in emissivity for the tin/glue combination, or in terms of Equations 1–4, $\varepsilon'_{Sn} \times \tau'_{glue} \sim \varepsilon_{Sn} \times \tau_{glue}$. Subtracting the preshot image and using a temperature calibration performed prior to the shot, we calculated the temperature of the shocked region, which is shown on the right in Figure 5. The average temperature for this experiment (a 2 mm sample shocked with PBX-9501) is about 825°C, consistent with prior work of Mabire (2000).

Conclusion

Two different MWIR pyrometry techniques were developed and tested. Both techniques provided valuable information about shocked radiance that extends our understanding of the limitations of pyrometry. The FTP showed spectral signs of the glue contribution, while the reflective imaging pyrometry technique verified that there is little dynamic change in emissivity for polished tin under a window.

References

Barnes, T. H., "Photodiode array Fourier transform spectrometer with improved dynamic range," *Appl. Opt.* **24**, 22 (1985) 3702–3706.

Mabire, C., P. L. Hereil, "Shock induced polymorphic transition and melting of tin," *AIP Conf. Proc., 1999 Shock Compression of Condensed Matter,* **505** (2000) 93–96.

Stevens, G. D., B. R. Marshall, "Fourier transform spectrometer," *Nevada Test Site–Directed Research and Development*, FY 2009, National Security Technologies, LLC, Las Vegas, Nevada, 2010, 105–112.

Turley, W. D., D. Holtkamp, G. Stevens, L. Veeser, "Improved understanding of windows for optical shock-wave diagnostics," *Nevada National Security Site–Directed Research and Development*, FY 2010, National Security Technologies, LLC, Las Vegas, Nevada, 2011, 11–20.

this page intentionally left blank

SINGLE-SHOT DETECTION OF PHASE TRANSITIONS USING THZ SPECTROSCOPY

Craig A. Kruschwitz,[1,a] *Michael Berninger,*[a] *and Robert A. Buckles*[b]

This project aimed to prove the concept of using time-resolved terahertz (THz) spectroscopy as a melt/phase change diagnostic on a single-shot experiment. Recent work has indicated that THz reflectance spectroscopy can be used to detect solid-solid phase transitions in metals and metal alloys. These experiments, however, used a Fourier transform infrared spectrometer that required lengthy scans to obtain a single spectrum. This SDRD project attempted to move the technology a critical step further by proving the concept in single-shot experiments, which is essential for a usable phase diagnostic for shock physics experiments. Experiments were attempted at the NSTec Livermore Operations THz facility, but were unsuccessful due to equipment problems.

Background

This SDRD project attempted to further explore phase transitions and laser-induced shock dynamics using time-resolved terahertz (THz) spectroscopy. Because a solid's THz spectral fingerprints are sensitive to its lattice structures and components, THz spectroscopy provides a powerful and sensitive method to identify solid-solid phase transitions. Combined use of laser-induced shock in a solid and time-resolved THz spectroscopy can generate a pump-probe scheme to study shock dynamics.

In the last few decades, experiments with hundreds-of-picoseconds time resolution using either impact or laser-driven shocks have been demonstrated in which picosecond, time-resolved, nonlinear coherent anti-Stokes Raman spectroscopy (CARS) was used to monitor shock-induced chemical reaction propagation on a metal surface, or vibrational sum-frequency generation (SFG) was used to watch a planar laser-driven shock front pass over a thick layer of molecules. We proposed to use time-resolved THz spectroscopy to study shock dynamics inside of solid metals on the same time scale. We expected that detection sensitivity of linear absorption THz spectroscopy would be much higher than for techniques such as CARS, SFG, and Raman spectroscopy (Carr, 2003).

Recent work (Kruschwitz, 2008; 2010) has demonstrated the feasibility of using THz spectroscopy to detect changing THz spectral signatures arising from solid-solid phase transitions in a metal/alloy. Experiments were conducted at the National Synchrotron Light Source (NSLS) at Brookhaven National Laboratory in FY 2007 and FY 2009 on the U12IR and U4IR infrared beam lines, respectively. These experiments used the synchrotron source and a Fourier transform infrared (FTIR)

---

[1] kruschca@nv.doe.gov, 505-663-2023

[a] Los Alamos Operations; [b] Livermore Operations

spectrometer with a reflectance setup to study the phonon spectrum for AuSn alloy and Sn foils. A heating/cryogenic cooling system was used to induce phase transitions in the samples. With this setup, attempts to detect static high-temperature solid-solid phase transitions in AuSn were successful, and dynamic pump-probe experiments using a high-intensity Ti:sapphire laser as a shock source were planned for the summer of FY 2009. While these experiments are an essential demonstration of the physics, the FTIR setup would not be compatible with a single-shot experiment. The FTIR-based experiments require long scans be performed to obtain a single spectrum, and, in the case of the pump-probe dynamic experiments, a single measurement requires several laser shots.

In FY 2010 we proposed to take the concept of time-resolved THz spectroscopy as a phase diagnostic a critical step further by demonstrating the technique in a single-shot setup. SDRD research at Livermore Operations (LO) (Buckles, 2008) over the past several years has led to the development of a THz spectroscopy system capable of measuring a spectrum with a single shot. This system provides an ideal opportunity to demonstrate the feasibility of a THz spectroscopy dynamic phase-change diagnostic that would be usable on a variety of shock experiments. We intended to adapt the current THz spectroscopy setup used by Buckles (2008) to perform pump-probe reflectance measurements, adding a high-intensity laser to induce the phase transitions. We planned to study Sn (investigating the beta-gamma phase transformation, which occurs near 9 GPa), and possibly Bi, given its rich solid phase structure in the 2 to 9 GPa pressure region. Prior to shock experiments, however, we proposed to conduct some preliminary static measurements to characterize the system and compare to results obtained at the NSLS in 2007 and 2009.

The phase structure of tin was of principal interest in the static experiments we performed in FY 2007 and 2009, and remained of some interest in this year's work. The transition from the low-temperature α phase (gray) to the high-temperature β phase (white) begins around 13°C. Gray tin has a diamond crystal structure, while white tin has a body-centered tetragonal crystal structure. The phonon density of states for the two phases is markedly different, as has been simulated using density functional theory methods and demonstrated by neutron diffraction experiments (Pavone, 1998). Tin, therefore, was an excellent candidate for our investigation, all the more so given its frequent use in shock experiments. Results from 2007 (Kruschwitz, 2008) and 2009 (Kruschwitz, 2010) were somewhat promising, but far from conclusive.

In FY 2009 we also investigated the phase structure of AuSn alloy with Sn atomic percentage between about 10% and 18%. At these concentrations and between the appropriate temperature ranges (above about 330 K), the alloy exhibits its ζ phase, a hexagonal close-packed structure. At temperatures below this range, the alloy exhibits some mixture primarily of the Au face-centered cubic phase and an Au_5Sn intermetallic compound structure (Chevalier, 1988). We planned to conduct some static experiments. The 2009 results strongly suggest that phase transition to the ζ phase was in fact obtained (Kruschwitz, 2010).

Project

The LO THz facility uses pulses from a femtosecond laser to produce pulses of THz radiation via either optical rectification or with a photoconductive antenna (also known as an Auston switch). Similar methods are used to detect the THz pulse. We refer the reader to previous work on the subject (Buckles, 2008) for a more detailed description of the THz generation/detection process. Figure 1 shows a typical THz time-domain waveform generated from the system and the Fourier transform of the waveform to yield the THz spectrum. The normal mode of operation for the facility is to collect a complete THz spectrum using a number of laser pulses, stepping through the entire THz pulse in small time steps. However, the LO facility is also capable of collecting a complete spectrum in a single laser pulse using a data collection method called optical sampling. With this method, which is illustrated in Figure 2, the laser pulse and the THz pulse intersect the electro-optic sampling crystal at an angle. This induces a temporal skew in the probe wave front relative to the THz wave front so that different points across the transverse probe beam field see the THz field at different times. Therefore, the time dependence is essentially mapped across the length of the crystal.

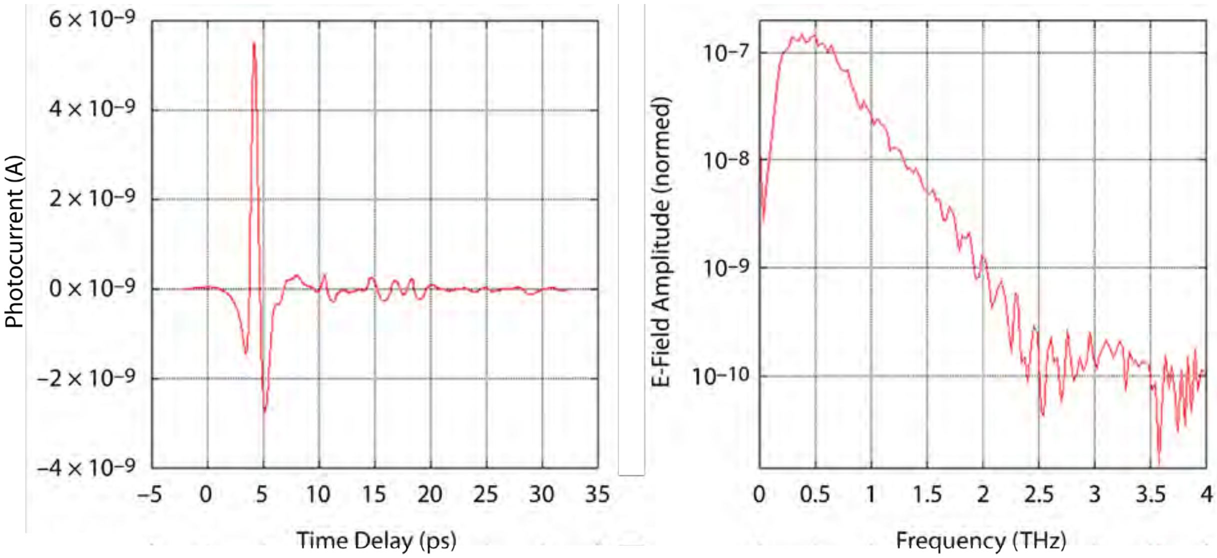

Figure 1. (left) Typical THz time-domain signal obtained at the LO THz facility; (right) Fourier transform of the time-domain waveform yielding the THz spectrum

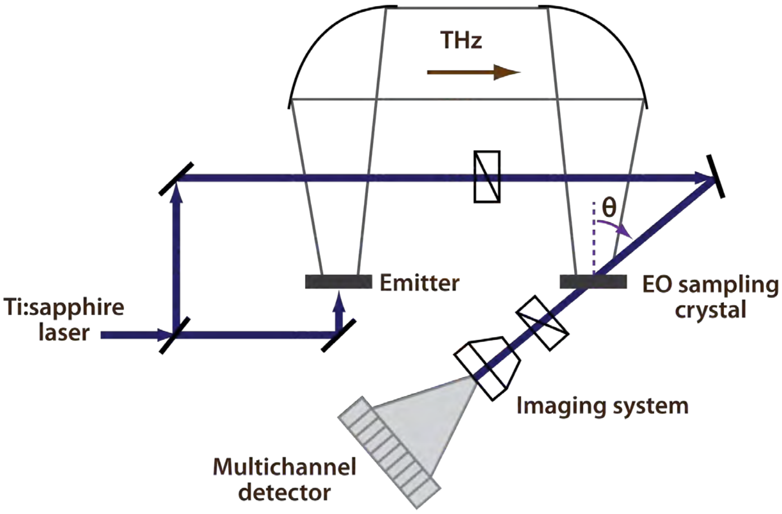

Figure 2. Schematic illustrating the principle of optical sampling. This method allows a full THz spectrum to be obtained in a single shot, rather than with multiple steps.

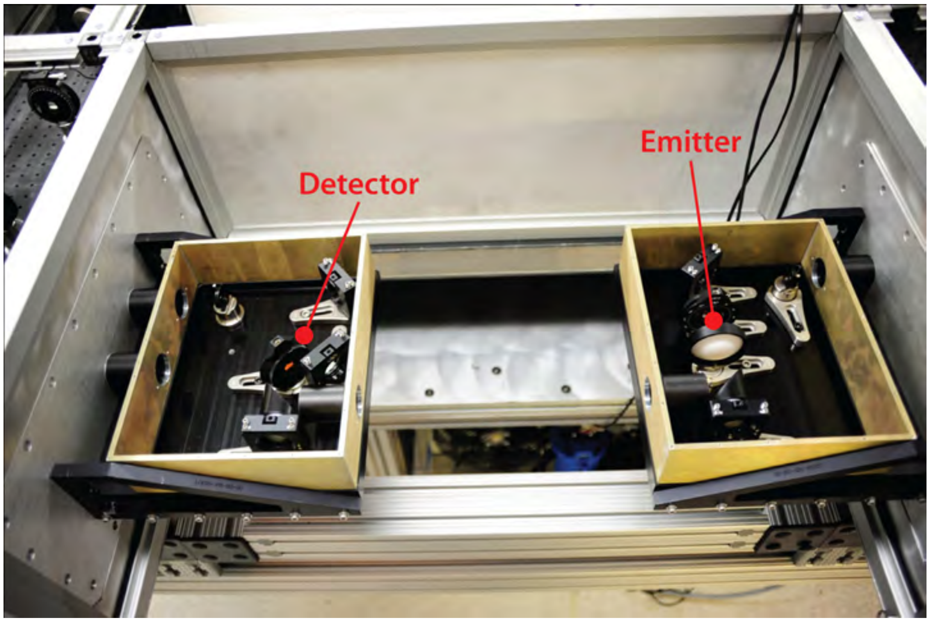

Figure 3. Sample region at the LO THz facility into which the Bruker Optics reflection sample mount had to be fitted

We proposed to conduct the experiments in two different phases. In the first phase, static experiments (no laser shock source would be used) would investigate how the system performed for reflectance measurements and in single-shot–data-collection mode. For this initial set of experiments, we planned to investigate the AuSn alloy previously studied and possibly Sn, Bi, water/ice, and water vapor. The second phase of the experiments would have been dynamic experiments using the laser shock source. These experiments would have most likely involved studying Sn and Bi.

Before experiments could be performed, however, modifications to the Bruker Optics reflection mount used in 2007 and 2009 needed to be made. The reflectance mount needed to fit in the confined space where samples were placed (Figure 3). Also, for the static experiments in particular, a method for raising and lowering the sample temperature needed to be incorporated into the design. Because of space limitations and problems with the liquid helium transfer line, the cryostat/heating unit used at the NSLS was not suitable for use at the LO THz facility. Thus, separate heating and cooling units were procured and designs were produced that allowed for samples to be heated and cooled in situ in the sample holders in the reflectance unit. Furthermore, a purge box was fabricated to allow the sample environment to be purged with dry nitrogen to improve the THz signal. The heating unit we obtained allowed us to achieve temperatures significantly higher than what was achievable with the cryostat/heater combination. In fact, temperatures above the melting point of Bi were possible. Thus, to enable us to detect this solid-liquid transition, we engineered a method to turn the reflectance stand vertically, so that the Bi liquid would remain confined in the sample region. Figure 4 shows the reflectance unit in its various configurations as well as the purge box.

In preparation for the dynamic experiments planned as a follow-up to the static experiments, we identified a laser we thought might be suitable as a shock source. The equipment necessary for fielding a photonic Doppler velocimetry probe on the dynamic experiments was also obtained.

Unfortunately, the Quantronix femtosecond laser, which is required to produce the THz radiation, was damaged early in the fiscal year and was not restored to working condition until quite late in the year; this delay, along with unforeseen difficulties incorporating the Bruker Optics reflectance unit into the LO THz sample region, hindered progress. Despite several attempts over the course of the year to conduct the static experiments, we could not obtain even these preliminary data.

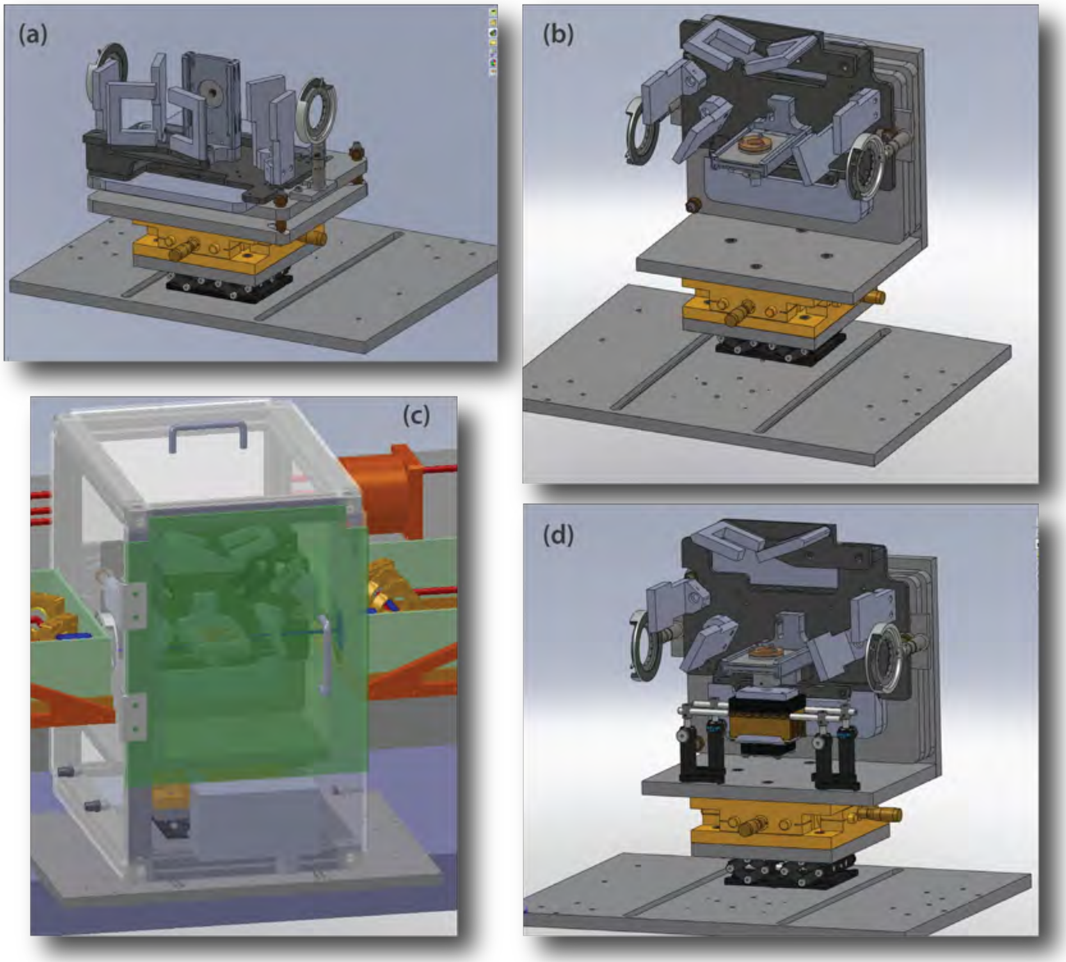

Figure 4. Schematic of reflectance unit in its various experiment configurations: (a) horizontal; (b) vertical with heating unit; (c) purge box with reflectance unit in vertical configuration; and (d) vertical with cooling unit

Conclusion

We attempted experiments this year that aimed to take the technique of detecting phase transitions with THz spectroscopy a step further than work done under previous SDRD projects (Kruschwitz, 2008; 2010). We planned to use the THz facility at LO (Buckles, 2008) to detect solid-liquid and solid-solid phase transition with a single THz pulse, first in a static configuration using heating and cooling units and later in dynamic experiments using a high-power laser shock source to induce phase transitions. Unfortunately, due to equipment issues, we were unsuccessful in obtaining even the static data. It would still be interesting to investigate solid-solid and solid-liquid phase transitions at the

LO THz facility, or a similar facility. In contrast to the NSLS experiments using an FTIR, which detected intensity of the THz radiation, the LO THz facility allows us to detect amplitude and phase of the THz electric field. Thus, it is a different measurement and may offer advantages.

References

Buckles, R., “Terahertz time-domain spectroscopy and imaging,” *Nevada Test Site–Directed Research and Development,* FY 2007, National Security Technologies, LLC, Las Vegas, Nevada, 2008, 239–248.

Carr, G. L., “Dynamics of GaAs photocarriers probed with pulsed infrared synchrotron radiation,” *Nucl. Instrum. Methods B* **199** (2003) 323–327.

Chevalier, P. Y., “A thermodynamic evaluation of the Au-Sn system,” *Thermochimica Acta* **130** (1988) 1–13.

Kruschwitz, C., M. Wu, “Exploring phase transitions/shock dynamics using THz spectroscopy,” *Nevada Test Site–Directed Research and Development,* FY 2007, National Security Technologies, LLC, Las Vegas, Nevada, 2008, 17–24.

Kruschwitz, C.A., M. Wu, M. Madlener, “Exploring phase transition/shock dynamics using THz spectroscopy,” *Nevada Test Site-Directed Research and Development*, FY 2009, National Security Technologies, LLC, Las Vegas, Nevada, 2010, 9–16.

Pavone, P., S. Baroni, S. de Gironcoli, “$\alpha \leftrightarrow \beta$ phase transition in tin: A theoretical study based on density-functional perturbation theory,” *Phys. Rev. B* **57**, 17 (May 1998) 10421–10423.

this page intentionally left blank

DARK-FIELD, PHASE-CONTRAST RADIOGRAPHY

Fletcher J. Goldin[1,a] and Michael Haugh[a]

This project investigated a novel grating-based type of phase-contrast radiography in which a diffraction grating generates a near-field Talbot pattern, and relative phase delays in various portions of the x-ray beam induced by a phase object create an image. This study was done as two successive SDRD projects. In FY 2009, the basic theory was developed (guided by the literature), numerical modeling of informative examples illuminated key features, and a visible-light analog test bed was constructed and used to verify both theory and modeling (Goldin, 2010). This understanding was then applied in FY 2010 to design and procure x-ray gratings (the central components of the system) that represented the practical limits in both fabrication and use; combine these with an appropriate x-ray source, phase objects, and imaging units to form an experimental system; and carry out x-ray tests. This effort generated new knowledge relative to design and technique. Unfortunately, the fabrication of the gratings proved more difficult than anticipated and the quality of the delivered parts was not adequate for proper operation, and Talbot interference was not observed.

Background

Phase-contrast radiography (PCR) normally creates an image simply from the constructive and destructive interference of various regions of the x-ray beam that have suffered differential phase delays from variations in thickness and/or material in corresponding regions in the radiographic object. A major limitation is that this amplitude signal is indistinguishable from amplitude variations induced by differential absorption—in effect, PCR and absorption-contrast radiography (ACR) are convolved. The alternative scheme studied here first uses an x-ray grating to create a Talbot interference pattern, which, with no phase object present, would be a uniform array of lines that mimic the grating. A radiographic object will displace the fringes proportionately to any gradients in the phase shifts the object impresses on the beam. Differential phase-inducing features in the object are thus encoded in displacements of interference fringes, rather than their intensities, so that this information is decoupled from any intensity variations caused by differential absorption. The fact that this signal is not riding on top of the amplitude signal gives rise to the nomenclature "dark field."

The basic concept of Talbot-interference radiography was first conceived by John Clauser in the late 1990s using absorption gratings only. He claims positive results (Clauser, 2009) but has not published these. A group at the Paul Scherrer Institut, Switzerland (Pfeiffer, 2006) initially used synchrotron radiation at the European Synchrotron Radiation Facility (France) for the advantages afforded

---

[1] goldinfj@nv.doe.gov, 925-960-2686

[a] Livermore Operations

by a coherent x-ray beam. But, as their focus is medical applications, they needed to be able to use simple, inexpensive bremsstrahlung sources; the central variation to achieve this is moving from absorption to silicon phase Talbot gratings. By the start of this project, the Institute had published results at 17 keV and has since achieved 60 keV (Donath, 2009). A group at the University of Tokyo, Japan, has closely followed the Swiss group and appears to be the only other group to have published radiographic results (Momose, 2009). Efforts at Lawrence Livermore National Laboratory (LLNL) now seek to develop this technique for characterizing the solid layer of hydrogen fuel in National Ignition Facility targets (Martz, 2007).

This project sought to replicate Talbot-based PCR achieved by others at x-ray energies in the ~20 keV range; if successful, we would then attempt to significantly increase the x-ray energies to a regime no longer accessible with a silicon grating. Calculations done in FY 2009 (Goldin, 2010), together with discussions with potential vendors, indicated that copper or nickel would give the maximum possible energy given fabrication limits to the grating geometry, with the maximum limit of approximately 60 keV. Therefore, approximately 40 keV was chosen as an exploratory but still realistic goal.

Project

In principle, the only grating needed is the Talbot grating; in fact, this was the only grating used in our FY 2009 SDRD visible light experiments. In practice, however, an x-ray system needs two others: a source grating to generate a beam with sufficient coherence (not needed with visible light because a laser was used), and a moiré grating just upstream of the recording sensor to generate moiré patterns with sufficiently large pitch to be resolved by the imaging elements (again, not needed in the visible case due to much wider interference fringes). The Talbot grating is between the source and moiré gratings, with any radiographic phase object close to it, either up- or downstream. In FY 2009 (Goldin, 2010) we found that for absorption Talbot gratings, the Talbot-to-moiré distance can be any multiple of $Z_T/4 = a^2/2\lambda$ (Z_T is the Talbot distance and a is the grating pitch), but for phase gratings it must be an odd multiple. This was chosen to be 1 to minimize the total system length. The source-to-Talbot distance can in theory be anything, as it simply changes the system magnification. However, as found in FY 2009, the pitch of the moiré grating needs to be half the pitch of the Talbot grating times any magnification. Therefore, a magnification of m = 2 was chosen (source-to-Talbot = Talbot-to-moiré) so that the Talbot and moiré gratings would have the same pitch and therefore could be fabricated with the same photomask.

X-Ray Source

The Livermore Operations (LO) High Energy X-ray (HEX) source, a conventional DC bremsstrahlung x-ray tube that illuminates a fluorescent target, resulting in a well-defined x-ray transition line, provided the beam for these experiments. The required low- and high-energy cases described above were realized with the 17.5 keV line of molybdenum, with niobium filter, and the 40.1 keV line of samarium, with neodymium filter. Potentially, the direct bremsstrahlung radiation, which is 4–5 orders of magnitude greater than the fluorescent beam, can be used directly, but there is not yet adequate room shielding to allow this beam out of the source enclosure. This led to very low signals, even with long exposures (hours). However, at least theoretically (as found in FY 2009), a narrow line instead of a wide bremsstrahlung spectrum should give a higher contrast Talbot interference pattern, compensating for the weaker intensity. In any case, this was the first (known) attempt to see Talbot interference with x-rays from a fluorescent source.

X-Ray Detection/Imaging

Three possibilities for recording the image were investigated: film, an x-ray phosphor storage imaging plate system, and a CCD x-ray camera.

Film would be most inconsistent and troublesome, but since films are available with grain size of a few microns, it held the possibility of imaging the Talbot interference pattern itself without using moiré patterns. However, visible light tests using an Optoliner did not show resolution better than a few 10s of µm for any film tested, which included Kodak TMX100, Kodak PX125, Iford PAN F Plus, and Rollei ATP. (Although these brands are not marketed as x-ray films, their sensitivity to x-rays in the energy range of interest was tested and found to be usable.) Film therefore appeared to offer no advantage over the CCD and was not used.

A Fujifilm FLA-5000 image plate system, previously transferred from LLNL to LO, was resurrected. The resolution (~50 mm even scanning at 25 mm steps) and noise were too poor to record quantitative data, but far greater sensitivity than the CCD allowed exposure times in the range of a minute, so the Fujifilm system was used for preliminary tests, alignment, etc.

A Princeton Instruments PI-SX:2048 back-illuminated CCD camera recorded quantitative data. The pixel size was 13.5 µm, for a 28 mm square active area, and the experiment was therefore designed for this format. We modified the camera envelope by fabricating a gas vessel with a minimally absorptive x-ray window; this addition let nitrogen flow around the CCD, but it also allowed us to place the moiré grating to within about 2 cm of the sensor. Because exposure times of an hour or longer were required for good statistics, we then used image plates for setup work.

Design of Talbot Phase Gratings

In FY 2009 we determined the relationship between grating design and system capability, and nominal design parameters for Talbot phase gratings that would achieve the limits to x-ray energy that were determined (Goldin, 2010). We concluded that Talbot-interference PCR could probably be stretched to ~60 keV, given the fabrication limits of the aspect ratio (height to width) of the walls and spaces. Nickel or copper would be optimal material for these walls (active material of a phase grating). Given the risk of grating fabrication and their use in the experiments, we aimed to achieve PCR at ~40 keV. The exact energy would need to be a transition line available with the HEX source, and the samarium $K\alpha$ line is 40.1 keV and relatively intense, so it was chosen. For this energy, the nickel height would be 14.1 μm. Because Talbot interference with x-rays had only been done a few times, and our experiment would be the first to attempt it with phase gratings other than silicon, while aiming for 40.1 keV with any material, we decided to proceed in two steps. First, we would duplicate the Swiss group's previous work, namely using a silicon grating (which only requires etching grooves into the wafer substrate, with no deposition needed) at an energy of ~17 keV (the energy most quoted by the Swiss group as the average energy of their bremsstrahlung source). Using the Kα molybdenum line at 17.5 keV dictated a groove depth of 22.5 μm for 180-degree phase shift. The second step was to use a nickel grating still tuned to 17.5 keV (nickel height 6.1 μm). Of course, the fourth combination imaginable, namely silicon at 40.1 keV, was not possible; if such a grating could be fabricated, there would be no need for nickel.

With other parameters equal, larger pitch gives higher grating quality but at the cost of greater working distance, i.e., the grating-to-interference pattern distance of $Z_T/4 = a^2/2\lambda$, where Z_T is the Talbot distance and a is the grating pitch. Therefore, for each of the three types of gratings (Si at 17.5 keV, Ni at 17.5 keV, and Ni at 40.1 keV), gratings of three different pitches were fabricated: 8, 12, and 16 μm, giving $Z_T/4$ distances of 452, 1016, and 1806 mm for 17.5 keV and 1035, 2328, and 4139 mm for 40.1 keV.

Design of Absorption Gratings

The natural material for the absorption gratings was gold, due to its high Z, high density, and (what was supposed to be) ease of fabrication. Unlike the case of a phase grating for which a particular energy dictates a particular wall height, absorption gratings need walls sufficiently high to absorb the majority of the radiation, with no sharp cut-off and no maximum. Therefore, gratings designed for the high-energy case could also be used at the lower energy.

For both source and moiré absorption gratings, gold walls would be deposited on a silicon wafer substrate. The spaces between the walls would essentially be open, with the wafer thickness of 200 μm, giving a transmission of 0.75 even for the lower energy. The height of the gold walls was specified to be at least 25 μm to give absorption of about 50% for the higher energy, the minimum deemed usable. Absorption would be over 0.99 at 17.5 keV.

The pitch of the moiré grating would need to be the same as that of the Talbot pattern at the detector, or half the pitch of the Talbot grating itself times its geometrical magnification. Therefore, the system layout was chosen with m = 2, so that for any Talbot grating, a moiré grating with the same pitch could be used, allowing both gratings to be fabricated with the same lithographic mask. To cover the 28 mm square CCD, the moiré gratings (and thus the Talbot gratings as well) were 30 mm square. The substrates for all gratings were 100 mm wafers. Since this accommodated four 30 mm squares, a fourth pattern was added, which, rather than a grating, was a 2 × 2 checkerboard of 15 mm squares. These large areas, with the same heights as the low and high lines of the gratings, would allow measurements of relative attenuation between these zones. For the Talbot grating wafers, they could also serve as phase-object targets.

Unlike the other gratings, the source gratings pattern was asymmetric in that the transmission zones were much narrower than the blocking zones. This is because (1) the width of each open zone, w_s, needed to be sufficiently small that the transverse coherence length, $c_t = \lambda d_1/w_s$, would be a few times greater than the Talbot pitch, while (2) their spacing, a_s, would also be a few times greater than the Talbot pitch. This gives sufficient coherence within the wave from each slit to form the interference pattern, but sufficient slit-to-slit incoherence that their patterns will simply add in amplitude. For both parameters, there is a trade-off of these dimensions against transmitted flux (increasing with w_s and decreasing with a_s). Because the optimal values would depend on many real-world effects impossible to account for in advance, a matrix of 12 combinations (at 15 × 20 mm each, the maximum number that could fit on one wafer) was incorporated into the photomask from which they would be fabricated. This matrix comprised open widths of w_s = 4, 6, and 8 µm with pitches of a_s = 40, 60, 100, and 160 µm for each open width.

Source Slit

The spatial resolution of the system would be the same as for conventional ACR, namely the source size times the source magnification (approximately 2 in these tests). The HEX fluorescer is a 1 cm diameter disk, thus requiring a limiting aperture to achieve useful resolution. However, resolution of 1 mm generated by a 500 µm aperture, for instance, would reduce intensity by ~300. However, testing all essential principles and behavior requires resolution in one dimension only. This same (typical) resolution, then, would only require a 500 µm wide slit across the full diameter of the fluorescer, reducing the total intensity by only a factor of ~16. Such a design was implemented by recycling an x-ray slit that had been used previously on LO's Henke system. This unit was adjustable within a range of approximately 0.1–1.0 mm, making accessible various trade-offs between resolution and flux. One modification needed was machining back the edges of the tapered tungsten jaws to increase the thickness (to 500 µm) for the higher energies of the HEX source.

Targets

To test the phase-contrast system, radiographic objects were needed that would introduce significant changes in phase but not intensity (i.e., have negligible absorption) of the x-rays. Additionally, for one-dimensional tests, such phase changes needed to occur in only one transverse direction. The objects were fabricated by stretching thin hydrocarbon membranes across the opening of a rotation stage mounted with its axis parallel to the x-ray beam so that a portion of the beam would pass through the membrane and a portion would bypass it, resulting in an abrupt phase change at the membrane's edge. The rotation stage allowed orienting this line relative to the gratings, with the apparent width of the transition, as seen at the CCD, being the length of the line (effectively CCD width) times the tangent of the "misalignment" angle.

For each energy, two membranes were mounted with edges parallel and 4 mm apart. For 17.5 keV, the areal densities were 2.5 and 5.0 mg/cm^2 (corresponding to carbon thicknesses of 11 and 22 µm), giving phase changes of 0.5π and 1.0π. The 40.1 keV targets were 10.1 and 30.3 mg/cm^2 (45 and 135 µm equivalent) for phase changes of 0.38π and 1.15π. It is worth noting that (for both energies) the transmission was calculated to be 0.998 and 0.996 for the thinner and thicker materials, so these samples, carefully chosen for maximum contrast in a PCR system, would be completely invisible in a conventional ACR system.

Mounting/Alignment

Other than the HEX source, all major components of the system—source grating, source slit, Talbot grating, phase object, moiré slit, and detector (imaging plate or camera)—were mounted on an optical rail for ease of achieving proper spacings (Figure 1). Jacks; translation, rotation, and tilt stages; and goniometers provided the necessary degrees of freedom; kinematic mounts allowed removal/replacement without loss of alignment. A Laser Tools L202A Dual Beam Alignment laser, which incorporates two 635 nm AlGaInP diode lasers mounted back to back, was used to align components in both displacement and angle. Tolerances for all three translation dimensions were large (~1 mm or more) and easily achieved, while angular alignment in the roll dimension was critical.

The two critical alignment angles were the angle of the Talbot grating relative to the source grating, and the moiré grating relative to the Talbot grating. The first is determined by the requirement that the top of one of the source grating's openings cannot be offset from the bottom by more than the interference pattern pitch (which is the same as the Talbot grating pitch); otherwise, the interference patterns created from each point of the slit will be displaced from each other enough to blur out the summed pattern. For the middle-value Talbot pitch of 12 µm and a source height of 10 mm, which is the HEX fluorescer height, this would be an angle of about 1 mR. However, for reasons discussed above, the source is apertured by a slit in the range of 1 mm (compromising flux vs resolution). The orientation of this slit relative to the gratings is arbitrary, as it is only required that the target's edge is oriented to the slit. So, the slit axis orientation was set to be 90 degrees to the grating axis, thereby reducing the grating opening heights by roughly x10 and relaxing the alignment tolerance by the same factor, to about 10 mR. Similarly, the tolerance for the Talbot/moiré angle would be essentially the Talbot pitch over the height of the pattern (effectively identical to the CCD's 28 mm) if it were required to have only one moiré band. However, because bands on the order of 1 mm could easily be seen by the CCD, the misalignment could easily be as great as the pitch over 1 mm, again giving about 10 mR.

Each grating's pitch and yaw were adjusted so that the alignment laser's reflected beam was along the incident beam, ensuring the grating was normal. Then, stanchions with millimeter scales were positioned on either side of the system, about 1 m apart, so that "dots" of the diffraction pattern produced by the grating appeared on each scale. Using a goniometer in its mounting stack, the grating's roll was adjusted until the height of the diffraction pattern above the optical table was the same on the two scales. The diffraction spots were about 1 mm in size, and the accuracy of height adjustment was estimated as also in the range of 1 mm. With a ~1 m baseline, the total error in roll was less than ~0.2 mR for each grating, well within the 1 mR requirement.

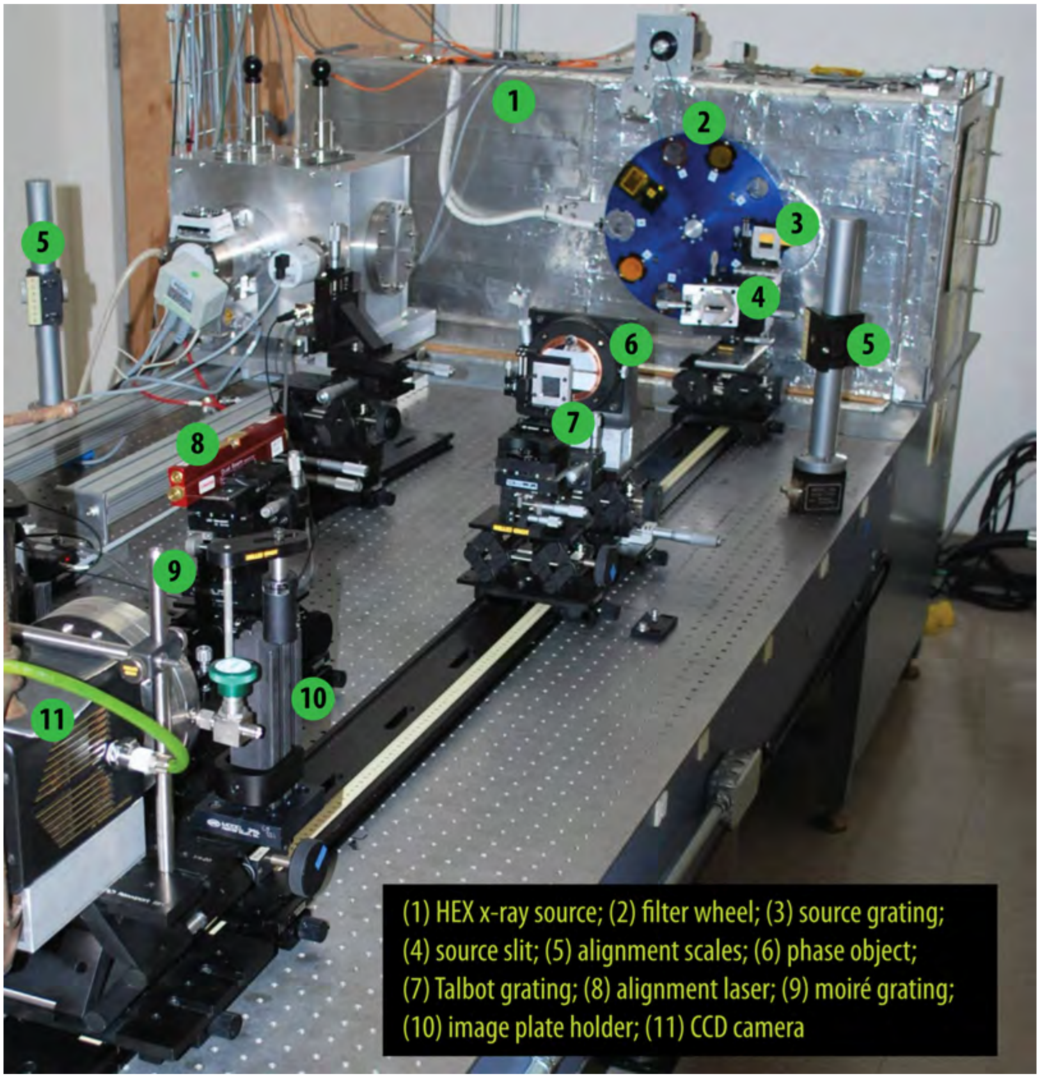

Figure 1. Phase-contrast system with components mounted on optical rail

Absorption Grating Fabrication

The Talbot phase gratings—both the pure (grooved) silicon wafers and the silicon with nickel deposition—were inspected on delivery. One nickel grating was cracked (two of every design was ordered), but otherwise, microscopic physical examination and optical diffraction testing showed all units to be of high quality. We experienced several problems with the gold-on-silicon gratings. Procurement and fabrication time was longer than expected and only half of these gratings were received. Of these, many were cracked and had significant gold deposition in undesired areas and too little in desired areas. Several weeks were spent in trying to make the gratings useable. Our efforts to create some functionality, which are described in the following paragraph, were not successful. The net result was inability to see any Talbot interference patterns using these gratings.

After several fabrication attempts by the vendor, the original design of gold walls deposited on the silicon substrate was never realized—primarily because the walls "grew" into each other before reaching acceptable heights. Therefore, an alternative scheme was attempted in which grooves were etched in the silicon substrate where the gold walls would have been, and then gold would be deposited into these to create the closed zones. Qualitative problems were as described above, and gold deposition was as seen in the electron micrographs of Figures 2 and 3 of typical source and moiré gratings. In the first case, it can be seen that the gold simply coated the entire surface, rather than just inside the groove as intended. In the moiré case, too little gold was deposited in the grooves for significant absorption (or contrast between would have needed to be open and closed zones), while there was also an "overcoat" over the top of the entire unit thick enough for significant absorption.

To try to salvage a functional source grating, we identified a patch to polish in an attempt to reopen the silicon wall zones. At ~10–15 µm (Figure 2) the gold in the grooves had a transmission of ~70% at 40 keV, but only about 5%–7% at 17.5 keV, a usable figure. Unfortunately, the polishing resulted in more destruction, but one small piece still seemed worth using.

In the moiré gratings (Figure 3), the gold in the grooves was only about ~6–8 µm, which would give ~80% transmission at the higher energy—far too high. However, at 17.5 keV, transmission would only be ~25%, and so the unit might create moiré patterns. At this energy, however, the gold overlayer of 10–12 µm would only transmit about 10%, so it was also polished off as well as possible. This was then used in combination with the salvaged piece of source grating described above and a silicon Talbot grating, but no interference pattern was observed.

A final attempt was made using what was to be the high-energy nickel Talbot phase grating as the low-energy moiré absorption grating. This grating's 14.1 µm high walls, designed for 180-degree phase shift at 40.1 keV, would absorb ~44% at 17.5 keV—far from ideal, but possibly enough contrast to be usable (and at m = 2, the pitch was correct). However, this combination of gratings still produced no observable interference pattern. Note that transmissions were calculated from thicknesses seen in the electron micrographs and verified with x-ray area-averaged flux measurements.

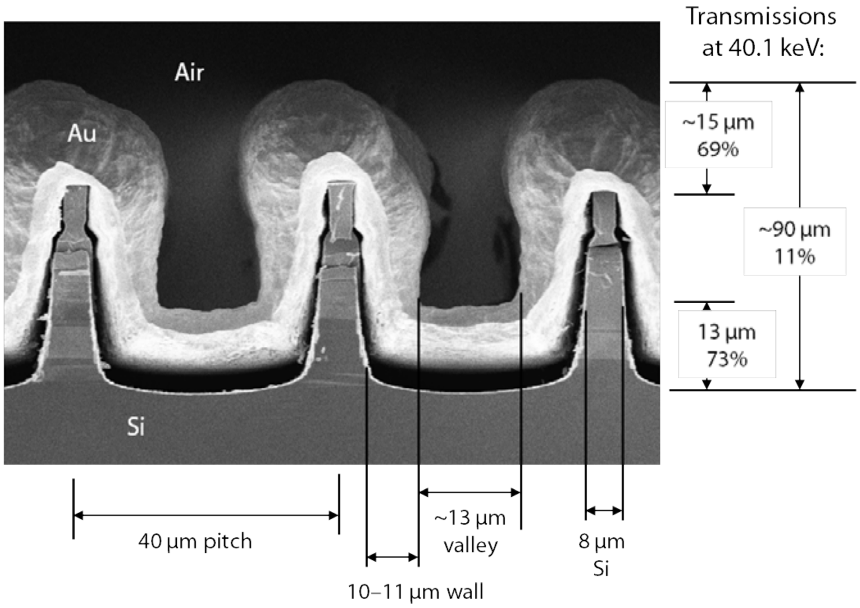

Figure 2. Typical source grating. Gold in groove centers was too thin for sufficient absorption, and gold on top of silicon walls was too thick for sufficient transmission, rendering this piece unusable as a source grating.

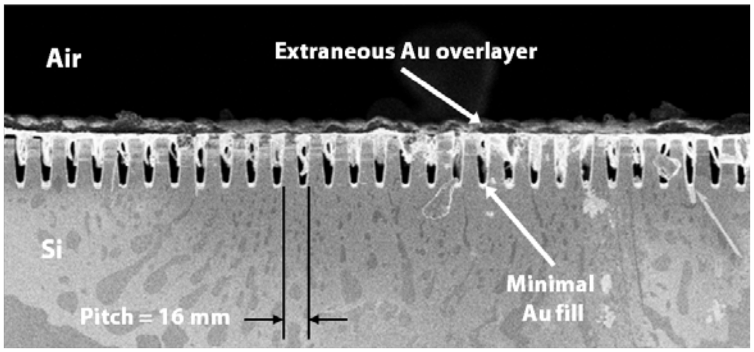

Figure 3. Moiré grating. As with source gratings, the original order was free-standing gold walls, but fabrication failed. The grating was changed to gold-filled grooves, but material in grooves was only ~6–8 µm, plus an unacceptable 10–12 µm gold overlayer.

Conclusion

While Talbot interference was modeled and used for imaging with visible light in our FY 2009 work and has been used for radiography by others, it was not seen with x-rays in this project. This lack stemmed from the inability of the gold (absorption) gratings, in the condition delivered, to produce either the necessary coherence for interference or, if interference did occur, a moiré pattern to render it observable. Attempts at creating some degree of functionality through polishing some of the least flawed units as well as using them in combinations other than originally intended were not successful. Otherwise, the detailed design of individual gratings, fabrication of phase gratings, phase targets, system geometry, and alignment and imaging techniques appeared to be viable.

Acknowledgments

Travis Pond was instrumental in setup, HEX operation, and data collection, and Albert Shellman performed polishing of the gold gratings. Also appreciated were technical conversations with Bernard Kozioziemski of LLNL.

References

Clauser, J., Private communications, 2009.

Donath, T., F. Pfeiffer, O. Bunk, W. Groot, M. Bednarzik, C. Grünzweig, E. Hempel, S. Popescu, M. Hoheisel, C. David, "Phase-contrast imaging and tomography at 60 keV using a conventional x-ray tube source," *Rev. Sci. Instrum.* **80**, 5 (2009) 053701.

Goldin, F., "Dark field radiography," *Nevada Test Site–Directed Research and Development,* FY 2009, National Security Technologies, LLC, Las Vegas, Nevada, 2010, 27–36.

Martz, H., B. Kozioziemski, S. Lehman, S. Hau-Reige, D. Schneberk, A. Barty, "Validation of radiographic simulation codes including x-ray phase effects for millimeter-size objects with micrometer structures," *J. Opt. Soc. Am. A* **24**, 1 (2007) 169–178.

Momose, A., W. Yashiro, H. Maikusa, Y. Takeda, "High-speed x-ray phase imaging and x-ray phase tomography with Talbot interferometer and white synchrotron radiation," *Optics Express* **17**, 15 (2009) 12540–12545.

Pfeiffer, F., T. Weitkamp, O. Bunk, C. David, "Phase retrieval and differential phase-contrast imaging with low-brilliance x-ray sources," *Nature Physics* **2** (2006) 258–261.

MEASUREMENT OF TAGGED NEUTRON FISSION ANISOTROPY

Raymond P. Keegan,[1,a] *Francis Tsang,*[a] *Daniel Lowe,*[b] *Robert O'Brien,*[b] *James Tinsley,*[c]
and Rusty Trainham[c]

The objective of this work was to determine whether measurement of prompt radiation anisotropy in fission is useful as a signature for fission identification purposes. If this anisotropy can be easily measured, then it could be used to complement other signatures of fission. This work used MCNPX simulations to determine whether anisotropy measurement is viable for fissionable material identification. Experimental principles were tested using sources such as ^{60}Co and ^{22}Na. We found that even though anisotropy is measureable for a simple geometry, it is not practical for use in field applications. However, we also realized that using a dense plasma focus machine to induce fission and counting delayed radiations as a function of time is a viable option for field interrogation work.

Background

Investigation of unique signatures produced by fission has become a very high priority for the U.S. government, particularly since the events of September 11, 2001. This work explored field applications of prompt radiation anisotropy in fission that can be observed in laboratory experiments (Bowman, 1962; Pringle, 1975; Gagarski, 2008). We sought to determine whether measurement of prompt fission anisotropy is useful as a signature for identification of fission. If prompt fission anisotropy proved practical to measure in the field, then this extra piece of information could be used as an additional indicator of fission, thereby reducing instrument false alarm rates.

The fission process usually results in the fissionable nucleus being split into two fragments of different mass and several prompt or delayed neutrons. Fission results in the fragment masses not being equal so that one fragment has slightly more mass than the other one. Conservation of energy and momentum means that the recoiling fragments travel at about 180 degrees relative to each other. Immediately after fission (within picoseconds), both prompt neutrons and gamma rays radiate off the fully accelerated fragments. About 90% of prompt neutrons are emitted by the fully accelerated fission fragments and the remaining 10% are emitted during the moment of fission (Figure 1). Prompt neutrons tend to travel in the direction of fragment movement; therefore, there will be a 180-degree correlation per fission between the prompt neutrons radiated from the fragments that should be measureable. The lower-mass, neutron-rich fragment is more unstable than the heavier fragment and emits a slightly higher flux of prompt neutrons.

---

[1] keeganrp@nv.doe.gov, 702-295-1005
[a] Remote Sensing Laboratory–Nellis; [b] North Las Vegas; [c] Special Technologies Laboratory

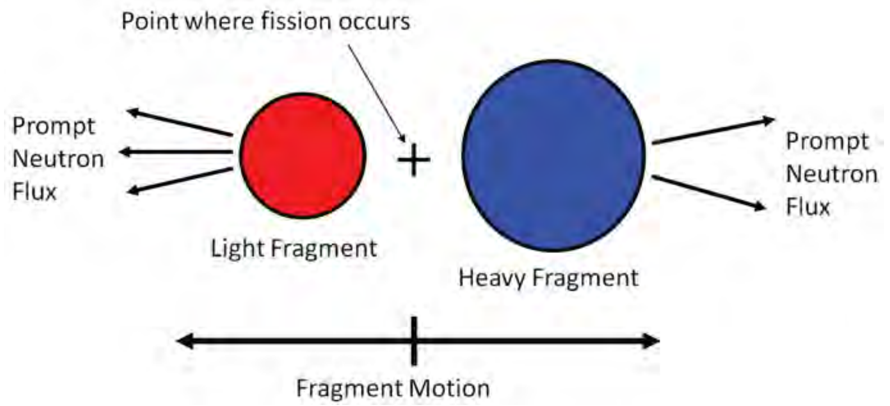

Figure 1. A simple representation of the fission process showing the light and heavy fragments, and how the prompt neutrons tend to radiate from these fragments. About 90% of the prompt neutrons radiate from the fully accelerated fragments with a slightly higher flux radiating from the neutron-rich lighter fragment.

Prompt gamma-ray emission is also known to be anisotropic, but to a lesser extent than that of prompt neutrons. The fission process also results in the emission of delayed radiations; however, these radiations are emitted when the fragments are no longer moving so that no angular anisotropy is expected. For this reason the work described in this report focused on the investigation of prompt neutron anisotropy only. For brevity, the use of the term anisotropy in the following text means prompt fission neutron angular anisotropy only.

Project

The project was divided into two portions to study: (1) fission anisotropy and (2) a potential homeland security application for dense plasma focus (DPF) systems. The lessons learned from this and earlier SDRD interrogation projects (Keegan, 2009; 2010) indicate that for the problem of interrogation of International Standards Organization (ISO) shipping containers, it is useful to generate as much fission as possible, and then count delayed radiations to reveal the presence of the fissionable material.

Fission Anisotropy

Each time a nucleus undergoes fission, prompt neutrons radiate away from the fully accelerated fragments and tend to travel in the same direction as the motion of the fragments. Because the fragments travel at 180 degrees relative to each other, it is reasonable to expect that this correlation will be preserved in the emitted neutron flux. In other words, on a fission-by-fission basis, prompt neutrons that travel to the left in the prescribed example will tend to be correlated with those that travel to the right. Anisotropy measurements can be performed by making coincidence measurements as a function of angle between two detectors (with the fission occurring at the apex of the angle made by the longitudinal axes of the two detectors). When the detectors are opposed by 180 degrees, the coincidence rate is higher than the rate when the detectors are separated by 90 degrees. Therefore, one may define anisotropy as the ratio of the 90-degree flux to the 180-degree flux.

A number of complications in measurement of anisotropy were discovered during the course of this project. The first one was that the location of the fissionable material relative to the detectors must be known to make such a measurement. This is illustrated in Figure 2 where the material is centered and then off-centered in a measurement system. If the material is off-centered, then inverse square law corrections need to be made to arrive at the anisotropy measurement. Identifying the location of the object would have to be done through radiography of shipping boxes or containers, and it would not be trivial to accurately measure anisotropy in this case.

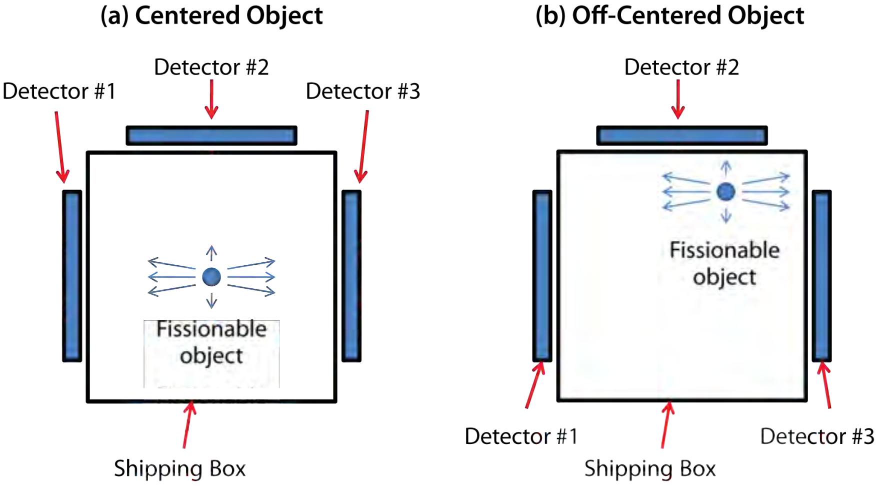

Figure 2. A hypothetical fissionable object in a measurement system located at (a) a centered position and (b) an off-centered position. Assuming that neutron scattering in the skin of the box is negligible, the anisotropy measurement needs to be inverse square law–corrected.

MCNPX simulations were performed to study anisotropy; the experimental setup in the model was that used on last year's SDRD project (Keegan, 2010). The simulations would determine whether it was worthwhile to proceed with experimental measurements. The geometry was constructed at half shipping container scale, meaning that if all the physical distances were multiplied by two, then the geometry would mimic the scale of a standard ISO shipping container.

Two sets of identical simulations were performed using two types of interrogation target: (1) a 2 cm diameter depleted uranium (DU) sphere and (2) a 19.65 cm square DU plate, 1.27 cm thick, facing the neutron generator. The plate dimensions and mass (9.3 kg) were those the team intended for experiments at NSTec Special Technologies Laboratory (STL). The neutron generator sent 5 × 10^7 14 MeV neutrons into a 13-degree cone that simulated the STL tagged neutron system. The DU target was placed 60 cm from the neutron generator target that was centered on the cone centerline so that the tagged beam irradiated the entire object. Two polyvinyltoluene (PVT) detectors (both of type BC-400 and 100 cm × 45 cm × 15 cm) were placed equidistant at 0.62 m on either side of the DU target at right angles to the neutron generator–DU line.

Coincidences were counted by opening up a 100 ns time window after a neutron interacted in one detector and waiting for an interaction in the other detector. Coincidences over all prompt neutron energies were tallied for each DU target initially with the detectors opposed by 180 degrees, and then with one detector rotated so that it was at 90 degrees relative to the other detector and the DU-generator axis. The coincidence comparison for the two DU targets is shown in Table 1. The coincidence tally for the sphere for the two detector orientations indicates that the anisotropy is less than expected. The tallies are reasonably comparable within the limits of uncertainty with the 180-degree count being slightly greater than the 90-degree count; however, it is not clear that the difference is due to anisotropy. The difference is likely due to the scattering of prompt neutrons inside the sphere, which smooths out the anisotropy due to fission.

Table 1. Coincidence comparison for the MCNPX runs for DU targets

Detector Orientation (degrees)	Sphere Counts	DU Plate Counts
180	336 ±18	17,482 ±132
90	308 ±17	19,502 ±140
Count Ratio (90/180)	0.92 ±0.07	1.11 ±0.01

In the DU plate simulations, the results were opposite those of the sphere, so that the 90-degree count was clearly greater than the 180-degree count. This effect was not due to anisotropy in the fission process, but to internal scattering of prompt neutrons inside the plate. It was in examining these results that we discovered the second complication: the result depends on the mass of fissionable material used and the 3-D shape of the material. The third complication is that the effect of shielding and masking material placed around fissionable material will also further "smooth out" any anisotropy. Based on these findings the tagged neutron experimental work at STL was cancelled.

Measurements were also performed to study angular anisotropy in the emissions of gamma cascade photons from ^{60}Co and ^{22}Na. Electronics purchased from Bridgeport Instruments, LLC, in an earlier SDRD project (Keegan, 2010) were used to collect list mode data from two 4" × 4" sodium iodide detectors. Event energy and registration times were recorded for each event in a given detector. The detectors were placed at several orientations at a set distance around each source to measure angular anisotropy. Data collected were analyzed by Rusty Trainham working on an allied NA-22 project (Trainham, forthcoming). The results, presented in the form of covariance maps for a point ^{22}Na source, are shown in Figure 3; a clear angular anisotropy was demonstrated for this source, which has negligible self-shielding. Covariance is a method for analyzing coincidence data that gives true coincidence rate, and the colors shown in the ^{22}Na source measurements represent the amplitude of the true coincidence rate. Further results and conclusions are presented in the second-year reports derived from that project.

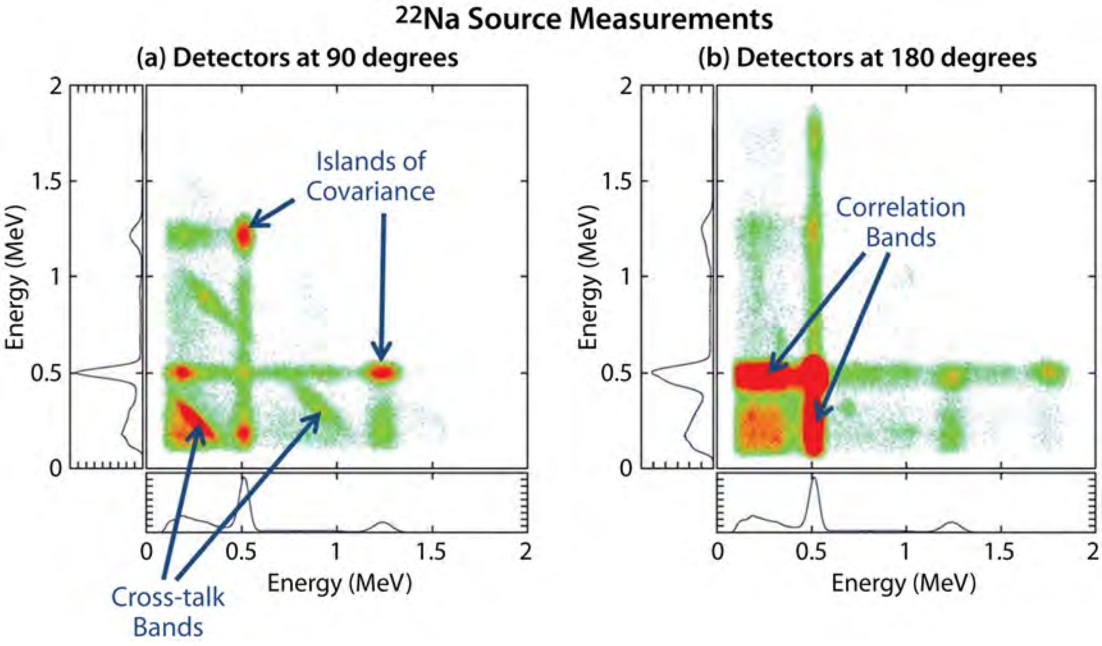

Figure 3. Covariance (correlation) maps for measurements performed on a ^{22}Na point source where the detectors were placed at (a) 90 degrees relative to each other and (b) 180 degrees relative to each other for a fixed source-detector distance. In the case of (a) note the islands of covariance between the 511 keV and 1.27 MeV gamma rays, and the cross talk of the 511 keV and 1.27 MeV gamma rays between the two detectors. In the case of (b) the cross-talk bands are weakened due to the increased distance between the two detectors; however, the clear angular correlation between the two annihilation 511 keV gamma rays is very clear. Also note the emergence of a new island of covariance at 1.78 keV (1.27 MeV + 511 keV gamma rays in one detector and a 511 keV gamma ray in the other). Angular anisotropy among gamma rays is easily observed in such small, simple point sources where self-shielding of the source is negligible.

DPF Simulations

Other work performed included MCNPX simulations investigating the use of a DPF to perform interrogation. This was done to determine whether the DPF has any potential for interrogation work. It was decided due to activation concerns that it would be better to examine the delayed gamma-ray and neutron fluxes in the seconds after the DPF burst. In the MCNPX models, the tagged neutron generator was replaced with a DPF device and simulations were performed using the same geometry and DU plate described above. In the MCNPX modeling, it is assumed that the detectors are 100% efficient. For a 5 × 10^{11} prompt neutron burst from the 2.45 MeV DPF, at 3 seconds after the burst, the gamma-ray flux integrated over all energies was estimated to be about 5.1 × 10^5 counts per second per detector; see Figure 4. It was also determined that the delayed neutron flux at this time would be about 4.2 × 10^4 counts per second. The 3-second time delay after the DPF burst was chosen to allow activation by-products to decay away in order to observe the delayed radiations. Based on the MCNPX results, it was determined that the use of a DPF and counting delayed radiations as a function of time after the burst is a viable technique and deserves further study.

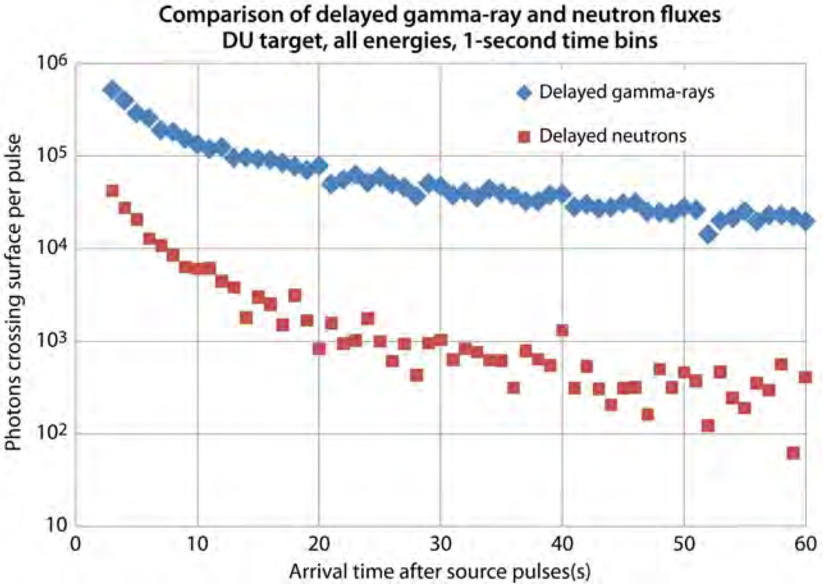

Figure 4. The MCNPX results showing the delayed gamma-ray and delayed neutron count rates in a single 100 cm × 45 cm × 15 cm PVT detector as a function of time after the 5 × 10^{11} prompt neutron burst from the 2.45 MeV DPF pulse. The geometry is half ISO shipping container scale so that the detector is located at 62 cm from the 9.6 kg DU plate. The plane of the DU plate was normal to the plane of the detector and centered on the detector.

Conclusion

There are three complications in the measurement of anisotropy. First, the position of the material must be known inside any shipping box or container. If the material is not at the center of the measurement system, then inverse square law corrections need to be made to arrive at the anisotropy measurement. Second, scattering of prompt neutrons within the fissionable material tends to smooth out the effects of anisotropy, making it impossible to differentiate from the measured data. Third, scattering of prompt neutrons within any shielding and masking placed around the fissionable material tends to further reduce the measured effects of anisotropy. The main conclusion is that measurement of anisotropy is not useful for real-world field applications, and is of academic interest only. It is best applied in fundamental nuclear physics studies of basic physical processes. The measurements analyzed in the covariance project show that covariance is capable of measuring angular anisotropy and performing identification of simple sources, such as ^{60}Co and ^{22}Na. The DPF studies indicate that the use of a DPF to perform interrogation is a viable technique and deserves further study.

References

Bowman, H. R., S. G. Thompson, J. C. D. Milton, W. J. Swiatecki, "Velocity and angular distributions of prompt neutrons from spontaneous fission of ^{252}Cf," *Phys. Rev.* **126**, 6 (1962) 2120–2136.

Gagarski, A. M., I. S. Guseva, V. E. Sokolov, G. V. Val'ski, G. A. Petrov, D. O. Krinitsin, D. V. Nikolaev, T. A. Zavarukhina, V. I. Petrova, "Neutron-neutron angular correlations in spontaneous fission of ^{252}Cf," *Bulletin of the Russian Academy of Sciences*: *Physics* **72**, 6 (2008) 773–777.

Keegan R. P., P. Hurley, J. Tinsley, R. Trainham, S. Wilde, "Neutron active interrogation using a small neutron generator," *Nevada Test Site–Directed Research and Development*, FY 2008, National Security Technologies, LLC, Las Vegas, Nevada, 2009, 107–112.

Keegan, R. P., P. Hurley, J. Tinsley, R. Trainham, "Portable tagged neutron triple-coincidence counter system," *Nevada Test Site–Directed Research and Development*, FY 2009, National Security Technologies, LLC, Las Vegas, Nevada, 2010, 137–143.

Pringle J. S., F. D. Brooks, "Angular correlation of neutrons from spontaneous fission of ^{252}Cf," *Phys. Rev. Lett.* **35**, 23 (1975) 1563–1566.

Trainham R., "Final report for covariance spectrometry for fissile material detection," Simulations, Algorithms and Modeling (SAM) portfolio, NA-22 project #NST09-CovarFisMat-PD06, forthcoming.

this page intentionally left blank

INSTRUMENTS, DETECTORS, AND SENSORS

NANOSTRUCTURED LANTHANUM HALIDES AND $CeBr_3$ FOR NUCLEAR RADIATION DETECTION

Paul P. Guss,[1,a] Ronald Guise,[a] Stephen Mitchell,[a] Sanjoy Mukhopadhyay,[b] Daniel Lowe,[c] Robert O'Brien,[c] and Ding Yuan[d]

Nanocomposites may enable the use of scintillator materials such as cerium-doped lanthanum fluoride and cerium bromide ($CeBr_3$) without requiring the growth of large crystals. Nanostructure detectors may allow us to engineer immensely sized detectors of flexible form factors that will have a broad energy range and an energy resolution sufficient to perform isotopic identification. Furthermore, nanocomposites are easy to prepare and very low in cost. It is much less costly to use nanocomposites rather than grow large whole crystals of scintillator materials; with nanocomposites fabricated at an industrial scale, costs are even less. We have fabricated nanoparticles with sizes <10 nm and characterized their nanocomposite radiation detector properties. This work also attempted to extend the gamma energy response on both low- and high-energy regimes by demonstrating the ability to detect low-energy x-rays and relatively high-energy activation prompt gamma rays simultaneously using nanostructured lanthanum bromide, lanthanum fluoride, or $CeBr_3$. Nanoscale properties of lanthanum halides and $CeBr_3$ hold promise to extend the gamma energy response on both low- and high-energy regimes. Nanostructured lanthanum halides and $CeBr_3$ may be able to detect low-energy x-rays and relatively high-energy activation prompt gamma rays simultaneously. Preliminary results of this investigation are consistent with a significant response of these materials to nuclear radiation.

Background

Scintillator materials are used to detect and, in some cases, identify gamma rays. Higher-performance scintillators are more expensive, difficult to manufacture, and fragile. Scintillators are less costly, easier to manufacture, and more rugged, but they offer lower performance. At issue is the question: Can the desirable qualities of each scintillator type be combined to achieve high performance at low cost?

This project sought to combine the advantages of both types of scintillator materials to overcome the disadvantages of each. We proposed that nanocrystals, 2 to 5 nm in diameter, of certain inorganic scintillator materials, packed densely in plastic or inorganic solutions, can capture most of the energy from photons, thus offering nearly the performance of large crystals. The resulting mixture would also have the desirable features of plastic or liquid scintillators.

---

[1] gusspp@nv.doe.gov, 702-295-8095

[a] Remote Sensing Laboratory–Nellis; [b] Remote Sensing Laboratory–Andrews; [c] North Las Vegas;
[d] Los Alamos Operations

In operation, when a gamma-ray photon strikes this material, its energy is absorbed by both the nanocrystals and the oleic acid (we used an inorganic solution rather than plastic), raising some atoms to a higher energy level. These atoms give off this energy as photons (referred to as optical photons) in the visible and near-visible regions of the electromagnetic spectrum. A phototransducer, either a photomultiplier tube or an avalanche photodiode, is employed to generate many electrons for each photon it receives from the contiguous detector material, to amplify this signal, and to collect the resulting amplified charge, thereby converting an optical signal to an electronic signal that can be counted (Medalia, 2010). The number of optical photons generated corresponds to the energy level of the photon striking the material. A multichannel analyzer counts the optical photons, determines the energy level of the photon striking the material, and increases the count of photons of that energy level by one, ultimately creating a gamma-ray spectrum.

Nanostructured radiation scintillator detectors may improve quantum efficiency and provide vastly improved detector form factors. Quantum efficiencies up to 60% have been seen in photoluminescence from silicon nanocrystals in a densely packed ensemble (Del Sesto, 2007). Nanocomposites may enable the use of scintillator materials such as cerium-doped lanthanum fluoride (LaF_3:Ce) without requiring the growth of large crystals. The chemical synthesis of the cerium-doped lanthanum halide nanoparticles are scalable (Del Sesto, 2007), and large quantities of material can be produced at a time, unlike typical crystal sizes resulting from crystal growth processes such as the Bridgeman process.

In order to create a new class of scintillator materials that combines good energy resolution, large size, and low cost, Del Sesto developed a large-scale synthesis of narrowly sized, distributed, <10 nm cerium-doped lanthanum bromide ($LaBr_3$:Ce) or LaF_3:Ce nanoparticles. In fact, nanoparticles of many candidate scintillating materials, such as $LaBr_3$:Ce, LaF_3:Ce, or even cerium bromide ($CeBr_3$), can all be cast into transparent oleic acid or polymer composites with up to 60% scintillator volume loading. Preliminary experiments showed that the LaF_3:Ce oleic acid–based nanocomposites exhibit a photopeak when exposed to ^{137}Cs source gamma radiation (Del Sesto, 2007). In general, lanthanum halides show the promise of being useful over a wide energy range of x-rays and gamma rays.

Project

We fabricated nanoparticles with sizes <10 nm, prepared two scintillating detectors employing these nanoparticles, and began the process to characterize their optical, physical, and radiation detector properties. The crystals used in this work were LaF_3:Ce mixed with oleic acid. The modified oleic acid is a scintillator material, so it increases the amount of energy converted to a detectable signal. A polymer composite produced by Radiation Monitoring Devices, Inc. (RMD), was used to make initial measurements of the 5% LaF_3:Ce–loaded and 25% LaF_3:Ce–loaded samples shown in Figure 1. We also prepared the detectors for interfacing to the phototube and electronics (Figure 2). Our initial results are reported here and compared to both modeling data and the data reported by Del Sesto.

Figure 1. Detector from RMD with 5% LaF_3:Ce and 25% LaF_3:Ce nanoparticle loading by mass

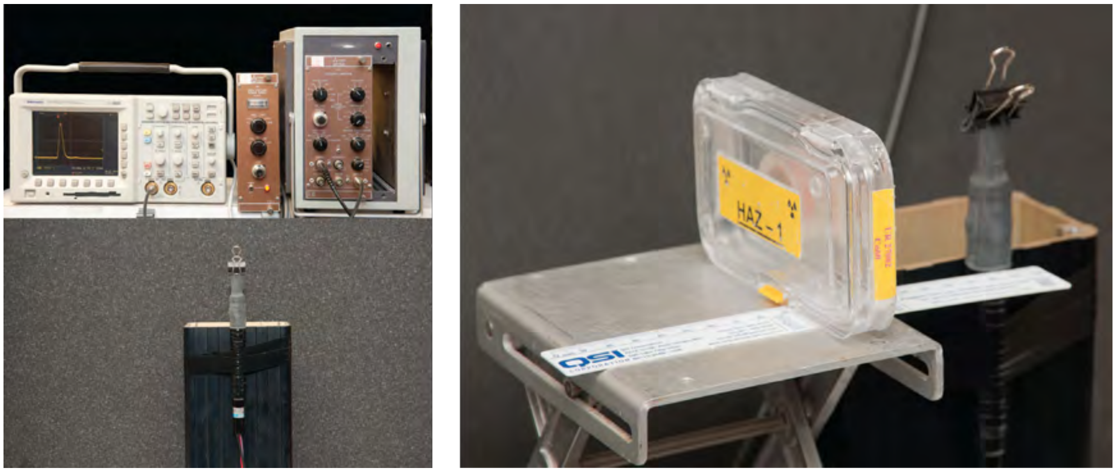

Figure 2. Detector setup for studying the nanocomposite detector. (left) The oscilloscope, power supply, and electronics are shown in the upper part of the photo, while the (liquid) detector assembly is shown below, resting on top of the photomutiplier tube, wrapped in black tape to make the assembly light tight. Signal and high-voltage cables are connected to the detector. (right) The detector assembly is to the right of the ^{60}Co source.

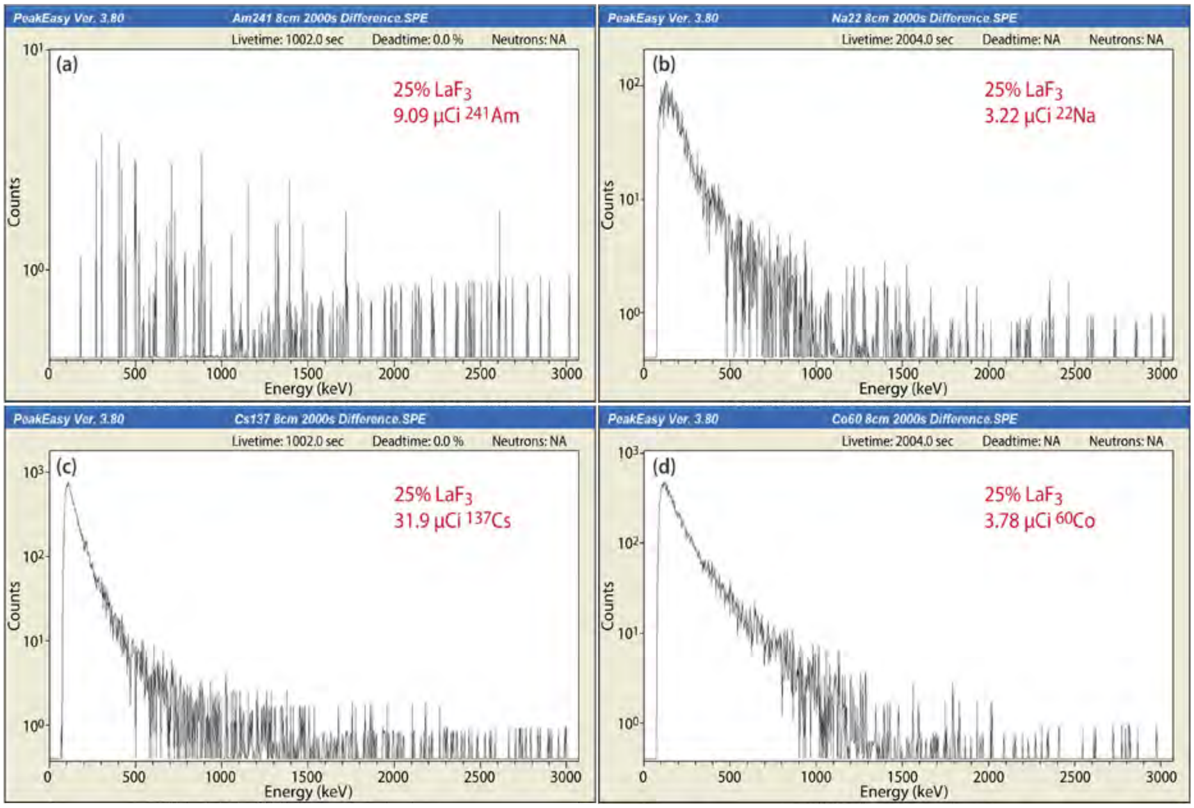

Figure 3. These are the first background-subtracted spectra for the 25% LaF_3:Ce nanocomposite detector. Significantly, they not only demonstate an excess in counts when background is removed, but in addition they demonstrate a different spectral shape for each different individual radiation source, which holds open the promise of performing some level of spectral discrimination and isotopic identification with nanocomposites.

Figure 3 shows the data from the first measurements we made with 25% LaF_3:Ce–loaded samples using the ^{241}Am (3a), ^{22}Na (3b), ^{137}Cs (3c), and ^{60}Co (3d) sources (ordered by photopeak energy of the lowest energy photopeak of significance). Figure 4 illustrates a slight energy dependence for the 25% LaF_3:Ce detector, based on the normalized spectra acquired with the ^{137}Cs and ^{60}Co sources. The ^{252}Cf data (not shown) also indicated a good neutron response by these detectors.

The nanocomposite scintillator material may even be able to discriminate between neutrons and gamma rays. Simulations support this case (Medalia, 2010). Los Alamos National Laboratory (LANL) investigators assert that basic physics calculations also support this case (Medalia, 2010). For instance, when neutrons interact with the hydrogeneous material, free protons are generated. When gamma rays interact with the material, free electrons are generated. The energy signatures for the two processes are different in magnitude and in time. Experiments demonstrating the ability of the material to detect neutrons and to differentiate them from gamma rays are required.

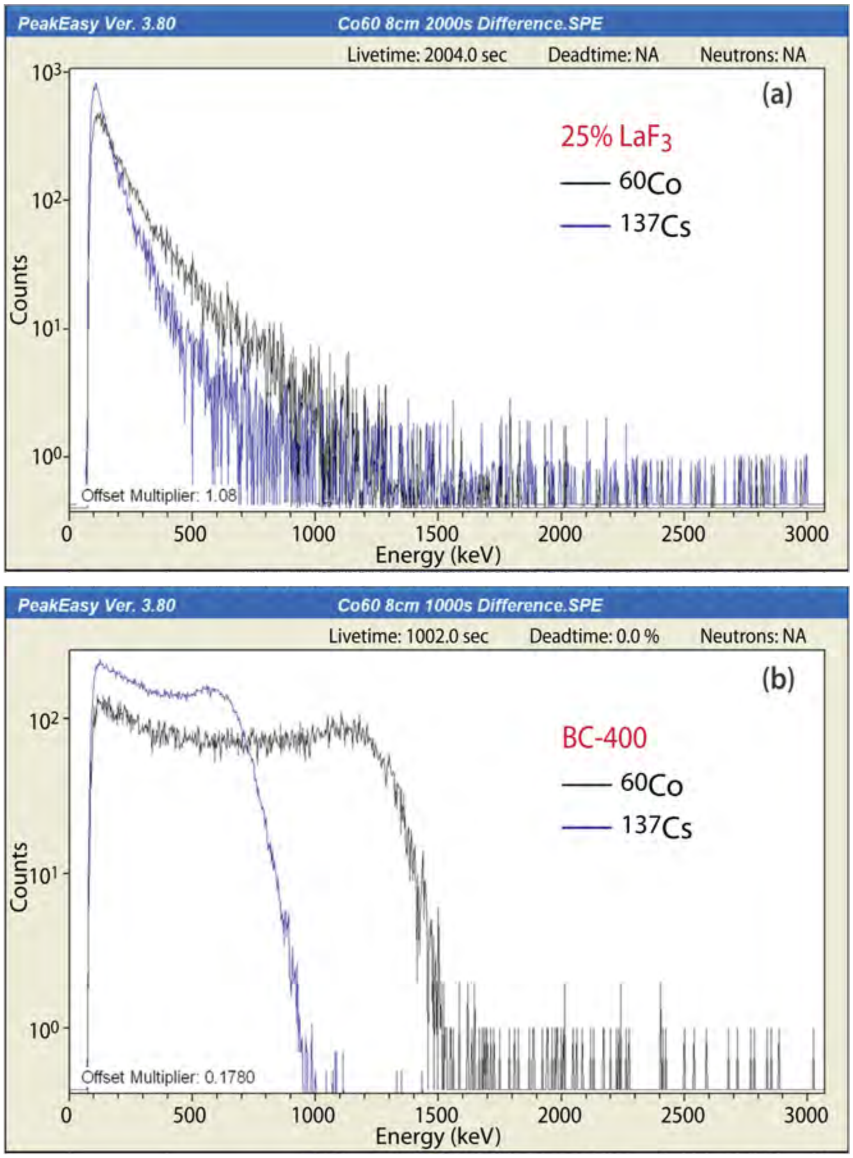

Figure 4. Background-subtracted normalized measurement of a different response for ^{60}Co and ^{137}Cs sources using the 25% LaF_3:Ce detector, which appears even more clearly when this difference is measured for a BC-400 detector. A slight energy dependence for the 25% LaF_3:Ce detector is evident.

Early in this work, we benchmarked the data that we acquired using a variety of different parameters, such as detector-to-source distances, source strengths, source types, and geometries. At this point, we have sufficient confidence in the predictive capacity of our models that we intend to use them for guidance in fine-tuning parameters for future nanoparticle detector developments. We began building our MCNPX models using the LANL 8% LaF_3:Ce nanoparticle systems, which have indicated the potential for detection of ^{137}Cs (Del Sesto, 2007).

Initial measurements of an energy spectrum (Del Sesto, 2007) for the unloaded and 8% LaF_3:Ce–loaded samples, shown in Figure 5, were first acquired by the LANL group, using ^{137}Cs sources. Their measurements show the expected Compton edge in the polymer-only sample, and the Compton edge and photopeak expected in the nanophospor composites that LANL produced (Del Sesto, 2007). We compared their data to our MCNPX model (Figure 5).

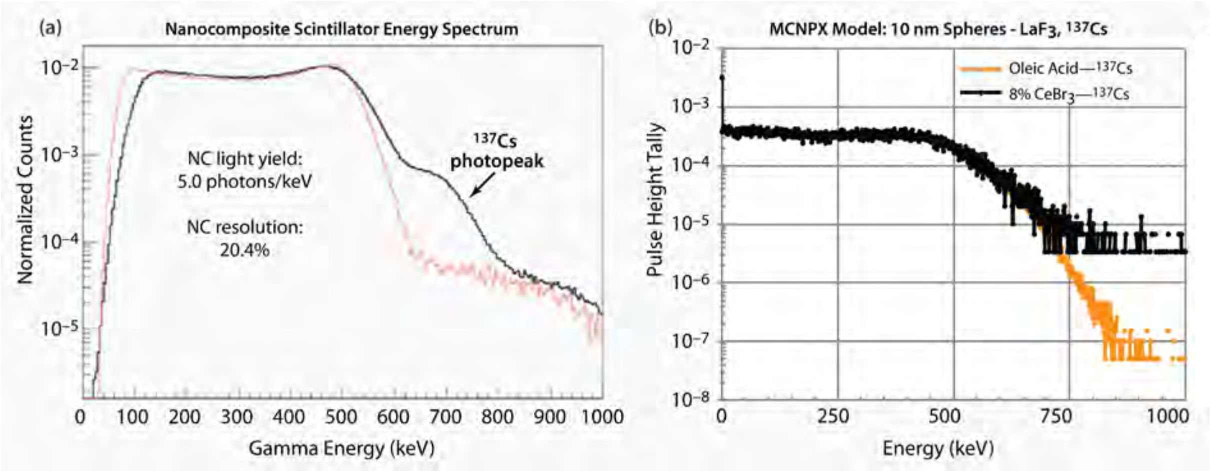

Figure 5. (a) Measured energy spectrum by Del Sesto (2007) for ^{137}Cs gamma irradiation of polymer only (pink curve) and polymer nanocomposite of 8% LaF_3:Ce with 10 nm spheres (black curve), and (b) our MCNPX model simulation and prediction. The measurements show the expected Compton edge in the polymer-only sample, and the Compton edge and photopeak expected in the nanophosphor composites. Our preliminary MCNPX calculation compares spectra for oleic acid and a polymer with 8% LaF_3:Ce exposed to ^{137}Cs (100 µCi) gamma irradiation and indicates reasonable agreement with measurements.

Technical Discussion

For an ideal scintillator, the energy resolution, *R*, is given by

$$R = \left[\frac{\Delta E}{E}\right]_{FWHM} = 2.35 \times \sqrt{\frac{(1+\nu(M))}{(N \times \varepsilon_t)}}, \tag{1}$$

where *N* is the average number of photons generated at a given energy *E*, $v(M)$ is the variance in the multiplication factor of the photomultiplier tube (PMT) (for a typical 10-stage PMT with a gain of 2×10^6, $v(M)$ is approximately 0.08), and ε_t is the average transport efficiency. $\Delta E/E$ is measured experimentally, $v(M)$ is a known constant, and combined histories and transport simulations can provide an estimate of ε_t. The only unknown parameter then is *N*, the number of photons generated in the material under an incident gamma energy. Létant and Wang (2006) determined a value of the average transport efficiency ε_t of 0.063 ±0.002 for their cadmium selenide nanoparticle with zinc sulfide shell (CdSe/ZnS core shell quantum dot) nanocomposite detector. By inserting ε_t in the energy resolution formula discussed above, the average photon output of the quantum dot glass material that Létant and Wang studied under 59 keV gamma-ray irradiation was estimated to be close to 4210 (while the number of photons generated by a sodium iodide [NaI] crystal under the same conditions was only 2600). For higher energies, the projected light output would be about 70,600 photons at 1 MeV, assuming the quantum dot medium has a linear response, which is a factor 1.75 better than the NaI crystal for which *N* is typically 40,000 (Létant, 2006). However, the data for our initial measurements reported in Table 1 are consistent with a lower efficiency and a lower light output typical of nanoparticle detectors that is not seen in BC-400 detectors. This may be due to the combination of the self-shielding effect contributed by the inorganic solution and the high concentration of the suspended nanocrystals. All of the other particulars depicted in Table 1, i.e., scaling with particle density and with source strength, are consistent with expectation.

Table 1. Count rate for 25% LaF_3:Ce, 5% LaF_3:Ce, and BC-400 detectors

Background Subtracted Count Rate versus Source (cps)				
Source	**Intensity (μCi)**	**25% LaF_3:Ce (cps)**	**5% LaF_3:Ce (cps)**	**BC-400 (cps)**
Background		4.7	2.6	1
^{22}Na (8 cm)	3.22	2.5	1.8	23.3
^{60}Co (8 cm)	3.78	11.2	7.9	34.4
^{137}Cs (8 cm)	31.9	10.4	7.0	193.6
^{137}Cs (16 cm)	31.9	5.3	4.1	0.6
^{241}Am (8 cm)	9.09	0.07	-	-
^{252}Cf (18 cm)	5.03	0.2	1.7	0.6

The work by Walters (2006), however, suggests a more intriguing aspect of nanocomposites. This work produced a measurement of 60% photolumicenscence quantum efficiency. Taken together with the work of Létant and Wang, this suggests nanocomposites have a potential for high quantum efficiency and good energy resolution for gamma-ray spectroscopy (Walters, 2006).

As the development of this material continues, the energy resolution is expected to improve and the photopeak-to-Compton ratio may become greater at higher loadings. These measurements indicate that the expected Compton edge and photopeak may be present in the new nanophospor composites that RMD will produce. For example, using a porous Vycor (VYCOR® Brand Porous Glass 7930, 2001) with CdSe/ZnS core shell quantum dots, Létant has obtained signatures of the ^{241}Am photopeak with energy resolution as good as thallium-doped sodium iodide (Létant, 2006).

Conclusion

Nanostructured radiation scintillator detectors may lead to techniques to improve quantum efficiency and exploit vastly improved detector form factors compared to currently used inorganic scintillators. Nanocomposites can dramatically change the size, shape, and luminosity of materials and, by being easily accessible to coupling to photodiodes, can offer higher quantum efficiency for detecting light quanta. This compares to PMTs that suffer from low quantum efficiency (1%–10%). We have prepared two nanocomposite detectors, one of 5% LaF_3:Ce nanoparticle loading by mass and one of 25% LaF_3:Ce nanoparticle loading by mass. The first results of detector response using these specific detector materials were compared to models and to prior nanocomposite detector data. In general, the agreement between data and models was good. We have determined that these nanocomposites' response to radiation is significant. Nanocomposites are sensitive to both neutrons and photons (gamma and x-rays). The first production nanocomposite detectors prepared for this work are weaker in terms of energy response than BC-400, and have yet to match the performance of plastic detectors. The 25% LaF_3:Ce nanoparticle loading by mass detector had better performance compared to the 5% LaF_3:Ce nanoparticle loading by mass detector, yet still roughly less than half the sensitivity (efficiency) of the BC-400 detector of comparable size. Key points are that nanocomposite detectors are cheap, easy to fabricate, and respond to nuclear radiation. We need more work to determine how best to obtain isotopic correlations and to optimize light yield.

Acknowledgments

The authors acknowledge Vivek Nagarkar of RMD of Watertown, Massachusetts, for the production of the nanocomposite detectors, for providing these detectors on loan to the Remote Sensing Laboratory, and for his support and advice. The authors also acknowledge Denis Beller and Anthony Santo Domingo of the University of Nevada, Las Vegas, for their measurement of $CeBr_3$ properties.

References

Del Sesto, R. E., E. A. McKigney, D. W. Cooke, R. E. Muenchausen, K. C. Ott, R. D. Gilbertson, T. M. McCleskey, M. Bacrania, L. G. Jacobsohn, A. K. Burell, B. L. Bennett, S. C. Sitarz, J. F. Smith, "Development of nanocomposite scintillators," LALP-07-030 Spring 2007. http://www.lanl.gov/orgs/mpa/files/mrhighlights/LALP-07-030.pdf, accessed September 15, 2010.

Létant, S. E., T.-F. Wang, "Semiconductor quantum dot scintillator under γ-ray irradiation," *Nano. Lett*. **6** (2006) 2877–2880.

Medalia, J., "Detection of Nuclear Weapons and Materials: Science, Technologies, Observations. Congressional Research Service. R401454. CRS Report for Congress," Prepared for Members and Committees of Congress June 4, 2010, http://www.fas.org/sgp/crs/nuke/R40154.pdf, accessed on November 5, 2010.

"VYCOR® Brand Porous Glass 7930," Corning Incorporated, 2001, http://www.corning.com/docs/specialtymaterials/pisheets/Vycor%207930.pdf, accessed November 16, 2010.

Walters, R. J., J. Kalkman, A. Polman, H. A. Atwater, M. J. A. de Dood, "Photoluminescence quantum efficiency of dense silicon nanocrystal ensembles in SiO_2," *Phys. Rev. B* **73** (2006) 132302-1–132302-4.

this page intentionally left blank

MINIATURIZING TIME-OF-FLIGHT MASS SPECTROMETERS

Manuel J. Manard[1,a]

The design of a proof-of-concept, prototype, reduced-size time-of-flight (TOF) mass spectrometer (MS) is described. The system is composed of an ion acceleration/focusing/steering region, an 8 cm field-free region, a 4 cm dual-stage reflectron, and a specialized miniature microchannel plate detector. Consequently, the resulting flight length of the system is 12 cm, approximately one order of magnitude less than typical TOF systems. Ion trajectory simulations were performed using a commercially available software package, Simion 8, to probe the theoretical performance of the miniaturized TOF MS. These calculations indicate that for a mass-to-charge ratio of 100 amu, a resolution of approximately 1000 can be theoretically obtained with the system.

Background

Time-of-flight (TOF) mass spectrometry is well known for its ability to combine high-resolution mass analysis with high sensitivity and selectivity. TOF is unique among mass analysis techniques due to its relatively simple implementation and its inherently unlimited mass range. Compared to other mass spectral methods that require the use of taxing experimental parameters such as a homogeneous magnetic field or high-amplitude RF electric fields to facilitate mass analysis, TOF requires only DC potentials and simple timing circuitry to generate a mass spectrum. TOF functions by accelerating a packet of ions in an electric field of a known strength. To a first-order approximation, this results in all ions in the packet having the same kinetic energy (E_k):

$$E_k = \frac{mv^2}{2}, \tag{1}$$

where m is the mass of the ion and v is the velocity of the ion. However, the velocity of an individual ion depends upon its mass-to-charge (m/z) ratio, with more massive ions moving more slowly than less massive ions. Since the length of the ion's flight path (l) is known, one can directly relate the flight time of an ion (t) to its mass by combining Equation 1 with $v = \frac{l}{t}$ to yield:

$$t = \frac{l\sqrt{m}}{\sqrt{2E_k}}. \tag{2}$$

---

[1] manardmj@nv.doe.gov, 805-681-2121

[a] Special Technologies Laboratory

Therefore, if the ion packet is pulsed into the system at a time $t = 0$, then the measured flight time of each ion is directly proportional to the square root of its mass, with lighter ions arriving at the detector with shorter flight times than heavier ions.

Two factors affecting resolution of the TOF measurement are the duration of the flight time of the ion packet and the kinetic energy distribution of the ion packet prior to acceleration into the TOF instrument. Relatively long flight lengths allow ions of similar mass to separate during their flight and thus give rise to the high-resolution mass analysis of the TOF mass spectrometer (MS). This becomes increasingly important for relatively high m/z measurements (≥500 amu), where the difference in flight times of ions varying in mass by ±1 amu can become exceedingly small. Lengthy flight times are not without their drawbacks however, as ion collisions with background gases can reduce the mass resolution of the TOF measurement. Therefore, as the flight lengths of the ions increase, their mean-free-path must also increase to retain the improved resolution. This leads to increased vacuum requirements for the system.

In order to correct for a spread in the initial kinetic energy of the of ion packet, a device known as a reflectron is used (Mamyrin, 1973). A reflectron is a series of resistively coupled ring electrodes. A repulsive electric field gradient is applied to the electrodes of the reflectron. As the ions enter the reflectron, the repulsive field slows the ions and turns them around, essentially reflecting the ion packet back in the direction from which it came. If two ions of the same mass but different kinetic energy values enter the reflectron, the ion that is moving faster will penetrate deeper into the repelling field than the slower ion. Thus, the faster ion will take a longer time to turn around and exit the reflectron. If the proper gradients are chosen for the total distance that the two ions travel, both ions will arrive at the detector at the same time, effectively correcting for their initial spread in kinetic energy.

Despite its relatively straightforward nature, TOF has remained largely a laboratory technique. This can primarily be attributed to the large size of the instrumentation. Most commercially available TOF MSs use flight tubes that measure 100 cm in length. Although reducing the size of the flight tube will reduce the vacuum requirements of the system, doing so will also have a negative impact on the mass resolution of the system. However, due to the extremely high resolution of most TOF instruments that use a 100 cm long flight tube, the reduced mass resolution that comes with miniaturizing the system will likely still produce mass spectra with acceptable peak separations. Additionally, existing techniques used to boost resolution in laboratory instruments, such as including a reflectron in the design of the system, can be applied to a miniaturized system to alleviate some of these effects.

Project

Theoretical Modeling

Simion 8 was used to generate ion trajectory simulations to probe whether a 12 cm TOF system could produce mass spectra with acceptable resolution for relatively low-mass analytes (m/z ≤300 amu), as chemical compounds encountered in the field generally lie in this mass range. Consequently, multiple simulations were performed to test the performance of key system components included in the TOF design. Figure 1 shows a Simion 8 simulation of the mini-TOF system. The primary components of the system are (a) the acceleration/focusing/steering assembly (AFSA), (b) the field-free region, (c) the dual-stage reflectron, and (d) the ion detector. The function and theoretical performance of these components are discussed below.

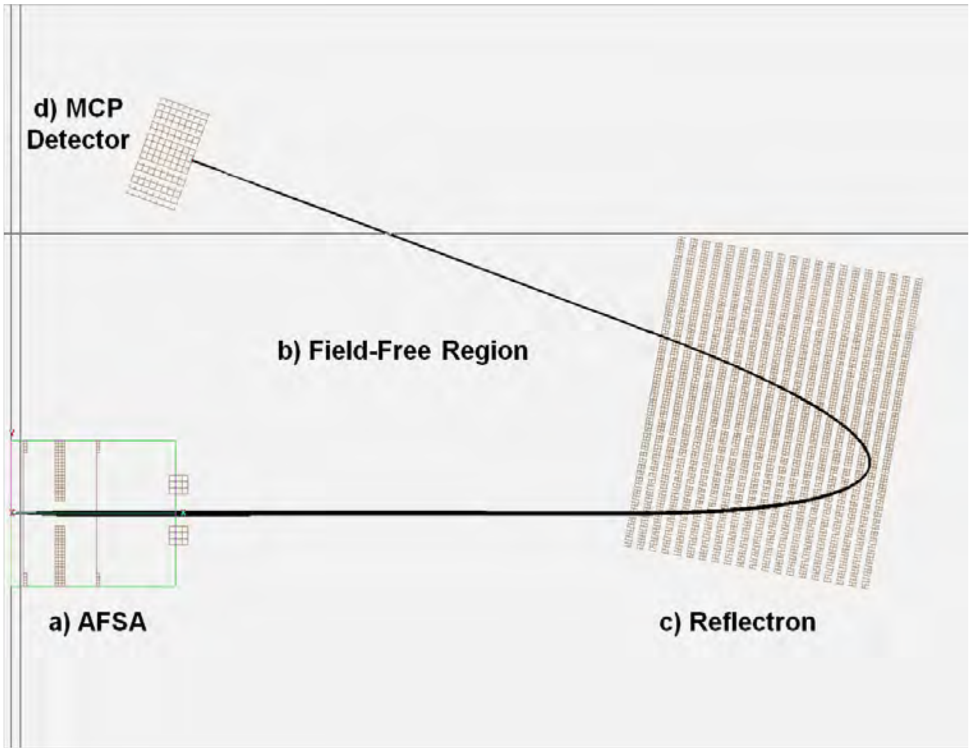

Figure 1. Ion trajectory simulation as generated by Simion 8. Ions travel along the black lines as indicated starting at the acceleration/focusing/steering assembly and eventually impinge on the microchannel plate (MCP) detector.

AFSA

The AFSA was designed to accelerate, collimate, and deflect the ion beam into the TOF system so that optimum mass resolution can be obtained at the ion detector. An acceleration potential applied to the first electrode provides the kinetic energy to the ions in the beam. The third electrode, held at the same potential as the first and positioned 10 mm from electrode 1, provides a secondary electrical reference point, biased to the acceleration potential. The second electrode acts as a lens to focus/collimate the beam; this ensures that all ions are traveling on a parallel path as they enter the field-free region. Essentially, the first three electrodes of the AFSA create an Einzel lens. Two sets of steering electrodes complete the AFSA (only one set is shown in Figure 1). They serve two purposes: (1) to deflect the beam to ensure that ions enter the reflectron with the proper trajectory to eventually impact the ion detector and, (2) for the last set of steering electrodes, to provide an ion gate. Here, the beam is pulsed into the field-free region, establishing $t = 0$ for the TOF measurement.

Field-Free Region

Most ion flight occurs in the field-free region, an area between the last steering electrodes of the AFSA and the first electrode at the entrance to the reflectron. Additionally, once the beam has exited the reflectron, it is the region between the first electrode of the reflectron and the ion detector. In the field-free region, the ion packet is not subjected to any external forces from applied electric fields. The field-free region of the mini-TOF MS measures 8 cm in length.

Reflectron

As previously described, the reflectron corrects deviations in the kinetic energy of the ions in the beam. Originally, the reflectron was designed as a series of 20 1 mm thick electrodes spaced 1 mm apart. This yielded a total length of 4 cm for the device. For our system, a dual-stage design was used. Here, two electric field gradients of differing magnitudes were applied to the reflectron's electrodes. Figure 2 shows schematically the two potential gradients applied to the reflectron. The first gradient, measuring 555 V/cm in magnitude, is applied to the first five electrodes of the system. A second gradient, measuring 345 V/cm in magnitude, is applied to the final 15 electrodes. With the dual-stage design, the relatively steeper gradient is applied over a shorter distance than the shallower gradient. This design has been reported to provide improved resolution for the TOF measurement over shorter distances when compared to a single-stage (one gradient) design (Wang, 1994). Our simulations support these findings.

The reflectron assembly is placed in the path of the ion beam, positioned at a 10-degree angle with respect to the ion beam's initial trajectory. This angle steers ions exiting the reflectron along a trajectory that impacts the detector (Figure 1). The orientation of the reflectron, along with the applied electric potentials, governs the final trajectories of the reflected ion packet.

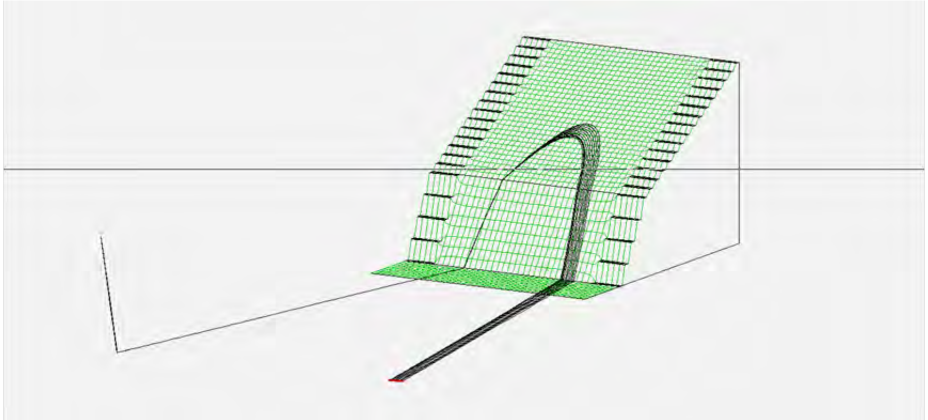

Figure 2. A potential energy surface plot, generated by Simion 8, illustrating the dual-stage design of the reflectron. The change in the electric field gradient (steeper at the entrance of the reflectron) occurs at a depth of 1 cm. Ion trajectories are shown in black.

Ion Detector

The ion detector, located directly above the AFSA, sits at a 20-degree angle, normal to the final trajectory of the ion beam (Figure 1). This placement orients the plane of the detector's active surface perpendicular to the trajectory of the reflected ion packet, to ensure that ions in a tightly focused, time-resolved packet of a given mass all strike the detector simultaneously.

To optimize system performance, the chosen detector must be capable of completely processing the signal produced by an impinging ion of a given mass before the arrival of the next ion of a different mass. This means the detector's signal rise/fall time must be faster than the flight times of two ions having similar masses. If this criterion is not met, broad, low-resolution peaks will be produced by the system.

Simulated Performance

Figure 3 shows a simulated TOF spectrum for m/z = 83 and 84 amu produced by the simulation shown in Figure 1. These masses were chosen because they correspond to two of the more-abundant, naturally occurring isotopes of krypton. From this plot, we see that the flight times of two masses differ by approximately 30 ns. This suggests that the system can resolve these two masses given that the signal processing time of the detector is faster than 30 ns. Additionally, an initial kinetic energy distribution of approximately 50 eV for both the ions of m/z = 83 and 84 was applied to the simulation to test the performance of the reflectron. Again, Figure 3 shows that ions having the same mass are arriving at the detector with nearly identical flight times. This result strongly suggests that the miniaturized system is capable of producing mass spectra with acceptable resolution for ions differing in mass by 1 amu.

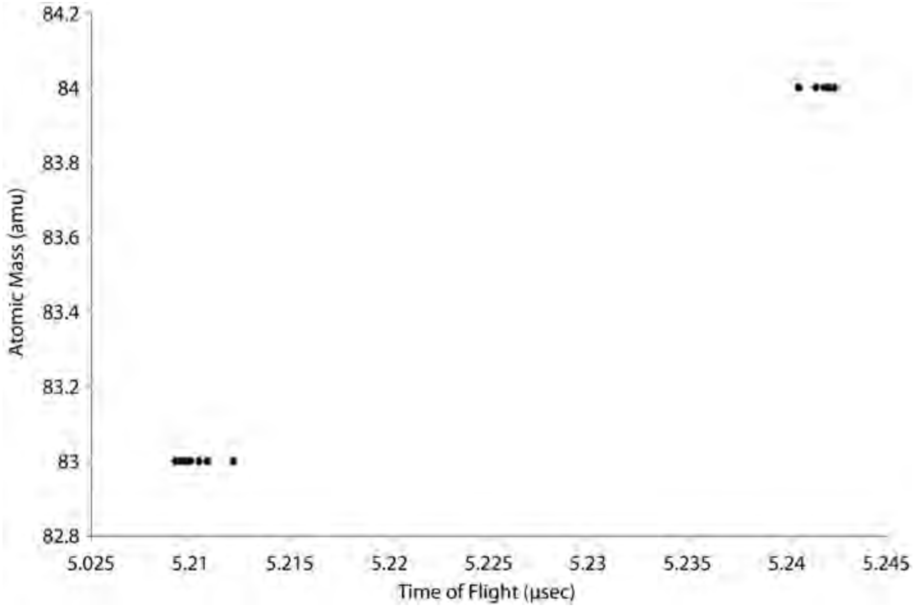

Figure 3. A plot of the simulated flight times of m/z = 83 and 84. From this plot, the expected difference in flight time of the two masses can be deduced.

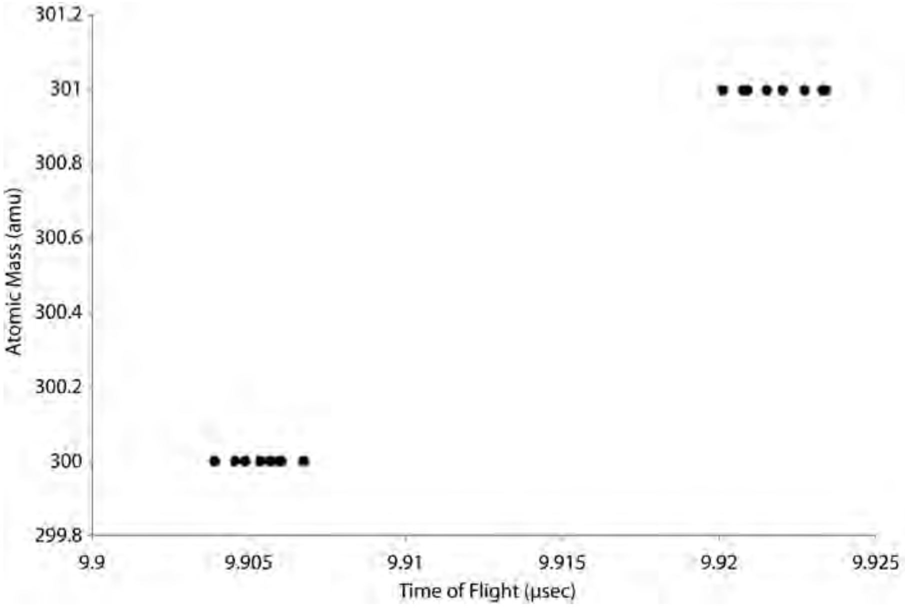

Figure 4. A plot of the simulated flight times of m/z = 300 and 301. From this plot, the expected difference in flight time of the two masses can be deduced.

Figure 4 shows the separation in time for ions with m/z = 300 and 301 amu. The data show that the separation in the flight times of the two masses has been reduced to approximately 15 ns. This demonstrates that as m/z values increase, the difference in flight time between two ions with similar masses decreases. However, Figure 4 suggests that the simulation shown in Figure 1 is capable of differentiating mass 300 from mass 301 if the proper ion detector is used.

The resolution of the mini-TOF system was theoretically determined for m/z = 100 amu, with an initial kinetic energy distribution equal to 50 eV. This was accomplished by measuring the flight times of 1000 ions arriving at the detector using the simulation shown in Figure 1. The flight times of each ion were counted, and the frequency of each occurrence was then plotted versus the flight time of the ions. Figure 5 shows a plot of frequency of arrival versus flight time resulting from this simulation. In order to determine the resolution of the system, the height of the peak at its center was divided by the width of the peak at half height. This yields a resolution of approximately 1000 for m/z = 100 and strongly suggests the mini-TOF system will be capable of producing high-resolution mass spectra.

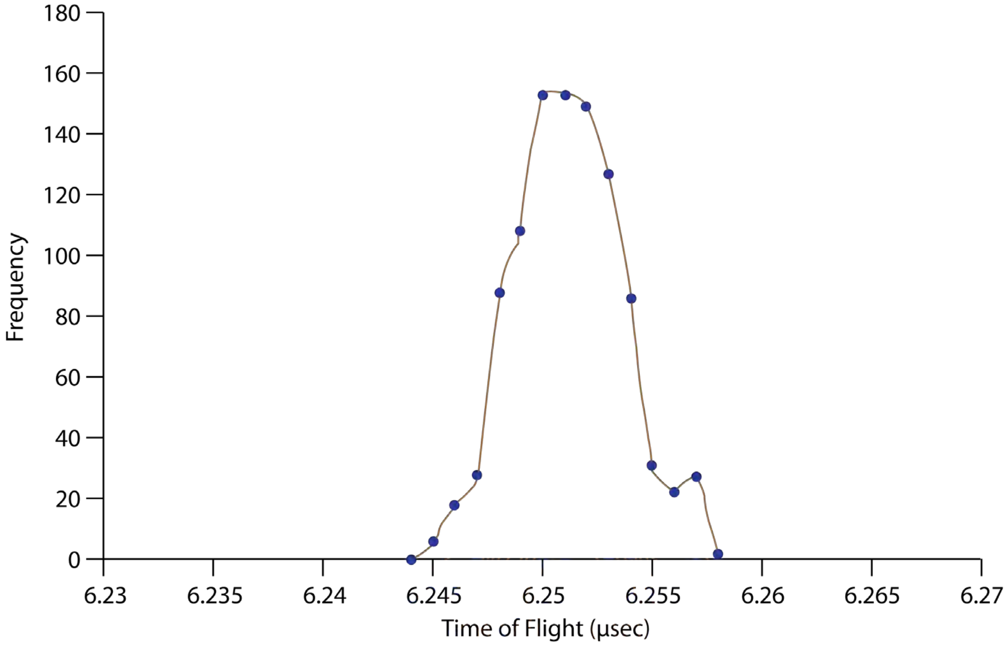

Figure 5. A plot of the simulated flight times of 1000 ions having m/z = 100. From the resulting data, a theoretical resolution of approximately 1000 has been measured for m/z = 100.

Mechanical Design

The ion trajectory simulations guided the physical design of the mini-TOF MS. Ions are generated by an electron impact source. An ion funnel, designed as part of an FY 2009 SDRD project (Manard, "Differential," 2010; "Differential mobility," 2010) guides and focuses the ion beam into the TOF chamber through a conductance-limiting orifice that measures 0.3 mm in diameter. The ion funnel is mounted to one side of a double-sided, 2¾-inch Conflat flange, with the AFSA mounted to the opposite side. As mentioned previously, the AFSA was designed to simultaneously accelerate and focus the ion beam into the mini-TOF. The first and the third electrode of the AFSA have inner diameters (IDs) of 20 mm and are 1 mm thick. A 90-percent-transmission nickel mesh was mounted with conductive epoxy to these two electrodes. The mesh provides a homogeneous electric field throughout the ID of the electrodes. The center lens, used to collimate the beam prior to introduction to the field-free region of the instrument, has an ID of 4 mm and is 2 mm thick. The two sets of steering electrodes, used to deflect and gate the ion beam, are spaced 10 mm apart and are 1 mm thick.

The dual-stage reflectron is made up of 11 electrodes (the hardware is pictured in Figure 6). The electrodes have 62 mm IDs, measure 1 mm in thickness, and are spaced 3 mm apart. Each electrode is electrically coupled using a resistor bridge. Originally, the reflectron was designed to be made up of twenty 1 mm thick electrodes spaced 1 mm apart. However, this design overly complicated the task of connecting the resistor bridge to the electrodes, so the device was redesigned to simplify the process. Simulations performed on the redesigned reflectron showed no observable change in performance.

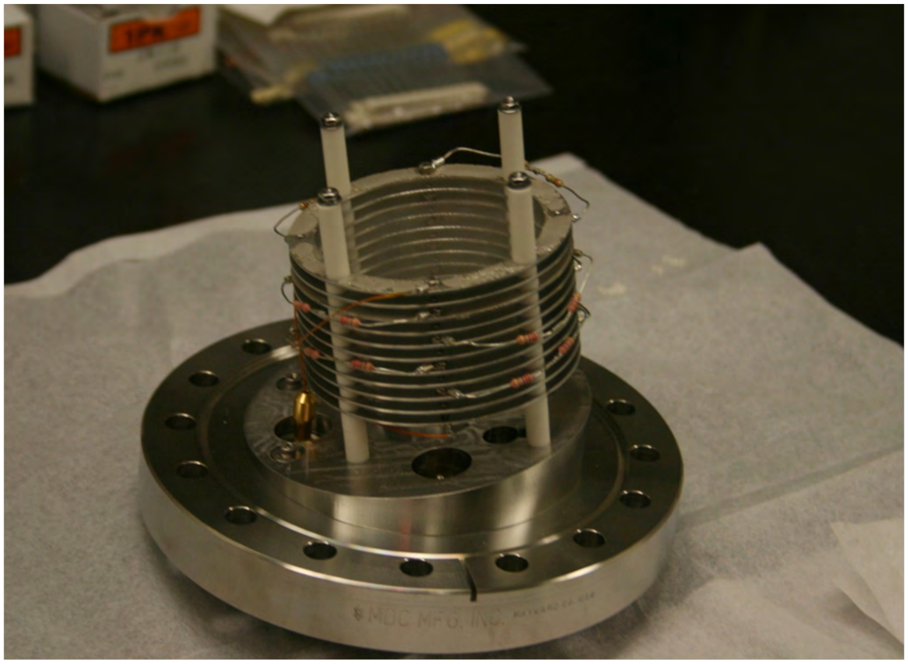

Figure 6. Mini-TOF reflectron with the resistor bridge shown outside of the lens stack

The first electrode of the reflectron is biased to the field-free potential. Two 2 MΩ resistors, connected in series for a total resistance of 4 MΩ, electrically couple the first three lenses of the reflectron and establish the first "steep" electric field gradient of the dual-stage design. The second gradient is generated by two 1.2 MΩ resistors also connected in series for a total resistance of 2.4 MΩ. This resistor bridge couples the third through the eleventh electrode of the device. As indicated by the simulations, the 90-percent-transmission nickel mesh is mounted to the first, third, and also the eleventh electrode using conductive epoxy, serving to provide a homogeneous electric field throughout the ID of the electrodes at the beginning and end of the reflectron, as well as at the third electrode, where the gradient changes.

The ion detector used for the TOF system is a commercially available miniature MCP detector (PHOTONIS Technologies). The detector is mounted to a 1.33-inch Conflat flange and is placed 2.2 inches above the AFSA (on center). The miniature MCP was designed specifically to be used with TOF MSs. The device has a reported average signal rise/fall time of approximately 0.5 ns. This indicates the MCP detector should be capable of processing ion signals arriving at the detector with separations in flight time on the order of 10 ns and thus will be able to resolve mass 300 from 301.

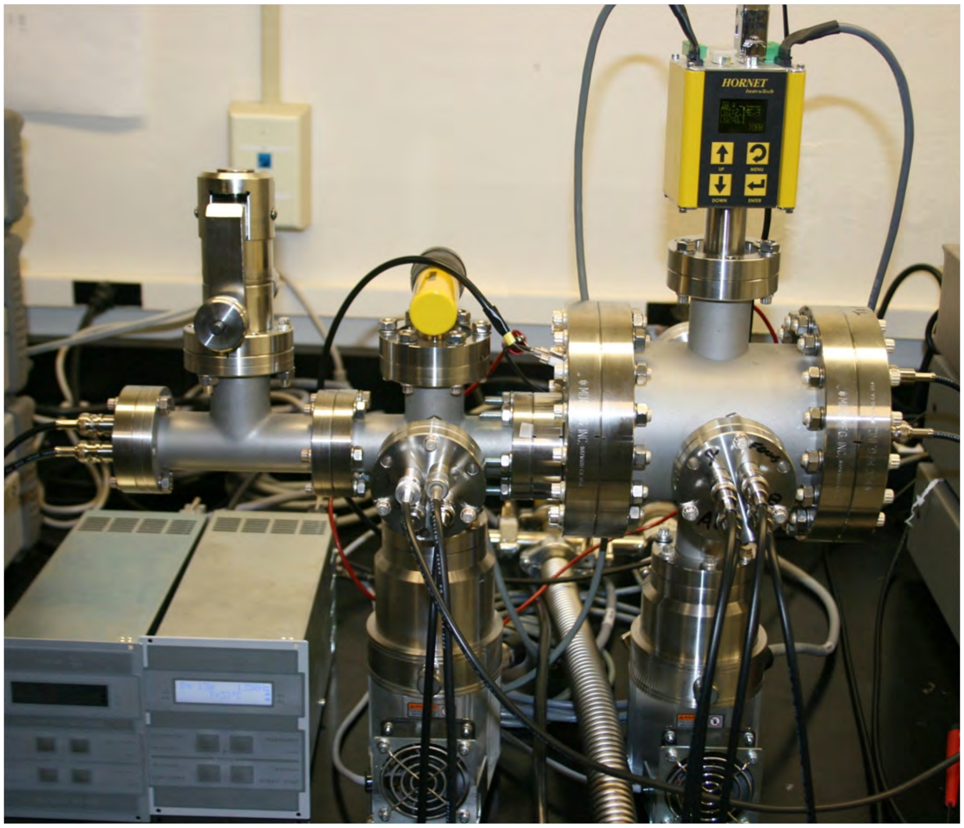

Figure 7. The mini-TOF MS benchtop system

The benchtop mini-TOF MS test system is shown in Figure 7. Much of the hardware pictured in the figure is needed to support the vacuum system, and is not representative of the true size of the core mass spectrometer hardware.

Results

Following the assembly of the system, initial tests were run to determine if the ion beam could be redirected by the reflectron and detected with the MCP detector. Accordingly, a −1500 V potential was applied to the acceleration and the steering electrodes. Additionally, −1500 V was applied to the first electrode of the reflectron and 100 V was applied to the last electrode. The MCP detector was also biased to −1500 V. An ion current of approximately 100 nA was measured by the MCP. This is approximately seven orders of magnitude greater than the dark current measured by the detector when no ions are present and strongly suggests that the ion beam is being manipulated by the system as intended.

Conclusion

The design of a 12 cm, proof-of-concept, prototype TOF MS was described. The system is primarily made up of an ion acceleration/focusing/steering region, an 8 cm field-free region, a 4 cm dual-stage reflectron, and a specialized miniature MCP detector. Ion trajectory simulations (Simion 8) were used to optimize ion transport though the instrument and to determine the theoretical mass resolution of the system. Once assembled, an ion current seven orders of magnitude greater than the dark current of the detector was measured for an ion beam directed into the reflectron. Currently, efforts are under way to pulse the ion beam into the system by applying a gate voltage to the steering electrodes of the AFSA, essentially generating a $t = 0$ for the TOF measurement. Furthermore, a modification to the instrument design will be made in which a tube, biased to the potential of the field-free region, will be mounted to the first electrode of the reflectron. This will essentially serve to shield the ion beam from the grounded flight tube and ensure the flight path is truly free from the influence of external electric fields.

Acknowledgments

The author would like to acknowledge Rusty Trainham, Tom Keenan, and Glen Anthony at NSTec for their contributions to the design and assembly of the TOF instrument.

References

Mamyrin, B. A., V. I. Karataev, D. V. Shmikk, V. A. Zagulin, "The mass-reflectron, a new nonmagnetic time-of-flight mass spectrometer with high resolution," *Sov. Phys. JETP* **37** (1973) 45–48.

Manard, M. J., R. Trainham, "Differential mobility spectrometry/mass spectrometer," *Nevada Test Site–Directed Research and Development*, FY 2009, National Security Technologies, LLC, Las Vegas, Nevada, 2010, 67–75.

Manard, M. J., R. Trainham, S. Weeks, S. L. Coy, E. V. Krylov, E. G. Nazarov, "Differential mobility spectrometry/mass spectrometry: The design of a new mass spectrometer for real-time chemical analysis in the field," *Int. J. Mass Spectrom*. **295**, 3 (2010) 138–144.

Wang, T. I., C. W. Chu, H. M. Hung, G. S. Kuo, C. C. Han, "Design parameters of dual-stage ion reflectrons," *Rev. Sci. Instrum.* **65**, 5 (1994) 1585–1589.

this page intentionally left blank

STRAW DETECTOR—DUAL FISSION METER FOR GAMMA AND NEUTRON MULTIPLICITY MEASUREMENTS

Sanjoy Mukhopadhyay,[1,a] *Ronald S. Wolff,*[a] *Stephen Mitchell,*[b] *Paul P. Guss,*[b] *and Richard Maurer*[a]

Counting neutrons emitted by special nuclear material (SNM) and partitioning them from the background neutrons of various origins is the most effective passive means of detecting SNM. Unfortunately, neutron detection, counting, and partitioning in a maritime environment is complex due to the presence of spallation neutrons (commonly known as "ship effect") and to the complicated nature of the neutron scattering in that environment. A prototype neutron detector was built using boron-10 (^{10}B) as the converter in a novel form factor called "straws" that would address the above problems by looking into the details of multiplicity distributions of neutrons originating from a fissioning source. The prototype provides a large-area, efficient, light-weight, more granular neutron-responsive detection surface (to facilitate imaging) to enhance the ease of application of fission meters (FMs). Presented here are the results of preliminary investigations, modeling, and engineering considerations leading to the construction of this prototype. This design is capable of multiplicity and Feynman variance measurements. This prototype may lead to a near-term solution to the crisis that has arisen from the global scarcity of ^{3}He by offering a viable alternative to FMs.

Background

Currently, commercially manufactured fission meters (FMs) are available that separate cosmic neutrons from noncosmic neutrons and quantitatively determine the strength of a fissioning source; however, these FMs use ^{3}He, which is becoming increasingly difficult to procure, and the size and weight of an FM is not conducive to manual searches onboard a ship. There is a critical shortage of ^{3}He gas for use in proportional counters as neutron detectors. Within the last few years, the amount of ^{3}He available for use in gas proportional counter neutron detectors has become more restricted, while the demand has significantly increased, especially for homeland security applications (Kouzes, 2010). Boron-lined proportional counters are a possible neutron detector replacement technology for ^{3}He-filled tubes. The boron-lined detector that was explored in this work operates on a design that utilizes multiple boron-lined proportional counters in a moderator assembly. These counters are referred to as "straws" because they are manufactured by rolling a copper strip into a tube in a manner similar to that used when making a straw. Straws are thin (only 4 mm in diameter) and can be closely packed to achieve very high neutron detection sensitivity. Because of their high sensitivity and granularity, straws are better FM elements than thick (1-inch-diameter) ^{3}He tubes. By reading out an individual straw, one can determine the neutron interaction point precisely and hence attempt to image the neutron source origin.

---

[1] mukhops@nv.doe.gov, 301-817-3319

[a] Remote Sensing Laboratory–Andrews; [b] Remote Sensing Laboratory–Nellis

Recently, Proportional Technologies, Inc. (PTI), from Houston, Texas, developed thin (2-mil-thick wall) copper tubes (with internal diameter of 4 mm) coated internally with 1 μm of enriched ^{10}B (Lacy, 2008) that were proposed to be used as elements of the prototype FM. Low-energy neutrons incident on a ^{10}B-coated surface will go through the following nuclear reaction:

$$^{10}B(n, \alpha)\ ^{7}Li + 2.792\ \text{MeV (ground state)} - 6\%\ \text{, and} \tag{1}$$

$$^{10}B(n, \alpha)\ ^{*7}Li + 2.310\ \text{MeV (excited state)} - 94\%. \tag{2}$$

The respective kinetic energies of the positive ions generated from Equation 2 are $E_{*Li} = 0.84$ MeV and $E_{\alpha} = 1.47$ MeV—this restricts the α-particles to have a mean free path of approximately 2 μm in ^{10}B bulk. This limitation on the kinetic energy available to the α-particles requires that the ^{10}B layer be thin so that the α-particles can be drawn from the ^{10}B surface out to the high-voltage anode wire of the proportional chambers. The thermal neutron cross section for the $^{10}B(n, \alpha)\ ^{7}Li$ reaction is 3840 barns. The cross section drops rapidly with increasing neutron energy and is proportional to 1/v (the reciprocal of the neutron velocity). The corresponding value for ^{3}He is 5330 barns, significantly higher than that for the boron reaction. This makes ^{3}He a better intrinsic neutron converter than ^{10}B. The gamma response can be separated completely by simple pulse height separation. A lower-level discriminator at 100 keV separates out the gamma-ray response from the neutrons. Only neutron pulse height is used by the proposed electronics. Gamma pulses separated from neutrons can be counted separately, and a gamma multiplicity distribution from spontaneous fission sources can be obtained.

The project intended to use straw detectors lined with ^{10}B to develop a high-efficiency, large-area, lightweight prototype neutron detector (with distinguishable and separable gamma sensitivity) that would work as a multiplicity counter in the presence of special nuclear material (SNM). The ultra-thin diameters of the straws provide unprecedented granularity; this feature will enhance our ability to image source and measure multiplicity distribution. The prototype would provide an immediate replacement for ^{3}He in neutron counting and measurements. Objectives for this research project included a preliminary exploration of an imaging capability for both gamma and neutron sources using fine-resolution tubes (Athanasiades, 2005); a study of the masking and occlusion processes to better image radiation source; and production of the first aerial system with directional sensitivity for neutron detection.

Project

Prototype Design

A commercial FM consists of one bare side; the other side is moderated with 1-inch-thick high-density polyethylene (HDPE). The prototype straw panel, shown in Figure 1, consists of 60 straws distributed in three equidistant rows within an HDPE matrix that is 5 cm thick. The straws are 70 cm long and 4 mm in diameter. The panel is 40 cm wide and 6.25 cm thick. The proposed FM will include 120 straws to provide a nominal neutron detection area of 0.56 m^2 (the effective ^{10}B area is significantly larger). The transistor-to-transistor logic output will be about 500 ns wide and 3.5 VDC in amplitude.

Figure 1. The prototype straw panel manufactured by PTI

MCNPX Work

The current Radiation Safety Information Computational Center Monte Carlo n-Particle Transport code 5 MCNP5 (1.5)/MCNPX (2.6) release includes the MCNPX Visual Editor (VISED). This version of VISED was used to perform Monte Carlo simulations of the low-energy neutron interactions with the ^{10}B coating on the straw walls. Design parameters of most concern were (1) neutron and gamma efficiency calculations for the prototype module, (2) angular response to point-like neutron sources, (3) incorporation of other neutron converter materials like ^{6}LiF or ^{6}Li-metal and comparison of the relative efficiencies with different thicknesses of ^{10}B coatings, and (4) variation of efficiency of neutron detection with converter layer thickness. In all applications, ^{252}Cf was used as the neutron source, and the neutron energy distribution from the spontaneous fission was described by the Watt spectrum $\chi(E_n)$ as follows:

$$\chi(E_n) = 0.64\ e^{-En/1.175} \sinh\ (1.0411E_n)^{0.5}. \tag{3}$$

The generic straw module as envisioned by the MCNPX is shown in Figure 2. Neutron detection efficiency by both an FM and a Detective-EX-100 (a combination of high-purity germanium gamma energy spectrometer and a neutron counter manufactured by ORTEC Corp.) is compared to that expected from the straw panel in Figure 3. For this calculation, only a single panel of straws was compared with a single panel of an FM, whereas the entire four-tube neutron array in the Detective-EX-100 was modeled.

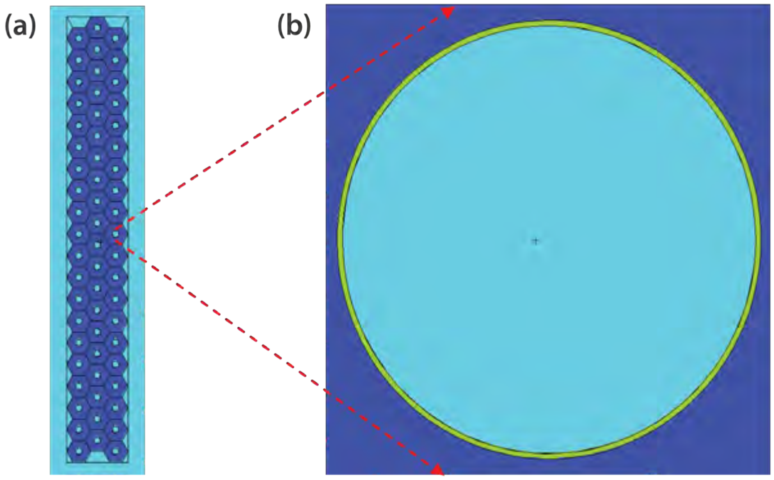

Figure 2. (a) A cross-sectional view of the panel depicted in Figure 1. Sixty straws are distributed in 20 rows by 3 columns (or 20 × 3). Each straw, 50 cm long and 4 mm in diameter, is shown in the middle of a hexagonal packed matrix of HDPE. Tubes are coated uniformly with ^{10}B 1 µm thick. (b) A single straw is enlarged to show to scale the ^{10}B layer (the green outlined circle), which is generally too thin to be visible in normal view.

Data Acquisition

To measure high statistics data related to neutron multiplicity, two data acquisition methods were used; they are described below.

Fission Meter Simulator Unit (FMSU) Data

The FMSU is the field-programmable gate array (FPGA)–based electronic data acquisition system being developed; it consists of both the hardware and software components of the data acquisition system for the proposed FM. This unit consists of an FPGA with logic and data acquisition software developed at NSTec. The FMSU records neutron arrival times at the detector array by accumulating events into a series of time bins. Arrival-time statistics are correlated in a histogram of the numbers of neutrons arriving within a time gate for a range of gate widths (1–512 µs). This technique provides the Feynman variance Y_{2F} measurements.

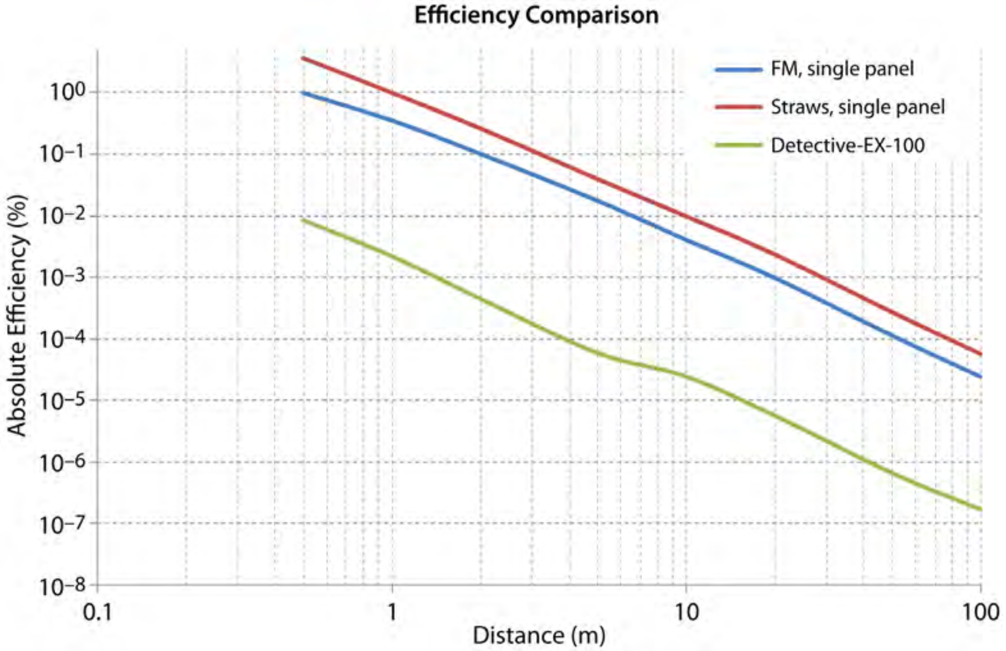

Figure 3. Detection efficiencies of thermal neutrons by Detective-EX-100 (green), a single panel of fission meter (blue) and the prototype straw panel (red) are shown. The efficiency values at different source-to-detector distances were calculated by using an MCNPX radiation transport simulation package.

The project team procured an FPGA (model PCI-7813R) from Nuclear Instruments, Inc. An FPGA is an integrated circuit designed to be configured by the application user. FPGAs can be used to implement any logical function, and they support thousands of gates. The system can obtain two types of data: (1) real-time static or mobile data, and (2) characterization or assay data. All data types can be taken simultaneously. The system initialization (SI), microsecond counter (MC), real-time data acquisition (RDA), and characterization data acquisition (CDA) comprise the four modules of the FMSU data acquisition system. The SI ensures that the system and memory are in a good state prior to executing the rest of the system modules; the MC, RDA, and CDA execute concurrently. Each module is described in more detail below.

The MC, operating within a 40 MHz timed loop or every 25 nanoseconds, examines the state of a pin for indication of a new pulse. If a new pulse is found, then the previous count data are incremented by one; otherwise the count data remain the same. After the pulse detection algorithm, the MC examines a counter to determine if 1 μs has elapsed. Once the MC has elapsed 1 μs, the MC examines the operating states of the RDA and CDA. If they are active, the MC will pass the collected count data to their respective first-in first-out (FIFO) buffers before resetting the count data to zero.

The RDA operates within a loop, which has two phases, Get Parameters and Acquire Data. In the first phase, the RDA continually gathers parameters. After the Acquire switch is pressed, the RDA passes the last gathered parameters and begins to acquire data. The RDA gathers microsecond count data from its FIFO, from which it builds the real-time log file. The RDA sums data from the FIFO (bin width/1 μs) times. It then increments the summed position in the multiplet array and resets the summed value to zero. After repeating the previous process, Bin Count times, the multiplet array is passed to the host computer via a second FIFO, and then the multiplet array is reset to zero. The host is responsible for generating the log file. While the RDA is acquiring data it can be stopped and reconfigured at any time. However, data collection will continue until a host FIFO completes a FIFO transfer. The RDA will then revert to gathering parameters.

Similar to the RDA, the CDA has two phases: Get Parameters and Acquire Data. The CDA continually gathers parameters until the Acquire switch is pressed. After the switch is pressed, the CDA passes the last gathered parameters and gathers microsecond count data from its FIFO, from which it constructs the 2A log file. The CDA sums data from the FIFO (bin width/1 μs) times. It then increments the multiplet matrix (MM) based on the summed count and the active gate. After incrementing the MM, the CDA returns to the previous step and collects data for the next gate. The summed count data is reset to zero after the data for the last gate/bin were incremented in the MM (also known as the completion of a cycle). A cycle's duration can be calculated as Bin Width × Bin Count. The above steps are repeated the number of times specified by the cycle parameter. The MM is transferred to the host when all cycles are completed. When data acquisition is complete, the CDA reverts to collecting parameters. The host is responsible for generating the log file.

The CDA can append data to previously acquired data by not clearing the memory for the MM. The previous data file will not be overwritten. The CDA Acquire Data routine can be stopped at any time; however, the routine will only halt after a full cycle is completed, at which point it will transfer the MM to the host computer and reenter the first phase.

Multiplicity Register Data Acquisition Method

A handheld stand-alone multiplicity register (JSR-15, 2010) manufactured by Canberra Industries, Inc., was procured to obtain multiplicity data directly from the straw detectors. The JSR-15 was procured to prove that in the absence of a working FPGA module a straw detector is capable of efficient neutron counting sufficient enough for multiplicity measurements. The JSR-15 counts and records the total number of pulses and the time correlation of the pulses to provide coincidence timing (Figure 4). Multiplicity distributions of the coincident events are recorded as well. The JSR-15 has an internal clock rate of 50 MHz and is therefore capable of handling high count-rate applications. It has been tested up to a count rate of 20 MHz using NDA 2000 software (Canberra, 2010), ensuring that the shift register will not be the limiting factor in any current or near-term practical counting situation. The JSR-15 has built-in batteries and can run for up to eight hours on a single charge when operated in battery-save mode. The battery capability, along with the compact size and light weight, make the instrument extremely portable.

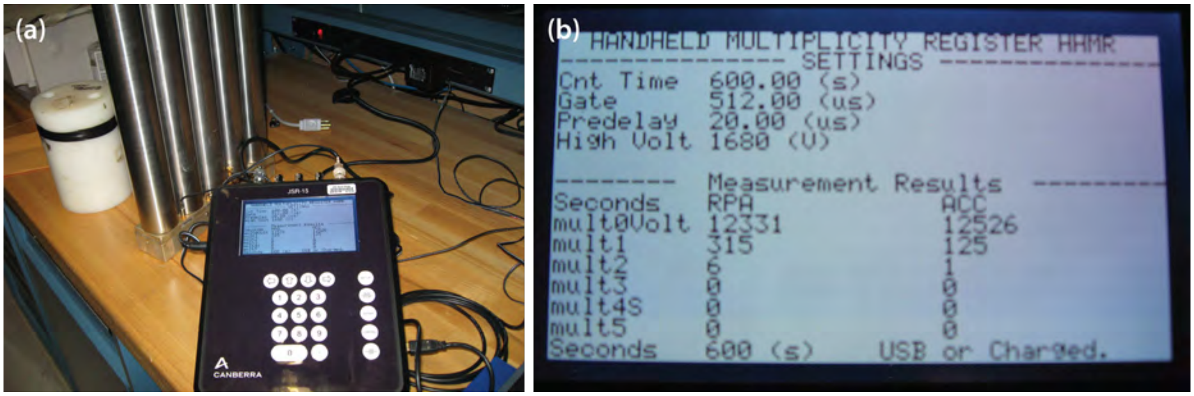

```
HANDHELD MULTIPLICITY REGISTER HHMR
--------------- SETTINGS ---------------
Cnt Time  600.00 (s)
Gate      512.00 (us)
Predelay  20.00 (us)
High Volt 1680 (V)

--------  Measurement Results  --------
Seconds   RPA              ACC
mult0Volt 12331            12526
mult1     315              125
mult2     6                1
mult3     0                0
mult4S    0                0
mult5     0                0
Seconds   600 (s)     USB or Charged.
```

Figure 4. (a) A stand-alone handheld multiplicity register, model JSR-15 manufactured by Canberra Industries, Inc., uses a (b) straightforward shift register technique to calculate true singles, doubles, triples, etc., and obtains a multiplicity distribution

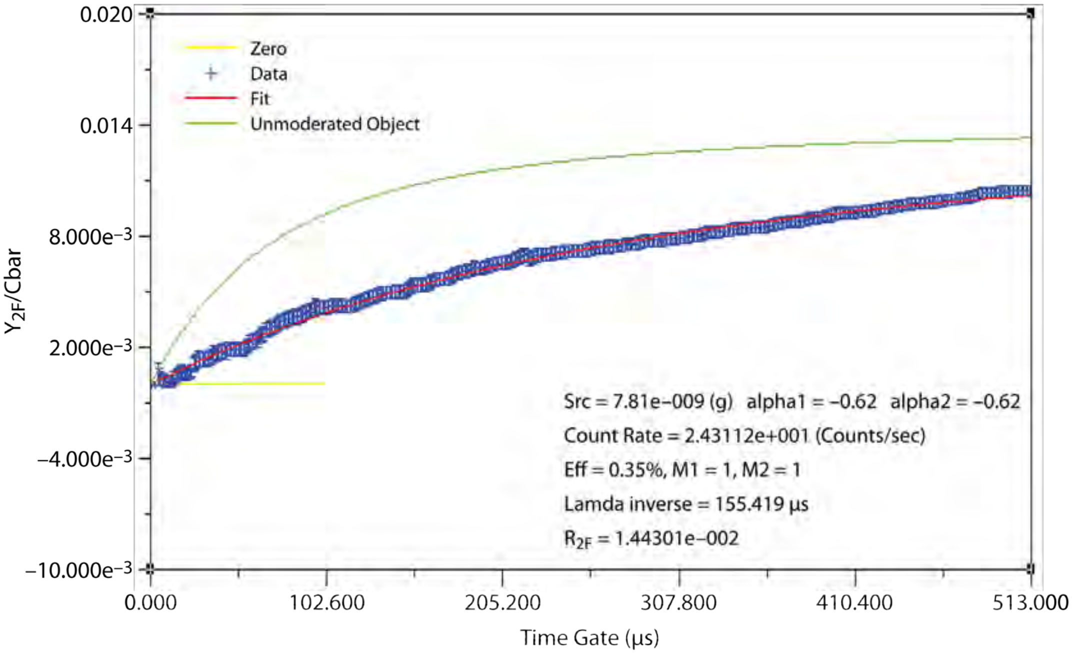

Src = 7.81e−009 (g) alpha1 = −0.62 alpha2 = −0.62

Count Rate = 2.43112e+001 (Counts/sec)

Eff = 0.35%, M1 = 1, M2 = 1

Lamda inverse = 155.419 µs

R_{2F} = 1.44301e−002

Figure 5. The Y_{2F}, normalized to average counts of neutrons, is positive and higher than background. Y_{2F} begins at 0.003 and smoothly rises to its asymptotic value of 0.0144. The characterization data also provide information about the surrounding hydrogenous materials (~3 inches of HDPE).

Results of Experimental Data with Straw Detection Systems

Lawrence Livermore National Laboratory uses a software package, Neutron Multiplicity Analysis Package, to obtain multiplicity distribution of neutron sources using an FM as a data acquisition system. This project used the same software to generate the Y_{2F} plot for multiple time gate widths as shown in Figure 5. The Y_{2F} measurement shown was made using our prototype FMSU. The measured characterization data provided information about the surrounding hydrogenous materials (about 3 in. of HDPE). As seen from Figure 5, the values increased smoothly and rise to its asymptotic value of 0.0144. The Y_{2F} values are definitely positive and higher than background.

With the recent delivery of a prototype straw tube panel from PTI, the next phase of the project will soon begin. Electronics for both data collection methods, FMSU and multiplicity register, will be separately configured with the straw tube panel. From the results reported in this report, it is anticipated that neutron multiplicity and Feynman variance can be measured using this ^{3}He-free system.

Conclusion

The success of an FM measuring the multiplicity of neutrons from spontaneous and induced fission depends on its efficiency for neutron detection; for example, the number of singles, doubles, and triples are respectively proportional to first, second, and third power of the efficiency. It has been shown that a single panel of 60 straw detectors (4 mm diameter, 70 cm long copper tubes with 1 µm ^{10}B deposition) embedded in a 50 mm thick HDPE distributed uniformly in three rows has better thermal neutron detection efficiency than a standard single panel of an FM. One of the successes of this project is that static or mobile data can be taken simultaneously along with the characterization data, unlike the FMs, where static and characterization data must be taken separately.

Acknowledgments

The authors acknowledge the support provided by PTI, in particular by Dr. Jeff Lacy, for the production of the straw panel and for his advice.

References

Athanasiades, A., N. N. Shehad, C. S. Martin, L. Sun, J. L. Lacy, "Straw detector for high rate, high resolution neutron imaging," in *IEEE Nuclear Science Symposium Conference Record* **2** (2005) 623–627.

"JSR-15 Handheld Multiplicity Register (HHMR)," Canberra, 2010, http://www.canberra.com/products/438296.asp, accessed on November 5, 2010.

Kouzes, R. T., J. H. Ely, D. C. Stomswold, "Boron-lined straw-tube neutron detector test," PNNL-19600, Pacific Northwest National Laboratory, Richland, Washington, August 2010.

Lacy, J. L., A. Athanasiades, C. S. Martin, L. Sun, T. D. Lyons, "Fabrication and materials for a long range neutron-gamma monitor using straw detectors," in *IEEE Nuclear Science Symposium Conference Record* (2008) 686–691.

this page intentionally left blank

PASSIVE 802.11B GEOLOCATION USING A FOUR-ELEMENT ANTENNA ARRAY

Yasashi M. Ono[1,a] *and Kelly D. Painter*[a]

A continuing need exists for methods of geolocating 802.11 mobile stations. To that end, this project explored creating a detection capability that can trigger on the media access control address of a target device in real time. We also began developing a mechanism to estimate the bearing to a target device based on the detection trigger. Mapping the coordinates of each detection event on a map with the estimated bearing to the target will, with multiple detections on a moving platform, localize the target.

Background

The emergence of location-aware applications is becoming increasingly valuable as more data are collected into these applications. 802.11b is one of the most common wireless standards being collected, yet it often lacks precise location information as only the collection location is known. In this project we addressed issues that current systems fail to solve for geolocating the data's source.

The most common 802.11b geolocation tools rely on receive signal strength indicator (RSSI) measurements to estimate the distance of the transmitter from the collection point. By collecting a number of RSSI values at various locations, a probability density map can be computed. This method can be very inaccurate due to major assumptions in the RSSI versus distance estimates as well as errors and variations in the raw RSSI readings.

Most 802.11 tools are off-the-shelf products cobbled together to build a working solution. These systems, which commonly use full-size wireless cards and embedded personal computers, are often large, power hungry, and difficult to operate. Typical 802.11b geolocation tools rely on active techniques that flood the channel with traffic and look for responses; however, this approach is conspicuous, causing overall traffic to be reduced; in addition, the accuracy of this method is low. The use of large, high-gain antennas to point to the location of the source is also ineffective; it requires a trained operator and only one source can be located at a time.

---

[1] onoym@nv.doe.gov, 805-681-2460

[a] Special Technologies Laboratory

Project

Wi-Fi Detector

The proposed design allows for simultaneous locations of all 802.11b traffic on a particular channel to be found inconspicuously while operating from a small package powered by a small battery. This basic design will apply not only to 802.11b traffic, but also to many other wireless standards if frequencies and filters are adjusted.

Our design uses a four-element antenna array with the ability to capture raw baseband, from which the exact time of arrival for each antenna can be calculated, yielding an angle of arrival of a packet. The four antennas can be small, circularly polarized chip antennas or larger, omnidirectional antennas for increased gain. 802.11b uses a direct-sequence, spread-spectrum signal that results in packets that are used to calculate the arrival times. The RF signal is down-converted to baseband and sampled as raw amplitude data, then passed through a matched filter to tag the arrival time of the packets. Because the four raw channels do not actually have to decode the raw signal, but merely match it to a reference 802.11b packet, the computation and hardware requirements are greatly reduced, resulting in reduced size and power requirements. The four arrival times combined give azimuth and elevation angle. With a single Wi-Fi chipset in monitor mode, each packet can be uniquely differentiated by a source address and filtered if needed. The end result provides a bearing and unique identifier to each 802.11b packet received. By collecting data on a moving platform, several overlapping bearings are produced such that accurately locating the mobile 802.11b station is possible. The addition of an inertial navigation unit (INU) to the antenna array would help track the receiver location at all times, resulting in much more accurate calculations from a moving platform such as a small unmanned aerial vehicle (UAV).

The design has several novel concepts. The most technically challenging part of the design is to accurately calculate the arrival time of the packets and correlate them to a captured packet. This is because the outputs come from two subsystems and require adjustment for the different latencies. Additionally, latencies from the INU+GPS need to be taken into account to obtain the most accurate calculations. Theoretically, accuracy down to the centimeter level is possible, but factors such as propagation multipath and noise will limit the technique to only submeter accuracy, even under ideal conditions.

Radio-Direction Finding

Two approaches to radio-direction finding were investigated. The first and most desirable is time-domain correlation. This method involves cross-correlation of the received signal from multiple antennas, which allows the antennas to be placed at an arbitrary spacing and provides an opportunity to discriminate multipath signals. If we assume a three-antenna configuration, as that in Figure 1, the center antenna is used as the reference and correlated against the other antennas to determine if the received signal is earlier or later, and by how much. From this, the angle of incidence can be computed.

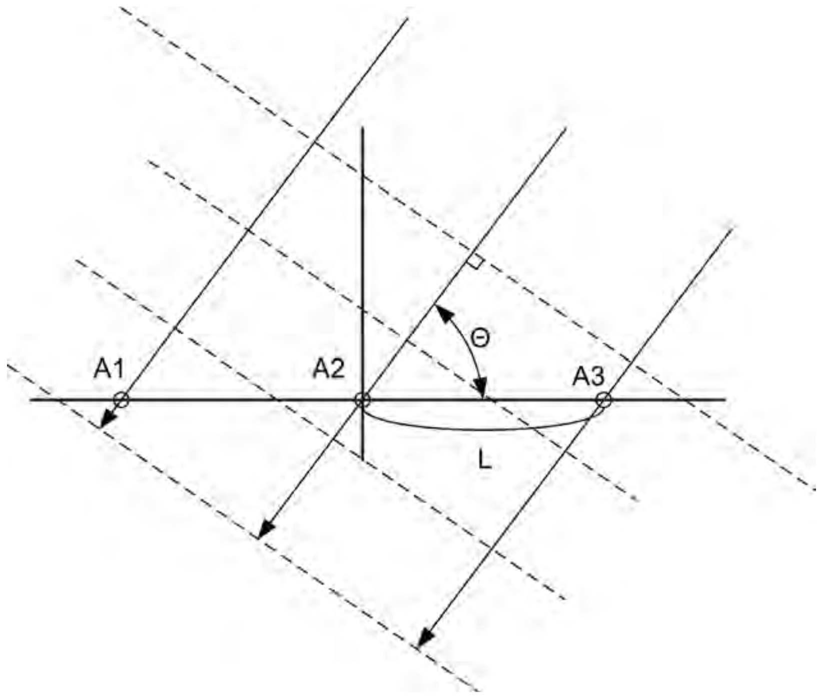

Figure 1. Wavefront diagram showing a three-element antenna array. As shown, the incident wavefront hits antenna 3 (A3) first, then antenna 2 (A2), and then antenna 1 (A1).

The antennas are separated by spacing "L." If the angle of the incident wavefront, Θ, were set to be 0 degrees, as drawn in Figure 1, the time delay from antenna 3 (A3) to antenna 1 (A1) is 2 × L/c, where c is the speed of light. At this angle, the delay will be the greatest. If the antennas are separated by 18 in. (4λ at 2.5 GHz) to make a reasonably sized system, the delay between antennas A3 and A1 is approximately 6 ns. At angles other than 0 degrees, the delay between the antennas is 2 × L/c × cos(Θ).

It can be shown that cos(Θ) = f × Δt/8, where f = frequency and t = time. To solve for for Δt we use 8 × cos(Θ)/f. In order to resolve signals at a 5-degree resolution at a 45-degree offset, we take the difference between Δt(40 degrees) and Δt(45 degrees), which is 188 ps. In order to resolve a difference in time to this accuracy, we need to sample at 5 GS/second (GS/s). Given that we do not know exactly when the trigger signal is going to occur, we would need to save three channels of data at this rate. Of course, if the incidence angle is 90 degrees, the signal arrives at each antenna at the same time and we will not be able to accurately determine the angle of incidence. To do this, we would need another array along the y axis and would have to save five channels at 5 GS/s. This would provide a tremendous amount of data, which would be problematic to store. For this reason, we determined that time-domain correlation is not practical for this application.

Therefore, we decided to use this same antenna arrangement to measure phase angle rather than time delay. To avoid ambiguities, our design restricted the antenna spacing to no more than λ/4. At 2.5 GHz, this results in a separation of 1.2 inches. If the spacing between antennas is λ/4, the angle of arrival relative to the y axis is given by $\Theta = \mathrm{asin}(\Phi_d/90 \text{ degrees})$, where Φ_d is the detected phase angle between A3 and A1.

We constructed an experimental three-channel receiver using SMA connector components. The receiver down-converts the received signal of each antenna to an intermediate frequency (IF) of 868 MHz with a bandwidth of 10 MHz. The phase difference between the antennas was measured using an AD8302 phase detector (Analog Devices, 2002). This apparatus was placed on a pedestal in our anechoic chamber (Figure 2). The angle of incidence was varied ±90 degrees relative to the transmit antenna. The 802.11b transmit signal, generated by an Agilent signal generator, transmitted continuously with very little delay between packets because we did not have any media access control (MAC) detection capability. Voltage measurement data were taken of the output of the two-phase detectors. The plot of the resulting data is shown in Figure 3. As can be seen, each phase detector provides only numerical angular data in one quadrant. However, the state of the output is at its maximum when the transmit antenna angle is in the opposing detector's quadrant. The difference between these two angle voltages results in a very linear plot with an approximate range of ±55 degrees. The zero-crossing occurs at –5 degrees. This agrees very well with the actual placement of the transmit antenna relative to the pedestal.

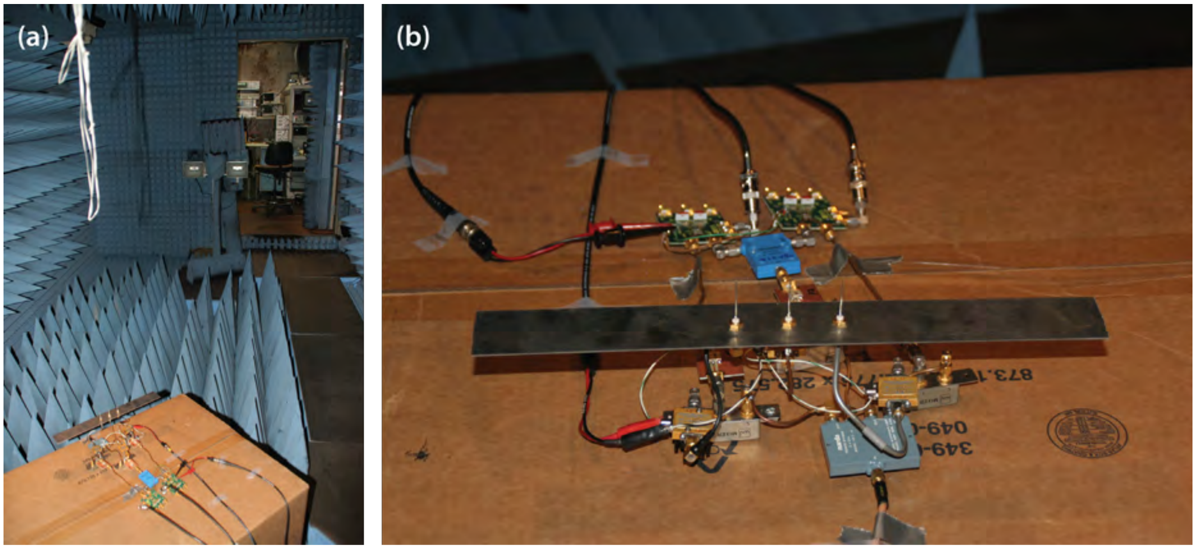

Figure 2. (a) Experimental three-channel receiver on the turntable pedestal in the anechoic chamber. One of the antennas shown in the background is emitting a target 802.11b signal. (b) Experimental three-channel receiver.

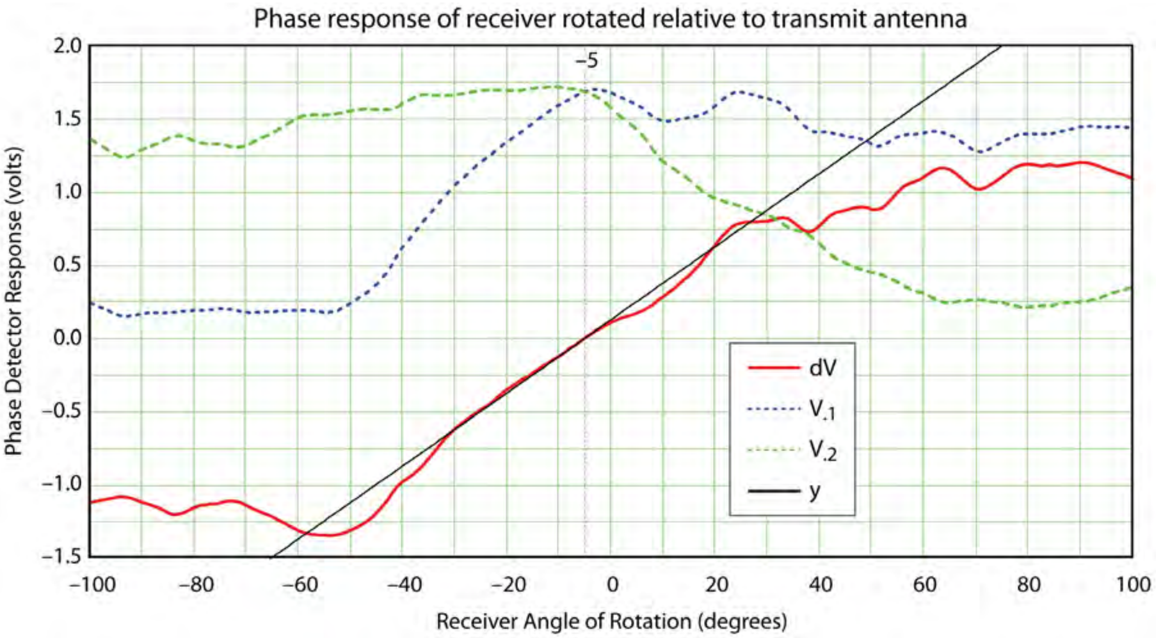

Figure 3. Plot of data obtained with the experimental three-channel receiver, showing that differential phase has good linearity between +50 to –50 degrees.

The ±55-degree range suggests that another three-element array located along the y axis would result in a 360-degree measurement capability because the ranges would overlap. Also, the quadrant indication capability exhibited by the phase detectors should be able to resolve quadrant ambiguities.

The data also show pronounced perturbations in the phase response beginning at approximately 30 degrees. We speculate that this is caused by distortions of the wavefront as it passes over the receiver apparatus components due to the rotation radius being about 2 ft. We speculate that if this is indeed the cause, locating the antennas in a cross-pattern arrangement would always result in phase distortion. This led us to consider another possible arrangement in the next experiment.

Six-Channel Receiver

The results of the first experiment indicated that five channels would be needed for a Cartesian-arranged antenna array. A cross shape with the reference antenna in the center is the most obvious arrangement. However, the phase distortion problems observed caused us to add another channel, for a total of six channels: a three-channel antenna array in the x axis and another three-channel antenna array in the y axis. The second antenna array can be located an appreciable distance away from the first array so that they do not interfere with each other.

A PCB-based receiver was designed with either arrangement in mind. Figure 4 shows the completed circuit board. The SMA connectors for each antenna are separated by λ/4. The PCB has the option to use five channels with one channel as the reference or as two independent arrays of three antennas. For each channel, the signal is down-converted to an IF of 868 MHz—the same frequency and bandwidth used in the first experiment.

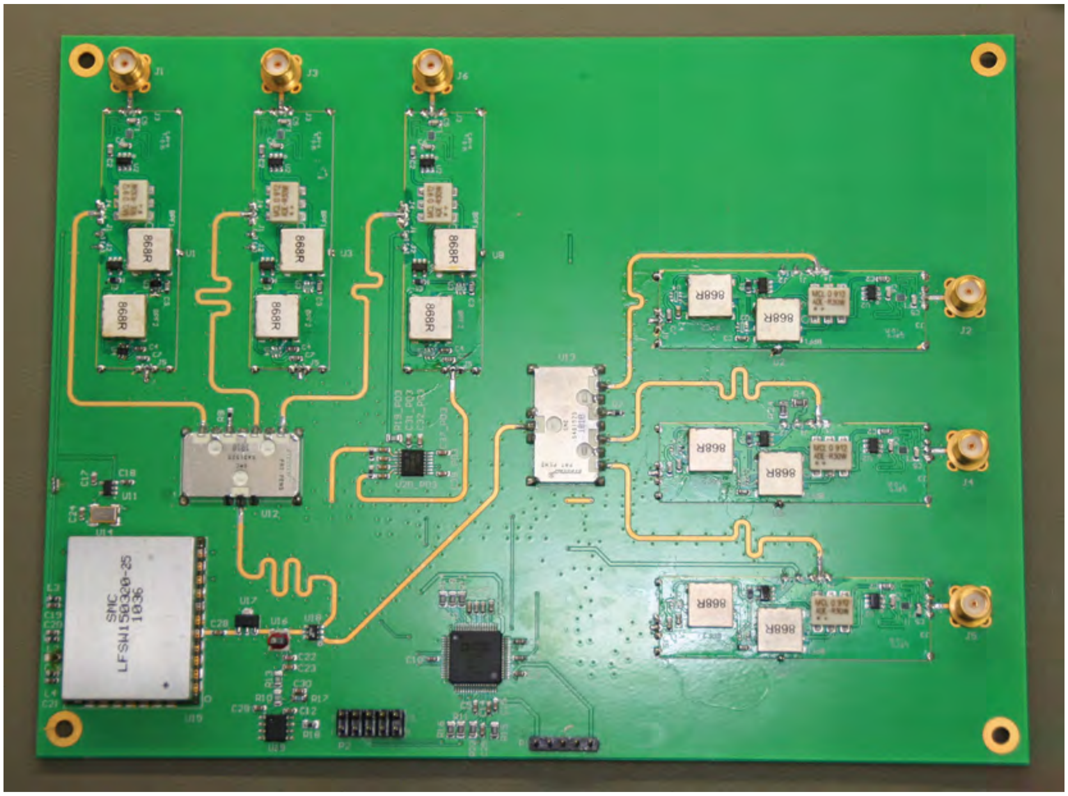

Figure 4. Six-channel direction-finding receiver PCB

The down-converter circuit is made as a module so that each channel is identical. The input preselection filter is a 2.4–2.5 GHz surface acoustic wave device. We anticipated testing the unit in a UAV; as such, it would be desirable to reject signals that are not of interest. The mixer is a high-dynamic range, double-balanced diode mixer. Two stages of IF filtering are provided for an overall gain of approximately 30 dB. A block diagram of the down-converter module is shown in Figure 5.

All signal paths on the board are phase balanced. The output of the down-converter modules connect to four phase detector circuits. Additionally, there is an RSSI for signal strength estimation, a frequency synthesizer, and a six-channel, simultaneous-sampling, 16-bit analog-to-digital converter.

Data control is via a serial peripheral interface bus that can be operated up to 18 Mbps. When operating at maximum speed, a direction measurement can be made and all data read out in 8 μs. A block diagram of the overall receiver is shown in Figure 6.

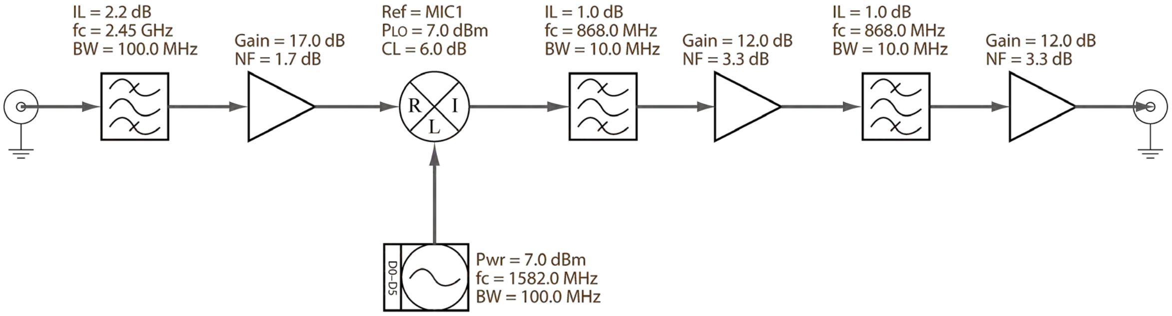

Figure 5. Down-converter module block diagram

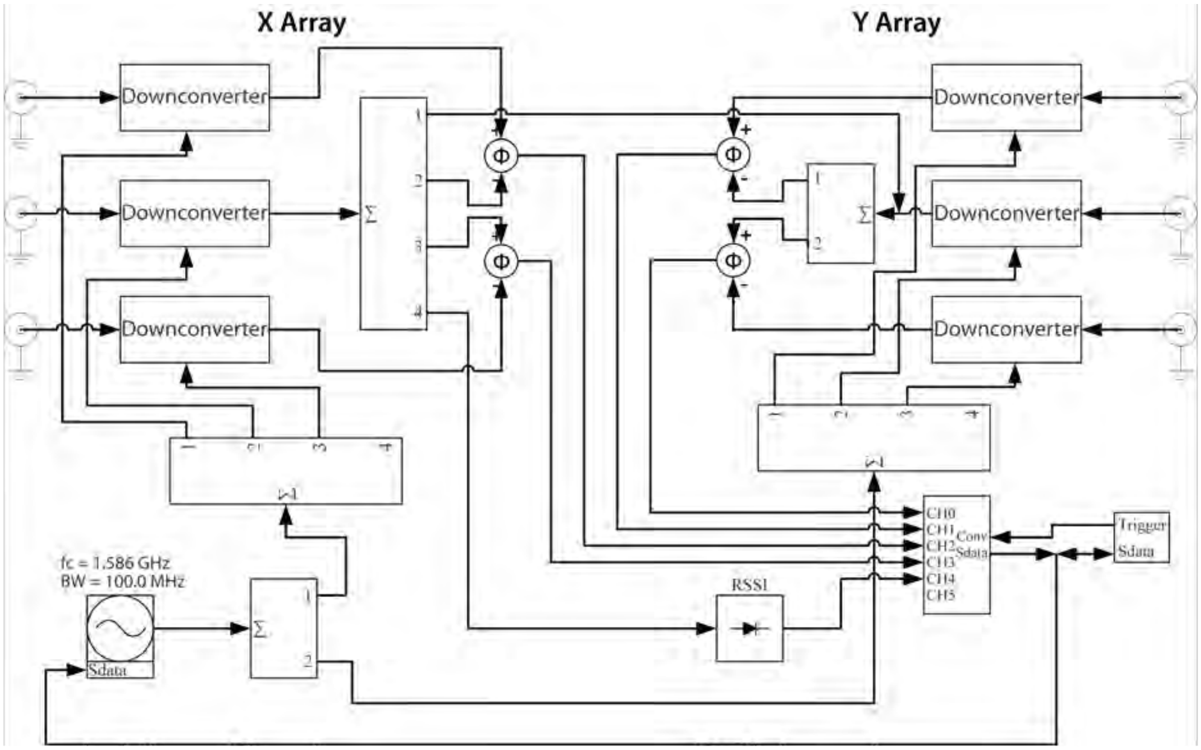

Figure 6. Six-channel direction-finding receiver block diagram

Wi-Fi Chipset Modifications

The UniFi CSR6026 Wi-Fi chipset, designed for handsets, cameras, and portable gaming solutions, was chosen due to its small size and low-power features. This chipset supports the IEEE 802.11b/g/n and the WPA/WPA2 security protocols.

In order to perform geolocation functions, some major modifications were made to the stock firmware that runs on the chipset. The most important modification addressed the ability to determine a valid Wi-Fi signal transmission; this information is used by the antenna array in calculating the bearing on an actual signal. A second modification was made to enable capture of raw data without being associated to an access point. This information helps determine the MAC address of the target transmitter. Finally, the firmware of most embedded chipsets only support major operating systems such as Linux, Android, and Windows. Modifying firmware for Wi-Fi chipsets is typically quite difficult, as vendors do not provide detailed specifications; typically, this information is either never released or released only to authorized third parties. For this project we worked with an available third party who made the required modifications. Although the modifications were received, we were unable to integrate the firmware into our system in time to meet the deadline.

Inertial Measurement Unit (IMU)

To precisely locate an antenna array, an IMU tracks its velocity, orientation, and location. Our IMU design consists of a three-axis accelerometer, three-axis gyroscope, three-axis magnetic sensor, absolute pressure sensor, and a GPS. Data from these components identify exactly where the array is located and where it is pointed. The IMU allows the antenna array to collect data from an automobile or UAV very quickly without requiring an operator to keep track of how everything is arranged.

Orientation is typically represented as pitch, roll, and yaw, also known as Euler angles. This gives rise to some issues, the first being order of operations. Changing the order of the Euler angles yields a different orientation. Another problem with Euler angles is the issue of gimbal lock, in which one loses control of one axis due to a set of rotations in the other two axes. In order to solve these problems, the system stores the orientation as quaternions (Hamilton, 1853). The formulae for quaternions are contained in the following equation:

$$i^2 = j^2 = i^2 = ijk = -1. \tag{1}$$

There are a number of other benefits to using quaternions, including mathematical properties such as ability to perform spatial rotation easily.

The IMU system design consists of two major boards. The first board is the six-channel receiver described above. The second board contains a 60 MHz, 32-bit processor, Wi-Fi chipset and all the IMU hardware, including GPS and antenna. This six-layer PCB was not fully assembled in time to test. Each component was tested individually before combining them on this single board, and they all functioned correctly.

Conclusion

We investigated a number of techniques of radio-direction finding and chose a phase-based method for our designs. Our first attempts with an experimental receiver tested in an anechoic chamber with a realistic RF source proved promising. The results showed that a three-antenna array could resolve an incoming wavefront direction to ±55 degrees. This led us to develop a system with two antenna arrays orthogonal to each other. We then successfully built an integrated sensor board consisting of a Wi-Fi chipset, GPS receiver, IMU, and the six-channel direction-finding receiver. Unfortunately, the sensor board and Wi-Fi firmware integration was not completed and thus, data fusion with the direction-finder was not achieved. We expect this device to enhance Wi-Fi location-aware applications by providing better accuracy, portability, and low power consumption.

References

Analog Devices, "LF–2.7 GHz RF/IF Gain and Phase Detector AD8302," http://www.analog.com/static/imported-files/data_sheets/AD8302.pdf, 2002, accessed January 11, 2010.

Hamilton, W. R., *Lectures on Quaternions*, London: Hodges and Smith, 1853.

this page intentionally left blank

RADIATION-HARDENED WIDE-GAP SEMICONDUCTOR DETECTORS

Ke-Xun (Kevin) Sun[1,a] and Larry MacNeil[a]

Finding new semiconductor technologies and developing radiation-hard and environmentally robust optoelectronic devices and detectors are crucial for meeting the needs of upcoming high-energy density physics experiments. This SDRD research expands previous research with AlGaN LED radiation hardness to photodiodes comprised with similar material. We successfully developed radiation-hard AlGaN photodiodes with responsivity centered at 255 nm. We demonstrated the extreme radiation hardness of custom-designed AlGaN photodiodes with 65 MeV proton irradiation at 3×10^{12} protons/cm^2 fluence level. The deep UV AlGaN photodiodes retained ~50% responsivity up to 3×10^{12} protons/cm^2 fluence.

Background

Unprecedented radiation hardness and environmental robustness are required in the new generation of high-energy density physics (HEDP) experiments to be conducted at the National Ignition Facility (NIF), the Z machine, the Linac Coherent Light Source, and other HEDP facilities. NIF break-even shots will have a neutron yield of 10^{15} or higher. Neutron damage to Si CCD cameras and other narrow-band semiconductor detectors are long-standing problems in energy measurement. The associated detector damage has become a major concern, often requiring a return to old film-based recorders, which have ~30%–60% less radiation susceptibility. However, the use of film causes delays in data collection, lower data quality, and additional safety hazards. Radiation-hard optoelectronic devices are thus extremely desirable.

The estimation for NIF neutron fluence generated in operation is ~1×10^{12} neutrons/cm^2 for 120 ignition shots per year in the experimental stage, and ~5×10^{12} neutrons/cm^2 for 700 ignition shots per year; for fusion power generation the neutron fluence is ~5×10^{12} neutrons/cm^2. The diagnostics must maintain their sensitivity during the entire course of physics operation.

Another important application for radiation-hard devices is deep-space exploration. The Europa Jupiter System Mission (EJSM), a NASA outer space flagship mission, will survey Europa, a Jupiter satellite potentially habitable by humans, but situated within the strong radiation zone. The EJSM will be subjected to a fluence of 10^{12} protons/cm^2. A radiation shield to protect traditional electronics and optics components may weigh up to 50% of the total spacecraft mass. Radiation-hard electronics will significantly reduce shielding, thus increasing the effective science instrument payload.

---

[1] sunke@nv.doe.gov, 925-960-2514

[a] Livermore Operations

GaN and its compounds have been investigated for radiation hardness. Recent research demonstrated a radiation hardness level two orders of magnitude higher than GaAs devices (Ionascut-Nedelcescu, 2002); however, the radiation source in this case was based on fast electrons (300–1400 keV). For our applications in HEDP and space exploration, proton and neutron tests are more relevant.

Sun recently led a team at Stanford University that demonstrated extreme radiation hardness of AlGaN UV LEDs up to a fluence of 2×10^{12} protons/cm^2 (Sun, 2006; Sun, "UV LED," 2009; Sun, "Space," 2009). It was our intent to extend this result from light emission devices to photodetectors based on the same type of semiconductor materials.

Project

This SDRD research focused on developing, testing, and improving radiation-hard, AlGaN-based photodetectors. Our ultimate goal was to develop GaN and AlGaN detector arrays for imaging applications suitable for HEDP experiments and space exploration. The project phases, which included determining experimental parameters, developing radiation-hard photodiodes, performing radiation modeling, designing experiments, testing radiation hardness of the photodiodes, and analyzing data, are described in the following paragraphs.

Experimental Parameter Determination

Proton Source Selection

Neutron and proton irradiation–induced damages are correlated. In general, the proton damage is more severe, due to the larger scattering cross section for charged particle interactions. It was therefore valid to use proton irradiation to provide a conservative assessment of the neutron radiation damage for our experiment. The proton source would have to have enough energy to simulate a deuterium-tritium reaction producing 14.1 MeV neutrons. In addition, sufficient flux would be needed to operate the radiation-hardness test at high fluence level in a short time. Having reviewed several proton sources, we selected the University of California (UC) Davis Radiation Effects Facility, Crocker Nuclear Laboratory, whose source produces a 65 MeV proton beam with a cyclotron accelerator. The experimenters are shielded from the proton beam by a 2-meter-thick concrete wall. The beam flux can be adjusted directly, or by specifying targeted proton fluence, total exposure time, and beam current.

Optical Wavelength Selection

We chose the photodiode response centered at 255 nm, which is below the 266 nm NIF and Omega temporal reference signals and the NIF 3ω at harmonics 354 nm. The demonstration of 255 nm photodiodes will directly impact next-generation diagnostics, as the new photodiodes will detect 266 nm UV fiduciary signal, and detect 355 nm NIF driver laser beam properties. In addition, 255 nm falls in the “solar blind” wavelength region, where many applications in security and space instruments can be found. Experimentally, the UV LEDs tested for radiation hardness have the emission wavelength centered at 255 nm, providing a reliable light source.

Real Time and In-Situ Irradiation Test

Typically, radiation-hardness experiments only measure the sample performance before and after proton irradiation, thereby producing discrete data sets. To characterize the sample parametrically, we designed our experiment to be in-situ and real-time. The sample would be placed in the beam and its performance remotely monitored without moving the sample. This experiment setup would be efficient and would not need optical realignments that could mar data accuracy. We monitored the photodiode response with many proton fluence levels.

Radiation-Hard Photodiodes

Device material and structural design determine radiation hardness performance. We contracted Sensor Electronics Technology, Inc. (SETI) for custom design and fabrication of specialty AlGaN photodiodes based on a P-i-N structure. The company successfully designed and fabricated a radiation-hard UV LED, as demonstrated in Sun (“UV LED,” 2009). The UV photodiode structure is similar to that of a UV LED.

We also attempted to evaluate UV-enhanced Si photodiodes and SiC photodiodes. However, these two types of photodiodes could not give usable responses with 255 nm deep UV illumination and we discontinued exploring them.

Radiation Modeling

We used the SRIM (stopping and range of ions in matter) software package to model the experiment in three aspects:

1. *The scattering process in AlGaN and GaN device structure.*

   The result showed that the proton beam with 14.1 MeV energy and 65 MeV energy will directly impact the photodiodes and very few stray scattering processes will occur. Figure 1 shows the proton beam path through an AlGaN quantum well structure and a GaN substrate with appropriate thickness. No significant angular dependence is found in the model. This implies the radiation dose can be simply calculated using the normal facing cross section.

2. *Radiation penetration on device windows and substrate.*

   The modeling showed that 65 MeV protons will penetrate through these layers without significant deceleration or back scattering.

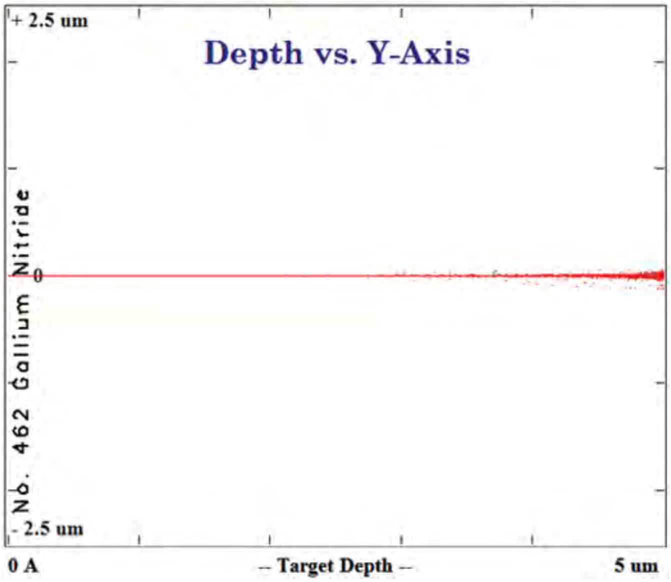

Figure 1. SRIM modeling of proton penetration through GaN plate as a representative process. Proton energy 65 MeV. Secondary scattering can be ignored.

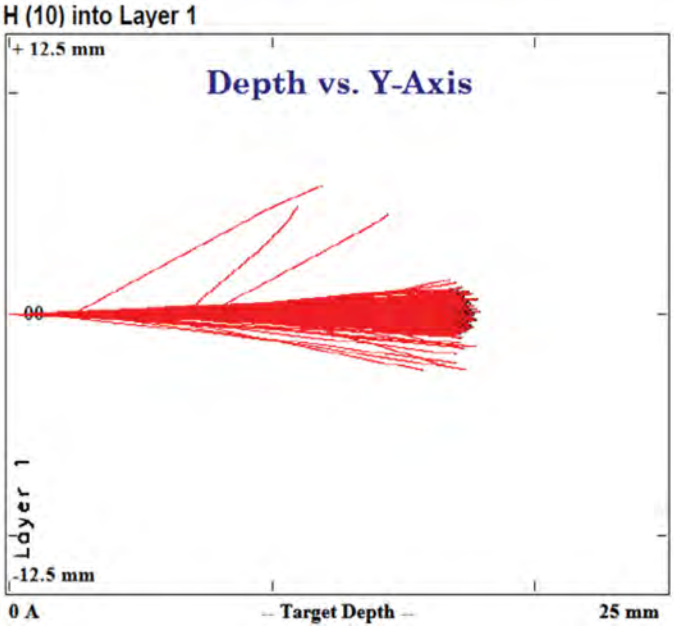

Figure 2. SRIM modeling of proton penetration depth in aluminum plate. Proton energy 65 MeV. The plot indicates that a 25 mm aluminum thickness is sufficient to shield the protons. The multiple scattering processes can be important.

3. *Radiation penetration and cascaded scattering modeling to determine safety precaution needed for the experiment.*

   The simulation in Figure 2 indicated that the 65 MeV proton beam can penetrate the aluminum plate up to 19 mm. Therefore, 25 mm (1-inch) aluminum plates would shield the proton beam to a safe level.

Experiment Setup

The experiment design and device preparation are shown in Figure 3. We used an aluminum plate aperture that shapes the protons into a rectangular beam with a well-defined cross section of 35 × 38 mm. The experiment test stand was designed in consideration of real-time observation and radiation worker safety. The AlGaN photodiode is mounted on a circuit board, then placed inside the proton beam to get proton fluence. UV LEDs emitting 255 nm light are placed near the photodiode to

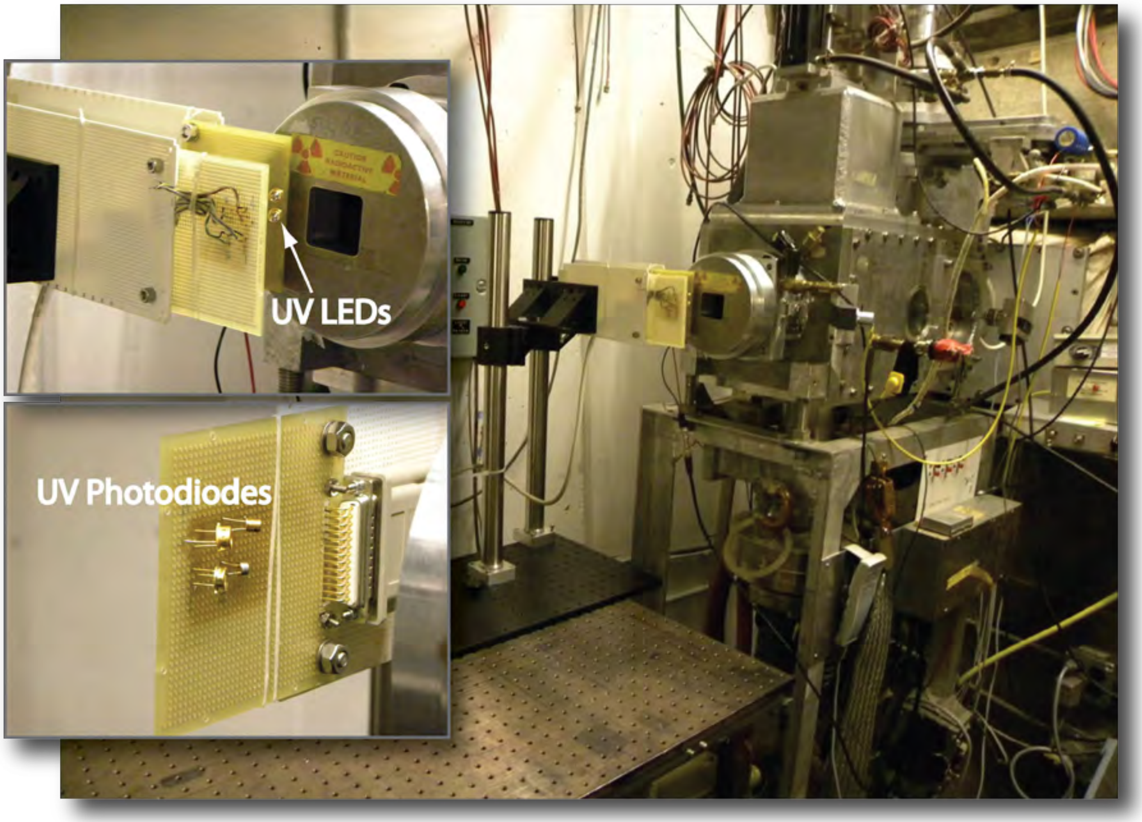

Figure 3. Proton irradiation scheme showing the proton beam, test stand, photodiode, and UV LED light source at the Crocker Nuclear Laboratory. The proton beam exit aperture and our photodiodes test board are shown inset at left. The darkened area on the circuit board is due to proton beam irradiation.

provide light input to the photodiodes. As illustrated, the UV LEDs are placed outside the proton beam to avoid proton irradiation. Therefore, the proton beam only irradiates the photodiode, and any drop in photodiode response to the UV LED light is caused by proton-induced degradation of the photodiode structure.

The UV LED light source was powered by a stabilized DC power supply that could be turned on and off remotely by the experimenter from the user control room. The UV LED drive current was ~5.26 mA. The UV output power was ~20 μW. The hemispherical lens on the UV LED limited the beam divergence to ~15 degrees. Shielded cables and connectors were used for running signal from the circuit board to the multimeter in the user monitor room. The shielding arrangement is sufficient to reduce electromagnetic effects from the cyclotron accelerator over a 60 ft cable length. The photodiode was operated in the photovoltaic mode; thus, the voltage across the photodiode was measured as the response to UV light. A five-digit multimeter was used to measure the photovoltaic voltage.

AlGaN Photodiode Proton Radiation Hardness Experiments

The photodiode radiation hardness is described by the photodiode responsivity at each proton fluence level.

The photodiode voltage when the UV LED light source was turned on and off were recorded at each fluence level, and are plotted in Figure 4 (Sun, “Radiation,” 2010; Sun, “GaN,” 2010). The net photodiode response to UV light is the difference between readouts of light source on and off, obtained by subtracting values in Figure 4b from values in Figure 4a. The photodiode response to UV light at each proton fluence level is shown in Figure 5a. The normalized response is obtained by dividing each value in Figure 5a by the maximum response. Figure 5b shows photodiode normalized net responses to UV light at each proton fluence level. The 100% response is defined as the maximum responsivity on the curve. As shown in Figure 5b, the photodiode responsivity reduces slowly when proton fluence increases. The overall smoothness of the measurement shows consistency and stability.

The most significant observation from Figure 5b is that the photodiode responsivity to UV light maintained ~50% from its peak value, up to a proton fluence of 3×10^{12} protons/cm^2. This important observation demonstrates that the AlGaN photodiode will satisfy the requirements of one to three-year operation at NIF, assuming that 1×10^{12} protons/cm^2 or equivalent is NIF’s one-year radiation fluence.

Further, it is important to notice that the lowest photodiode responsivity, ~46%, actually occurred at 2.2×10^{12} protons/cm^2. Higher photo responsivity of ~50% was observed when the fluence level was at 2×10^{12} protons/cm^2 and 3×10^{12} protons/cm^2. It is likely that the photo responsivity reduction entered a “plateau” region, where the photo responsivity was less affected by further proton irradiation. In this first round of experiments, the maximum proton fluence was limited by the facility operation time.

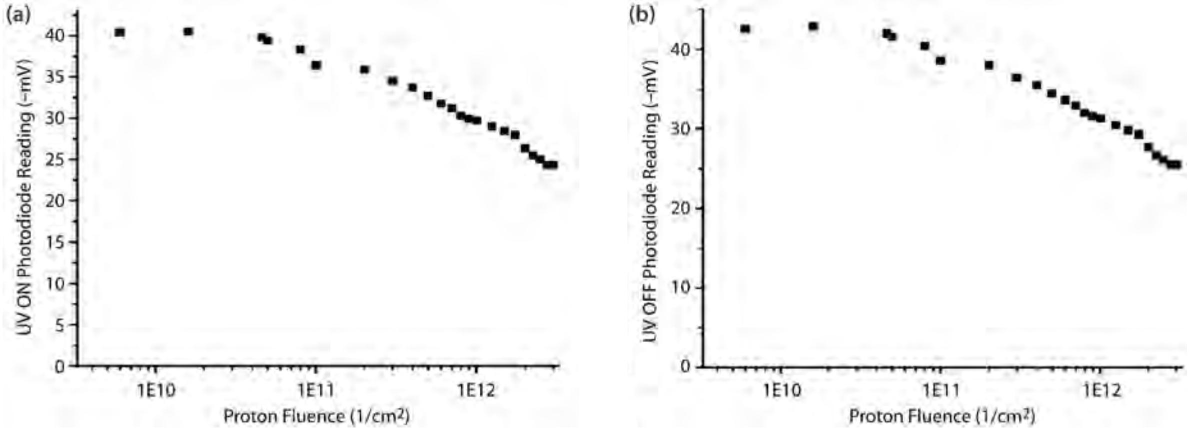

Figure 4. Photodiode readout for UV light on in (a) shows the photodiode response to UV illumination plus the dark voltage bias of the photodiode itself. The photodiode readout for UV light off in (b) measures the pure dark voltage bias, without external light input.

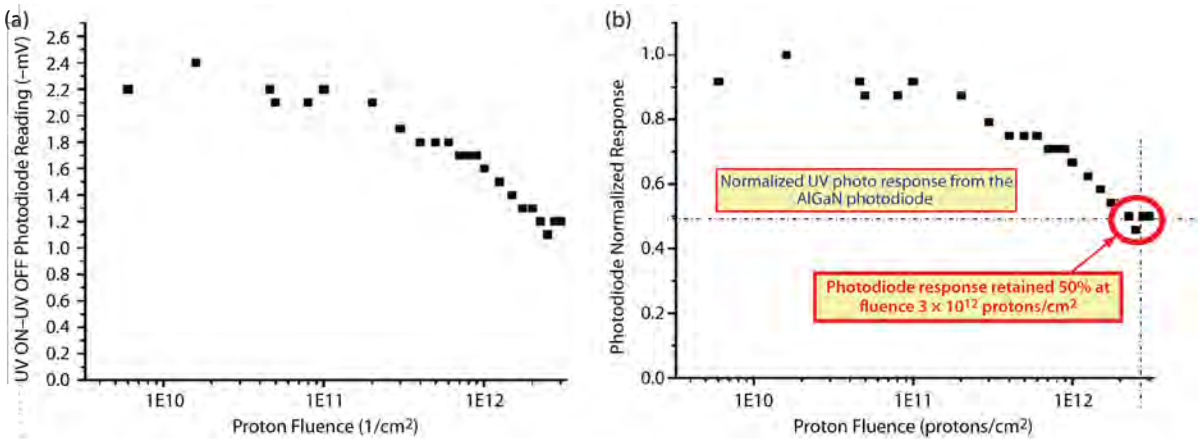

Figure 5. (a) Differential readout for UV light on and off, obtained by subtracting the readout in Fig. 4(b) from 4(a). This readout is considered as the photodiode response to UV light only. Figure 5(b) shows the normalized differential readouts for the cases of UV on–UV off, obtained by dividing each value in Figure 5(a) by the maximum differential readout of the second data point around proton fluence 2 × 10^{10} protons/cm^2. The value at each point represents the percentage response related to the maximum response.

In addition to proton irradiation, other physical effects can lower the photodiode responsivity. Thermal effects due to the proton beam heating, for example, could lower the responsivity. The blackened region on the circuit board was due to the heating effects of the proton beam, and was shaped by the rectangular shape of the aperture.

Conclusion

This research developed a customized AlGaN photodiode for high radiation environment experiments. We demonstrated extreme radiation hardness using a 65 MeV proton beam line. The AlGaN photodiodes retained ~50% responsivity up to 3×10^{12} protons/cm^2 fluence.

The SDRD investigation of AlGaN photodiodes hardness is important and will be applicable in a number of mission-critical applications. The radiation-hardened photodiodes can be used in NIF optical diagnostics for many high-yield shots, and in deep-space exploration throughout years of mission. Further development of AlGaN detector array will lead to radiation-hard imagers, which will lead a new generation of diagnostics for HEDP and fusion studies, simplify the mitigation for radiation damage, and reduce the cost substantially.

Acknowledgments

We thank Kenneth Cooke for logistical support and William Warthan for his help in building the test stand. In addition, SETI provided outstanding support with AlGaN photodiode design and fabrication services.

References

Ionascut-Nedelcescu, A., C. Carlone, A. Houdayer, H. J. von Bardeleben, J.-L. Cantin, S. Raymond, "Radiation hardness of gallium nitride," *IEEE Trans. Nucl. Sci.* **49** (2002) 2733–2738.

Sun, K.-X., B. Allard, S. Buchman, S. Williams, R. L. Byer, "LED deep UV source for charge management of gravitational reference sensors," *Class. Quantum Grav.* **23** (2006) S141–S150.

Sun, K.-X., "Space qualification for radiation hard UV LED," 3rd NASA EJSM Workshop, Applied Physics Lab, Johns Hopkins University, July 7–9, 2009.

Sun, K.-X., N. Leindecker, S. Higuchi, J. Goebel, S. Buchman, R. L. Byer, "UV LED operation lifetime and radiation hardness qualification for space flights," *J. Phys. Conf. Series* **154**, 1 (2009) doi: 10.1088/1742-6596/154/1/012028.

Sun, K.-X., L. MacNeil, "Radiation hardness of AlGaN photodiodes," 4th NASA/ESA EJSM Workshop, Jet Propulsion Laboratory, July 26–29, 2010.

Sun, K.-X., L. MacNeil, "GaN radiation hard properties and detectors," SPIE Hard X-ray, Gamma Ray, and Neutron Detection, San Diego, California, August 1–5, 2010, http://www.osti.gov/bridge/purl.cover.jsp;jsessionid=5B9E88B307E5001DE665ED20E96AD686?purl=/992594-QPRWXv/, accessed September 2, 2010.

Sun, K.-X., "Applications of robust, radiation-hard AlGaN optoelectronic devices in space exploration and high-energy density physics," Invited talk for Conference on Lasers and Electro-Optics, Baltimore, Maryland, May 1–6, 2011.

Lightweight High-Efficiency Thermal Neutron Detector

Michael McElfresh,[1,a] *Mark Raphaelian,*[a] *and Nickolas Brickner*[a]

Two approaches for thermal neutron detection based on semiconductors have been investigated: intrinsic semiconductors wherein the active nuclei (B, Li, Gd, etc.) are constituents of the semiconductor (i.e., boron phosphide [BP], boron nitride [BN], etc.) and converters where the active nuclei are in contact with a conventional semiconductor (silicon [Si] for example). Efforts to develop the former have not met with success. The latter have been investigated extensively and met with some success, although they generally suffer from very low detection efficiency.

Converter-type, solid-state neutron detectors using enriched boron (^{10}B) suffer from having two regions in the device: one that captures the neutron where it undergoes a nuclear reaction, and a second where the energetic particle emitted produces a measureable signal. In this SDRD project, pillars of Si in a ^{10}B matrix were used to identify a set of geometrical factors that can be optimized to produce an efficient detector. Computer simulations were used to test those variables for optimizing performance. The proportion of α-particle energy deposited between the Si and the ^{10}B matrix was modeled to identify the conditions that maximize the energy deposition in Si where the measurable signal is actually produced. Adjusting the density of the ^{10}B matrix was shown to change the amount of energy lost in the ^{10}B matrix energy and would no longer be available to produce a signal in the Si. Devices having a range of dimensions were fabricated to test the effects of the geometrical and material variables identified.

Background

Owing to the lack of charge, the detection of neutrons relies on the production of charged secondaries or gamma rays from neutron interaction with target nuclei. Thermal neutrons have a high interaction cross section with certain nuclei and the reaction products are heavily ionizing. For example, in the $^{10}B(n,\alpha)^{7}Li$ reaction (as shown in Equation 1), a thermal neutron generates an α-particle with 1.470 MeV of energy and a 0.48 MeV gamma ray by radiative decay.

$$\begin{array}{ll} n + {}^{10}B \rightarrow & {}^{11}B^{*} \\ Q = [2.310\ \text{MeV}]: & \quad \hookrightarrow {}^{7}Li^{*}\ [T_{Li} = 0.840\ \text{MeV}] + \alpha\ [T_{\alpha} = 1.470\ \text{MeV}] \\ & \qquad\quad \hookrightarrow {}^{7}Li + \gamma\ [E_{\gamma} = 0.48\ \text{MeV}] \end{array} \tag{1}$$

---

[1] mcelfrmw@nv.doe.gov, 925-447-5582

[a] Livermore Operations

Silicon-based semiconductor detectors, configured as a reverse-bias diode, are commonly used to detect ionizing radiation. The signal produced by the device is a current that is, ideally, proportional to the particle energy that will produce a linear response while allowing separate detection events and particles of different energies to be distinguished. When this condition is not met, multiple-particle events cannot be distinguished from single-particle events and the noise floor may interfere with detection.

In the device we studied, the nuclear reaction takes place in one region of the detector, i.e., the ^{10}B matrix, and detection (electron-hole pair generation and collection) occurs in a separate region of the detector, i.e., the depletion region of the Si device. This is problematic because the α-particle generated in the ^{10}B matrix will lose energy to that matrix. The neutron capture event becomes undetectable when too much energy is lost to the ^{10}B matrix and the remaining energy is no longer enough to generate electron-hole pairs in the Si.

This type of structure has been extensively studied by Lawrence Livermore National Laboratory and others (Nikolić, 2005; 2007; 2008; Conway, 2009). Our research took a different approach by using a point source simplification allowing us to separate out the geometrical effects on the energy resolution and study the proportion of a particle's energy loss between the ^{10}B and Si.

Project

This project modeled the performance of different detector designs. The basic geometry chosen for the device structure was a hexagonal array of Si pillars embedded in a ^{10}B matrix (Figure 1). A hexagonal pillar structure is the simplest geometrical structure because each pillar is equidistant from all nearest neighbor pillars. Here geometrical effects on device performance are studied by the variation of the Si pillar diameter d and the Si pillar pitch L, while the material effects on device performance are studied by the variation of ^{10}B matrix density ρ. Device performance effects are quantified by the ratio of the amount of energy deposited in the Si to that deposited into the ^{10}B matrix (defined here as the energy proportion ratio), the distribution of the energy values observed in the Si (resolution), and the neutron capture/conversion (efficiency).

We note that the geometry modeled differs somewhat from the structure likely to be found in practice, where the matrix is Si with embedded ^{10}B, with neutrons impinging nearly parallel to the pillars.

Modeling Tools

The MCNP code used in this project, and developed by Los Alamos National Laboratory, was specifically designed for modeling radiation detectors (James, 2009). A built-in CAD capability allows one to model the physical layout of the detector using libraries of material properties.

The core of MCNP is the TRIM (transport of ions in matter) code, which continually increases in fidelity as more experimental results are incorporated. Models based on MCNP can simulate the interactions of ions of known energy as they traverse a material, creating defects and losing their energy to the material. Our MCNP simulations included modeling of the neutron source, subsequent neutron capture in the simulated device, the resulting nuclear reaction, and the isotropic emission of energetic α-particles. The code then keeps track of the energy loss resulting from individual particles traversing each material, and the user is able to generate statistically significant results by running the model for large numbers of source neutrons. Another code used here, SRIM (stopping and range of ions in matter), is similar to MCNP, but allows the trajectory to be controlled so that a particle will traverse alternating layers of known thickness. In both the MCNP and SRIM codes, the amount of energy deposited at various stages on the particle's trajectory is tracked so that, for example, the amount of energy deposited in Si and that in the ^{10}B matrix can be differentiated. In the modeling done here, only the α-particles were tracked.

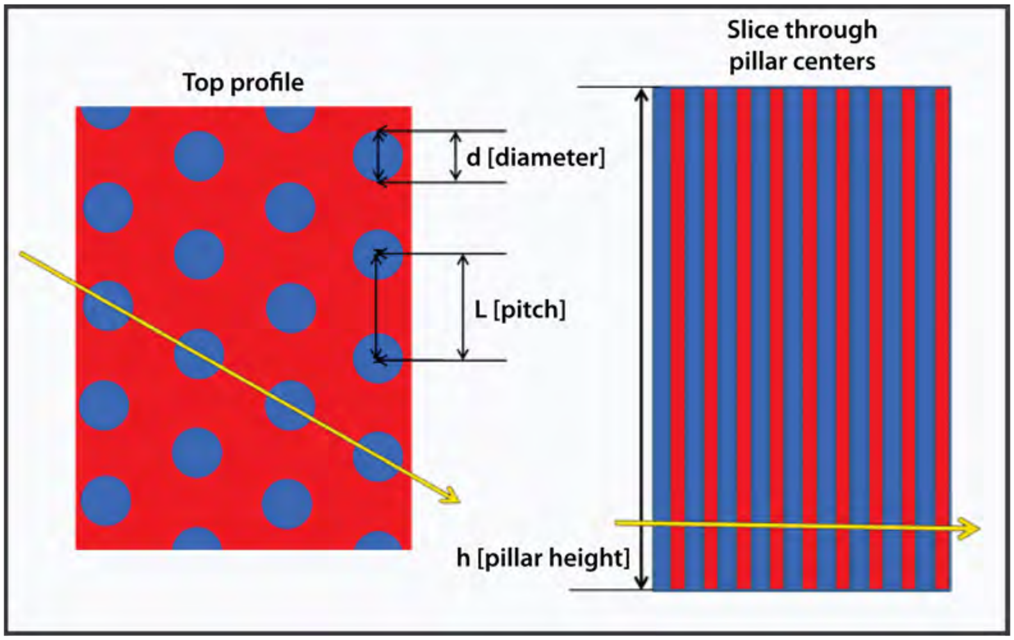

Figure 1. The top profile shows the arrangement of Si pillars (blue) in a ^{10}B matrix (red)

The generic geometry of the device modeled in this project is shown in Figure 1. A hexagonal array of silicon pillars of diameter d has a center-to-center spacing L. The pillars have a height h from the base to the pillar tops. For most of the calculations, the neutron source was modeled to be flat with neutrons traveling parallel to the Si pillar axes, in order to mimic a point source at a great distance. The α-particles produced in the $^{10}B(n,\alpha)^{7}Li$ reaction in the ^{10}B matrix recoil in random directions. In the calculations presented here, the ^{10}B matrix is assumed to be fully enriched ^{10}B rather than having natural abundance.

Modeling Results

In Figure 2, MCNP data are plotted as the distribution of energy deposited by groups of α-particles as a function of individual particle energy. Each plot in the figure represents a different ratio of pitch to diameter from *L/d* = 1 to 2, for 100 nm diameter silicon pillars. From these plots we can discern the way α-particle energy loss is distributed between the ^{10}B matrix and Si. Figure 2a (*L* = 2*d*) is similar to the configuration studied in previous work (Nikolić, 2005; 2007; 2008; Conway, 2009). This plot shows that only a small amount of the α-particle energy is deposited in the Si while the vast majority of the α-particle energy is deposited in the ^{10}B matrix. The sharp peak in Figures 2a and 2b at E ~1.5 MeV corresponds to cases where all of the α-particle energy is deposited in the ^{10}B matrix. As the ratio *L/d* decreases, the peaks cross in energy for *L/d* = 1.23 and reach a limit at *L* = *d*, where the vast majority of energy is now deposited in the Si. For *L* = *d*, the Si peak has a narrow width and is positioned at higher energies near the α-particle average creation energy. Both the higher energy and the narrower peak width are very favorable conditions for a detector.

Integrating the energy under each curve in Figure 2 gives the total energy deposited in the Si, defined as E_{Si}, and that deposited in the ^{10}B as E_B. The ratio, E_{Si}/E_B, defined as the energy proportion ratio, identifies the portion of energy available to generate electron-hole pairs. The quantity *L/d* is related to the area of Si, versus that of ^{10}B. Devices with a constant *L/d* have an identical effective projected surface area ratio regardless of Si pillar diameter.

The ratio *L/d* can be used as a device geometrical factor that relates the device pillar pitch to pillar diameter. A decrease in this factor changes the proportion of energy between the ^{10}B matrix and the Si in a favorable way by allowing more Si interaction. There is, however, the problem that the actual neutron capture area is also reduced as *L/d* decreases. It is clear that adjusting the device geometry by adjusting the *L/d* ratio provides a mechanism for tuning the performance of the device, and finding an appropriate balance of the variables identified in this project will allow this device to be optimized for different neutron detection applications.

Figure 3 shows plots of E_{Si}/E_B as a function of *L/d* for the silicon pillar diameters studied for two different densities of the ^{10}B matrix. Note that E_{Si}/E_B is essentially equivalent at constant *L/d* for the different Si pillar diameters. Deviations from equivalence increase with decreasing *L/d*. This is associated with the mean free path of the α-particle where the interaction with more pillars and non-pillar regions increases with decreasing pillar diameters.

Also observed in two of the plots in Figure 3 is the change in the magnitude of E_{Si}/E_B as a function of ^{10}B matrix density. Decreasing ^{10}B density not only decreases the direct energy deposition in the ^{10}B matrix, but also allows for a greater distance to be traversed by the α-particle, thereby increasing the interaction with more pillar regions. Therefore, decreasing the density of the ^{10}B matrix is similar to increasing the effective diameters of the Si pillars: it increases E_{Si}/E_B by allowing more Si pillars to be traversed by the α-particle and allowing more of the energy to be deposited in the Si. It also is similar to a scaling factor for the energy deposition ratio: a decrease by 50% in density produces approximately a *2x* enhancement of the energy deposition ratio.

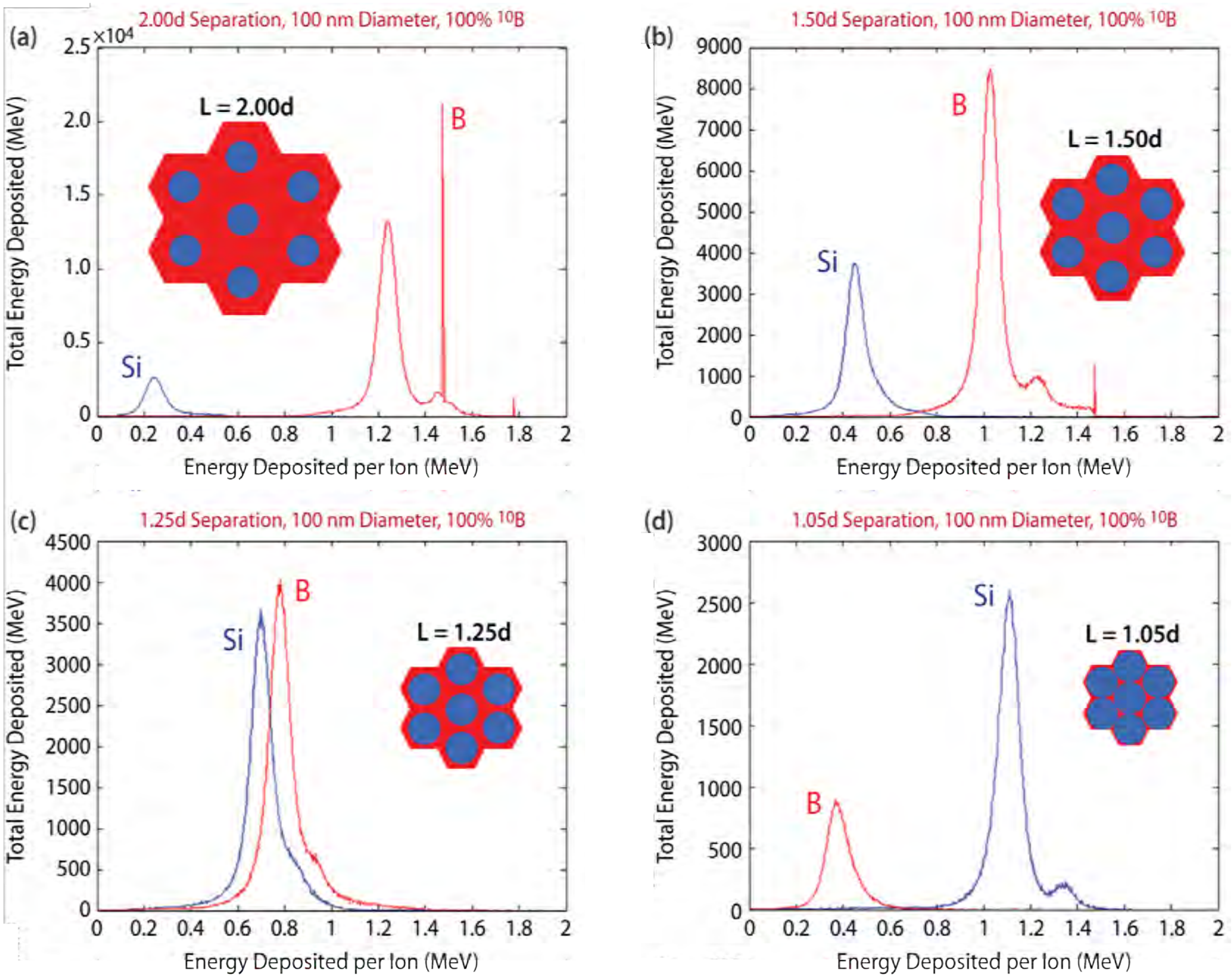

Figure 2. Plots show total energy in an energy bin versus the energy of that bin. In all plots the diameter $d = 100$ nm while L is varied from $L = 2d$ to $L = d$. For $L = 2d$ most of the energy is deposited in the boron, while for $L = d$ most of the energy goes into the Si.

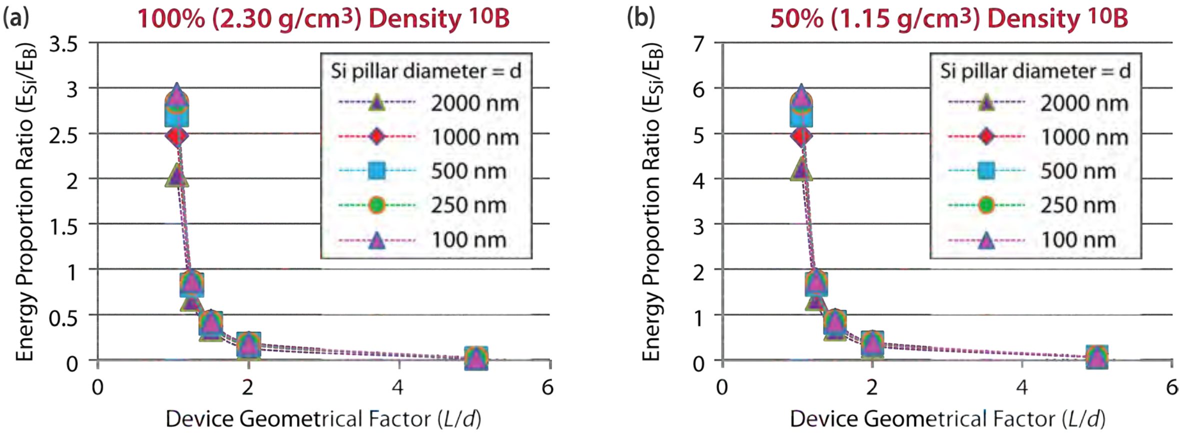

Figure 3. Energy proportion between ^{10}B and Si as a function of the ratio of *L* to *d* for (a) 100% density of ^{10}B, and (b) 50% density of ^{10}B

Because the Si has such a small cross section for capturing neutrons (7–10 millibarns for a thermal neutron), the area of the detector made up of Si is effectively transparent to neutrons. A larger, exposed ^{10}B area to increase neutron capture efficiency of the device can be accomplished by increasing the device's pillar pitch (*L*). However, as shown above, the trade-off in increasing the pillar pitch is a decrease in the energy of α-particles reaching the Si pillars due to energy loss in the ^{10}B matrix. In cases where maximum neutron capture is desired, it may be necessary to stack two or more detectors together so that the Si pillars in one layer overlap the ^{10}B regions of the second layer.

Since the amount of energy deposited in the ^{10}B matrix can be affected by a reduction in the density of the ^{10}B matrix, and the energy deposition is primarily related to the material's electron density, reducing the density of the ^{10}B matrix is a strategy for changing the device material's properties in order to deposit less energy in the ^{10}B and a greater portion in the Si. This material effect is most easily observed using SRIM model calculations where the alpha particle traverses repeating geometric cells of boron and silicon. Unlike MCNP, the modeled initial trajectories of the α-particles in SRIM are not isotropic but are directionally defined. Directionally defined initial trajectories allow the energy loss due to scattering in each of the cells to be more easily observed and modeled. The SRIM calculations in Figure 4 show the energy deposited as a large collection of α-particles traverses alternating layers of ^{10}B and Si of 1 μm thickness. As the ^{10}B matrix density decreases, the total length of the particle trajectory increases, and the energy loss decreases in ^{10}B and increases in Si. This code can be used to determine device geometrical ranges and material ranges to study, depending upon the purpose of the device.

The separation of device material effects from device geometrical effects is shown in Figure 5. In this figure the energy proportion (as calculated from MCNP), E_{Si}/E_B, varies as a function of percent ^{10}B for a constant device geometrical factor of 1.05. As with the variation with *L/d* (Figure 3), the halving of the electron density by decreasing the ^{10}B matrix density shows approximately a doubling in the proportion ratio. Devices targeting specific applications can be accomplished by tuning the device's geometrical and material parameters.

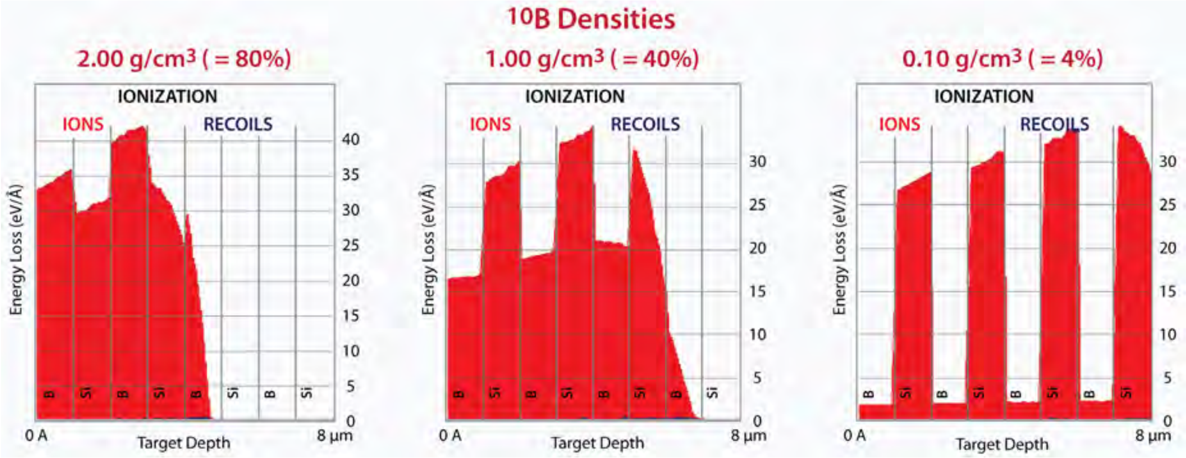

Figure 4. Energy loss per length: results of SRIM calculations for a 1.48 MeV α-particle impinging on alternating 1.0 μm thick layers of ^{10}B and Si. The density value refers to the density of the ^{10}B matrix.

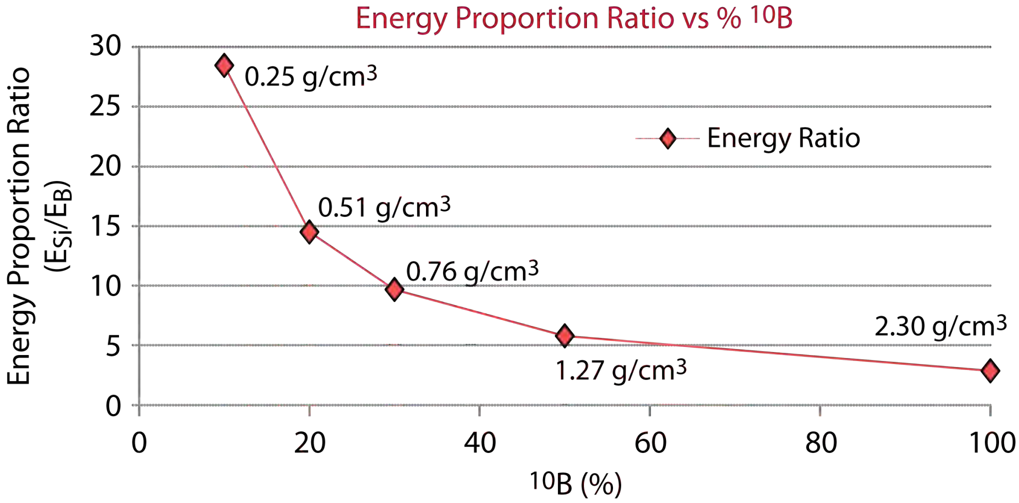

Figure 5. The energy proportion ratio E_{Si}/E_B, i.e., the ratio of the energy deposited in the silicon to that deposited in the boron, as a function of boron density for 100 nm pillar diameter and 105 nm pillar pitch (constant geometrical factor *L/d* = 1.05).

Figure 6 shows a series of curves for the percent of neutrons captured as a function of density for different values of ^{10}B matrix thickness (height) *h*. Useful Si-based semiconductor devices can be made to a thickness of about 2 mm depending on a number of factors. Because the neutron capture probability is directly related to the number of ^{10}B atoms in a given cross-sectional area, the loss in neutron capture cross section resulting from a decrease in density losses can be compensated by increasing the thickness of the ^{10}B matrix. For example, because the number of neutrons captured while traversing a region of ^{10}B increase linearly with traversed distance, then twice the distance traversed correlates to twice as many neutrons captured. While the larger the capture cross section the better, it can be seen from Figure 6 that the ^{10}B cross section is quite favorable for the dimensions of these studies.

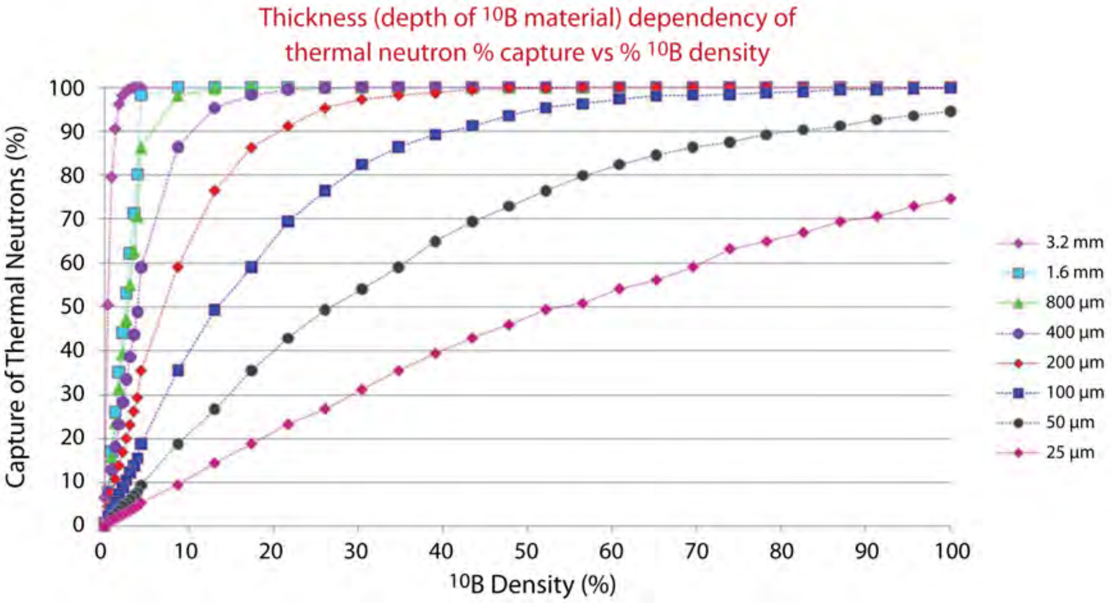

Figure 6. The percent capture for thermal neutrons versus density of a pure ^{10}B matrix. The different curves correspond to different thicknesses of the ^{10}B matrix.

Device Fabrication

Several parameters were identified as potential variables in the design of devices based on this Si pillar structure, including the density of the ^{10}B matrix, the matrix thickness *h*, the pitch *L*, and the dimension *d*. A matrix of parameter variables was created, and a wafer die map was designed with each chip having different parameters. In optimizing the placement of the dies on the wafer we considered several issues, including nonuniformity of the etch rate from center to edge, that larger features etch faster, and aspect ratio requirements. Figure 7 shows the basic layout of the wafer fabricated in this study, and Figure 8 shows the actual chips fabricated for experimental studies.

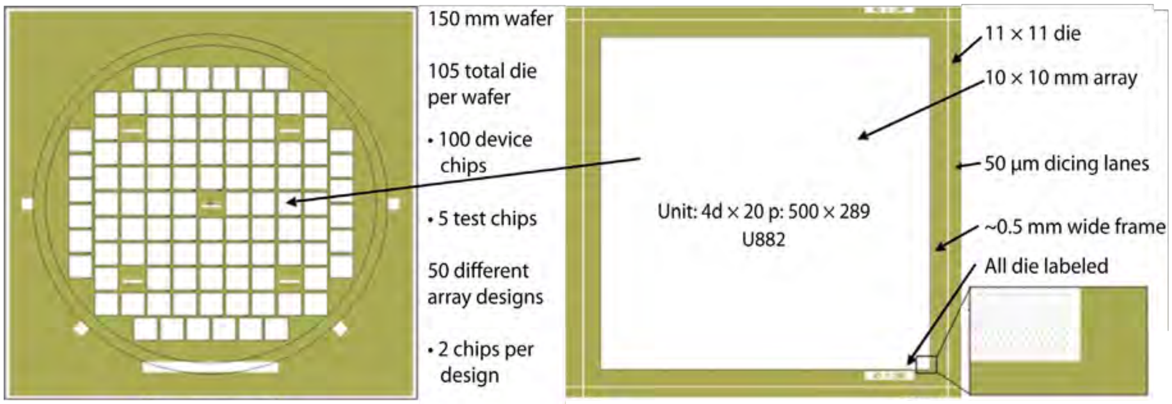

Figure 7. Schematic diagram of the wafer manufactured in this study. As shown in the schematic, die locations are populated throughout the wafer. Specific geometries associated with specific die locations were chosen to optimize the process conditions during the manufacture of the wafer.

Figure 8. Scanning electron microscope images of Si pillars, showing two different diameters and pitches in the three images

Conclusion

Using the Monte Carlo simulation codes MCNP and SRIM, an alternative geometry for a thermal-neutron, solid-state detector using Si pillars embedded in a ^{10}B matrix was modeled in order to identify the design variables that might lead to a higher-performance device. Four variables were identified: the diameter of the pillars d; the center-to-center spacing between pillars, L, or the ratio L/d; the height of the pillars h; and the density of the ^{10}B matrix ρ. We found that the ratio of the amount of energy deposited by α-particles in the Si to that deposited in the ^{10}B (the energy proportion ratio) (1) has a slight dependence on d, (2) decreases with increasing pitch L, (3) decreases with increasing ^{10}B matrix density, and (4) has essentially no dependence on h. However, h can be increased to offset the effects of decreasing ^{10}B matrix density. On the other hand, the neutron capture efficiency (1) is independent of L/d, (2) increases with increasing pitch L, (3) increases with increasing boron matrix density, and (4) increases with h. This set of variables allows the tuning of a detector system for different applications, from high neutron flux to high neutron sensitivity.

A set of Si chips that cover the variable parameter space were designed and fabricated, and testing the set remains to be done. After the experimental variable space has been identified, the next step would be to fabricate Si chips with optimized parameters and use a reverse-bias diode with blocking electrodes for the fieldable device configuration.

Acknowledgments

We would like to thank Zaheer Ali and Ken Cooke for their help and support.

References

Conway, A. M., T. F. Wang, N. Deo, C. L. Cheung, R. J. Nikolić, “Numerical simulations of pillar structured solid state thermal neutron detector: efficiency and gamma discrimination,” *IEEE Trans. Nucl. Sci.* **56**, 5 (2009) 2802–2807.

James, M. R., G. W. McKinney, J. W. Durkee, M. L. Fensin, J. S. Hendricks, D. B. Pelowitz, R. C. Johns, L. S. Waters, J. S. Elson, “MCNPX 2.7.X–new features being developed,” IEEE/NSS conference presentation, Orlando, Florida, October 25–31, 2009, https://mcnpx.lanl.gov/opendocs/misc/LAUR-09-06788.pdf, accessed June 15, 2010.

Nikolić, R. J., A. M. Conway, T. Graff, C. E. Reinhardt, T. F. Wang, N. Deo, C. L. Cheung, “Fabrication of pillar-structured thermal neutron detectors,” Nuclear Science Symposium, Conference Record N24-342, Honolulu, Hawaii, October 2007, 1577–1580.

Nikolić, R. J., A. M. Conway, C. E. Reinhardt, R. T. Graff, T. F. Wang, N. Deo, C. L. Cheung, “Pillar structured thermal neutron detector with 6:1 aspect ratio,” *Appl. Phys. Lett.* **93**, 13 (2008) 133502.

Nikolić, R. J., C. L. Cheung, C. E. Reinhardt, T. F. Wang, “Roadmap for high efficiency solid-state neutron detectors,” *Proc. SPIE* **6013**, 1 (2005) 36–44.

MUON COUNTING AS A GAUGE OF COSMIC-RAY ACTIVITY AND BACKGROUND NEUTRONS

Michael J. Hornish,[1,a] *Murray J. Kolander,*[a] *Thomas M. McCullough,*[a] *Sanjoy Mukhopadhyay,*[a] *Ethan X. Smith,*[a] *and Ronald S. Wolff*[a]

In order to better understand and track fluctuations in sea-level background neutrons and the cosmogenic processes that create them, this project developed detector systems that collect and archive cosmic muon and background neutron data. Two systems, a large fixed neutron and muon observatory and a compact portable muon detector system, were designed and assembled. The fixed system contains a large array of pressurized ^{3}He tubes for neutron detection and two large plastic paddles operated in coincidence for muon detection. This system will continuously collect data from the sensors, and relevant solar and meteorological information, and store the data in a database server that will be accessible via the Internet. The portable muon counter system consists of two small plastic-paddle scintillator detectors operated in coincidence and designed to be deployed on a maritime vessel for use as both a cosmic-ray muon monitor as well as a gauge of overhead shielding for different locations around the vessel. Both systems have been assembled, and preliminary test data reveal they are operating within specifications. Data collected with the fixed system have the added benefit of enabling any type of coincidence analysis to be performed, either with neutron or muon coincidences, or searching for muon-neutron coincidences generated by muon spallation.

Background

One method for conducting advanced radiological searches for neutron sources in the maritime environment (i.e., aboard maritime vessels) is the use of long-dwell neutron rate sensors. Measured count rates are compared against a model calculation of the estimated neutron background in order to search for an excess of counts that would be a signature for the presence of a neutron source amid a non-zero neutron background. This technique has been developed for use by the Nuclear/Radiological Advisory Team (NRAT) in the execution of its maritime advanced search mission. The technique relies on accurate predictions of the maritime neutron background, which depends on a variety of factors including type of vessel, location on vessel, cargo load configuration, latitude, barometric pressure, and solar activity (Heimberg, 2004).

The dependence of maritime neutron background generation on solar activity can be explained as follows. The neutron background, particularly at sea, is generally understood to be almost entirely cosmogenic in origin; this background is a combination of secondary and tertiary cosmic-ray neutrons as well as spallation induced by cosmic-rays of larger nuclei within the vessel (either the iron of the

---

[1] hornismj@nv.doe.gov, 301-817-3347

[a] Remote Sensing Laboratory–Andrews

ship or the cargo). The charged-particle, cosmic-ray flux incident on the earth's upper atmosphere is affected by the shape of the earth's magnetic field, which is in turn affected by the solar wind and other emissions of charged particles emanating from the sun. The measure to which the solar magnetic activity has an indirect impact on the flux of secondary and tertiary cosmic rays at the earth's surface can be gauged by measuring the sunspot number, or the 10.7 cm solar radio flux, which happens to have a cyclic behavior with a periodicity of 11 years (Hathaway, 2009).

In the current configuration, the maritime neutron background calculator software package does not rely on current solar activity information; rather it depends on a predicted curve of future solar activity. This predictive curve usually matches quite well with the average solar activity, but that activity can fluctuate fairly substantially from day to day, particularly during solar magnetic storms. The extent to which that fluctuation generally impacts the cosmogenic neutron background at sea level is not immediately obvious. However, it is true that solar magnetic storms that are relatively short in duration (on the order of hours) can significantly alter the sea-level neutron background. If this situation is not taken into account during a solar magnetic storm, one could draw the wrong conclusions about an enhancement in measured neutron count rate and claim it is due to a neutron source rather than a solar or cosmic phenomenon. Therefore, in order to provide an independent means of verification that background neutrons are not globally affected by solar or cosmic anomalies, a fixed neutron monitor was developed in an FY 2007 SDRD project for use as a baseline neutron detector system that can be accessed remotely via the Internet by a deployed maritime search team (Ashenfelter, 2008). A muon counter was also integrated into this system to provide a platform by which cosmic-ray muons and associated phenomena could be studied, while also allowing a detailed study of muon-neutron and neutron-neutron coincidences by time tagging each detection event.

Another important aspect of background neutrons is the extent to which cosmogenic background neutron rates can be predicted in real time by cosmogenic muon rates. Although the mechanism for muons to induce spallation and thereby create neutrons has a low cross section, it is nevertheless true that fluctuation of muons measured at sea level should have a behavior similar to fluctuation of cosmogenic neutrons measured at sea level. Therefore, a portable muon counter system can provide a means of tracking unusual cosmic-ray activity, providing a local capability that is independent of the fixed neutron-muon observatory. Secondarily, a portable muon counter can be used to indirectly quantify the amount of overhead material from ship or cargo materials at locations where neutron measurements are performed. This information could be important for precisely detailing how deeply within a vessel a corresponding maritime neutron measurement is relative to overburden, a factor that is important in the estimating the predicted maritime neutron background count rate at specific neutron measurement locations.

Project

One goal of this project was to develop two different detector systems, namely a large, fixed neutron-muon observatory and a portable muon detector system. A second goal was to utilize these systems to collect data and study cosmogenic muon and neutron behaviors and trends relevant to maritime neutron search operations. We achieved the first goal and had only begun work on the second goal near the conclusion of the project. The discussion below describes the systems developed.

Fixed Neutron-Muon Observatory

The fixed neutron-muon observatory was designed around a neutron module, consisting of large ^{3}He tubes and a muon detector system, consisting of two large plastic scintillator paddles operated in coincidence (Figure 1). In all, the neutron module was composed of 32 tubes segmented into 4 arrays of 8 tubes each; the tubes are 6 feet in length, 2 inches in diameter, and are pressurized with ^{3}He gas to 2.7 atmospheres. Signals from each of these detectors, as well as a GPS 1 Hz "heart beat" from a GPS server utilized for time synchronization, are fed to a data acquisition system. Data are then stored on a MySQL database that runs on a database server connected to the Internet for remote access. The system is currently mounted on a shelf unit at a temporary location in our aircraft hangar (Figure 1).

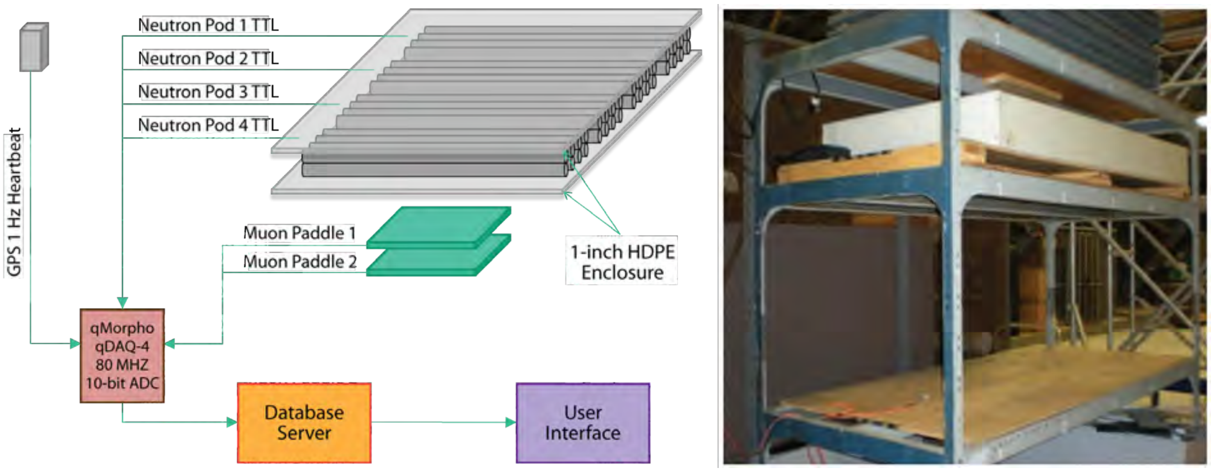

Figure 1. (left) Schematic of the fixed neutron-muon observatory, and (right) temporary location of the observatory in a hangar space

The neutron tubes used for this detector system had been in storage for a significant period of time and required refurbishment. A substantial effort was also made to check that each of the tubes was functioning properly, ensuring that the electronics package of each array was suitable and had similar response. Figure 2 demonstrates (1) that each of the four arrays of neutron tubes exhibit nearly identical spectral shape, and (2) that the pulse width of the neutron modules is on the order of 20 microseconds, by comparison to the standard Infield backpack system developed by NSTec that has a 6-microsecond pulse width. The large plastic paddles (Figure 3), 10 inches long, 8 inches wide,

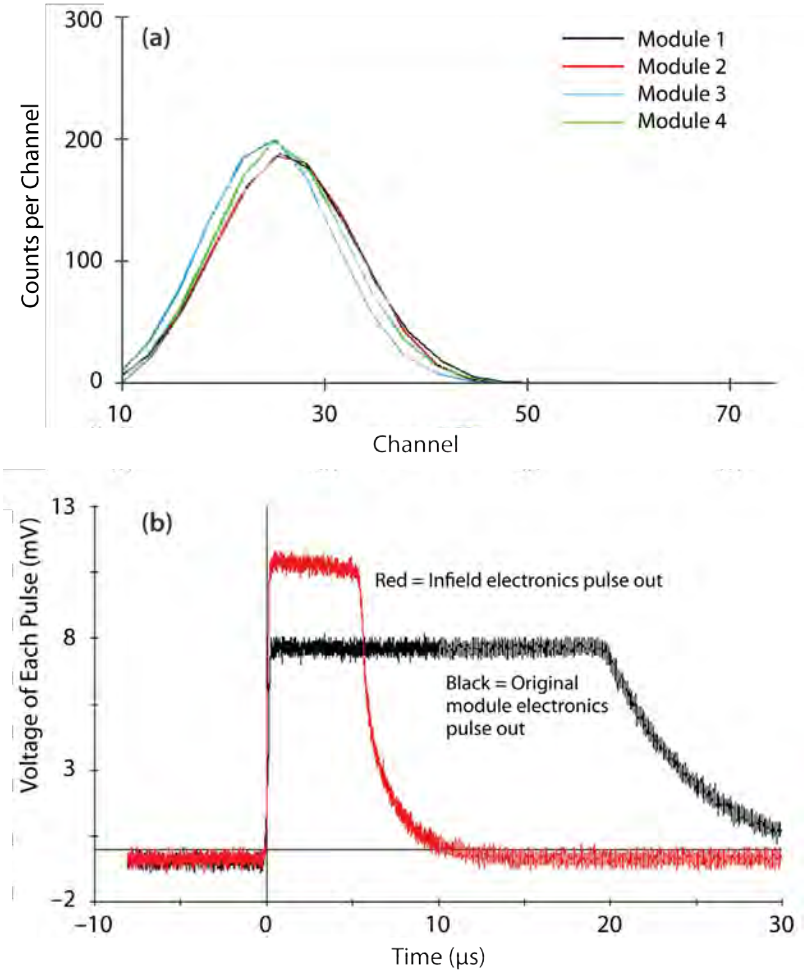

Figure 2. (a) Results from count rate tests for each of the four neutron tube arrays, and (b) a comparison of pulse width of existing array electronics versus Infield electronics

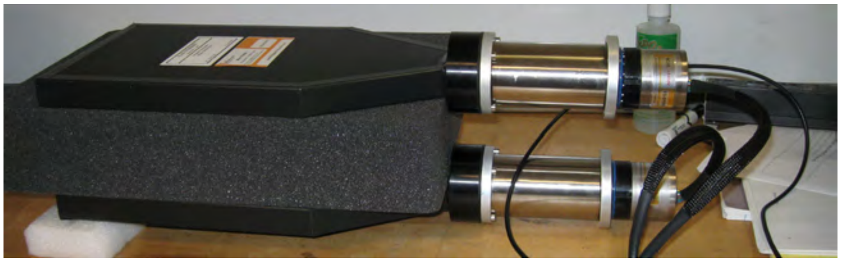

Figure 3. Two large plastic scintillator paddles that make up the muon channel in the fixed neutron-muon observatory

and 1 inch thick, were operated in coincidence and aligned horizontally and in parallel to maximize sensitivity to downward-traveling muons. Results from a calibration of one of the paddles, as well as a test of horizontal versus vertical orientation are shown in Figure 4.

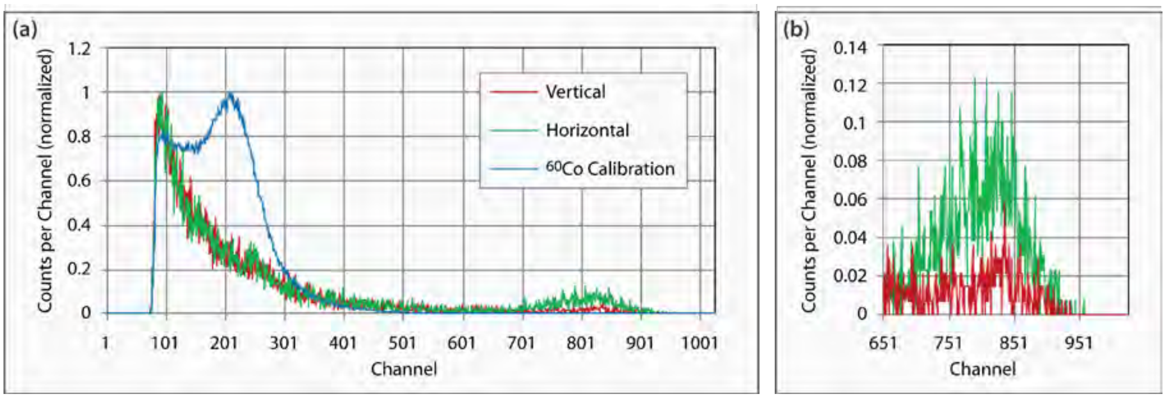

Figure 4. (a) Response of a single plastic scintillator paddle, showing curves for calibration with a ^{60}Co source; and (b) curves depicting the difference in response between horizontal and vertical alignment, which was a factor of ~4–5 difference, as anticipated

Significant amounts of relevant or potentially interesting or useful meteorological and solar data are also being tracked in the database. These data are collected by retrieving data from the Internet, such as barometric pressure, humidity, sunspot number, and 10.7 cm radio flux. The database on which this combination of detector and other data is stored will be connected to the Internet. Figure 5 shows a sample graphical interface used to retrieve and plot data residing in the database.

Due to some ongoing scheduling and technical difficulties, populating the database with neutron data from the neutron array has been delayed. However, a brief period of data collection with the fixed muon counter system was performed, and the results are summarized in Figure 6. For this data set, two large paddles were connected to the Bridgeport data acquisition system, which was in turn connected to the database server, and the two counters were operated both in singles and in coincidence. Because the region of interest for minimum-ionizing muons is from 4–6 MeV, a threshold just above 3 MeV was applied to the spectral data of each paddle, and the coincidence was based on a small time gate.

Portable Muon Counter System

A small, compact muon counter system is being developed for field deployment. This system could ultimately provide important information in the field to deployed maritime search teams on vessels. As a cosmic-muon monitor, the portable system may be used to decipher any strange or unusual cosmic behavior or as a tool to estimate effective depth by gauging muon attenuation by intervening decks.

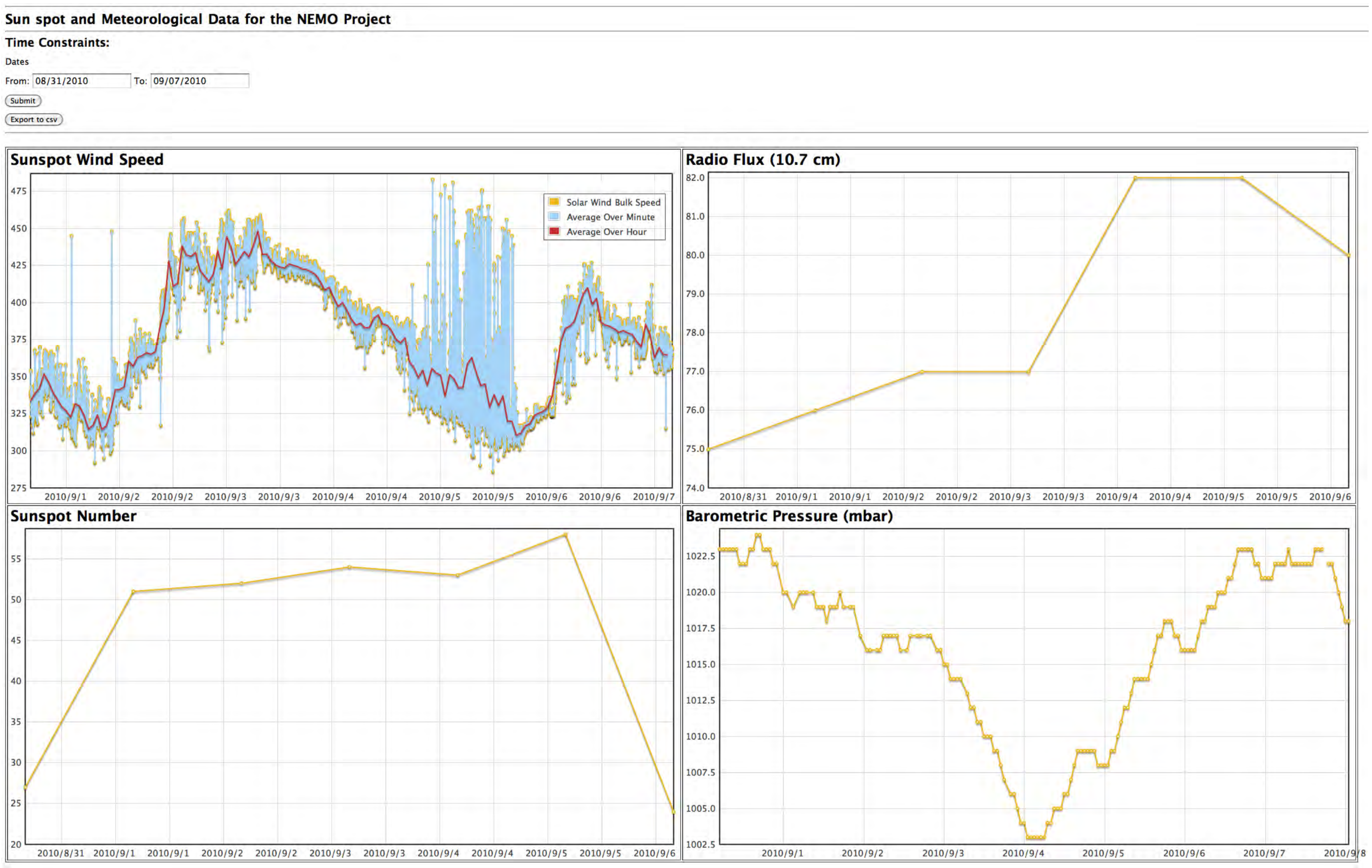

Sun spot and Meteorological Data for the NEMO Project

Time Constraints:

Dates

From: 08/31/2010 To: 09/07/2010

Figure 5. Sample web-based graphical user interface that enables retrieval of archived data from the database server for plotting and download

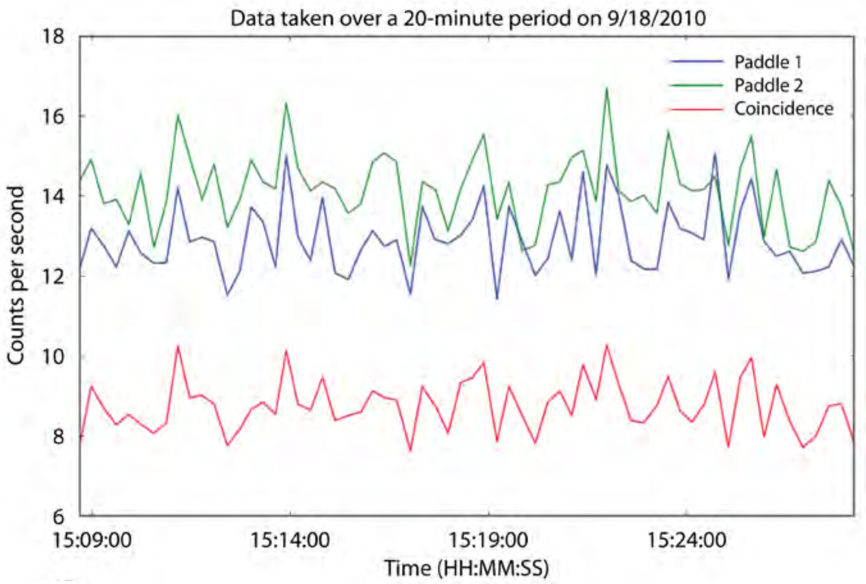

Figure 6. Twenty-minute sample data set from the fixed muon counter system revealing single-paddle count rates (blue and green) and the coincidence count rate (red) in counts per second, averaged over time bins of 20 seconds. This plot reveals that of all paddle counts above 3 MeV, more than half of them are due to muons that are detected in both paddles.

The system is simple and straightforward and involves two small plastic scintillator paddles operated in coincidence. The two paddles are each coupled to photomultiplier tubes (PMTs) that are in turn read out by digital multichannel analyzers. The system is low power and runs on the USB port of a connected laptop on which the user interface can track the muon count rate in real time. The system has been assembled, as shown in Figure 7.

Test data obtained with this system reveal that its response is similar to that of the fixed-system muon counter, but it delivers a smaller count rate due to the smaller detector size. Calibration with gamma sources has been completed, and preliminary testing in horizontal and vertical orientations confirms observations made with the large muon counter in the fixed system. Future work may include monitoring data collected in a variety of settings, such as tall buildings or large maritime vessels. Data could also be collected on different decks of vessels in order to verify the extent to which overhead material can be quantified by cargo weight and/or number of cargo containers. This measurement could be easily obtained by a reduction in muon count rate with increasing overhead due to shielding, or attenuation of the downward-traveling muons.

Figure 7. Portable muon counter made with two smaller-size paddles. Paddles were sized to fit within a small pelican case. The Bridgeport Instruments eMorpho TwinBase PMT bases are low power and can be powered by a single USB port on a battery-powered laptop.

Conclusion

The fixed muon-neutron observatory system is nearly completely assembled. Limited test data have been taken thus far that indicate the system and its components are operating as expected. A temporary location for the observatory has been established, but a more permanent location will have to wait until hangar renovation work is completed. When the system is fully up and running, data will be recorded and archived and any number of analyses can be run to search for potentially interesting cosmic phenomenon. A portable muon counter system was designed and built, and initial data show that it is functioning well. In the coming months, with the support of the NRAT, the system will be taken to predetermined locations (vessels, tall buildings, etc.) for further testing. Both fixed and portable systems will be able to support maritime missions for correlating solar and cosmic events with neutron data gathered on the earth's surface.

References

Ashenfelter, T., J. You, R. Hayes, "An ultrasensitive neutron spectrometer," *Nevada Test Site–Directed Research and Development*, FY 2007, National Security Technologies, LLC, Las Vegas, Nevada, 2008, 65–74.

Heimberg, P. C., W. J. Kernan, R. Detwiler, T. M. Haard, C. Okada, "Experimental study of the neutron ship effect," report, Bechtel Nevada, Las Vegas, Nevada, 2004.

Hathaway, D. H., "The sunspot cycle," National Aeronautics and Space Administration/Marshall Space Flight Center, http://solarscience.msfc.nasa.gov/SunspotCycle.shtml, accessed December 15, 2009.

LASER POLAR NEPHELOMETER FOR AEROSOL STUDIES

Michael P. Taylor[1,a] *and Daniel K. Frayer*[b]

The ability to measure the concentration and size of suspended aerosol particles is crucial for reducing the threat of harmful particulate inhalation. This project addressed the challenges of making such measurements in real time with the use of a laser polar nephelometer. Presented here are the results of measurements taken with the laser polar nephelometer system. This instrument is capable of collecting high-resolution data in less than 1 second. It has successfully quantified the light-scattering behavior of aerosolized water as predicted by Mie theory. As such, Mueller matrix element information associated with size distribution and shape were accurately determined for water droplets. Although there were some anomalies associated with data obtained for polystyrene latex spheres, anomalies are well understood and will be addressed in subsequent experiments.

Background

The monitoring of hazardous air pollutants is an area of increasing interest in a number of fields. Advances in techniques for in situ, real-time detection of aerosols have been driven by the concern over the health effects of airborne particulates, which vary with the size, concentration, and chemical composition. Radioactive aerosols and industrial aerosols can cause disease and respiratory problems in the work place and the environment (Willeke, 1993; Pope, 2006). Some airborne bacteria and viruses transmit infectious diseases and have been used as biowarfare agents. "Fine particulates" are of great concern; they can be inhaled deeply into the lungs and remain there indefinitely. The Department of Energy (DOE) is particularly interested in airborne beryllium (Be) particulates. Be plays a major role in the production of nuclear weapons and has been extensively used by DOE since the 1940s. The major hazard associated with Be processing is the inhalation of Be aerosol particulates. Those exposed risk the contraction of chronic Be disease, an incurable, often debilitating, and sometimes fatal, lung condition. There is a need for improved methods for rapid detection and characterization of aerosols in both indoor and atmospheric environments (McMurry, 2000).

The goal of this project was to investigate and test new optical methods for characterizing aerosols for particulate detection, smoke/plume studies, and field test programs. This was accomplished with the development of a laser polar nephelometer, which measures the angular distribution of the intensity and polarization changes of light from a laser beam scattered by airborne particles (Mueller calculus). Our instrument was designed to be an unattended unit, providing real-time, high-resolution data in a fraction of the time associated with most current systems (McMurry, 2000).

---

[1] taylormp@nv.doe.gov, 301-817-3308

[a] Remote Sensing Laboratory–Andrews; [b] Los Alamos Operations

Light scattering is conveniently described by Mueller matrix algebra. The state of polarization of a beam of light, along with its intensity, can be described by the Stokes vector, **F** = $\{I,Q,U,V\}$, where I = total intensity of light, $\langle E_l E_l^* + E_r E_r^* \rangle$; Q = ±90-degree polarization, $\langle E_l E_l^* - E_r E_r^* \rangle$; U = ±45-degree polarization, $\langle E_l E_r^* + E_r E_l^* \rangle$; V = circular polarization, $\langle i(E_l E_r^* - E_r E_l^*) \rangle$; and E_l and E_r are complex electric field vectors parallel and perpendicular to the scattering plane, respectively. When a beam of light is incident upon some obstruction, it scatters radiation in all directions, altering the intensity and, in most cases, the polarization state of the incident light. The efficiency of this scattering process depends on the physical and optical properties of the scatterer and therefore carries the signature of the scatterer. The effect of this scattering process can be represented by a 16-element Mueller matrix **M** that transforms the Stokes vector for incoming light to the vector representing scattered light (van de Hulst, 1957) such that $\mathbf{F}_s = \mathbf{MF}_i$:

$$\begin{pmatrix} I_s \\ Q_s \\ U_s \\ V_s \end{pmatrix} = \frac{1}{k^2 r^2} \begin{pmatrix} S_{11} & S_{12} & S_{13} & S_{14} \\ S_{21} & S_{22} & S_{23} & S_{24} \\ S_{31} & S_{32} & S_{33} & S_{34} \\ S_{41} & S_{42} & S_{43} & S_{44} \end{pmatrix} \begin{pmatrix} I_i \\ Q_i \\ U_i \\ V_i \end{pmatrix}. \qquad (1)$$

The subscripts i and s refer to incident and scattered light; k is the wave vector, and r is the distance from the scatterer to the detector. The elements of **M** are functions of scattering angle and contain all the elastic light-scattering information available at a given wavelength. The Mueller matrix is determined by size, structure, symmetry, orientation, and the complex index of refraction of the scatterers.

For a suspension of randomly oriented, arbitrarily sized particles with a plane of symmetry, the scattering matrix simplifies to:

$$\mathbf{M} = \begin{matrix} S_{11} & S_{12} & 0 & 0 \\ S_{12} & S_{22} & 0 & 0 \\ 0 & 0 & S_{33} & S_{34} \\ 0 & 0 & -S_{34} & S_{44} \end{matrix}. \qquad (2)$$

Furthermore, if the particles are spherically symmetric, $S_{11} = S_{22}$ and $S_{33} = S_{44}$. In this case, scattering can be predicted by Mie theory. Each Mueller matrix element, for any scatterer, may be expressed as a θ-dependent intensity curve by the appropriate adjustment of various optical element combinations fore and aft of the scattering medium. Measuring the normalized matrix elements is a more sensitive approach to characterizing scattering media. In this process, each matrix element, except S_{11}, is divided by S_{11} (Quinby-Hunt, 1989) and displayed in bold: $\mathbf{S}_{\mathrm{ij}} = S_{\mathrm{ij}}/S_{11}$.

In this work, we experimentally determined the two elements, S_{11} and $\mathbf{S}_{12}$ (the normalized S_{12} element), of the Mueller matrix. S_{11} is simply the total intensity as a function of scattering angle for unpolarized incident light. This matrix element, also referred to as the scattering phase function, provides information on particle size and is obtained from

$$I = I_{\perp} + I_{\parallel}, \tag{3}$$

where $I_{\perp}$ and $I_{\parallel}$ are scattered light intensities perpendicular and parallel to the scattering plane, respectively. $\mathbf{S}_{12}$, the ratio of the S_{12} and S_{11} elements, provides information on the degree of polarization and is given by

$$P = -S_{12} / S_{11} = \frac{I_{\perp} - I_{\parallel}}{I_{\perp} + I_{\parallel}}. \tag{4}$$

Polarization is an important quantity to exploit. With it, we can determine the particle's degree of sphericity and whether the particle is an oblate or prolate spheroid or cube, or some other irregular shape.

Project

Optical Design and Experimental Arrangement

Figure 1 shows a schematic of the optimized nephelometer system. The scattering volume is located at the first focus of an ellipsoidal reflector (Opti-Forms, Inc., Temecula, CA); the optical system treats this volume as an aperture stop in order to collect data by angle. Light is scattered from the beam within the scattering volume into a range of polar angles. Scattered light is reflected off the sides of the reflector towards the ellipse's second focus. Additional lenses are necessary to (1) remove the extreme field curvature created by the reflector; (2) collimate the light in an area with small angular extent, for the introduction of a polarization analyzer; and (3) bring the light to a focus on a camera imaging array. The optics image the scattered light such that various positions on the imaging array correspond to light scattered at a given angle in three-dimensional space.

Water droplets and polystyrene latex (PSL) spheres in distilled water were aerosolized with a constant output aerosol generator (TSI Inc., Model 3079), and the resulting flow was directed through an aperture at the vertex of the reflector. The reflector (Figure 2) has a semi-major axis of 5.96 in., a semi-minor axis of 4.23 in., and an eccentricity of 0.705. The diameter of the reflector is 7.25 in. and its depth is 2.126 in. A set of two holes, 0.197 in. in diameter, were cut through the reflector by means of electrical discharge machining (EDM). The aerosol particulates intersect a laser beam that passes through the EDM holes of the reflector, 1.761 in. from its vertex and perpendicular to its optical axis.

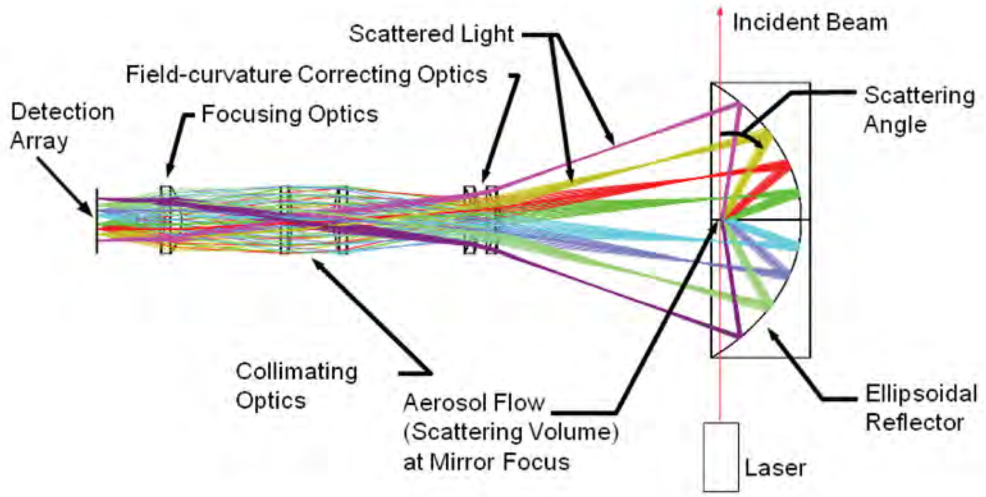

Figure 1. Schematic diagram of the scattering region and optics of the nephelometer system

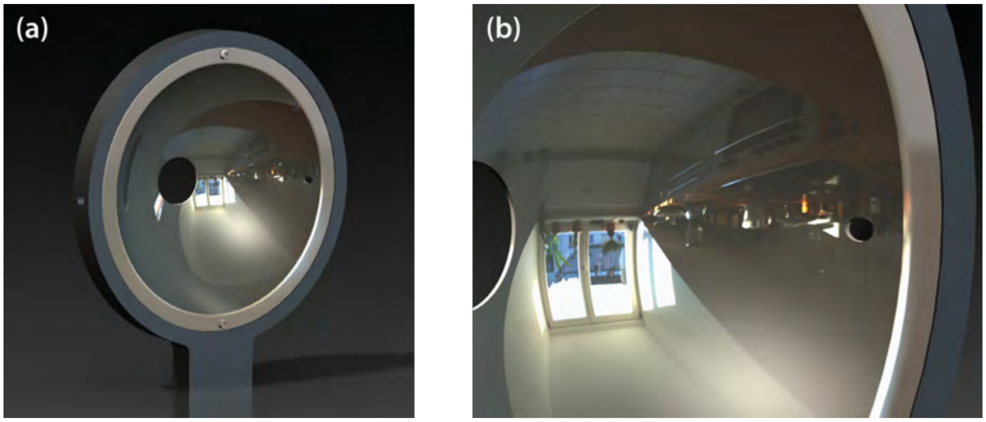

Figure 2. (a) 3-D rendering of the ellipsoidal reflector showing the reflector and custom mount, and (b) a close-up view that reveals one of the cut holes through which the beam enters and exits

The CCD imaging system, comprising the detection array (Princeton Instruments, Model PIXIS 1300B), was positioned at the imaging plane of the focusing optics. The light detected by each element of the CCD array could be traced back to a specific scattering angle (Figure 3). The scattering angle is defined relative to the direction of the incident beam. Forward scattering occurs at $\theta = 0$ degrees and backscattering at $\theta = 180$ degrees. The useful angular range of this device is ~10 degrees $< \theta <$ 178 degrees. The CCD camera is situated such that the scattered hemisphere maps to a circle with a radius equal to the linear dimension of the array. The system has an angular resolution of better than 1 degree, although not all scattering angles map linearly to positions on the array.

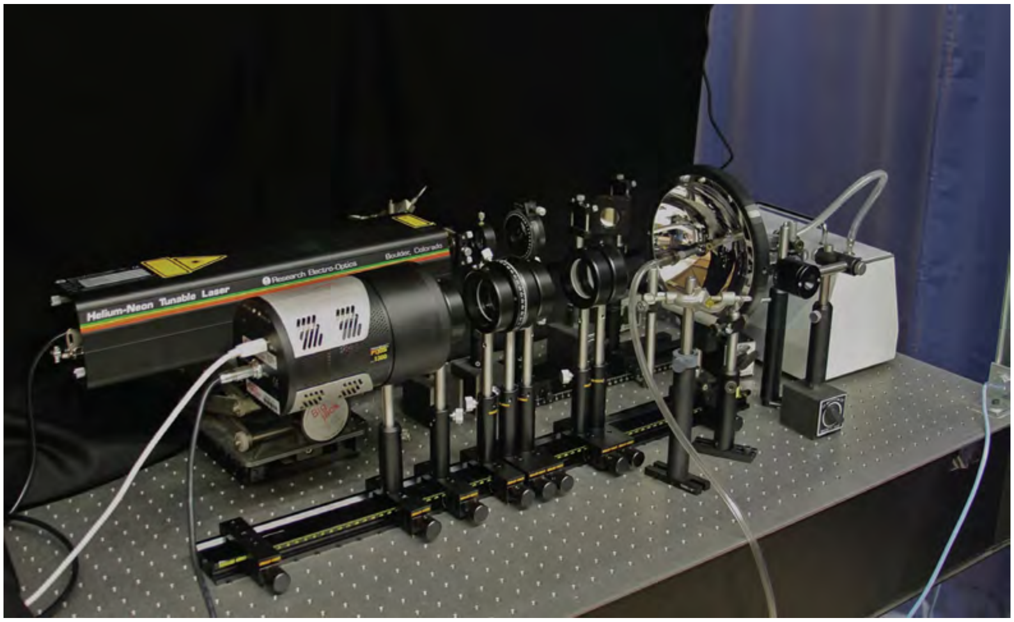

Figure 3. Experimental setup, including optical filters, polarizers, and lenses, a tunable HeNe laser, an ellipsoidal reflector, CCD camera, aerosol generator (to the far right), and a sampling pump (not seen) for collecting measured aerosols.

Results and Discussion

The CCD camera is typically set to image for 1 second. A typical image from the CCD array, corrected for background scattering, is shown in Figure 4. These initial measurements were taken for aerosolized water, with a refractive index of $m = 1.33$ and a laser beam wavelength of 543 nm. On the left side of each image is the hole in the elliptical mirror, through which the laser beam enters the sampling volume. The hole on the right side of the elliptical mirror, where the beam exits the mirror, is not shown. The hole on the right was blocked to prevent the saturation of the array by the forward-scattered signal. Even when a portion of the image was being obstructed, the dominant nature of forward scattering is evident. The concentric rings that span the entire image were initially thought to be caused by diffraction; however, their large scale and repeatability suggests they are more likely artifacts of the reflector's manufacture.

Figure 4a shows the scattering pattern for water droplets with the incident laser beam polarized perpendicular to the scattering plane. For each image, each pixel number was associated with a scattering angle from 0 (forward scattering at right) to 90 degrees (top of the image), to 180 degrees (backscattering at the left). Forward scattering is dominant, indicating the presence of larger particles. In the backscattered direction, structure is seen as a number of "rings" that appear to be concentric about the entrance hole of the reflector. Since the scattering plane is defined by the laser beam and any angle, θ, about the beam, this is expected. Figure 4b shows the scattering pattern for water droplets with the

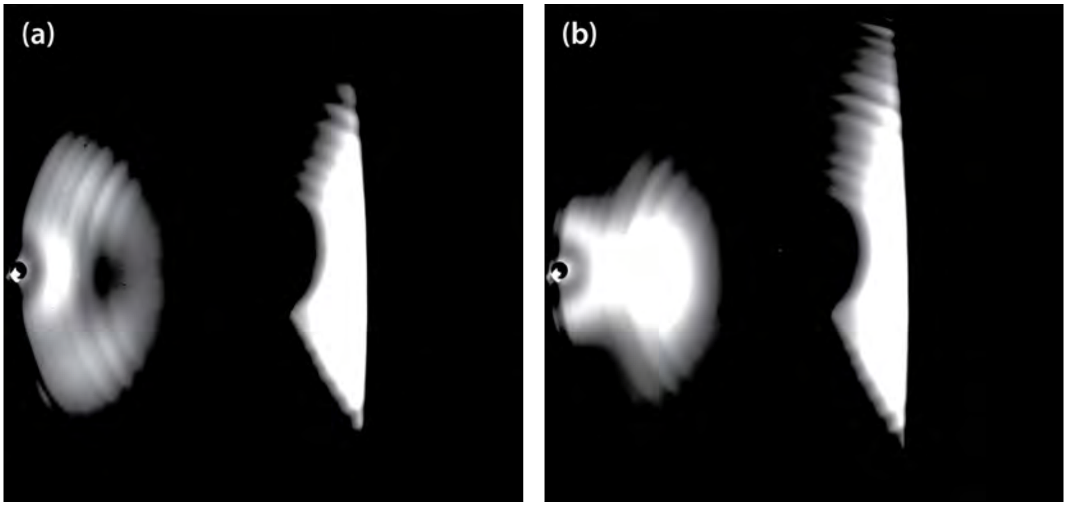

Figure 4. CCD image of scattered light from aerosolized water. The scattering patterns of incident light polarized (a) perpendicular and (b) parallel to the scattering plane are shown.

incident laser beam polarized parallel to the scattering plane. Again, forward scattering is dominant, as expected. Although the scattering patterns differ from those seen in Figure 4a, the overall signal is stronger. More forward-scattered signal is observed with a change in the backscattered patterns.

Figure 5 shows the results of mapping pixels from the CCD array to scattering angle. The results agree well with the literature (Daugeron, 2007) and theory associated with aerosolized water (Bohren, 1983). For water droplet curves, structure is largely absent. There are, however, some general features. For example, around 150 degrees, broad structure can be seen in the polarized scattering intensity curves. Comparing the measured scattering data to scattering calculations provides a means of accurately sizing particles. In fact, the relative peaks and valleys of the polarized intensities in this area of the curve, along with the behavior of the two curves seen at around 90 degrees, imply a size distribution of around 0.2–0.25 µm. The broad structure observed also indicates the possible onset of the fog bow, or cloud bow, a feature that develops rainbows for larger droplets.

Figure 6 displays the results of measuring the Mueller matrix elements S_{11} and $\mathbf{S}_{12}$ (the normalized S_{12} element). Note that the matrix element signals are noisy; this noise is caused by the number of particles fluctuating in the scattering volume. This behavior was also observed in Figure 5. This noise can be removed by implementing other matrix element normalization techniques. Once normalized, the number of particles in the aerosol flow becomes irrelevant. There is no new information to be gained by studying the results of measuring S_{11} alone (Figure 6a). However, in investigating the $\mathbf{S}_{12}$ matrix element, the degree of linear polarization, a few general conclusions can be made. Polarization diagrams for non-spherical particles do not have features near the rainbow angles (or their precursors for small particles). Polarization tends to be positive over a wide range of angles for nonspherical particles. Linear polarization of light scattered by nonspherical particles tends to be positive at middle

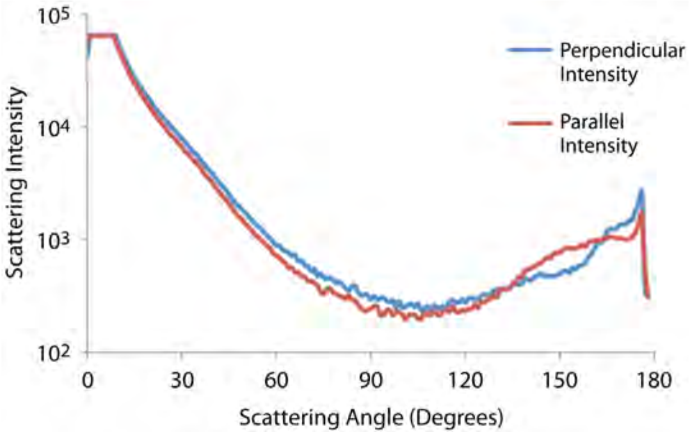

Figure 5. Polarized components for light scattering intensities as a function of scattering angle for aerosolized water

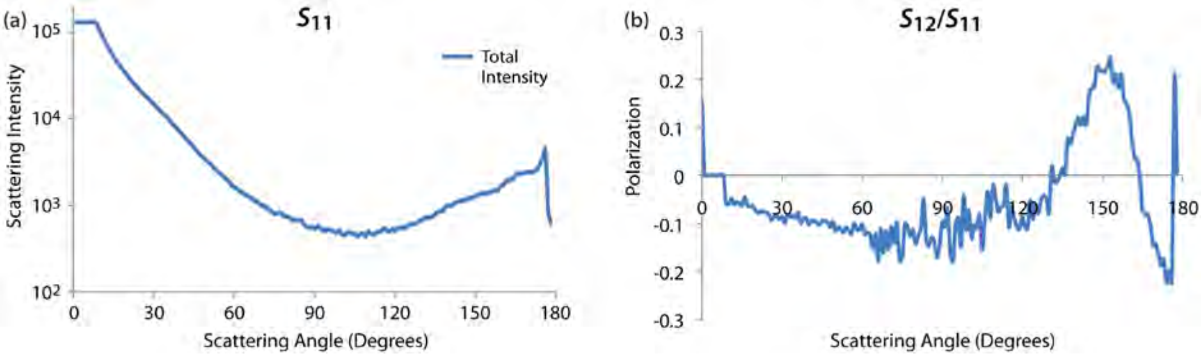

Figure 6. Measured Mueller matrix elements for (a) measured phase function, S_{11}; and (b) degree of polarization, S_{12}/S_{11}, for aerosolized water

scattering angles (Bohren, 1983). This last conclusion was based on extensive studies of randomly oriented prolate spheroids (Asano, 1979). By contrast, the polarization diagram of Figure 6b has broad features near 150 degrees and has negative values up to around 130 degrees, to include a negative value at 90 degrees. Recognition of these trends, combined with comparisons of the measured degree of polarization with theoretical calculations reveals that the shape of water aerosols generated for this study are spherical.

Figure 7 shows the polarized components of scattered light as a function of scattering angle for 0.903 µm PSL spheres (Thermo Fisher Scientific), a suspension of monodisperse spheres with a particle density of 1.05 g/cm^3 and a particle count of 10^9/ml. The index of refraction for these spheres is m = 1.59 at a wavelength of 589 nm. They were dispensed directly from the package via an eye dropper. Initial trials were performed using a single drop per 80 ml. The trials shown in Figure 7 were performed with a number of relatively high concentrations: 2.49 × 10^{-14} M (Conc1), 4.15 × 10^{-14} M (Conc2) and 6.23 × 10^{-14} M (Conc3).

Figure 7 illustrates a number of unexpected results. First, the overall behavior of the curves is similar to that of aerosolized water. There is strong forward scattering with moderate structure in the backscattered signal. Since structure is mainly in the backscattered region, our focus is in that area of the plot. For such large spheres, we expect several distinct peaks and valleys throughout. The absence of such behavior could be a result of significant moisture being introduced with the PSL spheres. They are aerosolized from aqueous solution; therefore, they are measured against a water background, and the water component is dominant. Second, there is a decrease in scattered intensity for PSL spheres as compared to water droplets. As these spheres are nonabsorbing, such a drop in scattered intensities is unexpected. This could be a result of diffraction associated with such large particles or rays being internally reflected within the spheres. Close observation and control in future experiments are required to rule out other experimental factors that may affect observations made in the experiment. Third, although there is an overall decrease in scattered intensities, it is clearly seen that as the concentration of particles increase within the scattering volume (Conc1 < Conc2 < Conc3), there is a relative increase in scattered intensities. Adjustments can be made to the experiment to improve results in this regard, such as drying the aerosols during the aerosol generation process.

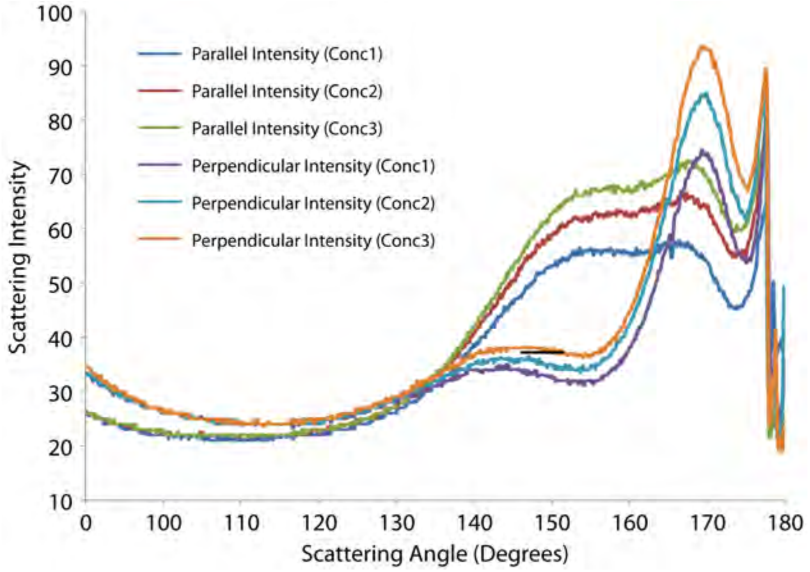

Figure 7. Polarized components for light scattering intensities as a function of scattering angle for 0.9 µm PSL spheres at a number of particle concentrations (Conc1 < Conc2 < Conc3)

Figure 8 shows the first steps toward the production and study of the full Mueller matrix. Represented here are combinations of Mueller matrix elements. Various polarizing elements were placed fore and aft of the scattering medium to yield the images displayed. In Figures 8a and 8b, incident light is polarized perpendicular to the scattering plane. However, in Figure 8a, a linear analyzer is positioned before the CCD array for horizontal polarization of the scattered light, producing the Mueller matrix combination, $\frac{1}{4}(S_{11} - S_{12} + S_{21} - S_{22})$. In Figure 8b, the analyzer is positioned for vertical polarization of the scattered light, producing the combination, $\frac{1}{4}(S_{11} - S_{12} - S_{21} + S_{22})$.

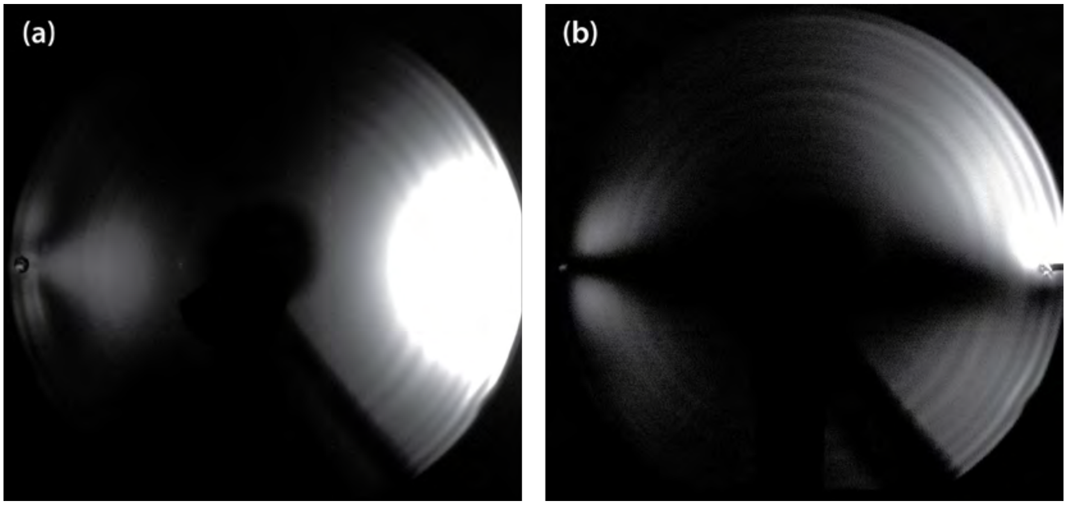

Figure 8. CCD images for two irradiances with a polarizer before the scattering medium and an analyzer before the CCD array. The measurements of (a) and (b) resulted in a combination of Mueller matrix elements, $\frac{1}{4}(S_{11} - S_{12} + S_{21} - S_{22})$ and $\frac{1}{4}(S_{11} - S_{12} - S_{21} + S_{22})$, respectively.

Conclusion

A proof-of-concept device for a robust, laser polar nephelometer has been developed and tested, offering a unique approach to vigorous, real-time aerosol characterization. Modeling efforts have set a foundation for system design, calibration, and the prediction of results. This instrument allows for comparison between measured optical properties and theoretical model calculations. The system requires no moving parts, offering a more reliable and accurate measurement scheme than current nephelometer systems. The nephelometer collects high-resolution data in real time. The phase function Mueller matrix measurements obtained agree with the literature and scattering theory. Anomalies associated with PSL spheres were identified; however, they are well understood and certain corrective actions for subsequent experiments have been identified.

The future presents the opportunity to perform a number of unique measurements for which this system is well suited. It is generally assumed, based on symmetry arguments, that scans from 0 to 180 degrees are identical to scans from 180 to 360 degrees. The literature reflects this assumption. However, this is not necessarily the case. Other than spheres, particles are likely to be azimuthally asymmetric; hence, 360-degree scans may provide information that is rarely collected. Such scans have the added benefit of showing instrument misalignment. The current nephelometer system design allows for such studies without loss of efficiency.

There are a number of important reasons to measure and study the full Mueller matrix for a scattering volume under consideration. Among them are information on shape and composition. We have shown in this study that the $\mathbf{S}_{12}$ (S_{12}/S_{11}) matrix element provides information on the degree of polarization, which provides a measure of nonsphericity. It turns out that $\mathbf{S}_{34}$ (S_{34}/S_{11}) is very sensitive to the characteristics of biological scatterers. Studies have shown that reproducible differences in $\mathbf{S}_{34}$ were found for particles that could not be readily distinguished by common means (Bohren, 1983). Further studies in this area may reveal the potential of this instrument to identify chemical and biological agents, as well as workplace contaminants.

Acknowledgments

The authors are grateful to Edward Van Keuren, Physics Department Head at Georgetown University, for his support in offering critical resources to make this work possible. The authors would also like to thank Steven G. Iversen, Stephan J. Weeks, and Kevin R. Kyle of NSTec for their support, advice, and many enlightening discussions.

References

Asano, S., M. Sato, "Light scattering properties of spherical particles," *Appl. Opt.* **18** (1979) 962–974.

Bohren, C. F., D. R. Huffman, *Absorption and Scattering of Light by Small Particles,* John Wiley & Sons, Inc., New York, 1983.

Daugeron, D., J. B. Renard, P. Personne, G. Brun, J. M. Andre, "Laboratory polarization nephelometer for measurements of optical properties of aerosols," *Meas. Sci. Technol.* **18** (January 2007) 632–638.

McMurry, P. H., "A review of atmospheric aerosol measurements," *Atmos. Environ.* **34** (2000) 1959–1999.

Pope, C. A., D. W. Dockery, "Health effects of fine particulate air pollution: lines that connect," *J. Air Waste Manage. Assoc.* **56** (2006) 709–742.

Quinby-Hunt, M. S., A. J. Hunt, K. Lofftus, D. Shapiro, “Polarized-light scattering studies of marine Chlorella,” *Meas. Sci. Technol.* **34**, 8 (1989) 1587–1600.

van de Hulst, H. C., *Light Scattering by Small Particles*, John Wiley & Sons, Inc., New York, 1957.

Willeke, K., P. A. Baron, *Aerosol Measurement: Principles, Techniques, and Applications*, Van Nostrand Reinhold, New York, 1993.

this page intentionally left blank

SPECTR—SPECTROSCOPIC PROOF OF CONCEALED EXPLOSIVES BY TERAHERTZ REFLECTOMETRY

Robert A. Buckles[1,a]

This project explored techniques to perform broadband time-domain reflection spectroscopy of concealed explosive material at a stand-off distance of 10 to 30 meters in atmosphere. For this project we developed a high-power, low-temperature (LT) gallium arsenide (GaAs) emitter with high-voltage, pulsed driver; a rapid-scan optical fiber delay line; and point-focus beam transport optics. The analytical development involved study of dielectric functions for concealing fabrics, and an adaptive deconvolution filter to account for atmospheric line absorption and concealing material, revealing the underlying material of interest.

Background

Currently, much attention is focused on using higher-power terahertz (THz) sources and low-power detectors for security applications with spectroscopy and imaging (Woolard, 2007). Laser-based difference frequency generation and THz quantum cascade lasers are steadily gaining in power, and have been employed for such purposes (Lee, 2006; Wanke, 2007). However, it is important to distinguish very similar technologies in different applications; whether used for object recognition, trace gas detection, or combined with high-contrast imaging, they each have signal trade-offs due to limits of available power and fidelity. Narrow-band imaging techniques suffer from multipath interference from common articles such as paper and clothing, while in the realm of spectroscopy, the tuning range is narrow, fine, and slow in real time. In both instances, narrow-band detection must operate on discrete lines where atmospheric absorption is minimal, and the item of interest is presumed to absorb power (Linden, 2005). However, solid materials (such as high explosives [HE]) exhibit very broad spectral features, and do not necessarily exhibit high absorption contrast. Nevertheless, both methods may work well in one facet of interdiction; developments such as phase-sensitive imagers (Federici, 2005) and rapid frequency tuning show promise. However, it seems overly optimistic to envision an all-in-one method that will spectroscopically image objects. Rather, a monochromatic, flood-illuminated imager paired with a single-point spectrometer may be the ideal interdiction tool.

Our goal was to show how the time-domain method, with existing technology, can be successfully applied to the interdiction problem, yet this has some trade-offs as well: power is spread out spectrally as opposed to spatially, and the time-delay scan must be long and rapid, requiring a high-peak-power, high-duty source. The power must be focused instead of flood-illuminated, and the distance to target must be known and tracked within a precise delay offset. It is expected that other existing surveillance

---

[1] bucklera@nv.doe.gov, 925-960-2520

[a] Livermore Operations

technologies are employed to spatially scan, track, and define the region of interest for probing. With the use of broad-band, phase-resolved coherent techniques, water vapor absorption is not problematic, and interfaces are resolved. With sufficient THz power and understanding of the intervening materials, we should be able to probe a human being and determine spectrally what lies at a specific point beneath their clothing, within a short real-time duration.

Project

Much of the experimental hardware was leveraged from previous SDRD projects (Buckles, 2009; 2010). The THz excitation source used a Quantronix Integra-C laser with a 130 fs pulse width, 2.5 mJ peak energy, and 1 kHz repetition. To maximize use of the laser energy and THz conversion, we procured a custom 15 mm aperture LT-GaAs chip from Del Mar Photonics (Figure 1), and adapted an 8 kV stacked BiMOSFET streak camera driver to pulse-bias the emitter. A 25 ns charge-line was used to set the pulse width and charge, while an UltraVolt high-voltage modulator was used to set and control the bias modulation sinusoidally 0–8 kV, 0–1 kHz (Figure 2). The pulser was back-terminated to allow the full 8 kV pulse to erect on reflection from the unterminated chip, and be absorbed back at the driver with minimal ringing. Synchronous operation of the pulser and laser was achieved by phase locking a Stanford Research DG645 delay generator to the laser seed pulses and directly triggering the pump laser, regenerative Pockels cells, and pulser from the DG645. The phase error of the unlocked pump RF is by design inconsequential due to regen saturation, and the pulser jitter was inconsequential, having a 25 ns pulse.

Figure 1. LT-GaAs emitter/receiver chips

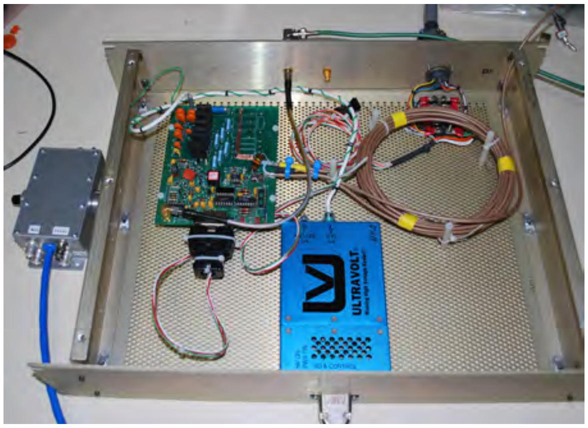

Figure 2. Emitter bias pulse modulator

The receiver was also an LT-GaAs chip (and silicon lens), although with 50 μm electrode spacing, optimized for high sensitivity and fiber coupling. We tried three chips in all, one from Del Mar Photonics, and two mounted chips (antennas) from T-Ray Science. We did not make a comprehensive comparison, only noting adequate behavior of the T-Ray model. Fiber coupling was achieved with single-mode 780 nm fiber from Nufern, with negligible dispersion, and minimal intensity, although reliable operation was extremely delicate as the fiber ends must be precisely aligned with the laser and LT-GaAs chip, and yet still be able to align the whole transmission path. (A manufactured unit such as the Picometrix head might be obtainable, although it is typically sold with a whole system.)

The fiber delay line design emphasized rapid, accurate delay with no mechanical moving parts, as this would allow a repetitive, precise delay at each laser pulse, over a variable range to 30 meters. It consisted of two main subsystems: a piezo fiber stretcher from General Photonics (Figure 3) for fine analog delay from 0 to 40 ps, and coarse-stepping discrete 12-bit binary switched delay from 0 to 133 ns in 33 ps increments (Figure 4). The minimum insertion delay, 67 ns, is through about 12 meters of fiber (mostly in the piezo stretcher) for a round-trip reflection from a target at 10 meters. The selection of maximum delay, 200 ns, would correspond to reflection from a target at 30 meters. The crystal switches from Agiltron can be synchronously switched at several kilohertz, resolving any desired delay from 10 to 30 meters for each laser pulse. Such a device is readily available for standard fiber communication wavelengths, even with polarization-maintaining (PM) fiber. However, the smaller 780 nm fiber requires tighter alignment tolerances in the switch to make an 800 nm device expensive to produce. We explored the possibility of producing it in-house, and decided we had the expertise to precisely cleave and fusion-splice PM fiber to subpicosecond length tolerance. However, purchasing and modifying the crystal switches involved greater time, cost, and labor than anticipated, as well as great reluctance from the vendor due to lack of market for 800 nm devices. Production of this design is deferred to future work.

Figure 3. Fine analog delay with fiber stretcher

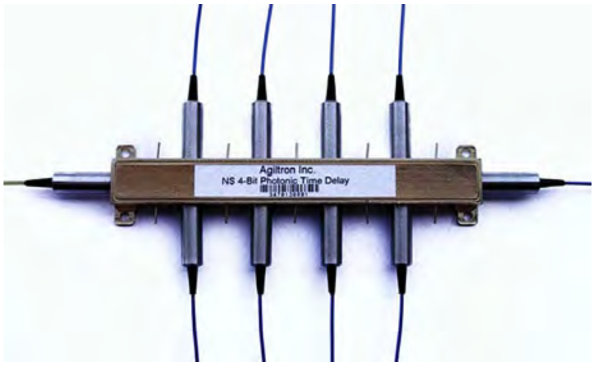

Figure 4. Coarse binary delay with fiber switches

For transport optics, we used a 15 mm diameter high-resistivity silicon hyperhemispherical (aplanactic) lens to aid output coupling of the THz emission, with 50 mm focal-length Teflon plano-concave lenses to collimate the THz beam. We designed a pair of 300 mm diameter off-axis ellipsoidal mirrors and Teflon expander lens for achieving a 30 mm focal spot at 30 meters. Construction was deferred until the fiber delay line could be completed for the sampling path. More appropriate for a fieldable system would be a programmable, lightweight adaptive mirror adjustable to any focal length in the range of 10 to 30 meters that could also provide tracking/scanning capability. A Bruker reflectometry stage (Figure 5), borrowed from another project, produced a focused spot on a sample at 200 mm distance. The insertion of the reflectometry stage added a 400 mm path length to the usual transmission path, so we installed a high-resolution, highly stable Newport linear stage with 300 mm travel (in lieu of a fiber delay line) to span both the reflection path and the straight-through transmission path. One nice aspect of the reflectometry stage was a hermetically sealed dry box with humidity monitoring and nitrogen flow control. However, the stage exhibited astigmatism due to spherical mirrors (as opposed to off-axis paraboloidal mirrors) and had difficulty focusing at a single point, effectively dispersing the target.

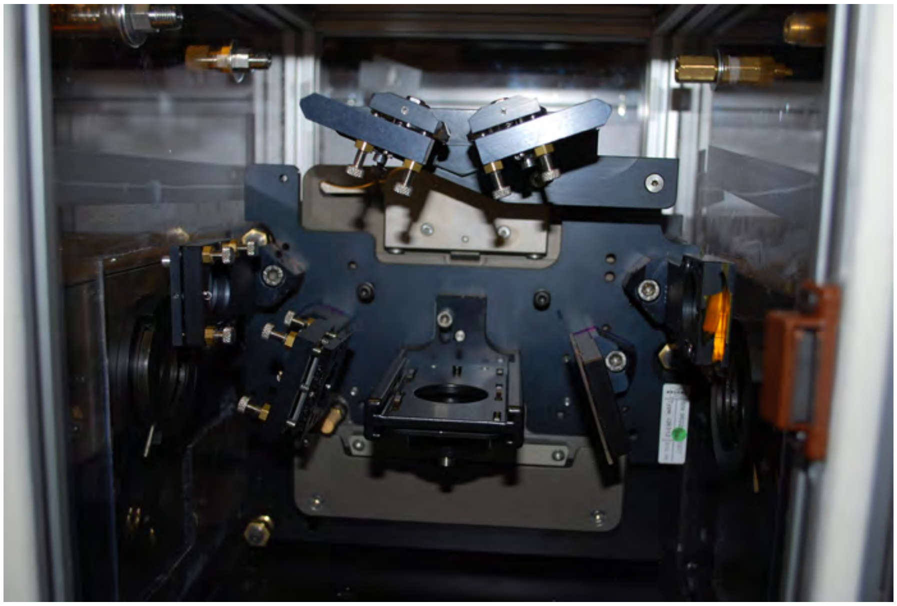

Figure 5. Bruker reflectometry stage

Figure 6 shows the THz signal trace resulting from the high-power, pulsed, biased emitter and fiber-coupled detector chips, measured with a Stanford Research 830 lock-in amplifier, with output to a Tektronix 7104 digital scope. The plot is a real-time record showing a slow delay scan rate of 100 fs/sec, and 1-second filter time constant. Full-scale output of ±10 volts per 5 μA sensitivity corresponds to a peak THz signal of 2 μA, which is nearly 1000 times greater signal than previously observed in-house via optical rectification. When we obtained this data, the stage and modulation controls were not fully developed. The high-voltage bias modulator with pulser was current-limited to a laser pulse rate of only 200 Hz with full modulation at 77 Hz. Therefore, a very slow scan rate and long filter time constant was used. The pulser is capable of exceeding 1 kHz pulse rate; however, the current limit of the high-voltage bias supply needs further work to achieve the higher rate.

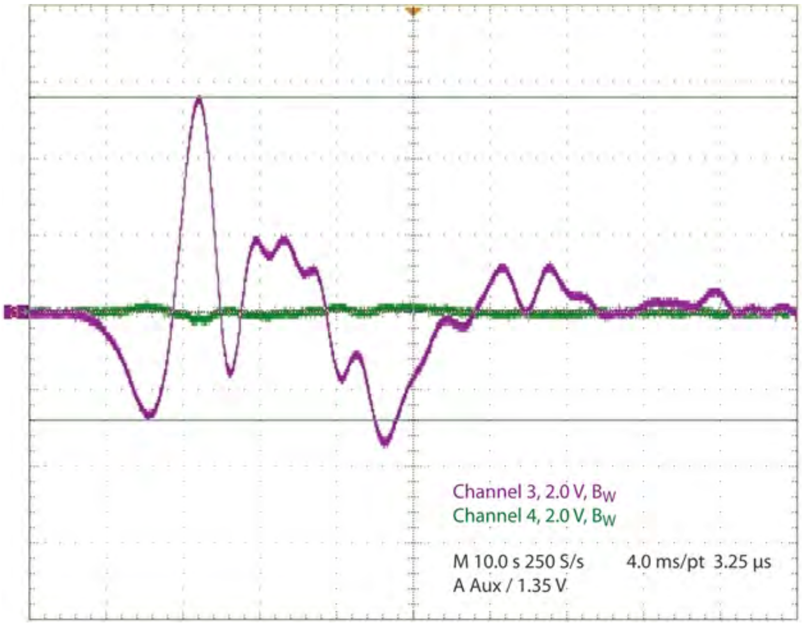

Figure 6. Pulsed bias emitter/receiver waveform

Fabric Measurements and Adaptive Deconvolution

We formed a collaboration with Dr. Farid Dowla of Lawrence Livermore National Laboratory and the University of California at Santa Cruz for generating the adaptive deconvolution routines. His previous computational work on water vapor deconvolution (Dowla, 2007) would work very well with the time-domain method, and could be adapted to work equally well with other intervening materials, such as clothing. The adaptive nature is a means of ignoring the water-vapor line absorption, with unspecified humidity/density/thickness, and reinterpolating the broadband spectral characteristics. The goal was to take transmission measurements of various cloths, in a dry nitrogen–purged atmosphere, both on reflection from a known substrate such as metal or flesh, and in direct transmission, and then identify such spectra, adaptively weighted for integrated density. We would also measure reflection spectra of bare and concealed known explosive material substrates and by comparison, extract the unknown quantities of intervening material (including atmosphere), revealing the substrate material spectra for identification. Given the coherent detection method, the spectra and filters are complex valued, and free from phase ambiguity. The THz-TDS method can directly measure amplitude/phase reflection and transmission coefficients of the materials under test.

We made transmission measurements of fabric materials and attempted to fold these into an adaptive deconvolution routine. We leased a Ti:Sapphire oscillator from DelMar Photonics and used it with the small THz-TDS spectrometer purchased from EKSPLA (Buckles, 2009). These were measured in a dry nitrogen–purged atmosphere with long/slow scans to collect multiple (albeit small) reflections from within the fabric material. Figure 7 shows, to first order, the transmission amplitude and phase shift spectra of denim, cotton, wool, polyester, nylon, and a 70/30 cotton/nylon blend, along with air (water vapor) for spectral calibration, and a comparison of two nitrogen references. Fabric density and thickness are indicated on each. In each case, the scan rate was 0.5 ps/sec with a scan length of 110 ps, and a filter time constant of 100 ms. Peak average photocurrents were 1–3 nA, with a noise equivalent power spectral density at –60 dBnA/THz. Useful signal-to-noise ratio exists from about 80 GHz to 1.5 THz. Figure 7g indicates the air sample, with excellent agreement to known principal water lines (van Exter, 1989). These lines are overlaid in pale green on each figure, clearly showing that resonant behavior is not due to any residual atmosphere. We believe the broad slow

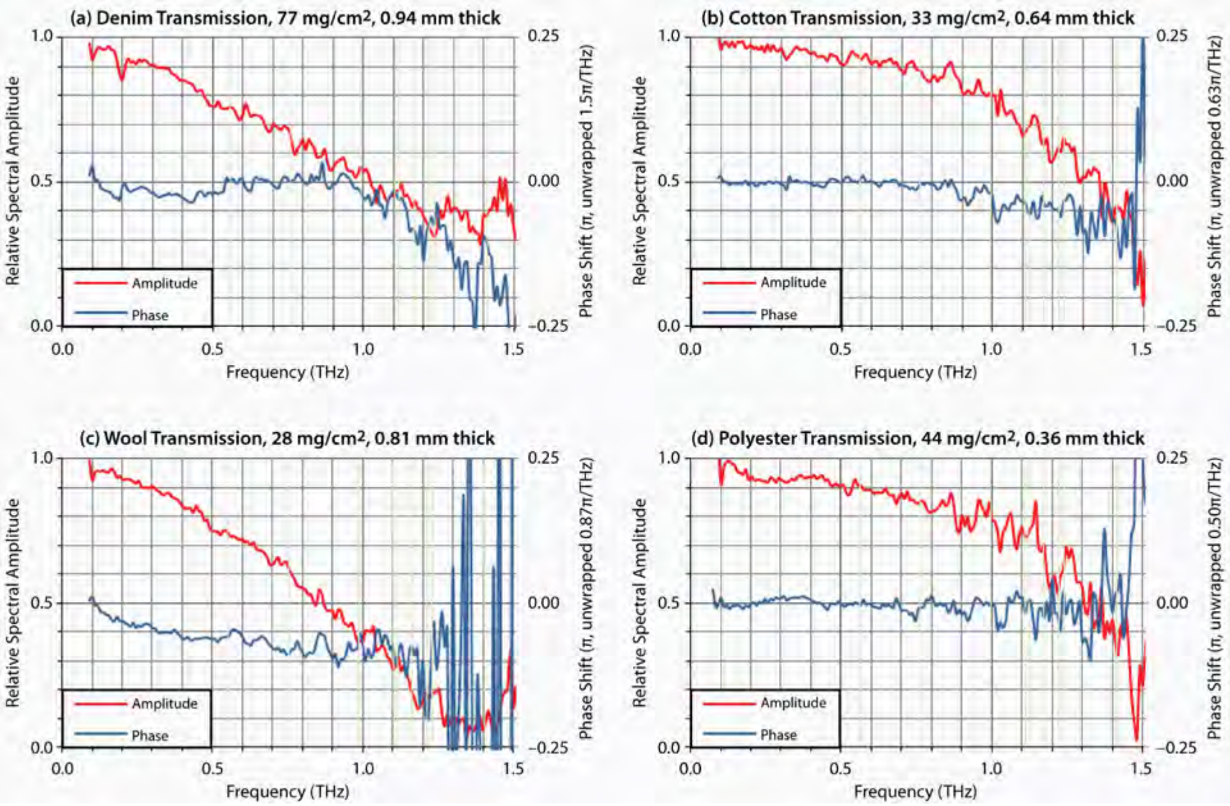

Figure 7a–d. Amplitude transmission and phase shift spectra for various cloth materials and densities with principal absorption lines shown in pale green

trend in loss at progressively higher frequency is due to a type of Mie scatter due to the fabric weave, while the resonant losses are etalon effects due to the fabric thickness and weight. Odd harmonics of a quarter wave thickness will resonantly interfere. Additionally, each integer subharmonic of these frequencies (e.g., eighth, sixteenth, etc.) can resonantly interfere with multiple round trips, yet are sequentially weaker. Of course, a short temporal scan window will never detect these subharmonics, so our scans were made long enough to pick up multiple etalons for mm-sized material. The first two absorption resonances in Figure 7a (denim), near 100 and 200 GHz, are such a pair of etalon subharmonics. An adaptive method that integrates the phase through each resonance (which should be proportional to the strength of the resonance) should recover the smooth material properties in spite of the resonances (Duvillaret, 1999). It is not necessary to know the material thickness beforehand, as this is yielded as a best-fit parameter to the measurements, along with the index. This behavior is further complicated by multilayer interactions, although a harmonic analysis can sift out the details.

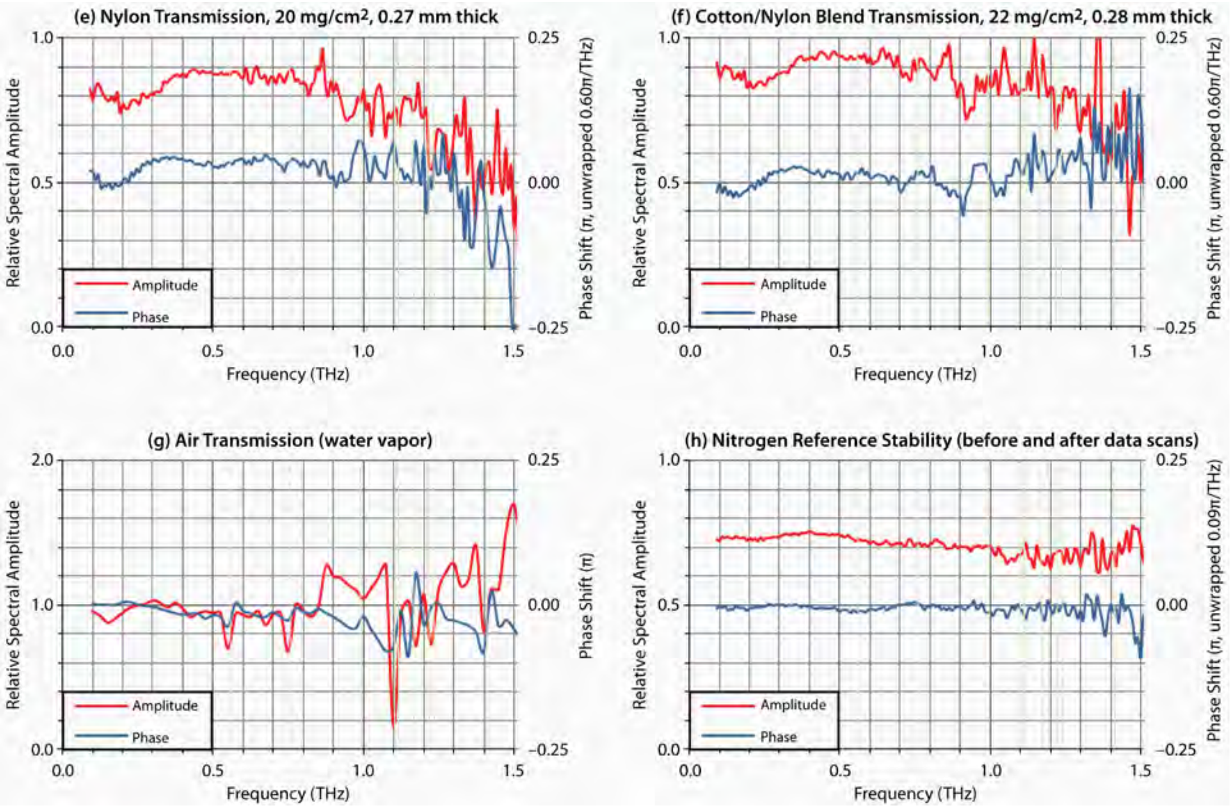

Figure 7e–h. Amplitude transmission and phase shift spectra for various cloth materials and densities with principal absorption lines shown in pale green

Our approach was to first test the individual samples in transmission, then again with reflection off a metal or flesh substrate, and finally in mixed layers. Our goal to incorporate these dielectric models within the adaptive deconvolution routine in collaboration with Dowla was not realized. Ultimately we were unable to test HE materials. Furthermore, our pump laser had a failure in the first quarter that required replacement of the lasing and doubling crystals, which took about six months to effect. This lengthy repair delay, and competing for THz hardware and resources committed to other projects, prevented us from completing our measurement and analysis goals.

Conclusion

We have successfully measured transmission spectra of common clothing material, and presented a means of identifying such using spectral characteristics of phase-resolved time-domain spectroscopy. We believe identification of such intervening material, in addition to atmosphere, is necessary to identify concealed HE. We have also demonstrated a suitably high-power THz source and presented achievable designs for precise, fast, time-delayed scans using a fiber-based delay line. Although further engineering is needed to realize the time-delay stage at 800 nm, such hardware is readily available using standard communication fiber. Fiber-based, 1300–1550 nm, high-power, ultrafast lasers already exist, and the reduction in size and complexity, with corresponding increase in rapid portability would offset the cost of such lasers. Improving the reflectometry stage optics would be a necessary step to further studies, and an adaptive optics package for stand-off measurements would represent advancement toward a ready for field use instrument.

Acknowledgments

We thank Dr. Farid Dowla for useful discussions concerning dielectric models and adaptive deconvolution routines, and are hopeful that future development along this path will prove fruitful.

References

Buckles, R., “Terahertz time-domain spectroscopy and imaging,” *Nevada Test Site–Directed Research and Development*, FY 2008, National Security Technologies, LLC, Las Vegas, Nevada, 2009, 215–226.

Buckles, R., “Terahertz DPFA plasma probe,” *Nevada Test Site–Directed Research and Development*, FY 2009, National Security Technologies, LLC, Las Vegas, Nevada, 2010, 55–65.

Dowla, F., M. Burke, G. Klunder, R. Deri, “Standoff detection of high explosives using THz imaging spectroscopy,” LLNL LDRD 05-ERD-76, UCRL-JRNL-235289 (2007).

Duvillaret, L., F. Garet, J.-L. Coutaz, “Highly precise determination of optical constants and sample thickness in terahertz time-domain spectroscopy,” *Appl. Opt.* **38**, 2 (1999) 409–415.

Federici, J., D. Gary; R. Barat; D. Zimdars, "Terahertz imaging using an interferometric array," *Proc. SPIE* **5790** (2005) 11–18.

Lee, A., Q. Qin, S. Kumar, B. Williams, Q. Hu, J. L. Reno, "Real-time terahertz imaging over a standoff distance (>25 meters)," *Appl. Phys. Lett.* **89**, 14 (2006) 1125–1128.

Linden, K., W. R. Neal, J. Waldman, A. J. Gatesman, A. Danylov, "Terahertz laser based standoff imaging system," IEEE Computer Society, Proceedings of the 34th Applied Imagery Recognition Workshop, Washington, D.C. (2005) 8–14.

van Exter, M., Ch. Fattinger, D. Grischkowsky, "Terahertz time-domain spectroscopy of water vapor," *Opt. Lett.* **14**, 20 (1989) 1128–30.

Wanke, M. I., M. Lerttamrab, I. Waldmueller, W. Chow, "THz quantum cascade lasers for standoff molecule detection," http://prod.sandia.gov/techlib/access-control.cgi/2007/076686.pdf (2007), accessed September 30, 2010.

Woolard, D., *Terahertz Science for Security and Military Applications (Selected Topics in Electronics and Systems*, Hackensack, New Jersey: World Scientific Publishing, 2007.

this page intentionally left blank

ORGANOPHOSPHATE DETECTION USING EPM SENSORS

Cenobio Gallegos[1,a] *and Richard J. Venedam*[b]

Piezoresistive microcantilever sensors may be used in a variety of sensing applications, including chemical analytes and some types of biological species. These sensors employ a tiny piezoresistive microcantilever functionalized with a "sensing material" that acts as a probe for the desired analyte. In this study, the microcantilever was partially embedded into the sensing material, producing a sensor element that is highly rigid and resistant to shock, making it suitable for portable or handheld operation. The sensing material matrix used was Hypol, a hydrogel capable of preserving the biofunctionality of molecules embedded into it. This matrix was combined with acetylcholinesterase to form the finished sensing material. Results of exposing these sensors to a VX simulant, Malathion, are presented for both vapor and liquid environments. This project also explored the miniaturization of the electronics package and integrated the capability to monitor several sensor channels.

Background

Piezoresistive microcantilever sensors in which the microcantilever is partially embedded into the sensing material have been referred to as embedded piezoresistive microcantilever (EPM) sensors (Porter, 2003). These EPM sensors operate by embedding or partially embedding a small piezoresistive microcantilever into a "sensing material." The sensing material is synthesized in such a way as to respond volumetrically to the presence of a particular analyte species. In many cases, chemical, physical, or other reactions with the sensor material may produce the desired volumetric shift. Sensing materials used in EPM applications may include common organic polymers, composite polymer/biomolecule materials, or polymers functionalized with other active particles or chemicals. When they are exposed to the analyte species, the sensing material volume change causes a bending or strain in the embedded cantilever, which is subsequently measured as a resistance change by the sensor electronics. Volume changes in the sensing material may be due to diffusion of the analyte molecules into the sensing material, probe-target binding on the material surface or bulk, or surface or bulk chemical reactions between the analyte and sensing material. In many cases, only tiny volumetric changes are needed to successfully detect the target species, as microcantilever strains of only a few angstroms are measurable. Electronics for these sensors are generally simple and inexpensive, as only the resistance of the microcantilever is measured. Previously, these types of sensors have been used to detect volatile organic compounds (Porter, 2003), bacteria in solution (Kooser, 2003), viruses (Gunter, 2003), carbon monoxide (Kooser, 2004), cyanide (Porter, 2007), hydrogen fluoride, and other analytes.

---

[1] gallegch@nv.doe.gov, 505-663-2056

[a] Los Alamos Operations; [b] North Las Vegas

V-series nerve agents are part of the larger group of organophosphate nerve agents, first studied as pesticides in the 1920s. The V series itself (organophosphate esters of substituted aminoethanethiols) were studied intensively beginning in the 1950s by British scientists. Several V-series compounds were eventually produced, including VG, VE, VM, VR, VS, and the well-known VX. Many of these deadly compounds function by binding to and thus inhibiting the enzyme acetylcholinesterase (AChE), which is present at the synapse between nerve and muscle cells. V-series and other organophosphate nerve agents disrupt the nervous system by inhibiting the AChE by forming a bond with the site of the enzyme where acetylcholine normally undergoes hydrolysis. Exposure to V-series nerve agents leads to rapid contraction of pupils, excess salivation, convulsions, and eventual death by asphyxiation as control is lost over respiratory muscles. Many of these nerve agents are easily deployable in aerosol form, with subsequent human exposure through the respiratory system. They may also be absorbed through the skin if exposure occurs in liquid form.

Project

VX (simulant) sensors were fabricated by immobilizing the enzyme AChE in a hydrogel matrix. The gel host used was Hypol, a biologically compatible material from Dow Chemical. Hypol has been shown to immobilize many different types of biological molecules while preserving the biological activity of the immobilized species. The enzyme was loaded into the liquid Hypol host at approximately 10% ratio by mass. The material was then deposited onto a Si substrate, and the microcantilevers partially inserted into the compound with the use of a micromanipulator. The material with cantilevers embedded was allowed to cure in air at room temperature for 72 hours prior to use.

The piezoresistive microcantilevers (PMC) used for both the VX experiments were produced by Cantimer, Inc., Menlo Park, CA (Figure 1).

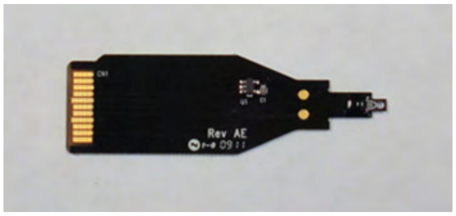

Figure 1. PMC die (far right) attached to a plastic circuit board for plug-in to a standard mini-SD connector

The microcantilevers, contained in a die, are approximately 200 microns in length and 40 microns wide. The nominal resistance of an unstrained cantilever is approximately 2.2 kΩ. Each cantilever extends into a small circular area on the die in order to contain the sensing material and also to partially protect the cantilever. In addition, each cantilever die also contains an integrated thermistor to correct temperature if needed. For the VX sensing experiments, a single-chip AD7793 24-bit analog-to-digital converter (ADC), which functions as a 6½ digit multimeter, was used to directly measure the cantilever resistance. The AD7793 chip was interfaced to a laptop computer through a USB interface provided by a USBmicro 421 chip. The user interface and data collection were performed on the laptop computer using LabVIEW. Experiments were performed in a chemical hood using a plexiglass test chamber with flow-monitoring capability (Figure 2).

Figure 2. Test chamber with LabVIEW interface to laptop computer

Discussion

Figure 3 shows the sensor response for a larger exposure (100 ppm) to the VX simulant, Malathion. Here, the test chamber was set up with a dry nitrogen flow at a rate of approximately 1 l/min. Liquid-form Malathion (0.5 ml) was then injected into the nitrogen flow line. The time of the Malathion injection is indicated in Figure 3 by the arrow. The Malathion exposure within the test chamber was simply the vapor from the evaporating Malathion as it flowed through the chamber. Based on the slow rate of evaporation of the Malathion liquid entering the test chamber, we estimate that the maximum sensor exposure experienced by the sensor was approximately 100 ppm. This 100 ppm exposure level was essentially continuous, and occurred throughout the time period indicated in Figure 3. Evaporation continued for many more minutes after data recording ended. The sensor response to the simulant occurred within a few seconds of initial exposure. Also, the sensor continued to react to the simulant for over 300 seconds after the first exposure. After approximately 350 seconds of exposure, the sensor began to saturate, indicating that no additional response to the Malathion was occurring.

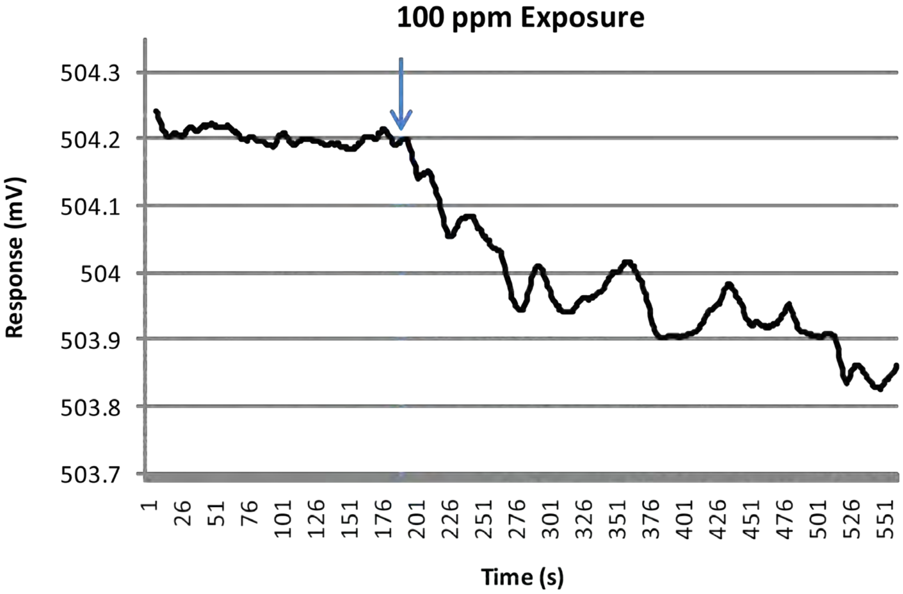

Figure 3. Sensor response to 100 ppm Malathion exposure. The Malathion detection occurred at about 180 seconds (blue arrow).

For the next exposure, the sensor was replaced with a new unit, and the dose of Malathion was reduced by a factor of 10. The corresponding vapor concentration is approximately 10 ppm throughout the course of the evaporation. The nitrogen flow conditions were unchanged. The time of Malathion injection is indicated by the arrow in Figure 4. At this low exposure level, the sensor response is seen to be near the background noise level of the sensor itself. We conclude that exposures at this very low level are generally difficult to detect with the current sensor configuration, although some response is indicated here. Future improvements to the current sensor configuration may be possible through lowered electronics noise levels or changes to the sensor itself, including different matrix/enzyme ratios. These changes and their results for very low exposure levels will be reported in a future publication.

These EPM sensors can also be submersed in liquids for detection of various analytes in water or other solvents. To test this capability, we immersed a new sensor in a beaker containing 250 ml of nanopure water. The sensor was allowed to come to equilibrium prior to addition of the VX simulant. After reaching equilibrium, Malathion was added to the water. The concentration of the Malathion in the water was 100 ppm. Here, the sensor response was rapid and immediate (Figure 5). The total sensor response is approximately 0.35 mV, indicating a large direct exposure when in aqueous environment, and rapid saturation.

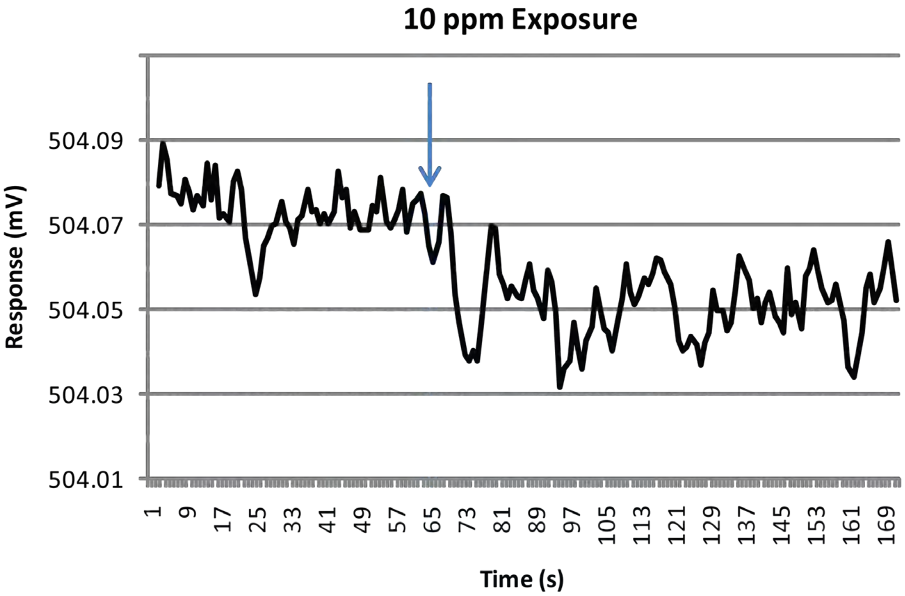

Figure 4. Sensor response to 10 ppm exposure to Malathion indicating that future experimentation should include optimization of the coating layer

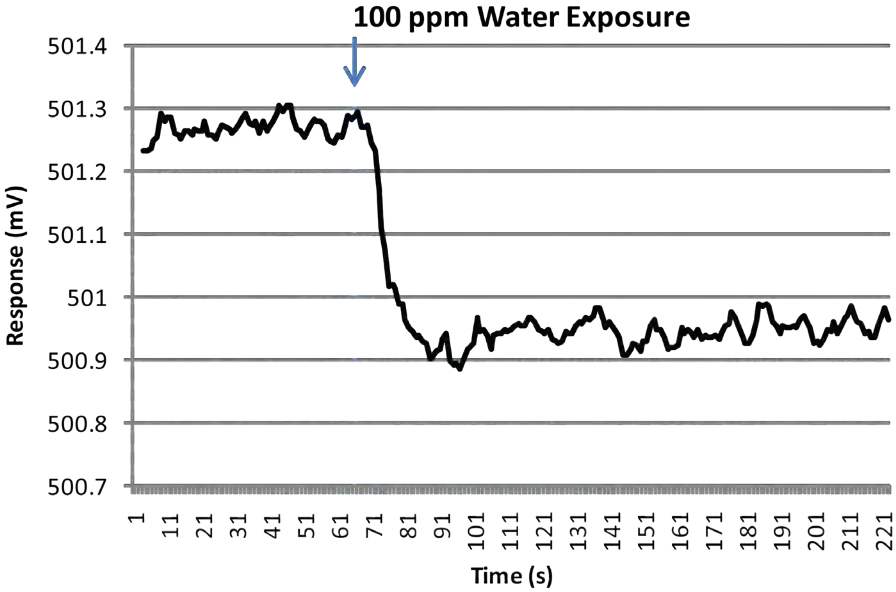

Figure 5. Sensor response to aqueous exposure to Malathion at 100 ppm, representing total sensor response of 0.35 mV, shows large direct exposure in an aqueos environment and rapid saturation

Miniaturization

A circuit board designed to operate with the EPM was miniaturized and fitted into an off-the-shelf container for portability. The team produced a schematic and verified that the circuit was operating properly. The circuit can be programmed to monitor several sensors (in this case a microcantilever and a thermistor), provide a visible or audible output, and store data to be read out later.

A miniaturized circuit board was produced from the original schematic. The layout consisted of four layers of circuitry with surface mount components. Figure 6 shows top and bottom views of the miniaturized board.

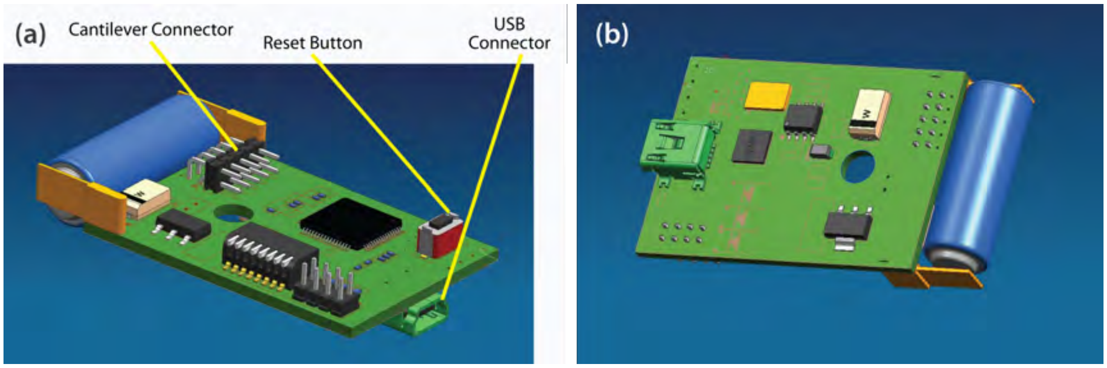

Figure 6. (a) Top and (b) bottom views of the miniaturized board. The connector for the cantilever and thermistor is next to the battery, which operates for about 45 minutes.

The connector for the cantilever and thermistor is next to the battery. A logic-reset button is next to the processor chip (MSC1211Y5). The processor chip contains four 16-bit ADCs that provide the data measurements required to run the microcantilever detector. The unit's battery (blue cylinder in Figure 6) is an A23 12 V battery. The green connector (Figure 6b at left) is a USB connector for computer communication. The board is 1.74 × 1.24 inches.

Option switches (piano-type switch in Figure 6a) provide for some fixed offsets, values, or reporting options to be selected as canned options. The software (from the original unit) runs in a terminal program and provides a means to set parameters for the ADCs in the processor.

An off-the-shelf enclosure (Figure 7) has been selected to house the circuit board, which can be carried on a person like a badge or placed in a remote location.

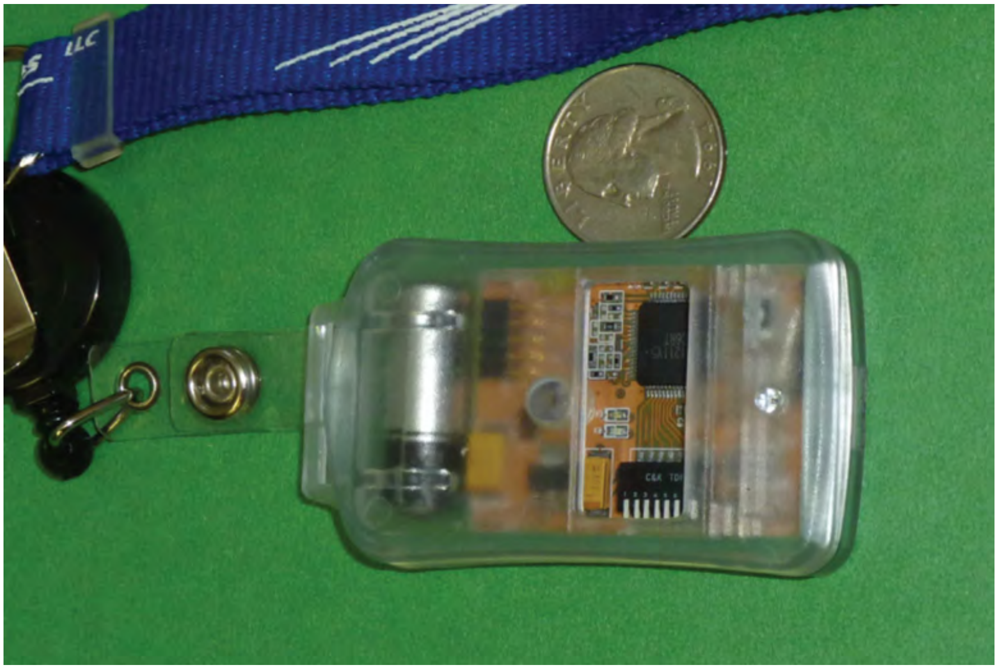

Figure 7. Handheld key fob enclosure

Conclusion

The sensor responses in vapor-like or aqueous environments indicate that this sensor material may be suitable for detecting gases such as VX as a chemical fuse, essentially for one-time use if on the order of 100 ppm. At these levels, the sensor essentially integrates the total exposure, eventually reaching saturation. At very low exposure levels, such as 10 ppm, the sensor response, in its current configuration, is near its detection limit. Future experiments would include studying improvements to the sensor electronics package, as well as different formulations to the sensing material itself.

The miniaturization process and packaging required sizable effort but yielded a compact, portable device with extended functionality. The miniaturized version operates for approximately 45 minutes on a battery, which is not acceptable for operation in the field. It was determined that some of the circuitry draws current unnecessarily and needs to be redesigned. The software from the original circuit was loaded into the miniature version producing the same results. A new program would enhance the capability and simplify operation, extending the life of the battery.

The miniaturized circuit functions properly. The programmability provides the versatility to expand its capabilities as a standalone system or an array of sensors with remote communication to a base station while maintaining the small physical footprint. A new processor chip has been found that has more processing power, is smaller, and requires less power to operate. A redesign with the new processor would increase our capability, dramatically improve battery life, and make the circuit board significantly smaller.

References

Gunter, R. L., W. G. Delinger, K. Manygoats, A. Kooser, T. L. Porter, "Viral detection using an embedded piezoresistive microcantilever sensor," *Sensors and Actuators (A)* **A107** (2003) 219–224.

Kooser, A., R. L. Gunter, W. D. Delinger, T. L. Porter, "Investigation of the antigen antibody reaction between anti-bovine serum albumin and bovine serum albumin using piezorsistive microcantilever sensors," *Biosensors and Bioelectronics* **19** (2003) 503–508.

Kooser, A., R. L. Gunter, W. D. Delinger, T. L. Porter, "Gas sensing using embedded piezoresistive microcantilever sensors," *Sensors and Actuators* **99**, 2-3 (2004) 430–433.

Porter, T. L., M. P. Eastman, C. Macomber, W. G. Delinger, R. Zhine, "An embedded polymer piezoresistive microcantilever sensor," *Ultramicroscopy* **97** (2003) 365–369.

Porter, T. L., T. L. Vail, M. P. Eastman, R. Stewart, J. Reed, R. Venedam, W. Delinger, "A solid-state sensor platform for the detection of hydrogen cyanide gas," *Sensors and Actuators (B)* **123**, 1 (2007) 313–317.

CODED APERTURE THERMAL NEUTRON IMAGING DIRECTIONAL DETECTOR

William Quam[1,a] and Harry McHugh[a]

With a radiation transport model of a gamma source, lead mask, and gamma detector array we sought to prove the utility of simulations of a simple coded-aperture geometry. The simulations, executed for a simple, planar, pixilated neutron aperture coupled to a multi-element neutron-detector array, were used to predict the utility of the technique if configured in a small-scale laboratory system. The model results guided the design of a laboratory system that was then tested with a ^{252}Cf neutron source. Tests of the neutron coded-aperture system yielded a minimum detectable neutron activity of 667 neutrons per second, a neutron source resolution sensitivity of about 0.1 cm at a distance of 100 cm from the source, and a gamma sensitivity of about 10^{-5} counts/gamma at the detector array.

Background

The coded-aperture design described in this report is intended to provide a relatively simple and compact hardware package that may be used to determine the position of a neutron source at a distance. The coded-aperture design was described by Fenimore (1978), Gottesman (1989), and Etzion (2009) and, for the present application, consists of an array of "pinholes" (the mask), an array of detectors, and a moderated ^{252}Cf source. One of the advantages of the coded-aperture detection approach is a reduction in off-axis background coupled with source localization. Both of these should improve the detection of the signal-to-noise (S/N) ratio. Originally we intended to use this coded-aperture technique with a planar boron-coated silicon (Si) diode array. The 90-pixel array finally provided by the Palo Alto Research Center (PARC) had a very poor S/N ratio due to the large diode capacitance inherent in the thin amorphous Si. Eventually a few of the diodes operated correctly, but not well enough to enable creation of an image. Thus, as a backup, we switched to ^{3}He tubes exposed end-on to simulate a pixelated array.

Project

Most of the work reported here was done at a source-to-detector distance of 100 cm. The mask was placed at 50 cm and was sized to enable illumination of an area somewhat larger than the detector array. The first elements of this work were done using an MCNP transport computer code, which enabled simulation of the detector responses due to various sources. The first simulation was done with 122 keV gammas, a lead mask, and a NaI scintillator array. This proved successful and

---

[1] quamwm@nv.doe.gov, 805-681-2465

[a] Special Technologies Laboratory

we proceeded to a ^{252}Cf neutron source, a cadmium (Cd) mask, and an array of ^{3}He proportional counters, the ultimate objective. The detector array and the masks used in the experiment are shown in Figures 1 and 2, respectively.

Figure 1. The 4 × 3 array of 2.5 × 3.8 cm ^{3}He tubes used in the experiments, viewed end on. The tube array is shielded by 0.1 cm thick Cd and 5 cm thick polyethylene. The numbers on the tube ends are part of the MCNP input data.

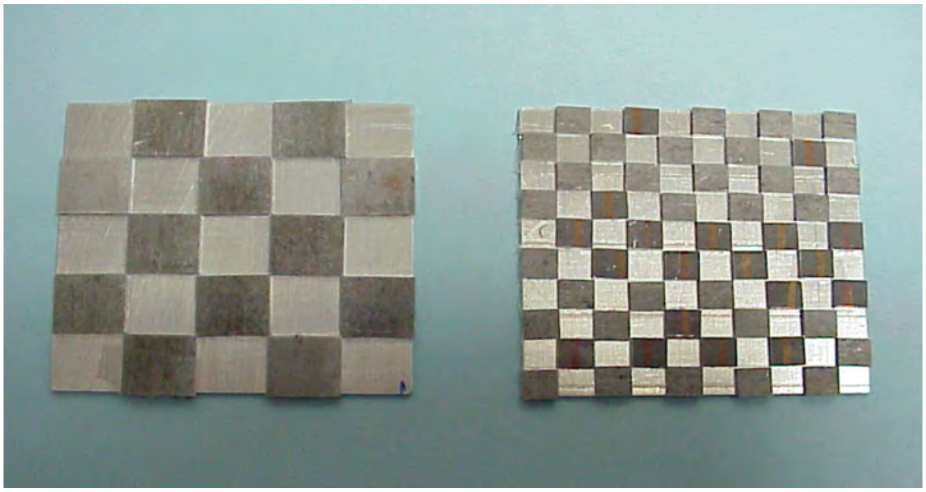

Figure 2. Two masks: a 5 × 5 (left) and a 10 × 10 (right) used in the experimental work

The ^{3}He tubes used were 2.5 × 3.8 × 28 cm and were placed end-on in a close-packed, rectangular array to minimize the detector area facing the source. The MCNP simulations suggested that Cd between the detector tubes in this array was not needed, but the simulations did show that a Cd and polyethylene shield around the whole array was needed to minimize room scatter.

Two masks were originally used with this array (see Figure 2). Each mask consists of an aluminum backing plate with Cd squares glued on the surface. These Cd squares and the open spaces adjacent to them are the actual mask components. In the 5 × 5 array, each pixel is 1.34 cm (horizontal) × 1.08 cm (vertical). In the 10 × 10 array, the pixel size is 0.648 × 0.544 cm. Each Cd square is 0.2 cm thick.

The devices shown in Figure 2 were placed one at a time into a square hole in a 50 cm square Cd sheet (0.1 cm thick) that served as a shadow shield. This shadow shield was located 50 cm from the source and hence 50 cm from the ^{3}He tube array.

Neutron Position Data

Initially we used MCNP to explore the proposed method. Because the aperture mask and the detectors are configured as arrays, we can process the data using the following matrix representation:

$$\mathbf{S} = \mathbf{AD}. \tag{1}$$

The array **S** is the measured data array, **A** is the mask (see Figure 2), and **D** is the desired image. The MATLAB convolution tool box used was *convn*, solving for the image **D** by inverting Equation 1.

An MCNP calculation processed in this way resulted in the image shown in Figure 3. The MCNP source position was x = –0.57, and y = –1.1. Figure 3a shows a maximum at this location. This maximum is also presented in Figure 3b as the dark red pixel displaced slightly down and to the right.

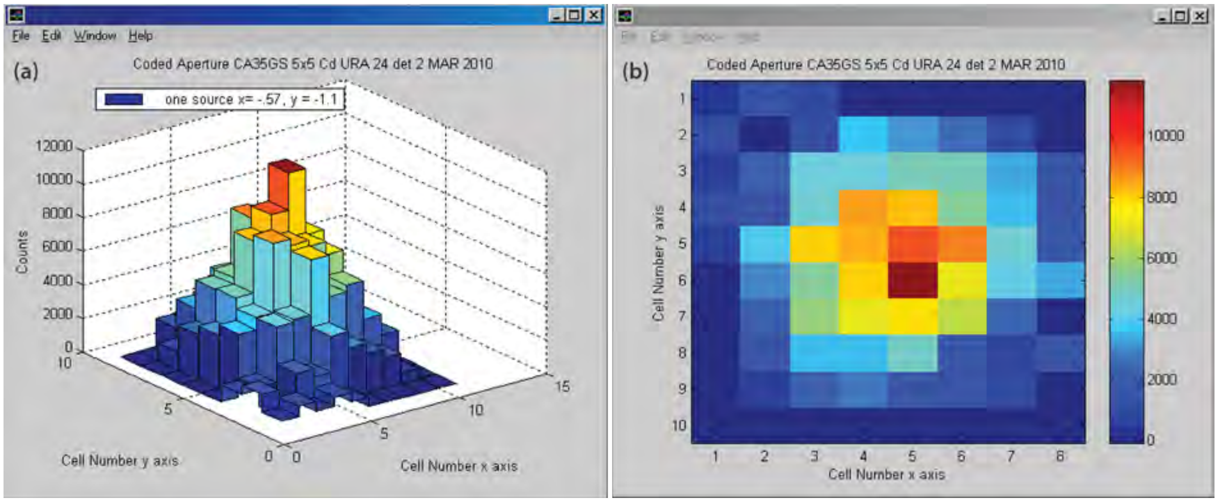

Figure 3. A 5 × 5 Cd aperture response from MCNP for the source at x = –0.57 and y = –1.1

This calculation also revealed the lack of cross-talk between the 12 detector tubes, perhaps due to self-shielding. These results encouraged us to undertake the experiments. We created an experimental arrangement in a small laboratory room.

We acquired data from a number of experimental runs and both masks using MATLAB as the matrix convolver. Figure 4 presents a sample of the acquired data convolved using MATLAB. The actual experimental data did not produce such a nice image, however, and a different analysis approach was used as described below.

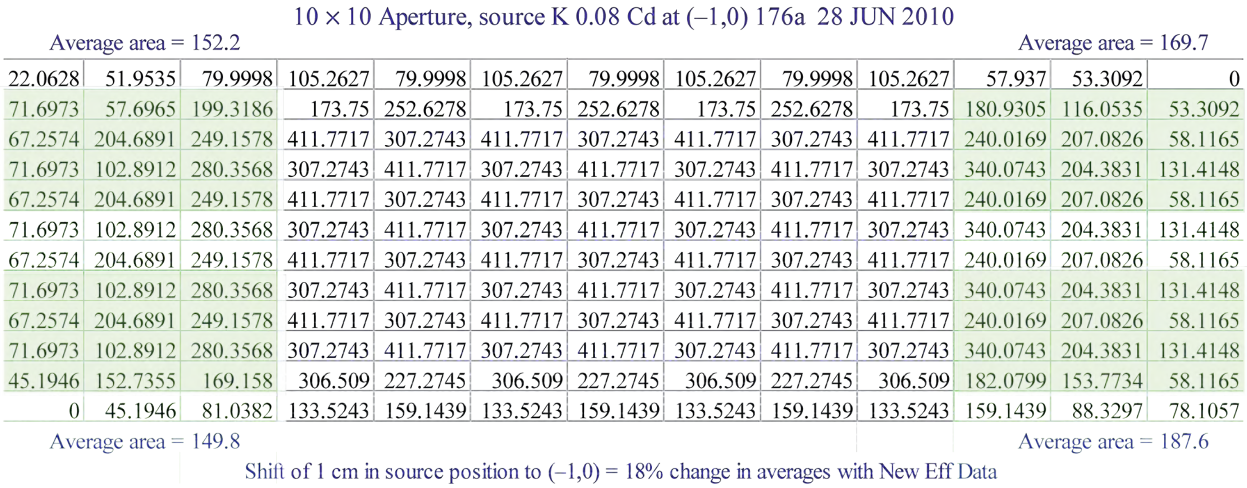

10 × 10 Aperture, source K 0.08 Cd at (–1,0) 176a 28 JUN 2010

Average area = 152.2

Average area = 169.7

22.0628	51.9535	79.9998	105.2627	79.9998	105.2627	79.9998	105.2627	79.9998	105.2627	57.937	53.3092	0
71.6973	57.6965	199.3186	173.75	252.6278	173.75	252.6278	173.75	252.6278	173.75	180.9305	116.0535	53.3092
67.2574	204.6891	249.1578	411.7717	307.2743	411.7717	307.2743	411.7717	307.2743	411.7717	240.0169	207.0826	58.1165
71.6973	102.8912	280.3568	307.2743	411.7717	307.2743	411.7717	307.2743	411.7717	307.2743	340.0743	204.3831	131.4148
67.2574	204.6891	249.1578	411.7717	307.2743	411.7717	307.2743	411.7717	307.2743	411.7717	240.0169	207.0826	58.1165
71.6973	102.8912	280.3568	307.2743	411.7717	307.2743	411.7717	307.2743	411.7717	307.2743	340.0743	204.3831	131.4148
67.2574	204.6891	249.1578	411.7717	307.2743	411.7717	307.2743	411.7717	307.2743	411.7717	240.0169	207.0826	58.1165
71.6973	102.8912	280.3568	307.2743	411.7717	307.2743	411.7717	307.2743	411.7717	307.2743	340.0743	204.3831	131.4148
67.2574	204.6891	249.1578	411.7717	307.2743	411.7717	307.2743	411.7717	307.2743	411.7717	240.0169	207.0826	58.1165
71.6973	102.8912	280.3568	307.2743	411.7717	307.2743	411.7717	307.2743	411.7717	307.2743	340.0743	204.3831	131.4148
45.1946	152.7355	169.158	306.509	227.2745	306.509	227.2745	306.509	227.2745	306.509	182.0799	153.7734	58.1165
0	45.1946	81.0382	133.5243	159.1439	133.5243	159.1439	133.5243	159.1439	133.5243	159.1439	88.3297	78.1057

Average area = 149.8

Average area = 187.6

Shift of 1 cm in source position to (–1,0) = 18% change in averages with New Eff Data

Figure 4. A sample of the MATLAB-convolved output from an experiment with the neutron source placed at x = 1 cm off axis. The shaded areas and their associated averages are used to quantify the source position.

Shown in Figure 4 in the shaded area at the left are the averages 152.2 and 149.8, and on the right are the averages 169.7 and 187.6. These shaded areas, for lack of a better word, are directly related to the experimentally determined counts and are a measure of the position of the displacement of the source. For example, when the right area increases, the left area decreases, indicating a source displacement to the right. Figure 5 shows the displacement data.

The four shaded areas illustrated in Figure 4 enable one to estimate the shift in the position of the overall data, in this case for a source movement from 0 to 1 cm. In this example, an 18% shift in these areas (on the MATLAB–convolved output) compared to the same analysis at a source location at the center line is seen. This process was repeated at source locations from 0 to 5 cm with the results shown in Figures 5 and 6.

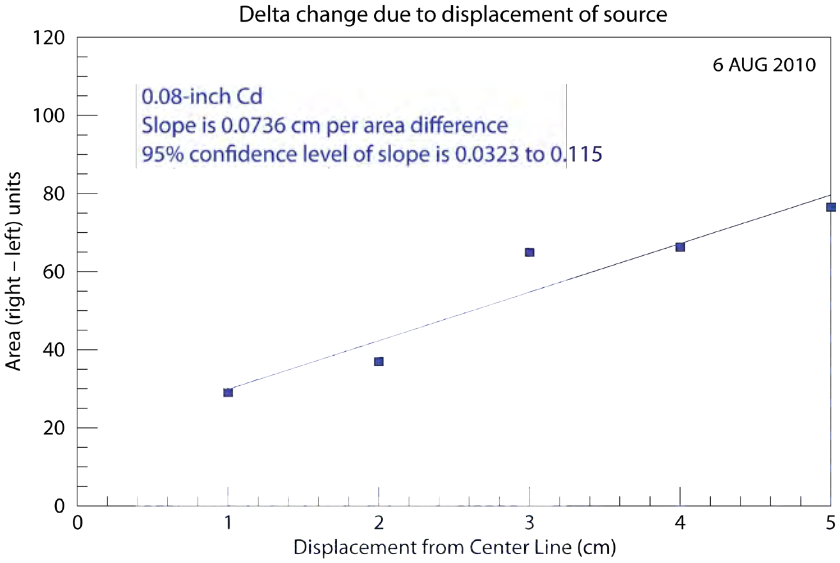

Figure 5. Plot illustrating the difference between left and right areas as the neutron source is moved off axis

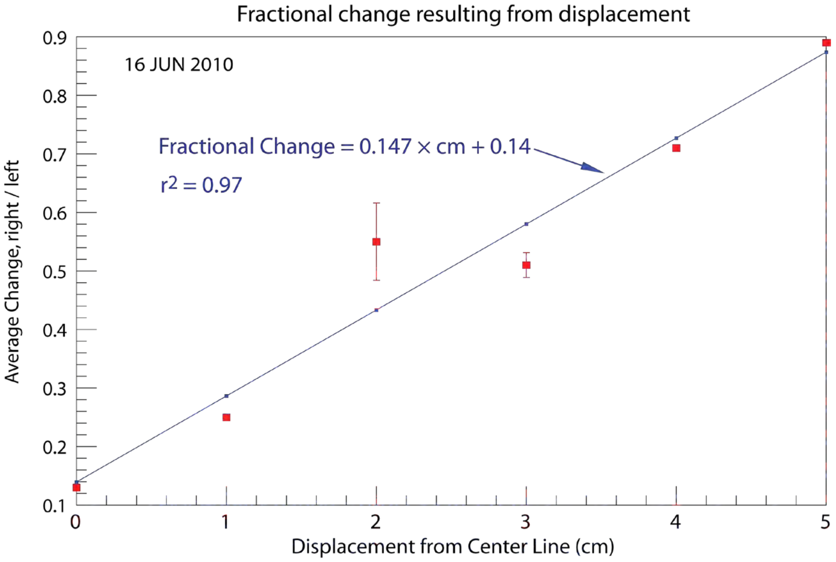

Figure 6. Fractional change in the right and left areas as the source is moved off axis

In Figure 5 the data for five source positions (from 0 to 5 cm displacement) show a slope of 0.0736 cm/area difference, where the distance in cm refers to the source displacement on the x-axis. The area difference is the term used to quantify the array counts, after convolution with the antimask, at the edges of the final image. As such, we would claim that the coded aperture used here has a spatial resolution of approximately ±0.07 cm at 100 cm (the source-to-detector array distance).

Figure 6 presents a different view of the data after convolution, using fractional change in counts relative to the zero position. This type of analysis suggests that the ratio of areas delivers a spatial resolution of approximately ±0.15 cm at the 100 cm source-to-detector distance.

Gamma Sensitivity of the Neutron Detectors

The gamma sensitivity of the ^{3}He tubes was expected to be small. It was measured to be 8.64×10^{-6} c/γ incident on the detector face using a ^{57}Co source (122 keV). The ^{252}Cf source gamma emission rate was 4.03×10^{4} γ/h incident upon this same detector face (sum for gammas less than 1 MeV) (Prince, 1969). This predicts that the detector sensitivity to Cf gammas is about 0.348 counts per hour (c/h). This sensitivity is small compared to the hundreds of counts per hour due to the neutrons. Even the cosmic ray–induced neutron counting rate, approximately 22 c/h, exceeds this gamma signal by a large factor. We conclude that source gammas are not a significant part of the data collected.

Neutron Sensitivity of the Coded Aperture

The coded-aperture system, consisting of a detector array and the coded aperture, sits in a small room in an industrial-type building. The detector array itself is surrounded by a side shield of 2 in. thick polyethylene lined with Cd on its interior. The end of the detector array views the source location and is centered on the experimental axis. The neutron sensitivity estimate is therefore relative to the environment that exists in this room.

To best determine the coded-aperture neutron sensitivity, we created a series of exposures that were used to subtract out the various background effects (see Table 1). The term (0,0) is the x, y location of the Cf source (i.e., it is centered on the experimental axis). The column of "Net" values is that with background subtracted, as described below.

The frame is a large (50 cm square, 0.1 cm thick) Cd sheet, with a cutout on the experimental center line. This cutout can contain one of the following configurations: (1) a solid Cd sheet (0.1 cm thick), (2) a Cd 10 × 10 coded aperture in place of the solid Cd sheet, or (3) no Cd sheet nor coded aperture. In Configuration 4, the frame itself is removed, leaving just the Cf source in its poly moderator at (0,0). In Configuration 5, the poly moderator around the Cf source is removed. In Configuration 6, the Cf source is removed.

Table 1. Neutron sensitivity estimation data

#	Configuration	Ave Gross c/h*	Ave Net c/h*
1	Cf in poly moderator at (0,0) + frame + Cd in aperture	526.4	0
2	Cf in poly moderator at (0,0) + frame + mask	590.8	64.4
3	Cf in poly moderator at (0,0) + frame	638.3	111.9
4	Cf in poly moderator at (0,0)	817.4	291
5	Cf bare (no poly moderator) at (0,0)	364	-
6	No Cf	21.69	-

*Count averages are over all detectors.

Configuration 1 shows that a Cd sheet in place of the coded-aperture array yields an average array counting rate over all detectors of 526.4 c/h. We take this as background, composed of room scatter and whatever transmission occurs.

In Configuration 2, we replaced the blocking Cd sheet with the 10 × 10 coded-aperture mask. This is the usual configuration used to acquire data. The net c/h = 590.8 – 526.4 = 64.4.

In Configuration 3, we have the expected neutron counting rate through the frame opening without either the Cd blocking sheet or the coded-aperture mask. This rate is the maximum counting rate expected. Thus, the coded-aperture detection efficiency is 64.4 / 111.9 = 0.58 for a Cf source in a 6 cm diameter polyethylene moderator (the poly moderator has a 2.54 cm wall thickness) at 100 cm from the source center to the face of the detector array.

Note that removing the frame in Configuration 4 yields a much higher counting rate, which is composed of direct and room-scattered (and moderated) neutrons. Configuration 5, compared to Configuration 4, shows that the moderator increases the ^{3}He counting efficiency as it should. Finally, Configuration 6 is the cosmic ray–produced neutron contribution to the array counting rate, which should be constant for all four experiments noted above.

The conclusion is that the coded-aperture counting efficiency for a moderated Cf source is about 58% in the experimental room for a source at 100 cm. Note that this room is fairly small and has some scattering materials (a thin concrete floor and gypsum walls) that add significantly to the background.

Minimum Detectable Neutron Activity

The minimum detectable activity (MDA) is usually defined as the source strength (for example, Ci or n/s) that is equal to three (or more) times the standard deviation of the background of the detector. In the present case the source yields approximately 59 c/h average for the 12 detectors before convolution. This is approximately 13 σ above the normal average background (see Table 1, Configuration 6) of the array, so the MDA for the ^{252}Cf source in a 2.54 cm thick polyethylene moderator is 3/13 × 2890 = 667 n/s at 100 cm, where 2890 is the Cf source spontaneous fission emission rate. (Note that this is for a nominal 1-hour counting time calculated from 24 hours of data.)

Conclusion

The simple coded aperture made of small Cd pieces together with an array of rectangular ^{3}He tubes has a spatial resolution range of approximately ±0.07 to ±0.14 cm for neutron detection at a distance of 100 cm from a ^{252}Cf source moderated with 2.54 cm of polyethylene. The overall neutron sensitivity is 58% for a ^{252}Cf source in a 6 cm diameter polyethylene moderator at a distance of 100 cm. The MDA is greater than 600 n/s for a ^{252}Cf source surrounded by 2.54 cm of polyethylene at a distance of 100 cm for a 1-hour collection time.

Acknowledgments

Robert Vogel designed and tested the ^{3}He detector electronics, and Ron Justin created the data collection program.

References

Etzion, T., "Sequence folding, lattice tiling, and multidimensional coding," Cornell University Library article arXiv:0911.1745v1 online, http://arxiv.org/abs/0911.1745 (November 2009) 1–21, accessed December 1, 2009.

Fenimore, E. E., T. M. Cannon, "Coded aperture imaging with uniformly redundant arrays," *Appl. Opt.* **17**, 3 (1978) 337–347.

Gottesman, S. R., E. E. Fenimore, "New family of binary arrays for coded aperture imaging," *Appl. Opt.* **28**, 20 (1989) 4344–4352.

Prince, J., "Nuclear and physical properties of Cf-252," *Proceedings of a Symposium on Californium-252*, USAEC Report CONF-681032 (1969) 48.

MICROCANTILEVER-ENABLED NEUTRON DETECTION

Kevin R. Kyle,[1,a] Timothy L. Porter,[b] Michael J. Mendez,[a] and Richard J. Venedam[c]

A new concept for neutron radiation detection was demonstrated using piezoresistive microcantilevers as the active sensing element. Microcantilevers were used to measure the tiny volumetric changes in a sensing material upon absorption of neutron radiation and transmutation into a new element. Highly ordered inorganic crystalline lattices of boron-rich materials dispersed in polymeric rubber matrices were shown to act as volumetric neutron transducers.

Background

The principal means of detecting the thermal neutron signature of fissile nuclear materials is a helium-3 (^{3}He) gas detector, wherein absorption of neutrons forms charged particles that are then detected as a current in a gas-filled tube. This isotope of helium has a small natural abundance on earth, 1.38×10^{-4}% (Friedlander, 1981). The main source of ^{3}He for neutron detectors has been from the beta particle decay of tritium (^{3}H), which at one time was manufactured in quantity for use in nuclear weapons. However, production of ^{3}H in the United States ceased in 1988 (U.S. Nuclear Regulatory Commission, 2009). With the current need for neutron detectors to detect and deter the smuggling of nuclear materials through ports and other border entry points into the United States, it is estimated that the demand for ^{3}He is 10 times the current worldwide supply (Wald, 2009). However, plans to deploy neutron detectors to points of entry into the United States have halted, as viable alternatives to ^{3}He neutron detectors are currently unavailable (Snider, 2010).

Project

Boron-10 (^{10}B) has a neutron absorption cross section (3838 barns) comparable to that of ^{3}He (5330 barns) (Friedlander, 1981). And, the natural abundance of ^{10}B (19.8%) is nearly six orders of magnitude greater than that of ^{3}He, making it an attractive alternative to ^{3}He. The absorption of thermal neutrons by ^{10}B produces a lithium atom (^{6}Li, with energy of 0.84 MeV) and an alpha particle (α, 1.47 MeV). Gas-tube neutron detectors based on the gaseous boron compound BF_3 exist and operate on a principle similar to that of a ^{3}He detector. Solid boron materials have been used as moderators and absorbers of neutrons in reactors, as well as shielding in other neutron-producing devices. The use of solid, condensed-phase materials rich in boron (greater than 50% by weight) for use as the active neutron absorber is attractive due to their greater density (neutron absorber per unit area), their chemical inertness, and their cheap commercial abundance over gas-phase materials.

---

[1] kylekr@nv.doe.gov, 805-681-2283

[a] Special Technologies Laboratory; [b] University of Nevada, Las Vegas, and Sencor Scientific; [c] North Las Vegas

Prior work has shown that solid materials consisting of highly ordered boron-rich lattices undergo morphological changes upon neutron irradiation (Koval'chenko, 1966; Ogorodnikov, 1969; Shikama, 1991; Froment, 1992). Changes in volume, hardness, and physical integrity (fissuring) have been attributed to both the transmutation of boron atoms in a rigid lattice into lithium ions, which disrupts the chemical bonding and charge balance of the material, and the accumulation of helium within voids in the material. Additionally, lattice damage and concomitant material volume change occur due to the passage of these energetic ions through the material. The goal of this project was to exploit this neutron-induced volume change as a means of neutron detection. The means of transduction of this volume change into an easily detectable electronic response is a microcantilever.

Microcantilever-based sensors may operate as static coated devices, vibrating cantilever devices, contact-mode devices, or embedded sensors (Porter, 2003). Both piezoelectric (actively driven) and piezoresistive (passive readout) cantilevers have been demonstrated in various chemical-sensing applications. Embedded piezoresistive microcantilever (EPM) sensors provide a simple, low-cost, and effective platform for the detection of analytes (Porter, 2003; Kooser, 2004; Porter, 2007; Venedam, 2009). In the EPM sensor, a piezoresistive microcantilever is embedded or partially embedded into a sensing material. An embedded microcantilever is in contact with a much greater volume of sensing material compared to a microcantilever sensor based on a thin coating on the cantilever itself. This is important in radiation sensing because it provides a much greater interaction volume for the radiation to be detected. The sensing material can be a polymer, composite polymer, or inorganic material that acts as a probe for the desired analyte. Upon analyte exposure, reactions within the sensor probe material result in a volumetric change, which is measured as a resistance change within the piezoresistive microcantilever due to a change in bending strain. This volumetric shift in the sensing material may be due to diffusion of the analyte into the sensing material, probe-target binding on the material surface or in the bulk, or surface or bulk chemical reactions between the analyte and sensing material. The latter interaction is representative of radiation sensing, wherein ions produced in the sensing material result in molar volume changes due to the bond breaking in the crystalline lattice structure, electronic repulsions, and lattice damage due to deposition of excess energy. Any swelling or contraction of the material in contact with the cantilever tip results in an immediate, easily measurable change in the cantilever channel resistance. This change is in linear proportion to the amount of the material swelling; therefore, a simple ohmmeter circuit is sufficient to record the sensing activity. Cantilever strains of only a few angstroms are measurable. The simplicity of the EPM readout circuitry allows for small size and long-life battery operation.

Sencor Scientific was contracted to supply the microcantilever sensors utilized in this project. The microcantilevers, contained in a die, are approximately 200 microns long and 40 microns wide (Figure 1a). The nominal resistance of an unstrained cantilever is approximately 2.2 kΩ. Each cantilever extends into a small circular area on the die in order to contain the sensing material. The sensing material was applied as a bead of organic liquid solution onto the die; the resulting polymeric drop coated the microcantilever (Figure 1b). In addition, each cantilever die also contains an integrated thermistor if temperature correction is needed. The entire cantilever was packaged on a printed circuit board with a mini-SD-type connector (Figure 2). For the neutron detection experiments, an Agilent 34410A 6½ digit datalogging multimeter was used to directly measure the cantilever or thermistor resistance as a function of time.

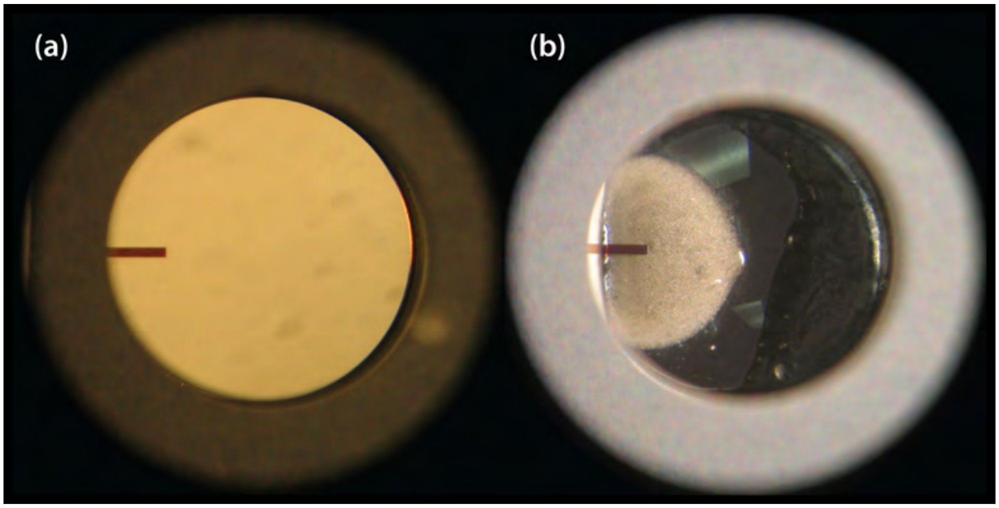

Figure 1. (a) Bare microcantilever in a round metal die; (b) microcantilever embedded in a dispersion of $^{11}B_4C$ in polydimethylsiloxane (PDMS)

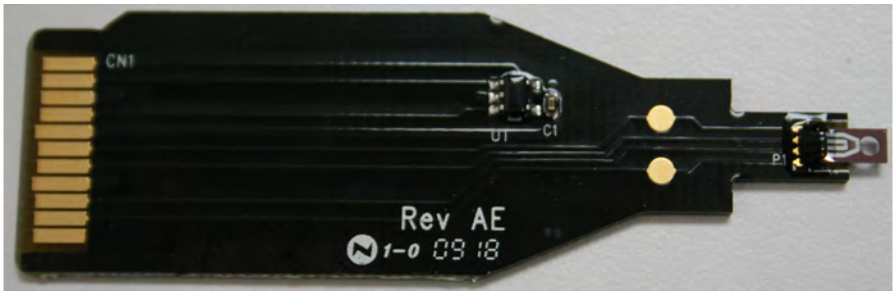

Figure 2. Fully assembled microcantilever with a standard SD connector

The criteria used for selecting boron materials were (1) a high (>50%) boron content for efficient neutron absorption; (2) a rigid, highly ordered crystal structure; (3) low-cost commercial availability; and (4) low chemical reactivity. The metal hexaborides were prime candidates. Calcium and lanthanum hexaboride (MB_6, M = Ca, La) are available from Aldrich Chemical as natural abundance boron (19.8% ^{10}B, 90.2% ^{11}B), fine-mesh crystalline powders. These compounds consist of highly ordered covalently bonded octahedra of B_6^{-2} linked in a three-dimensional (3-D) network via B-B bonds, with the metal counter-ion located at the octahedral center of symmetry (Lundström, 1985). Prior work on neutron irradiation of these metal borides demonstrated the large degree of physical change induced by the transmutation of boron into lithium and α, wherein expansion of physical dimensions, fissuring, hardness, and changes in chemical bonding as reflected in x-ray diffraction patterns were reported (Koval'chenko,1966; Ogorodnikov, 1969; Shikama, 1991). Natural-abundance boron nitride (BN) was also used due to its ubiquitous low-cost commercial availability.

Boron compounds enriched as either ^{10}B or ^{11}B were procured from Ceradyne Boron Products, LLC. Enrichment in these isotopes allows the decoupling of neutron-induced effects (in the ^{10}B) from background effects such as temperature and gamma-ray interactions, owing to the negligible neutron absorption by the ^{11}B isotope (0.005 barns). Because the isotope-enriched metal hexaborides were unavailable, boron carbide (B_4C) was purchased as both the 96% ^{10}B and 99+% ^{11}B forms. B_4C also fit the selection criteria, consisting of well-ordered icosahedra of B_{12} covalently bonded to three carbons, and linked in a 3-D network via B-B and B-C-B bonds (Thévenot, 1990). Prior work on neutron irradiation of B_4C demonstrated the large degree of physical change induced by neutron absorption (due to trapping of ^4He) and scission of B-C-B bonds (Froment, 1992; Simeone, 2000).

Coupling of the solid borides to the microcantilevers was accomplished via dispersion in a polymer rubber matrix, either polydimethylsiloxane (PDMS) or tert-butyl (*t*Bu) rubber. Dispersions were prepared by dissolving the polymer in toluene or trichloroethylene, and adding 25 to 30 weight percent of the boride.

Neutron irradiations were performed using a californium-252 (^{252}Cf) neutron source. As the average neutron energy of this source is 2.1 MeV, a 1 inch thick, high-density polyethylene (HDPE) moderator was used to thermalize the neutrons (0.025 eV). The experimental setup is shown in Figure 3.

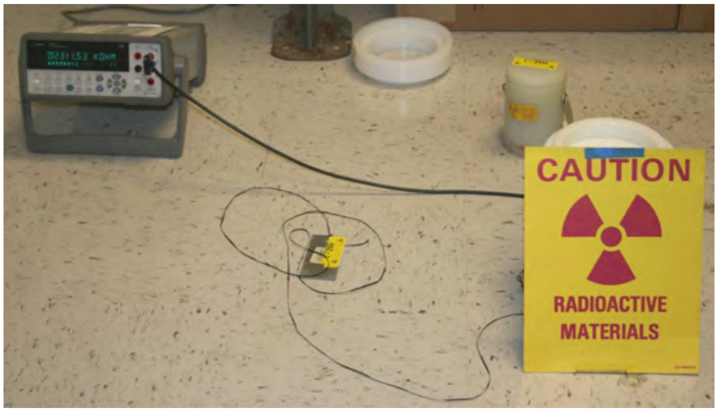

Figure 3. Experimental neutron setup. The ^{252}Cf source was placed outside of the HDPE enclosure. The EPM detectors were placed inside the enclosure. The HDPE functioned as a neutron energy moderator.

The ^{252}Cf was placed outside of a 1-inch-thick HDPE cylinder. The microcantilevers (up to three at a time) were placed on the inner wall of the cylinder for exposure to thermal neutrons. The microcantilever resistance was logged every five minutes using the Agilent datalogging multimeter. The neutron flux was measured by the gold foil technique, wherein a gold foil (sensitive to all neutrons) or a cadmium-shielded gold foil (epithermal neutrons only) was activated by neutron absorption, and the gamma counts were measured with a cooled germanium detector. The thermal neutron flux, calculated by subtracting the epithermal flux from the total flux, was measured to be 5.7 neutrons per cm^{2}s. This number translates to roughly 0.25 neutrons per second at the microcantilever, a number lower by three orders of magnitude than expected for this experiment. The consequence of the low neutron flux was null results in the chemical and physical characterizations of the effect of neutron absorption on our candidate materials. It also greatly enhanced the effect of the temperature background relative to the neutron effect. Figure 4 shows the effect of temperature on a bare microcantilever over time. The microcantilever response correlates very well with the measured response on the built-in thermistor.

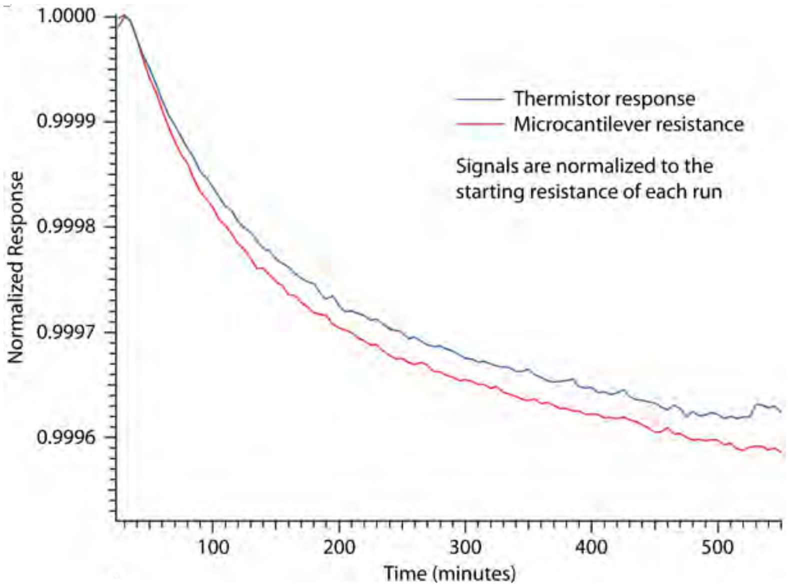

Figure 4. Temperature response of a microcantilever device as measured by microcantilever resistance and on-board thermistor response shows the effect of temperature on the piezoresistance of the device

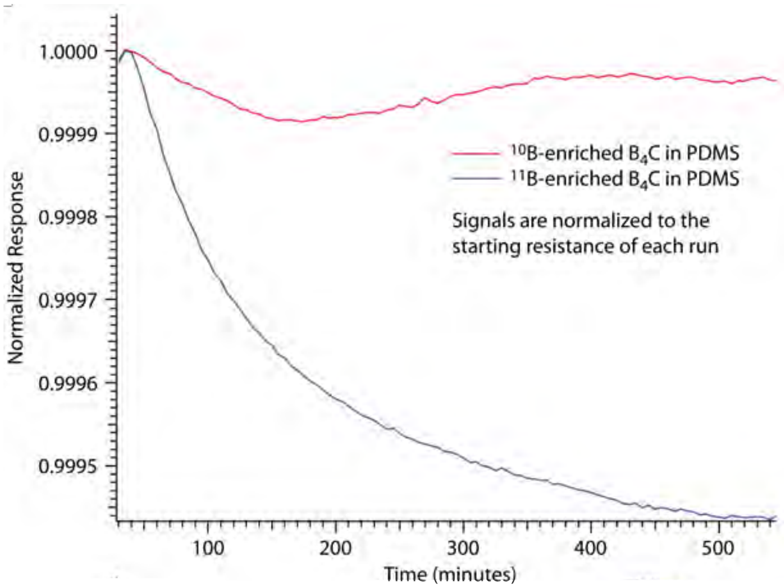

Figure 5. Response of ^{10}B and ^{11}B boron carbide microcantilever devices to neutron irradiation indicates that the device is responsive to neutron absorption (^{10}B) independent of the temperature effect (^{11}B)

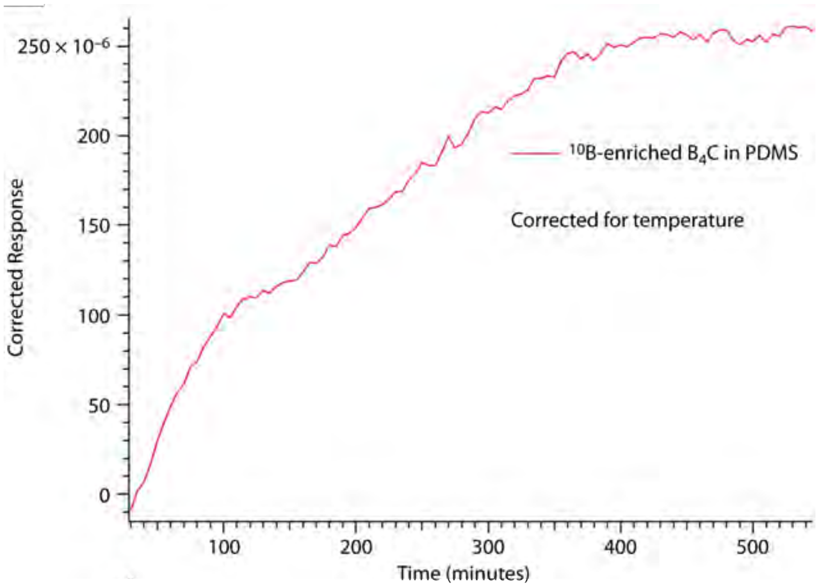

Figure 6. Response of ^{10}B boron carbide PDMS microcantilever devices to neutron irradiation, corrected for temperature, shows that the piezoresistance of the device increases as a result of neutron absorption over time

The effect of neutron absorption on the microcantilevers can be seen in the comparison between $^{10}B_4C$ and $^{11}B_4C$ in PDMS shown in Figure 5. The ^{11}B trace is due solely to temperature drift in the neutron irradiation setup. The ^{10}B trace exhibits a response that is counter to the downward temperature drift. The response due to neutron absorption is shown as a positive response when corrected for temperature as shown in Figure 6. Similarly, the response of boron lanthanum (LaB_6) in *t*Bu gives an increase in microcantilever resistance under neutron irradiation when corrected for temperature, as shown in Figure 7. Additional sensors tested included CaB_6 in *t*Bu, CaB_6 in PDMS, and BN in PDMS. An increase in microcantilever resistance as a function of neutron irradiation was noted for each of these sensors. While the low neutron flux did not allow a more quantitative analysis due to the much greater temperature effect, the data do show that the detection of neutrons by mechanical transduction using microcantilevers is a feasible means of detecting and measuring thermal neutrons.

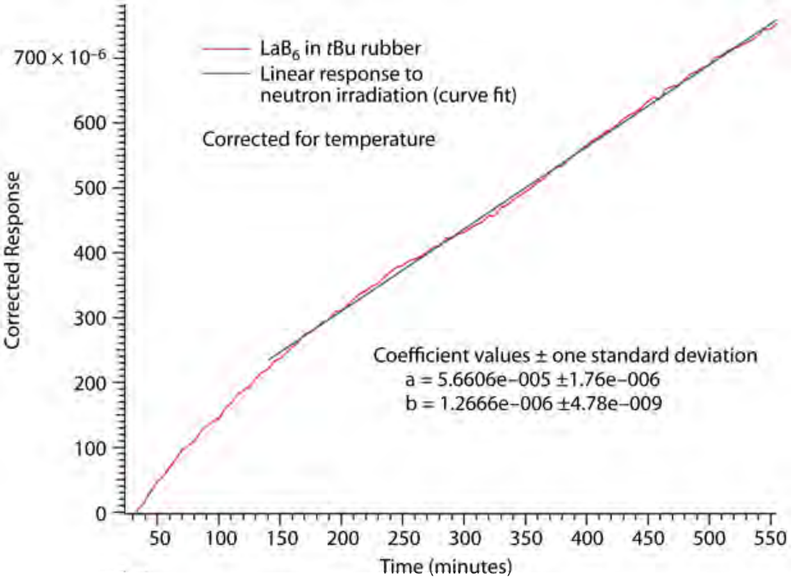

Figure 7. Response of natural abundance LaB_6 *t*Bu rubber microcantilever device to neutron irradiation, which shows an increase in piezoresistance as a result of neutron absorption over time

Conclusion

A mechanical means of neutron detection was successfully demonstrated. Piezoresistive microcantilevers were shown to function as a means of detecting the change in volume in a boron-rich crystalline inorganic material upon absorption of a neutron and transmutation into a lithium ion and alpha particle. The microcantilever resistance proved to be sensitive to temperature, requiring temperature monitoring during the neutron absorption experiment and data correction afterward. Further research is required to quantify and calibrate the effect. Additional experiments with a higher-flux neutron source would allow the origin and magnitudes of the neutron-induced volume changes to be measured. Finally, research toward a reversible neutron transducer would allow the use of the microcantilever system as a reusable neutron detector.

Acknowledgments

We acknowledge the invaluable support provided by Dr. Timothy Porter's teams at the University of Nevada, Las Vegas; Northern Arizona University; and Sencor Scientific.

References

Friedlander, G., J. W. Kennedy, E. S. Macias, J. M. Miller, *Nuclear and Radiochemistry,* 3rd edition, John Wiley & Sons, New York, 1981, 270–272.

Froment, K., D. Gosset, M. Guéry, B. Kryger, C. Verdeau, "Neutron irradiation effects in boron carbides: Evolution of microstructure and thermal properties," *J. Nucl. Mater.* **188** (1992) 185–188.

Kooser, A., R. L. Gunter, W. G. Delinger, T. L. Porter, M. P. Eastman, "Gas sensing using embedded piezoresistive microcantilever sensors," *Sensors and Actuators B: Chemical* **99**, 2–3 (2004) 474–479.

Koval'chenko, M. S., V. V. Ogorodnikov, A. G. Krainii, "Effect of neutron irradiation on the structure and properties of lanthanum hexaboride," *At. Energ.* **21**, 6 (1966) 1168–1174.

Lundström, T., "Structure, defects, and properties of some refractory borides," *Pure and Applied Chemistry* **57**, 10 (1985) 1383–1390.

Ogorodnikov, V. V., M. S. Koval'chenko, A. G. Krainii, "Effect of neutron irradiation on the electrical resistance and color of high-melting compounds," *Powder Metallurgy and Ceramic* **8**, 5 (1969) 411–414.

Porter, T. L., M. P. Eastman, C. Macomber, W. G. Delinger, R. Zhine, "An embedded polymer piezoresistive microcantilever sensor," *Ultramicroscopy* **97**, 1–4 (2003) 365–369.

Porter, T. L., T. L. Vail, M. P. Eastman, R. Stewart, J. Reed, R. J. Venedam, W. Delinger, "A solid-state sensor platform for the detection of hydrogen cyanide gas," *Sensors and Actuators B: Chemical* **123**, 1 (2007) 313–317.

Shikama, T., H. Kayano, "Structural changes of deposited $Ti_{1-x}B_x$ films due to neutron irradiation," *J. Nucl. Mater.* **179–181**, 1 (1991) 465–468.

Simeone, D., C. Mallet, P. Dubuisson, G. Baldinozzi, C. Gervais, J. Maquet, "Study of boron carbide evolution under neutron irradiation by Raman spectroscopy," *J. Nucl. Mater.* **277**, 1 (2000) 1–10.

Snider, A. D., "Subcommittee Investigates the Shrinking Global Supply of Helium-3," House Committee on Science and Technology, http://science.house.gov/press/PRArticle.aspx?NewsID=2805, accessed June 24, 2010.

Thévenot, F., "Boron carbide—A comprehensive review," *Journal of the European Ceramic Society* **6**, 4 (1990) 205–225.

U.S. Nuclear Regulatory Commission, "Fact sheet on tritium production," http://www.nrc.gov/reading-rm/doc-collections/fact-sheets/tritium.html, accessed November 17, 2009.

Venedam, R. J., "Detection of chlorine gas," *Nevada Test Site–Directed Research and Development,* FY 2008, National Security Technologies, LLC, Las Vegas, Nevada, 2009, 185–190.

Wald, M. L., "Shortage slows a program to detect nuclear bombs," *The New York Times,* http://www.nytimes.com/2009/11/23/us/23helium.html?_r=2&partner=rss&emc=rss, accessed December 8, 2009.

this page intentionally left blank

COMPUTATIONAL SCIENCES

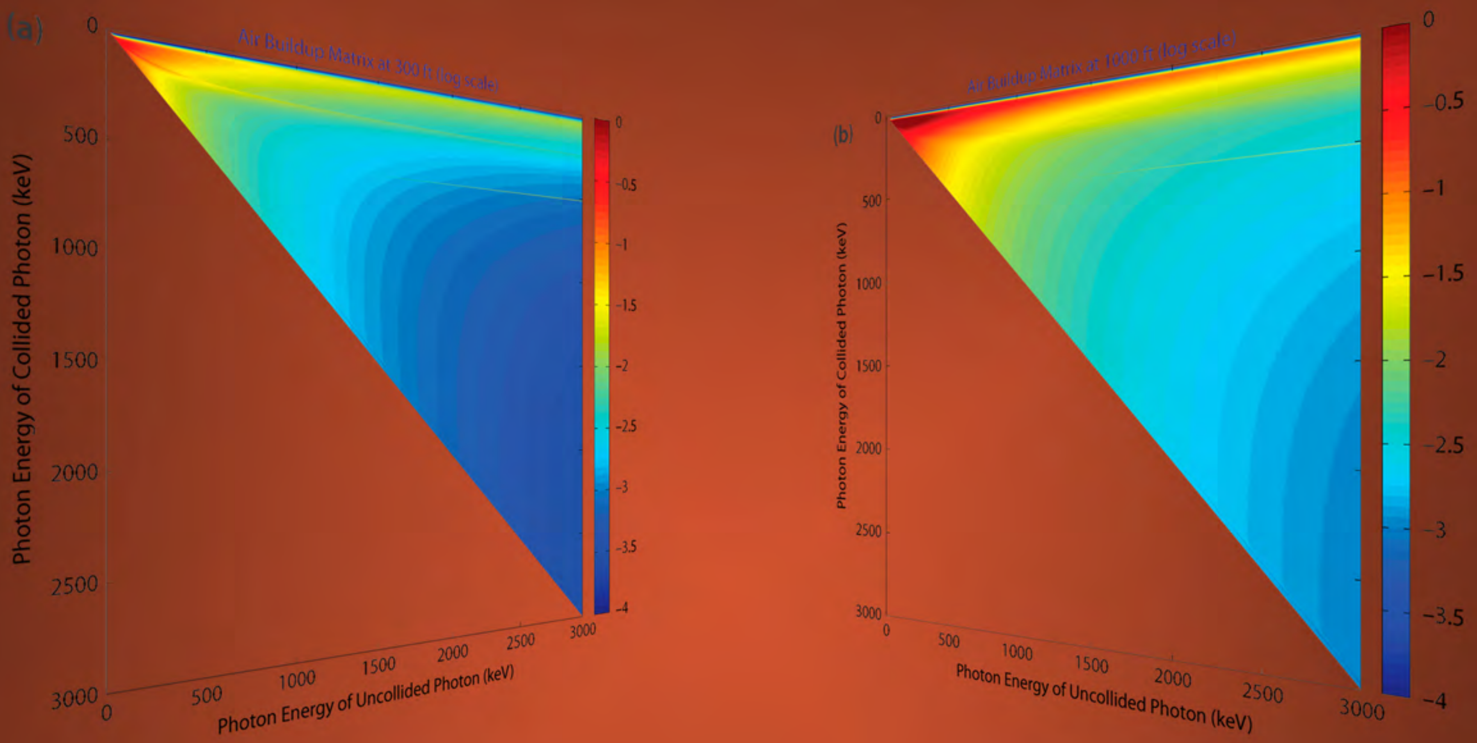

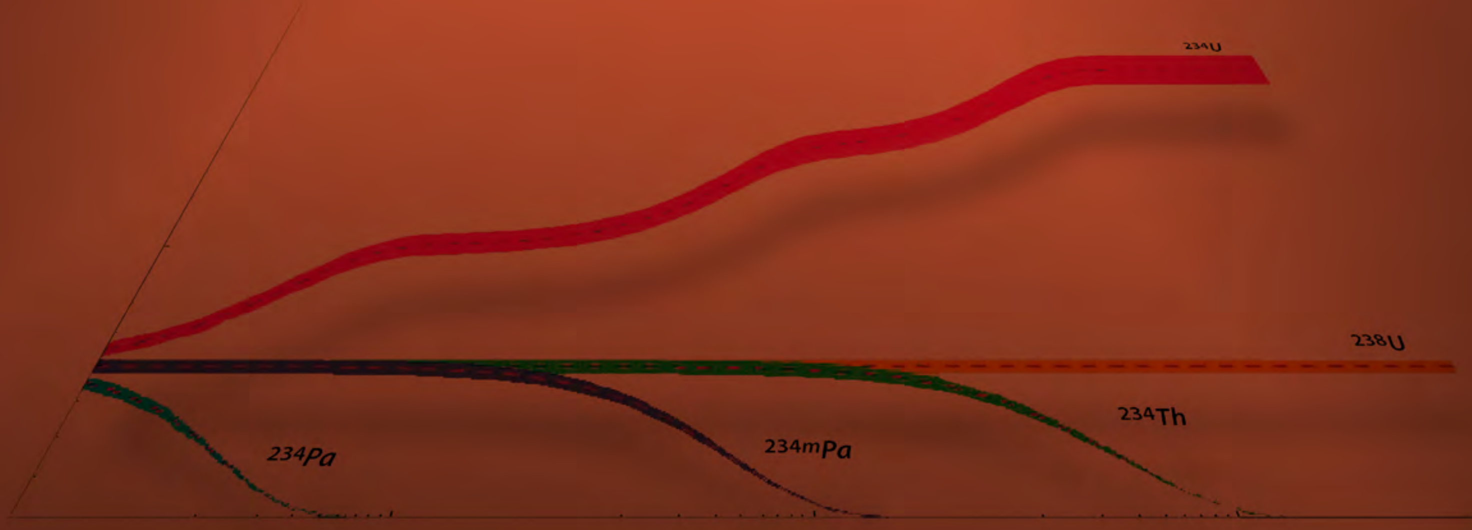

DENSITY FUNCTIONAL THEORY COMPUTATIONS FOR URANIUM CHEMISTRY

Rusty Trainham[1,a] *and Manuel J. Manard*[a]

Calculations of density functional theory have been applied to hexavalent uranium in solution to investigate solvation properties on optical activity. Our results suggest that the dramatic effect of pH on optical properties is probably a chemical effect, and not a physical perturbation of molecular structure. Calculations of the tetravalent molecules uranium dioxide and plutonium dioxide have been attempted with mixed success. For isolated tetravalent molecules, the calculations fail to break axial rotational symmetry, so condensation into solid-phase bent molecules presumably does not occur by simple crystallization, but rather is driven by a chemical reaction. Calculations of the solid-state structure of alpha-phase uranium metal have also been attempted, but the initial calculations were not able to reproduce the correct lattice symmetry or the lattice distortion caused by a charge density wave.

Background

Our previous report (Trainham, 2010) discussed the application of density functional theory (DFT) to the optical structure of the hexavalent uranyl radical UO_2^{++}. Those calculations were restricted to the isolated gas-phase uranyl radical, with and without ligands coordinated in the equatorial plane. We found that our calculations were in reasonable agreement with experimental results. This project investigated the effects of solvation on the uranyl radical by enclosing it in a water "box." Using the NWChem software package (NWChem, 2010), we determined the number of molecules and their locations for successive layers of water encasing the UO_2^{++} radical, and found that two solvation layers largely explain the perturbative effects.

The neutral tetravalent UO_2 molecule superficially looks to be quite similar to the doubly charged hexavalent UO_2^{++} uranyl radical. With ligands bound to the uranyl radical, the charge difference is eliminated, and the bond lengths to the ligands are significantly greater than the UO bond lengths, so the ligands act as perturbations. Thus, one could inquire why the two species are so different. The hexavalent radical is highly water soluble, yet the tetravalent molecule is insoluble. The hexavalent strongly luminesces in the green, whereas the tetravalent species is black.

The obvious differences between the two structures are that the UO bonds are double bonds for tetravalent uranium, and triple bonds for hexavalent uranium. Also, the tetravalent molecule is in a $^3\Phi_u$ ground state, and the hexavalent molecule is in a $^1\Sigma_g$ ground state. For otherwise very similar molecules, these differences are profound, so one might wonder why both states are stable in nature.

---

[1] trainhcp@nv.doe.gov, 805-681-2248

[a] Special Technologies Laboratory

In fact, the tetravalent state is the more stable species, and hexavalent uranium does eventually convert to the tetravalent form. The changes in structure are quite different, and, consequently, the rates of conversion are slow, so a variety of intermediate compounds are routinely present in the environment.

DFT originated as a discipline for ab initio molecular structure calculations, but the power of the technique lent itself readily to solid-state structure calculations. The essential extra element was to impose periodic boundary conditions on unit cell structures. Another aid was to implement the calculations in reciprocal (i.e., momentum) space in the Brillouin zone rather than in the Wigner-Seitz cell. We began our solid-state structure calculations of uranium compounds using the ABINIT code (ABINIT, 2010), and here we report results on alpha-phase uranium metal. Alpha uranium is a solid that is reasonably well understood and has a very unusual feature of lattice distortion due to a charge density wave (Lander, 1994).

Project

Solvation Structure

Experimentally, solvation and pH have dramatic effects on the optical absorption and emission properties of hexavalent uranium. Coordinated water molecules around the UO_2^{++} radical act as a perturbation on the optically active UO bonds. The coordination draws electron density away from the UO bonds, causing the bonds to lengthen. We have calculated a series of water molecule bondings to the UO_2^{++} radical, and have determined that the first hydration cell consists of five water molecules located in the equatorial plane (see Figure 1). We find that the UO bond increases in length by about 2.3% to 1.75 Å. The second layer consists of 10 water molecules, so the complete first and second solvation layers sum to 15 water molecules (see Figure 2). The final UO bond length is 1.76 Å. Additional coordinated water molecules have little effect on the uranyl radical; thus, a water box of 15 molecules largely isolates the uranyl radical from further perturbations.

Our calculations of the water solvation did not account for pH, which means that our calculations are essentially for uranyl dissolved in a solution of pH 14. pH is the negative logarithm of free proton (or of hydronium ions, H_3O^+) molar concentration in solution. One might be tempted to incorporate protons or hydronium ions into the water box, but with a water box consisting of merely 15 molecules, the resulting pH from a single replacement would be driven to 1. The perturbative effect of the ion would depend on whether it is in the first or second layer of the water box, and close proximity of a positive ion would likely provoke a chemical reaction. Given the isolating nature of the water box, intermediate pH values would be difficult to calculate. Therefore, a more likely explanation of the pH effect on the absorption and emission of uranyl in solution is the driving of chemical reactions. Experimentally, it is found that in acidic solutions the uranyl radical tends to be free, and in basic solutions the uranyl radical tends to be bound to carbonates or other ligands (Gabriel, 2001).

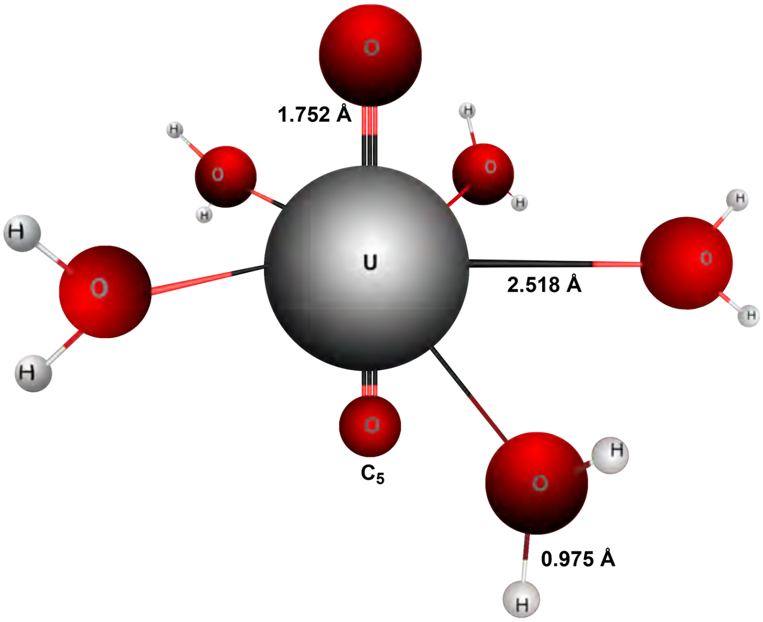

Figure 1. The hexavalent uranyl radical, UO_2^{++}, enclosed within the first solvation shell of five water molecules. The UO bond length has been stretched from 1.71 Å to 1.75 Å. The water ligation has also stretched the OH bond in the water molecules from 0.96 Å to 0.97 Å. The equatorial bond length from the uranyl radical to the water molecules is 2.52 Å.

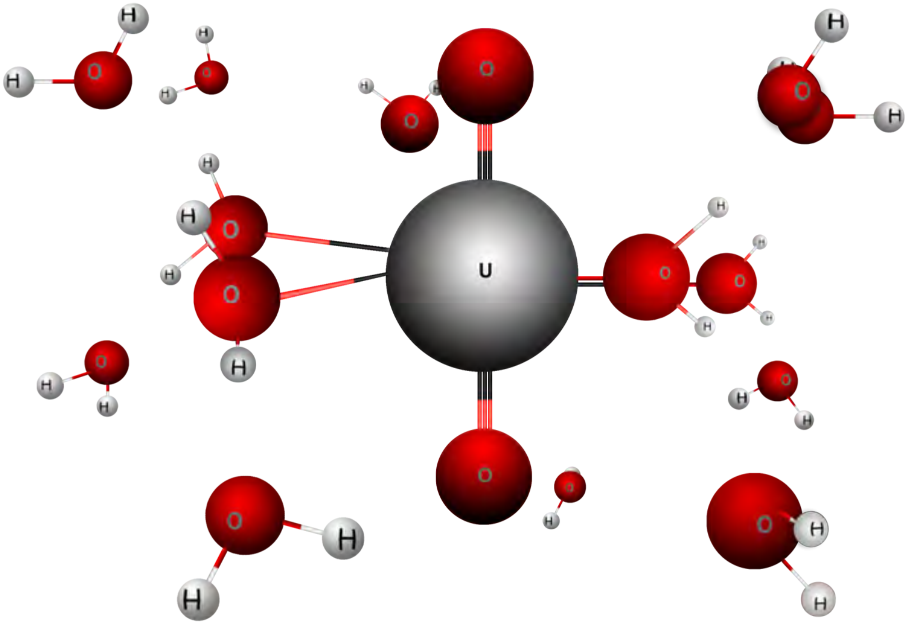

Figure 2. The 15-molecule water box enclosing the uranyl radical constitutes two solvation layers. Our calculations suggest that two layers are predominantly responsible for the perturbation structure. A third layer has negligible added effect on the structure and spectra of the radical. Note that one molecule in the first solvation layer is hidden behind the uranium.

Tetravalent Uranium and Plutonium

Two commonly studied dioxide molecules are CO_2, which is a linear molecule, and SO_2, which is a bent molecule. The hexavalent uranyl radical UO_2^{++} and the tetravalent UO_2 are two different dioxides with identical atomic constituents but different ground-state configurations. One may wonder whether one or both of these molecules are bent like SO_2 or straight like CO_2, and to what extent the ground-state configuration affects the geometry. There is considerable hybridization of the 5f and 6d orbitals in the uranium valence shell, so one might expect the molecule to be bent. Our previous DFT calculations (Trainham, 2010) confirmed that the hexavalent UO_2^{++} is a linear molecule and that ligand coordination occurs in the equatorial plane. Tetravalent UO_2 crystallizes into face-centered cubic (fcc) structure in the solid state, however, so one might reasonably expect UO_2 to be a bent molecule. Our calculations indicate, nevertheless, that UO_2 in the gas phase is a linear molecule, has a triplet ground state, with double UO bonds, and a UO bond length of 1.86 Å. The ground-state configuration appears to be $^3\Phi_u$.

The calculations for plutonium dioxide (PuO_2) yield similar results. PuO_2 is a linear molecule, with a triplet ground state, double bonds, and a bond length of 1.87 Å. Comparison to experimental results has been problematic because all of the literature that we have found documents oxides in the solid state. As the bonds in fcc solids are bent, it would appear that our calculations of a linear UO_2 and PuO_2 are for species that are rare in nature. Because a transition from a linear molecule in the gas phase to a bent molecule in the solid state requires bond breakage, recoordination, and passage over an energy barrier, we tentatively conclude that formation of UO_2 into the solid state probably does not occur by simple crystallization, but rather by precipitation from other parent molecules driven by a chemical reaction.

Alpha-Phase Uranium Metal

Metals tend to form crystals in one of three close-packed arrangements: fcc, body-centered cubic, or hexagonal close packing. In metals, the valence electrons are completely delocalized, and the residual atomic cores are centrosymmetric closed shells, so metallic crystallization is essentially a case of packing spherical marbles. Alpha-phase uranium metal, however, is unusual in that the 5f electrons are not buried in the atomic core, and they are strongly correlated. Thus, the uranium atomic core is not spherical, which means that uranium is a case of close packing of ellipsoids, not spheres. Rather than forming an fcc lattice, similar to aluminum, the uranium unit cell is stretched and compressed into a face-centered orthorhombic cell (see Figure 3). Additionally, because of the high degree of electron correlations, a charge density wave forms in the crystal that pushes some of the atoms off lattice sites (Lander, 1994).

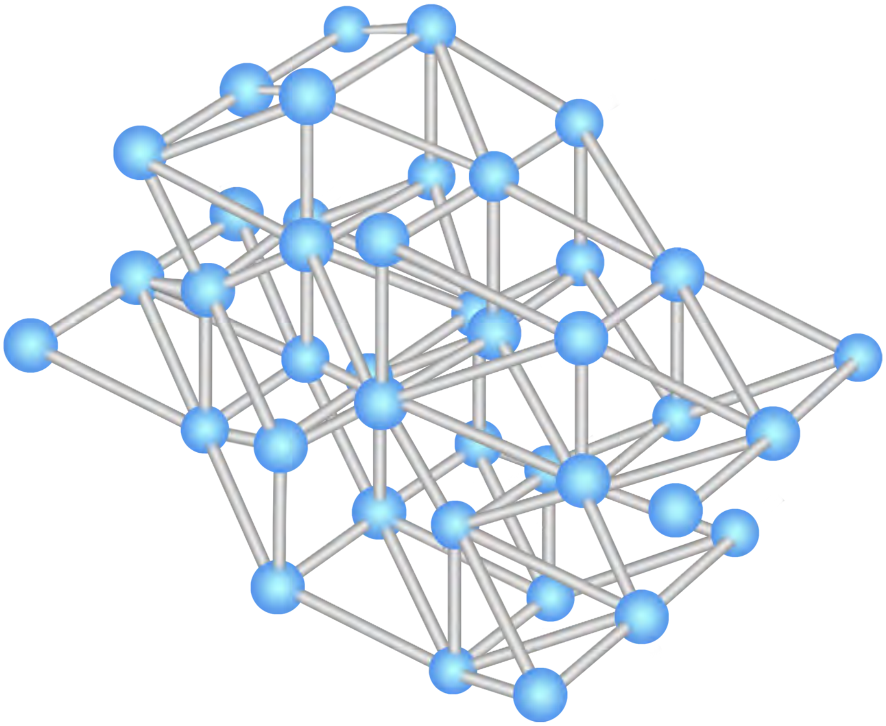

Figure 3. Crystalline structure of alpha-phase uranium. The unit cell is a face-centered orthorhombic.

We have attempted several solid-state calculations of alpha-phase uranium using the ABINIT code (ABINIT, 2010) but have found the results to be extremely difficult to interpret or to visualize. The test cases of Al and Si work as expected with reasonable results. Both of these test cases are fcc solids, so they are reasonable starting points for attempting the α-U calculation. For the fcc unit cell, the three lengths of the unit cell are the same. For face-centered orthorhombic, the basic structure is the same, but the three lengths of the unit cell are all different. Our first attempt to calculate α-U was to construct an Al lattice with the Al replaced by U. The DFT code was allowed to relax the cell structure to search the minimum energy state. The outcome of that series of calculations was a different overall cell size, but the fcc symmetry remained intact. We are, as yet, unsure if we properly instructed the code to allow symmetry breaking to deviate from fcc when performing the cell relaxation. Our second attempt was to define a Wigner-Seitz unit cell, but we are unsure if we properly coded the cell into the ABINIT input file. Unfortunately, ABINIT does not readily export its geometries to standard molecular viewing file formats. We did find a code called V_Sim (V_Sim, 2010) that claims to be able to use ABINIT as a preprocessor for viewing ABINIT input geometries. However, we were unable to successfully compile the code with the ABINIT feature enabled, although it did compile and run successfully without the ABINIT switch enabled.

Conclusion

We have applied DFT calculations to uranium compounds to investigate the solvation properties of the hexavalent uranyl radical UO_2^{++}, the tetravalent electronic structures of UO_2 and PuO_2, and the solid-state structure of alpha-phase uranium metal. The calculations have been of mixed success. The solvation results seem reasonable. The calculations for oxides are tentative, and the calculations of solid alpha-phase uranium are clearly incorrect, although the ABINIT code does a good job of calculating Al and Si. The handling of electron correlations is probably where the code is breaking down on the solids calculations, but operator error cannot be dismissed. We require further experience in calculating and interpreting results of uranium solids before reaching further conclusions. We have found that interpreting the DFT calculations can be very challenging, and that it is quite easy to perform errant calculations. In our opinion, DFT will always require a high degree of physical and chemical insight to properly interpret calculations and to cull out unphysical results. DFT is not, and probably will never be, a calculational black box.

References

ABINIT (software), http://www.abinit.org, accessed September 30, 2010.

Gabriel, U., L. Charlet, C. W. Schläpfer, J. C. Vial, A. Brachmann, G. Geipel, "Uranyl surface speciation on silica particles studied by time-resolved laser-induced fluorescence spectroscopy," *Journal of Colloid and Interface Science* **239**, 2 (2001) 358–368.

Lander, G. H., E. S. Fisher, S. D. Bader, "The solid-state properties of uranium: A historical perspective and review," *Adv. Phys.* **43**, 1 (1994) 1–111.

NWChem (software), http://www.newchem-sw.org, accessed September 30, 2010.

Trainham, R., M. Manard, "Density functional theory computations for uranium chemistry," *Nevada Test Site–Directed Research and Development*, FY 2009, National Security Technologies, LLC, Las Vegas, Nevada, 2010, 157–163.

V_Sim (software), http://inac.cea.fr/L_Sim/V_Sim/index.en.html, accessed September 30, 2010.

Deterministic Transport for Quantification of AMS Data Products

Michael Reed[1,a]

The goal of this project was to determine whether modern particle transport capabilities and processing power in conjunction with formalized inverse techniques could advance the state of the art with regard to quantification of aerial measurement system data products. An algorithm capturing the dominant photon transport mechanisms was designed, and test problems were run. The techniques provide the basis to convert measured count rates at altitude to quantitative data products. The methods perform well within the relevant parameter space, and the work appears to have many programmatic applications in remote sensing.

Background

The aerial measurement system (AMS) deploys large sodium iodide (NaI)-based detection systems over regions of radiological contamination and provides insight into the characteristics of that contamination. The predominant data products provided by the AMS include either the gross count-rate response or some scalar multiple of that value (Kiser, 2010). Although careful experimental measurements may be used to inform the derivation of such multiplicative constants, these methods tend to be more qualitative in nature than a true quantitative result such as μCi, μCi/m^2, or μR/hr (Kiser, 2010). Most importantly, such an experimental approach requires careful ground-truth measurement and allows for very little extrapolation to other scenarios. The primary objective of this work is a proof-of-principle illustrating that theoretical methods, in conjunction with careful experimental benchmarking, can significantly advance the degree of quantification that is possible within AMS data products.

Project

Photon Transport Model

Modern transport codes based on either Monte Carlo models or discrete ordinate methods solve the forward radiation transport problem whereby a user specifies information about radiation sources and the medium surrounding them, and the code returns information about the distribution of particles throughout the domain. For this work we chose to use a simplified treatment in which the fundamental phenomenon is captured by a model that is both computationally efficient and easy to use. The basic equation modeling photon transport that was used for this work is:

$$\underline{D} = \int_{t_{acq}} dt \int_{space} dA \sum_{\text{detectors}} \sum_{\substack{\text{detector}\\ \text{faces}}} \underline{\underline{R}}\left[\underline{\underline{B}}\left(S\eta_g \underline{Y} \otimes p_s\right)\right]. \tag{1}$$

---

[1] reedms@nv.doe.gov, 702-295-8695

[a] Remote Sensing Laboratory–Nellis

Here $\underline{D}$ gives the expected count rate in each channel of a 1024-channel spectrometer calibrated to 3 keV/ch. This spectrum is obtained by performing a temporal integration over the expected count rate as a function of time. The source contributions are obtained by integrating over a collection of point sources or, in the general case, a deposition pattern. In this equation $\underline{Y}$ represents a photon yield vector giving the expected number of photons emitted with energies characteristic of each of the 1024-channel energy discretization. The p_s vector gives the uncollided survival probability that a photon in each energy bin travels without collision through a given thickness of air. The $\otimes$ operator denotes element-wise multiplication between the uncollided survival probability and yield vectors. The geometric efficiency is a scalar quantity denoted η_g that represents the probability that a source photon is emitted in a direction that would ultimately cause it to strike the face of a detector. More specifically, the geometric efficiency is the fraction of the solid angle subtended by a detector face in relation to a point source lying on the ground. The source strength is denoted as S and gives the total decay rate for a point source or the decay rate density in space for a generalized planar deposition. The $\underline{\underline{B}}$ term refers to a 1024 × 1024 upper-triangular buildup matrix that converts uncollided response to total response. The $\underline{\underline{R}}$ appearing in Equation 1 is a scintillator response function that maps spectral photon incidence on a detector face into the detector's observed spectra. The response function is a 1024 × 1024 matrix described in detail in a previous work (Reed, 2010).

Although all arguments within Equation 1 have been suppressed for simplicity, this method is in general a hybrid method that treats different aspects of the problem with varying fidelity. More specifically, the geometric efficiency is treated without approximation as fully four-dimensional in space and time. The yield vector represents isotope decay data, and the response matrix is discrete with respect to each detector/face pair. The uncollided survival probability and the buildup matrix are treated as one-dimensional functions of the air thickness present between the detector and source. For typical AMS aircraft operating characteristics, this has proven to be a reasonable approximation given careful construction of those terms.

Buildup Matrix Construction

The complexity of the photon transport problem is hidden in the two matrices appearing in Equation 1. The construction of the response matrix and the intricacies associated with its interpretation were performed under an FY 2009 SDRD project (Reed, 2010). A major portion of the current work concerned the construction of buildup matrices. The motivation behind the buildup matrix can be understood by considering it as a generalization of the typical scalar-valued buildup factor tabulated many times in health physics literature (Turner, 2007). The generalization is that the matrix accounts for buildup for each initial photon energy to each down-scattered energy. The buildup matrix may therefore be thought of as mapping uncollided photon fluence to total photon fluence:

$$\underline{\phi} = \underline{\phi}_{unc} + \underline{\phi}_{col} = \underline{\underline{B}} * \underline{\phi}_{unc}. \tag{2}$$

Here the total fluence present at a point in space is denoted as $\underline{\phi}$ and is decomposed into contributions from particles that have incurred collision $\left(\underline{\phi}_{col}\right)$ and particles that have not $\left(\underline{\phi}_{unc}\right)$. The uncollided contribution may be computed with very little approximation from the so-called point-source kernel. A buildup matrix computed for a certain air thickness must be upper triangular with ones along the main diagonal. This result follows by noting that in the regimes of interest photons may not up-scatter in energy. Photon scattering from one energy bin into the same energy bin is ignored but is also essentially impossible. Coherent scattering is not considered because there is no loss of energy associated with this event.

To understand the form of the buildup matrix, it is instructive to consider a simple case in which 663 keV photons are emitted from the center of an infinite medium of air. If the photon fluence present on the surface of an imaginary sphere positioned at some distance away from the point source was measured, it would be composed of both collided and uncollided photons. As the radius of the imaginary shell is increased, the relative contribution from scattered photons increases. If this photon fluence was measured and scaled such that the uncollided fluence was unity, one would obtain a single column of the buildup matrix. For a 663 keV photon, this would be column 222 of the buildup matrix associated with some air thickness.

Obviously the simple experiment described above could be repeated 1024 times to obtain a complete buildup matrix representing the spectral buildup for photons in the range of 0 to 3 MeV for a single air thickness matrix. Repeating this at many altitudes and interpolating could theoretically give a scheme for determining an appropriate buildup table for any air thickness. For this work a set of MCNP runs were performed to simulate these experiments. Approximately 15 buildup matrices were constructed at discrete air thicknesses ranging from 1 to 1000 m. Three different geometries were considered: an infinite medium of air, a finite spherical medium of air, and a one-dimensional average, implementing a juxtaposed set of ground/air hemispheres. These simulations represent approximately 50,000 MCNP runs. Using the 15 discrete buildup matrices, a nonlinear fit was performed in order to obtain an interpolation for any thickness. Of the several types of fits used, a four-parameter log-normal fit performed best. By individually fitting every entry in the buildup matrix versus air thickness, the 15 discrete matrices were fit to a matrix-valued, log-normal fit with three coefficient matrices. This equation has the form:

$$\underline{\underline{B}}(x) = \underline{\underline{A}}\exp\left(\frac{\ln^2\left(x/\underline{\underline{B}}\right)}{\underline{\underline{C}}}\right). \tag{3}$$

The three coefficient matrices $\underline{\underline{A}}$, $\underline{\underline{B}}$, and, $\underline{\underline{C}}$ are used in conjunction with the air thickness x in order to construct a buildup matrix at that thickness. A colorized depiction of response matrices is given in Figure 1. The matrices are upper triangular and indicate increased buildup with air thickness and increased buildup for lower photon energies at the same thickness. The matrices denote the presence of the air-scatter peak at 80 keV and the annihilation peak at 511 keV for energetically possible scenarios. Note that for the 1000-foot case the channel-wise buildup actually exceeds unity in the air-scatter peak.

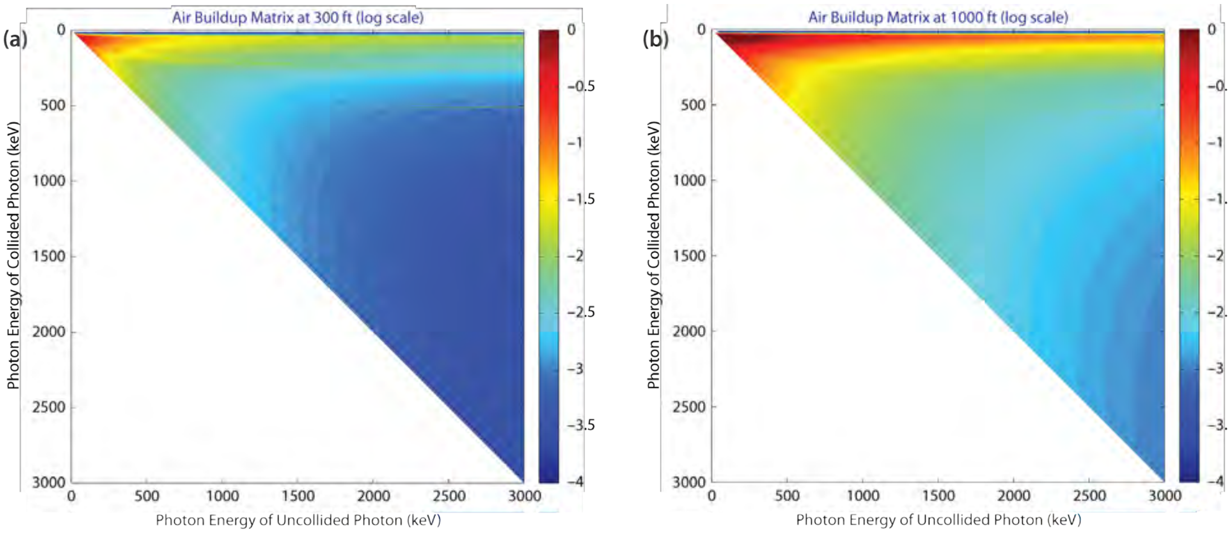

Figure 1. Representation of air buildup matrix evaluated at (a) 300 ft and (b) 1000 ft (log scale, uncollided normalized)

By parameterizing the aircraft position as a function of time and considering straight-line passes of an aircraft over a source, it is possible to use Equation 1 to generate the mean value of the spectra observed by a detection system as it passes over a source. If the source strength is modeled as either a point or an infinite planar distribution, then the source strength appearing in Equation 1 is a constant and may be determined via inversion. Likewise, if this equation is normalized to unit source strength, the result gives a formula for the spectral sensitivity of the detection system:

$$\left.\frac{\underline{D}}{S}\right|_{ch_L}^{ch_R} = \sum_{ch_L}^{ch_R}\left[\int_{t_{acq}} dt \int_{space} da \sum_{\text{detectors}} \sum_{\substack{\text{detector}\\ \text{faces}}} \underline{\underline{R}}\left[\underline{\underline{B}}\left(S\eta_g \underline{Y} \otimes p_s\right)\right]\right]. \tag{4}$$

In Equation 4 the system sensitivity is integrated over a spectrometer window extending from channel ch_L to channel ch_R, allowing one to evaluate photopeak, gross count, or general window sensitivities. Starting with measured spectra it is possible to convert from measured count rate to estimated source activity on the ground.

A program was written to generate these sensitivities for point sources and infinite-plane depositions. A program screen is shown in Figure 2. The application implements an isotope library of over 300 sources; performs calculations for the single-detector, fixed wing and the 12-detector helicopter systems; exports spectral shapes for external processing; and supports shielding point sources.


Aerial Measurements Shape Builder -- Version 0.1.0.0

Source: Th-232

Shielding

Material: Steel

Thickness:

Units: ● cm ○ in

Unshielded Source

Det Package: Fixed Wing

Units: ○ m ● ft

Calculation: ● MDA ○ MDD ○ Photo-Peak ● Gross-Counts

Altitude: 1000.00

Source Strength: Ci

Direct

MDA: 55.308 milli-Ci

MDD:

Sensitivity: 1.281 cps / milli-Ci

Offset

MDA: 188.604 milli-Ci

MDD:

Sensitivity: 375.775 cps / Ci

Figure 2. Screenshot of the aerial shape builder and sensitivity calculator application

The sensitivity calculator's performance was evaluated using an experimental data set obtained by flying survey patterns at various altitudes over known point sources of ^{241}Am, ^{137}Cs, ^{133}Ba, and ^{60}Co, representing a range of photon energies. By subtracting representative background and using the sensitivity calculator, estimates for the activities of the point sources on the ground were determined. Subsequent comparison to the known activities provided a benchmark for the methods. Although analysis of this data set is incomplete, initial evaluation indicates good performance in most regimes. Deviation in the results occurs for low-energy photons and is believed to be associated with self-shielding of the source and neglect of the detector container pod by the model. For ^{137}Cs and ^{60}Co the results are in agreement within 60% of the ground truth, accounting for uncertainties in the experimental results. For the analysis portion, difficulties were encountered in obtaining high-precision experimental data for a range of altitudes.

In addition to the sensitivity evaluations, the tool also provides a mechanism to build spectral shapes for patterning algorithms. More specifically, a common approach used in spectral analysis is to assume that a measured spectra $\underline{D}_{measured}$ is actually a linear combination of contributions from known spectral shapes $\underline{\phi_i}$ and unknown scale factors a_i. This is written as:

$$\underline{D}_{measured} = \sum_{i=1}^{I} a_i * \underline{\phi_i}. \tag{5}$$

In practice a measured spectrum is patterned by providing candidate spectral shapes. Through variations of a matrix inversion, the unknown amounts of each candidate are determined. A well-known example is exemplified by decomposing background spectra into unknown amounts of potassium, uranium, and thorium. The method suggested by Equation 5 is well established and has been shown to be fairly successful given ample counting statistics. But for AMS applications the method described above falls short in that the candidate spectral shapes are altitude dependent. Obtaining high-fidelity spectral shapes for all isotopes at any altitude is experimentally intractable. Using the methods developed in this work, it is possible to estimate those shapes over a very large parameter space in a matter of seconds. Figure 3 shows the results of building spectral shapes for a direct pass over a ^{152}Eu point source at various altitudes. The calculation was done for the 12-detector helicopter system, although the shapes vary little for other systems of the same detector type.

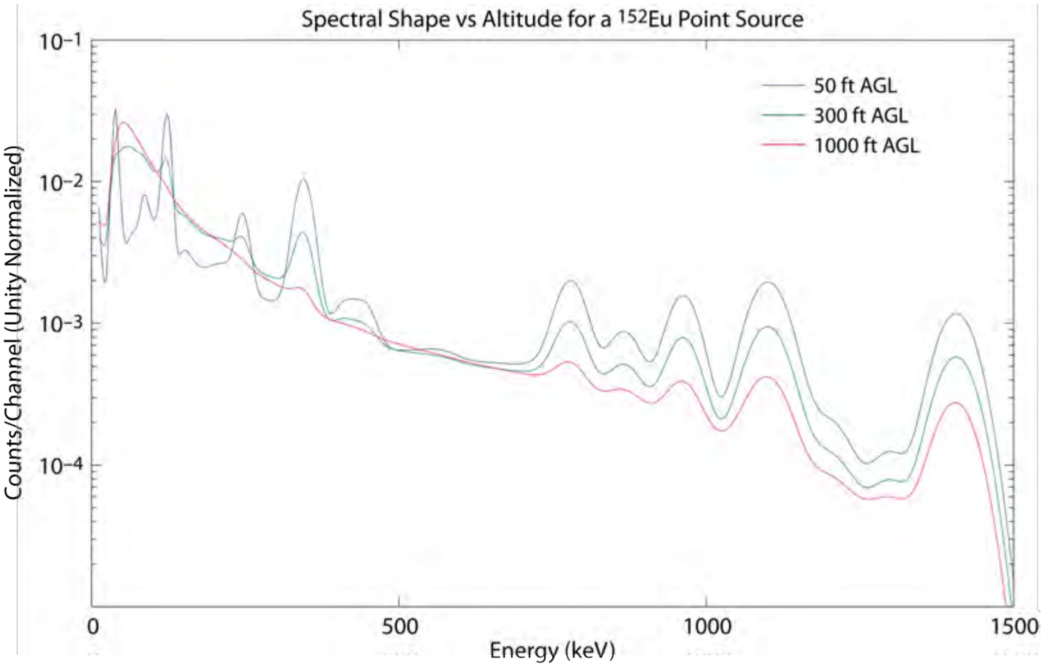

Figure 3. Spectral shapes for a ^{152}Eu point source at various altitudes above ground level (AGL); results obtained from aerial shape builder tool

Conclusion

The simplified photon transport model used in this work proved to be an adequate balance between computational complexity and accuracy. This model was shown to be very successful in determining appropriate sensitivity factors to be applied to measured data in order to produce quantitative estimates of ground truth. The model runs in less than one second on a modern workstation and generates reasonably accurate sensitivities and spectral shapes for patterning. Though not detailed in this summary report, other work performed included investigating inversion of the buildup and response matrices integral to the method. Careful collapse and subsequent inversion of these matrices proved to be successful in forming the basis for estimating other ground-truth properties such as photon exposure rate. The formal implementation of these techniques will greatly advance the state of the art with respect to AMS data products. Finally, these techniques can be applied to much more general radiation detection problems such as advanced isotopic identification and ground-based radiation detection.

References

Kiser, M., "An aerial radiological survey of the Paducah Gaseous Diffusion Plant and surrounding area," report, National Security Technologies, LLC, Las Vegas, Nevada, 2010.

Reed, M., "Interpreting radiation measurements using inverse transport," *Nevada Test Site–Directed Research and Development*, FY 2009, National Security Technologies, LLC, Las Vegas, Nevada, 2010, 165–172.

Turner, J. E., *Atoms, Radiation, and Radiation Protection*, 3rd Edition, Wiley-VCH Verlag GmbH & Co., KGaA, Weinheim, Germany, 2007, 476–477.

this page intentionally left blank

SNM END-OF-ENRICHMENT (EOE) TIME AND CONSTITUENCY RECONSTRUCTION (PHASE II)

Ding Yuan,[1,a] *Paul P. Guss,*[b] *and Raymond P. Keegan*[b]

This report outlines the progress made during FY 2010 on developing a new methodology for calculating the time that has elapsed since the enrichment of special nuclear material (SNM) and of the original assay of this material. This investigation has resulted in the production of a new prototype software, Decay Interaction Visualization and Analysis (DIVA), alpha version. We have achieved excellent agreement between SNM test sample properties and results obtained with our methodology. Our work suggests that the DIVA software is capable of supporting age dating and original constituency reconstruction analysis for SNM.

Background

This work has direct relevance to two areas of keen interest to the nuclear forensics science community, and each is related to the origin of illicit special nuclear material (SNM): the material's age and original composition (Moody, 2005; Keegan, 2003). This two-year project was proposed to develop appropriate age-determination algorithms and alternative reconstruction methods based on earlier decay calculation work previously reported (Yuan, 2007) and an appropriate software platform for supporting the end-of-enrichment (EOE) age determination and composition reconstruction.

This report focuses on (1) progress made on age and event analysis, (2) the prototype Decay Interaction Visualization and Analysis (DIVA) software as delivered, and (3) the test and evaluation results of the software using SNM sample data. More detailed discussions of the theoretical and mathematical background and related research efforts can be found in the multiple publications listed in the references for Yuan ("Explicit solutions," 2007; "Multi-nuclide decay calculation and recent progresses," 2010; "Decay Interaction," 2010; "Linear transformation," 2010; "SNM," 2010; "End of enrichment" 2010; "Multi-nuclide decay calculation using software," 2011).

Project

Age and Event Analysis

As discussed by Moody (2005) and Keegan (2003), age dating of SNM is a complicated issue. Most current age-dating methods are based on certain child–parent ratios derived from simplified decay formulas. Generally, at least one assumptive condition is required in addition to the formulae offered by Bateman equations in order to determine the age of the material (Yuan, "SNM," 2010). Different age-determination methods can be derived by imposing different restrictive conditions. For instance,

---

[1] yuand@nv.doe.gov, 505-663-2085

[a] Los Alamos Operations; [b] Remote Sensing Laboratory–Nellis

four types of age-determination methods were identified and reported by Yuan ("SNM," 2010); these methods are (a) decay rate analysis method (e.g., ^{238}Pu), (b) growth rate analysis method (e.g., ^{241}Am), (c) equilibrium analysis method (e.g., ^{241}Pu and ^{237}U), and (d) stable isotope method (common method in geological dating). Only methods (a), (b), and (c) are generally applicable to SNM. The age derived when using method (a) corresponds to a maximum atomic abundance in the past of the decayed nuclide. The age derived when using method (b) corresponds to a minimum atomic abundance in the past of the accumulated nuclide. Most existing ratio methods discussed in Moody (2005) are essentially variations of method (b). If we consider the maximum atomic abundance of one nuclide, the minimum atomic abundance of another nuclide, and the secular equilibrium between a nuclide pair as historical events in the decay dynamics of a nuclide decay chain, then age determination becomes key event determination. Subsequently all possible age estimates derived using methods (a), (b), or (c) can be calculated through relevant event detection methods, where events can be maximum abundance events, minimum abundance events, or secular equilibrium events. We incorporated the event detection concept and implemented the concept into an event detection module in DIVA software. However, DIVA's event detection approach is more than a collection of analytic methods yielding potential age estimates. For instance, DIVA's event detection functionality can be used for detecting possible interruption events to the "normal" decay process of the material, such as remixing, reprocessing, spoofing and even detonation.

For a natural decay system, if it is (1) a closed system, that is, it contains all parent and child nuclides of the chain (no escaping), and (2) the atoms generated through alpha decays (^{4}He) are unaccounted for (no addition), then the total number of the atoms for all nuclides in the chain is a constant. This is the atomic abundance conservation (of individual as well as of multiple chains) concept we are interested in exploring for SNM age dating. Practically, not all nuclides in a nuclear mix are tracked in the Bateman calculation. For instance, short-lived nuclides and stable nuclides at the end of the decay chain are usually ignored in the calculation. There are possible computational leaks for those untracked atoms using the Bateman calculation, as observed and discussed in our sample data test and evaluation section.

Software Development Effort

Compared with the earlier skeleton version of DIVA developed in 2009, the current version is much improved. Most notably, an event-detection capability was added to the software. Now the system allows users to compute predefined events (mostly related to age estimates) and even allows users to define their own events and detect them using DIVA. A user may be interested in detecting events that satisfy the following conditions at time $t = 0$:

$^{241}\mathrm{Am} = 0$	(accumulative nuclide)
$^{239}\mathrm{Pu} = 93\%$	(depletive nuclide)
$^{241}\mathrm{Am}/^{241}\mathrm{Pu} = 0$	(ratio method)
$^{241}\mathrm{Am} + {}^{238}\mathrm{Pu} + {}^{239}\mathrm{Pu} + \ldots + {}^{241}\mathrm{Pu} > 2.0 \times 10^{11}$	(atomic conservation checking)
$(^{241}\mathrm{Am}/^{241}\mathrm{Pu}) \times (^{234}\mathrm{U}/^{238}\mathrm{Pu}) < 10^{-20}$	(detecting age of material of multiple chains)

DIVA software will do forward and backward calculations starting from the present time $t = 0$ and check if and when any of the above conditions can be satisfied. This is quite convenient for users interested in age and interruption analysis. For instance, if DIVA has detected a condition of $^{241}\text{Am} = 0$ at time $t = 15{,}010$ days for a given SNM sample data, then we are somewhat confident that this SNM has an age about 15,010/365.25 = 41.1 years. Essentially, DIVA can calculate all ratios discussed in Moody (2005) as well as many other quantities.

The time series of the events detected by DIVA is displayed on the event axis in most visualization plots produced by the DIVA software. Additionally, DIVA offers a convenient way to group a number of related events and to calculate the group statistics, such as the mean time, standard deviation of the mean time, minimum time, and maximum time, of a group of selected events. The DIVA software also includes a stacked areal plot option. The stacked areal plot may be used for inspecting if the atomic conservation rule has been maintained in the reversed calculation. If not, this atomic conservation broken point might just be the EOE point of the SNM. This concept will be further discussed and illustrated in the next section.

SNM Sample Data Test and Evaluation

Three data sets from SNM samples were used for the test and evaluation of the algorithm and software. The assays for samples 1 and 2 are from Keegan (2003), and sample 3 assay is from Mukhopadhyay (2010). The current nuclide compositions of the samples, together with their known ages and DIVA age estimates are listed in Table 1. A discussion of these assays and their DIVA age derivations follows.

Table 1. Three SNM sample data sets tested with DIVA age analysis method

#	Comments and Data Source	Nuclide	Quantity	Known Age (yrs)	DIVA Age Est. (yrs)
#1[a]	Measured in atomic abundances	^{241}Pu	4.69×10^{16}	18.97 ±1.0	18.91
		^{241}Am	6.90×10^{16}		
		^{233}Pa	4.13×10^{7}		
#2[a]	Measured in atomic abundances	^{241}Pu	7.96×10^{17}	41.2 ±2.4	41.10
		^{241}Am	4.79×10^{18}		
		^{233}Pa	1.48×10^{10}		
#3[b]	Measured in mass concentrations	^{238}Pu	0.05%	19~20	19.90
		^{239}Pu	87.23%		
		^{240}Pu	12.09%		
		^{241}Pu	0.41%		
		^{242}Pu	0.20%		
		^{241}Am	6510 ppm		

[a] Keegan; [b] Mukhopadhyay

Sample 1 is an aged weapons grade plutonium sample with a known age of about 19 years. Keegan (2003) derived that the age of the material was about 18.97 ±1 year using alternative gamma counting approach. The decay dynamics of sample 1 were calculated in DIVA and plotted in Figure 1a. The horizontal axis is the time axis (bidirectional) measured in days. The vertical axis shows the atomic abundances (measured in number of atoms per picogram) of the nuclides in the sample material. Using the event detection approach implemented in DIVA software described in earlier sections, an age event of LeftZero for ^{241}Am at –6910 days was identified. (LeftZero is an event defined as a turning point in time for a function that changes in value from zero to positive as time increases. It indicates the time when the relevant nuclide begins to accumulate or the time of the beginning of the natural decay.) This number is very close to the known age of the sample (about 18.97 years). Sample 1 assay

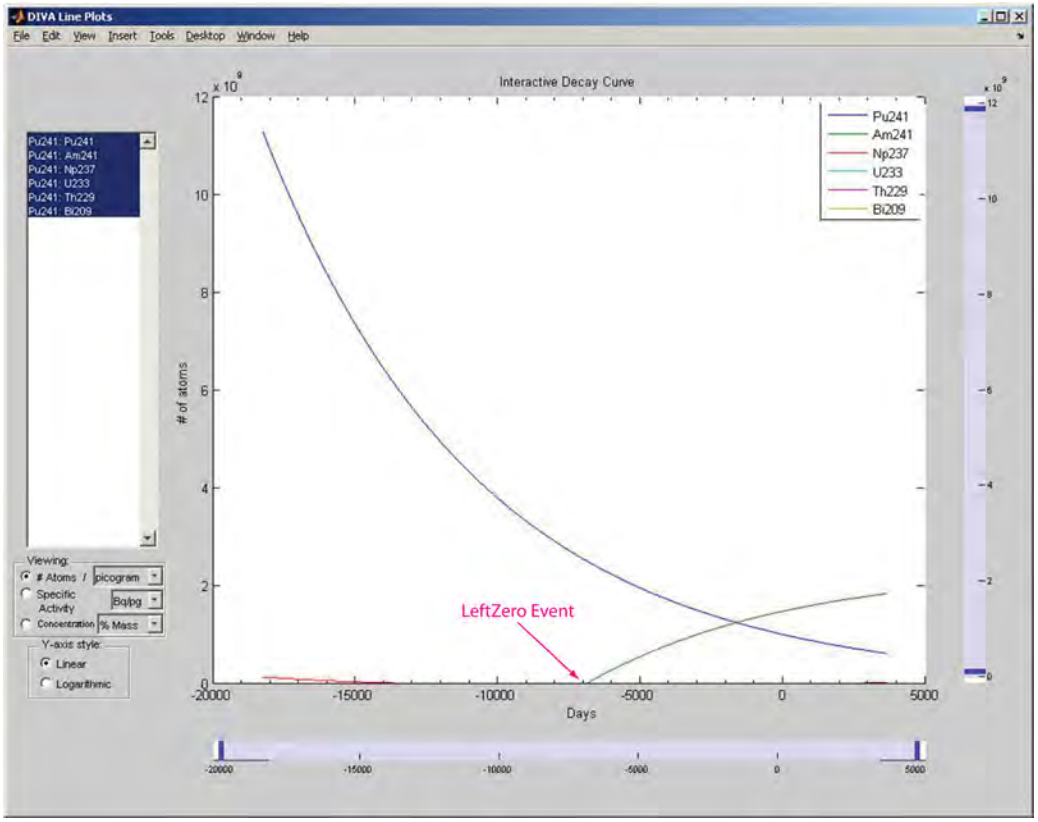

Pu241: Pu241
Pu241: Am241
Pu241: Np237
Pu241: U233
Pu241: Th229
Pu241: Bi209

Viewing: ● # Atoms / picogram
Y-axis style: ● Linear

Figure 1a. Sample 1 decay dynamics shown in multiple lines. The horizontal axis is the time axis (bidirectional) measured in days from the time when the assay was made. The vertical axis shows the atomic abundances (measured in number of atoms per picogram) of the nuclides in the sample material. As shown in the plot, a LeftZero event for ^{241}Am at *t* = –6910 days was detected by DIVA.

constitutes only measurements of nuclides in the ^{241}Pu chain. The total atomic abundance of the nuclide in the ^{241}Pu chain should be in atomic abundance conservation mode as long as sample 1 exists, less computational leaks due to unaccounted stable and short-lived nuclides in Bateman calculation. When the backward calculation in time for sample 1 was proceeded using Bateman solutions, we observed that the total atomic abundance conservation pattern was followed between 0 and –6910 days. However, this conservation pattern was abruptly interrupted at around –6910 days, as shown in Figure 1b. Clearly, this breaking point for the chain-based total atomic abundance conservation pattern can be a valuable age indicator for sample 1.

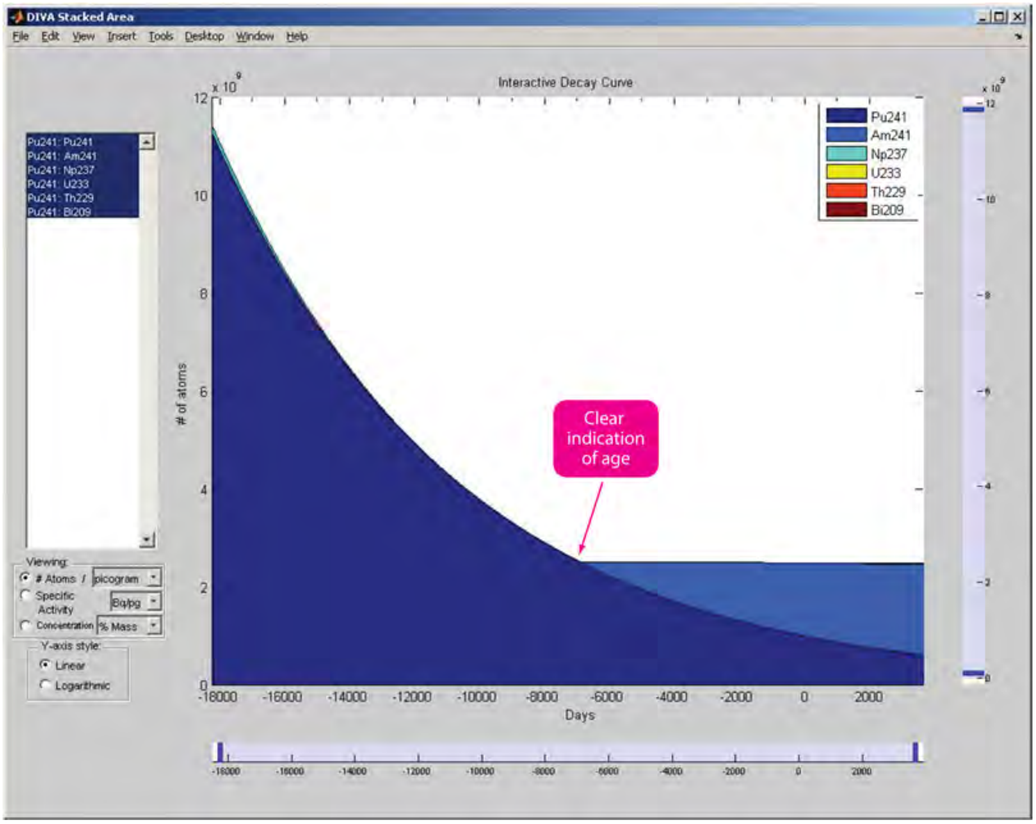

Viewing:
● # Atoms / picogram
○ Specific Activity Bq/pg
○ Concentration % Mass

Y-axis style:
● Linear
○ Logarithmic

Figure 1b. The sample 1 total nuclide atomic abundance (and stacked areal atomic abundance) plot as calculated with respect to time. The horizontal and vertical axes of the plot are similar to those in Figure 1a. It is observed that between –6910 and 0 days, the total atomic abundance of sample 1 is essentially flat (chain-based conservation). This conservation pattern was interrupted at –6920 days, which is another indication of the age of the material.

Sample 2 assay was also from Keegan (2003). The actual age of the material was estimated at about 41.2 ±2.4 years at the time the assay was made. The decay dynamics of sample 2 were calculated and are plotted in Figure 2a. Similarly, an age event LeftZero for ^{241}Am was detected at −15,010 days using the DIVA event detection module. This event points to an age estimation of the material at 41.1 years. Evidently, this is a very good estimate of the age of sample 2.

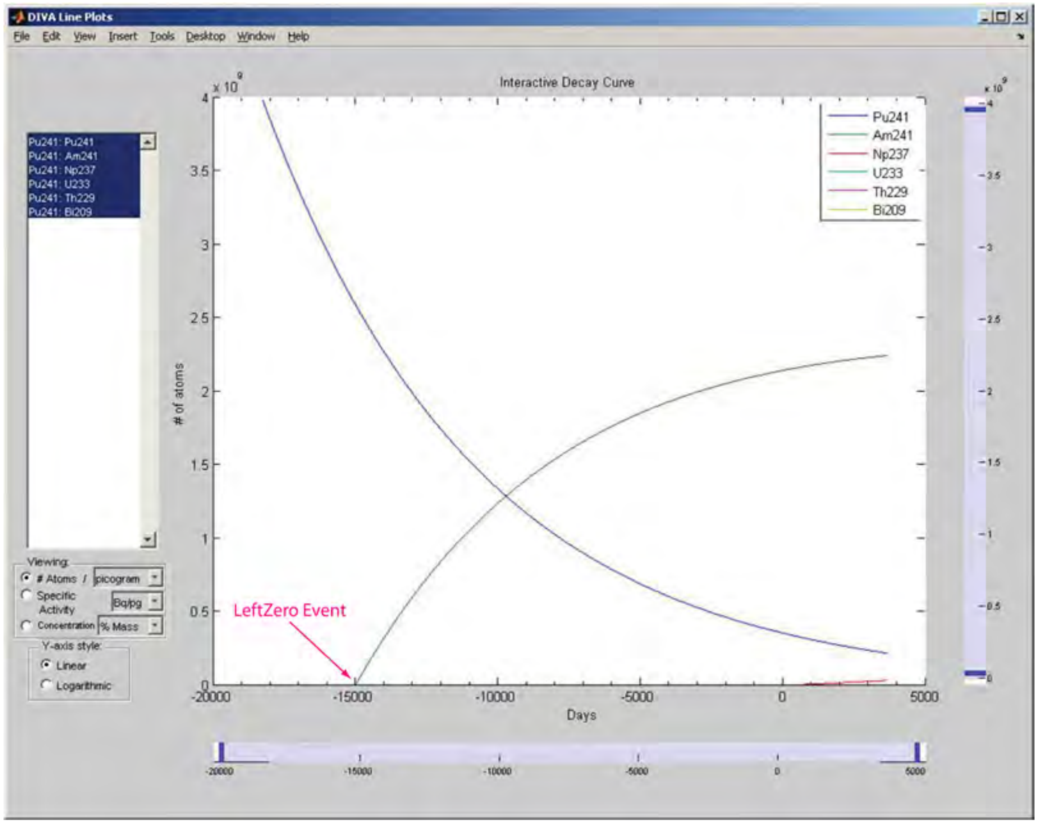

Pu241: Pu241
Pu241: Am241
Pu241: Np237
Pu241: U233
Pu241: Th229
Pu241: Bi209

Viewing:
● # Atoms / picogram
○ Specific Activity Bq/pg
○ Concentration % Mass

Y-axis style:
● Linear
○ Logarithmic

Figure 2a. Sample 2 decay dynamics shown in multiple lines. The horizontal and vertical axes of the plot are similar to those in Figure 1a. As shown in the plot, a LeftZero event for ^{241}Am a t = –15,010 days was detected by DIVA.

The total and the stacked areal atomic abundance of the nuclides in the ^{241}Pu chain were calculated and plotted in Figure 2b. As was expected, this total atomic abundance curve (the outer curve) largely resembles a straight line with a gentle slope between –15,010 and 0 days. This is because the total atomic abundance of the nuclides in a given chain should be conserved—if every nuclide in the chain is accounted. In practice, this conservation line is gently sloped due to the leaks of the uncounted nuclides in the calculation. At about –15,010 days, this gentle slope changed into a much steeper slope. This rapid change in slope in the total atomic abundance curve is also indicative of the age of sample 2.

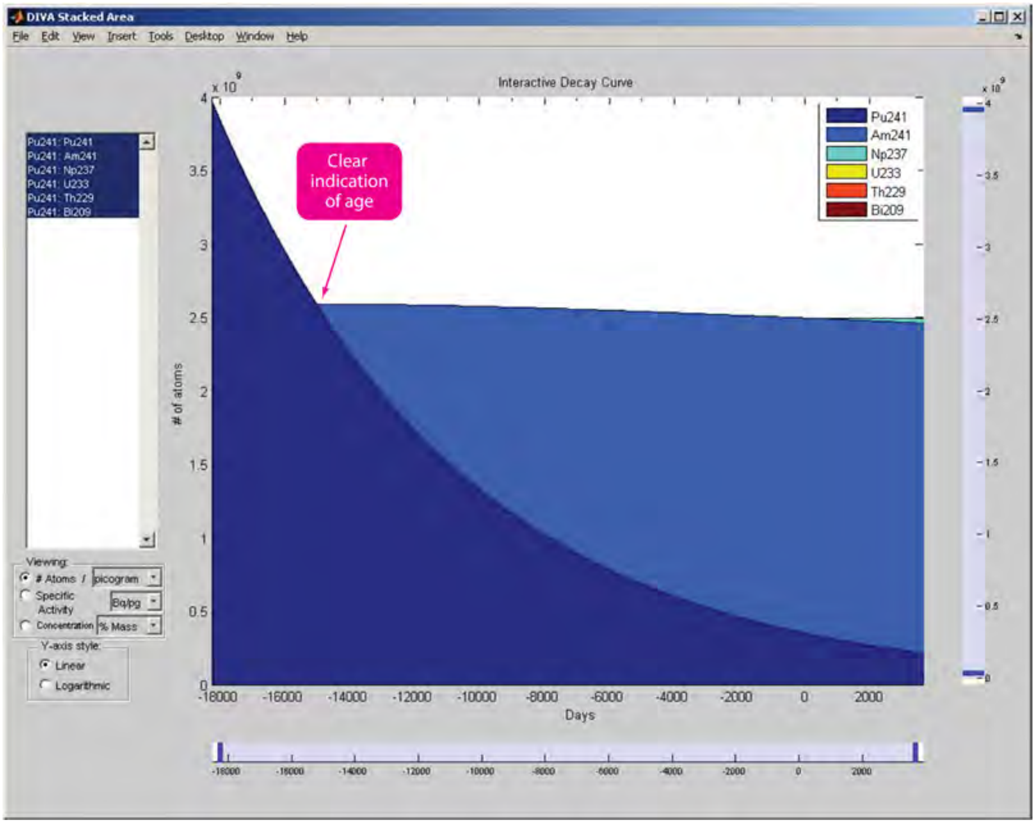

Clear indication of age

Viewing:
● # Atoms / picogram
○ Specific Activity Bq/pg
○ Concentration % Mass

Y-axis style:
● Linear
○ Logarithmic

Figure 2b. The sample 2 total nuclide atomic abundance (and stacked areal nuclide atomic abundance) plot as calculated with respect to time. The horizontal and vertical axes of the plot are similar to those in Figure 2a. It is observed that between –15,010 and 0 days, the total atomic abundance of sample 2 is gently sloped (chain-based conservation less computational leaks). This conservation pattern (gentle slope) changed into a much steeper pattern at –15,010 days—this is another indication of the age of sample 2.

Sample 3 data are from an aged weapons-grade plutonium sample with nuclides from all four major plutonium chains. For simplicity, only those child products with a half-life longer than one year were calculated using DIVA; the results are plotted in Figure 3a. Through age event detection using DIVA, a LeftZero event for ^{241}Am (an event where ^{241}Am reaches zero from right) was detected at –7270 days (measured from present time at *t* = 0 days). This translates to an age estimate of 19.90 years. It is very close to the known age of the sample (Table 1).

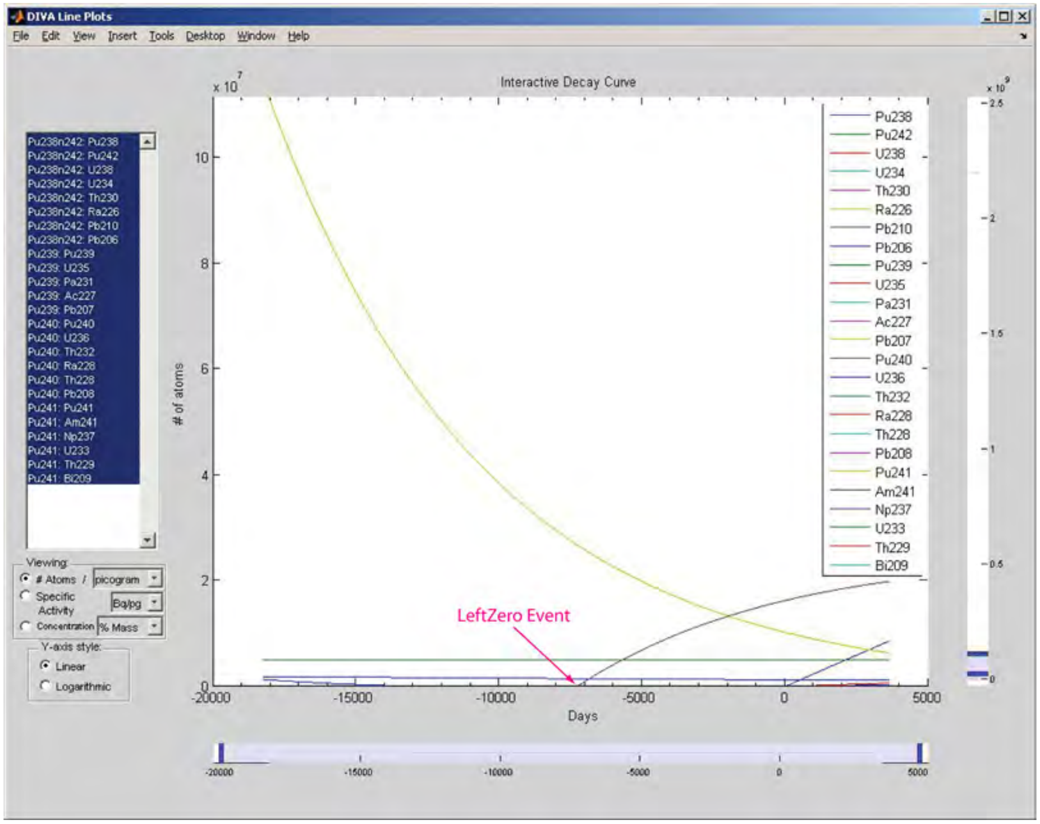

Viewing:
● # Atoms / picogram
○ Specific Activity Bq/pg
○ Concentration % Mass

Y-axis style:
● Linear
○ Logarithmic

Figure 3a. Plot of sample 3 decay dynamics. The horizontal and vertical axes of the plot are similar to those in Figure 1a. Total 25 nuclides (with half-lives longer than 1 year) of the four plutonium chains are calculated. DIVA has detected a LeftZero event for ^{241}Am at *t* = –7270 days. This translates to an age estimate of 19.90 years of the SNM sample.

The stacked areal nuclide atomic abundance plot for sample 3 is shown in Figure 3b. Unlike samples 1 and 2 (Figures 1b and 2b), the slope change of the curve for total atoms in sample 3 was not as exaggerated. This is because we now have four independent decay chains to track in the calculation, and a rapid change in the decay can be hidden among those slow changes. It is better to examine the atomic conservation principle within individual decay chains. For instance, if we select only the nuclides in the ^{241}Pu decay chain, then we have a new stacked areal plot with nuclides in ^{241}Pu decay chain only (Figure 3c). This time the abrupt change in the slope of the curve for the total number of atoms in the chain became obvious. Now the slope change point in Figure 3c is exactly the LeftZero point in Figure 3a. It is clear that when we apply the atomic conservation concept for SNM age estimation, selecting an appropriate decay chain suitable for the physical sample is important.

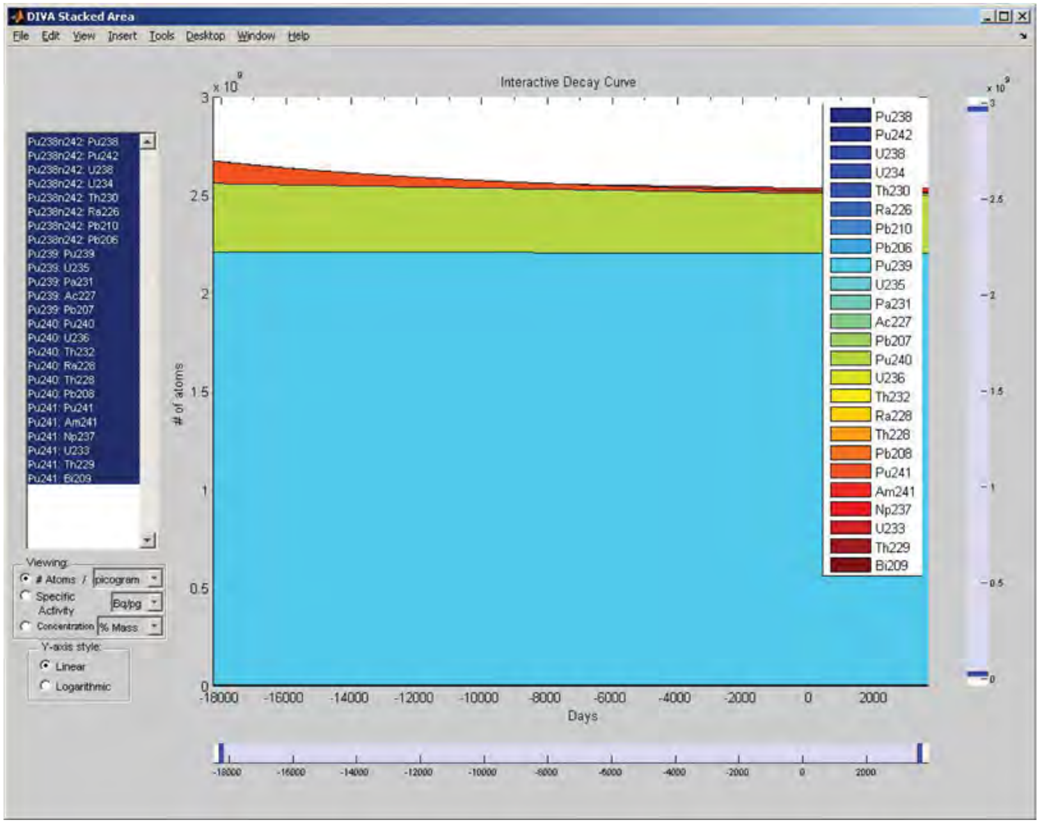

Viewing:
● # Atoms / picogram
○ Specific Activity Bq/pg
○ Concentration % Mass

Y-axis style:
● Linear
○ Logarithmic

Figure 3b. Stacked areal nuclide atomic abundance plot as calculated using sample 3 data. The horizontal and vertical axes of the plot are the same as those defined in Figure 2b.

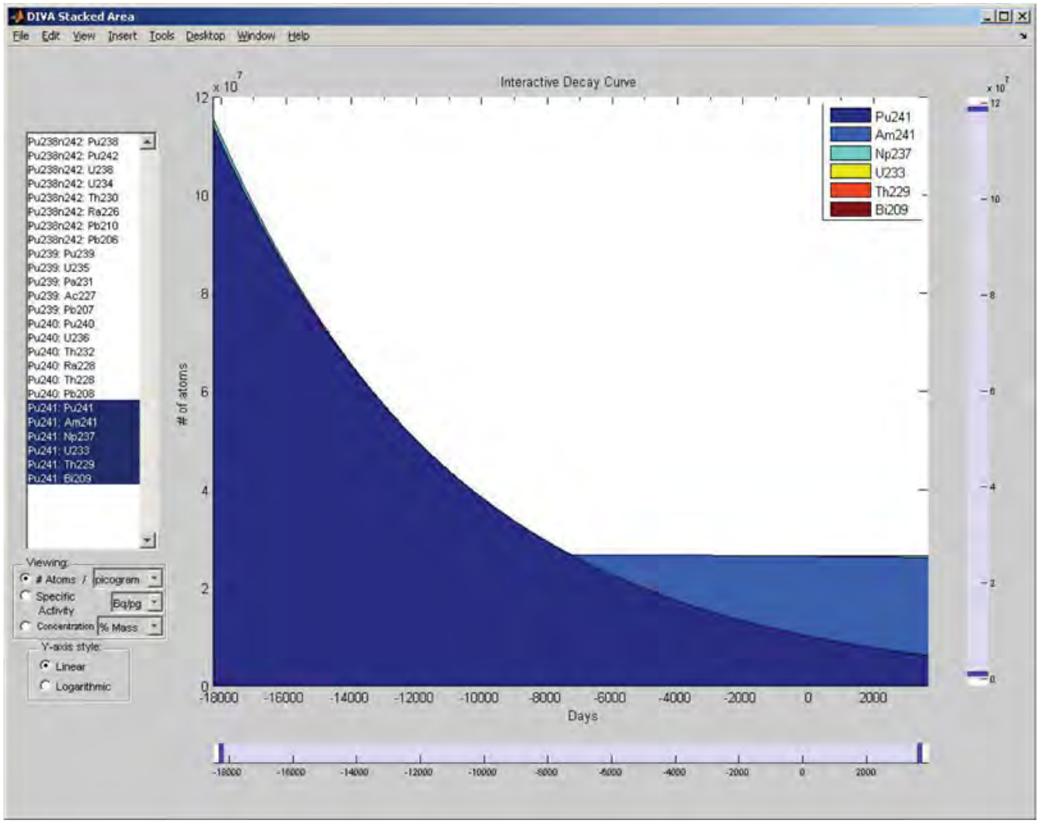

Viewing:
● # Atoms / picogram
○ Specific Activity Bq/pg
○ Concentration % Mass

Y-axis style:
● Linear
○ Logarithmic

Figure 3c. Sample 3 stacked areal nuclide atomic abundance plot with ^{241}Pu chain selected

Uncertainty Research

Uncertainty propagation was investigated this year. Basically, we can show that if the Bateman decay solution is written in a linear transformation as $N(t) = F(t)N_0$, then the uncertainties in the measurement follow the similar decay dynamics $N(t) + \Delta N(t) = F(t)(N_0 + \Delta N_0)$, or $\Delta N(t) = F(t)\Delta N_0$. This suggests that if the uncertainty in the initial measurements ΔN_0 is about 5% (of N_0), then the relative uncertainties due to the decay calculations will be about the same; that is, $\Delta N(\pm t)$ is about 5% of $N(\pm t)$, as shown in Figure 4. However, the uncertainty tool has not yet been implemented in the DIVA software.

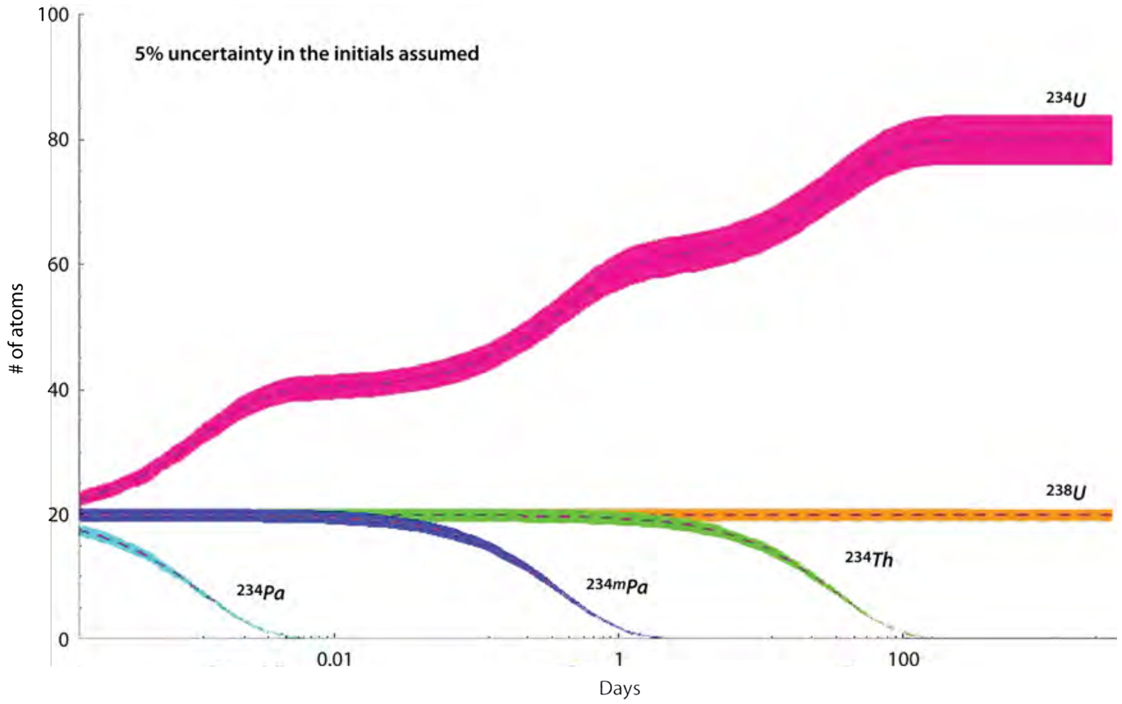

Figure 4. A sample uncertainty propagation plot illustrating the 5% uncertainty envelopes derived from the uncertainties in the present measurement (t = 0). The horizontal axis is the time axis in days in logarithmic scale, and the vertical axis is in atomic abundance percentage. The $^{238}U \rightarrow ^{234}U$ decay chain is used for the illustration.

Conclusion

Over the past two years, this project team has developed a set of algorithms for chain and sample calculation, manipulation, and age determinations. Some of the algorithms have been implemented in a prototype software platform (DIVA) for interactive decay and age analysis. SNM sample data test and evaluation results suggest that the algorithms and the DIVA software performed well and are of great value for supporting nuclear forensic applications.

Acknowledgments

The programming work was provided by the University of Nevada, Las Vegas, DIVA development team through a subcontract task to Dr. Evangelos Yfantis of Computer Science. Drs. S. Freid, S. Mukhopadhyay, F. Tsang, H. Clark, A. Plionis, A. Klingensmith of the Remote Sensing Laboratory and N. Wimer of Lawrence Livermore National Laboratory reviewed, participated, offered data, and assisted the project in many different ways.

References

Keegan, R. P., R. J. Gehrke, "A method to determine the time since last purification of weapons grade plutonium," *Applied Radiation and Isotopes* **59** (2003) 137–143.

Moody, K. J., I. D. Hutcheon, P. M. Grant, *Nuclear Forensic Analysis,* Taylor & Francis, Boca Raton, Florida, 2005.

Mukhopadhyay, S., Private communication, 2010.

Yuan, D., W. Kernan, "Explicit solutions for exit-only radioactive decay chains," *J. Appl. Phys.* **101** (2007) 094907/1–12.

Yuan, D., R. Keegan, P. Guss, "SNM end-of-enrichment (EOE) time and constituency reconstruction," *Nevada Test Site–Directed Research and Development*, FY 2009, National Security Technologies, LLC, Las Vegas, Nevada, 2010, 183–189.

Yuan, D., P. Guss, R. Keegan, E. Yfantis, C. Watkins, "Decay Interaction Visualization and Analysis (DIVA) for supporting multi-nuclide decay calculations," *American Nuclear Society Joint Topical Meeting*, Las Vegas, Nevada, April 18–23, 2010.

Yuan, D., "End of enrichment reconstruction," presented at the DOE LDRD/SDRD Annual Symposium, Washington, D.C, June 9, 2010.

Yuan, D., P. Guss, R. Keegan, E. Yfantis, C. Watkins, "Multi-nuclide decay calculation and recent progresses in methodology," *American Nuclear Society Annual Meeting*, San Diego, California, June 13–17, 2010.

Yuan, D., "Linear transformation method for multi-nuclide decay calculation," *Am. J. Phys.* **78** (2010) 10.

Yuan, D., P. Guss, R. Keegan, E. Yfantis, C. Watkins, "Multi-nuclide decay calculation using software DIVA (Decay Interaction Visualization and Analysis)," to be published in *Nuclear Technology* in 2011.

Enhanced Methods of Object Recognition and Classification within a Scene

Mary D. O'Neill,[1,a] Marcus Jang,[b] and Pamela Robinson[a]

We have explored methods to extract meaningful data from video and condense them into very small packets that can be sent over low-bandwidth telecommunication paths. As part of this study, we conducted a thorough review of current object recognition methods, collected a large quantity of video data, began categorizing and organizing this data, and developed preliminary algorithms for recognition of automobile types. Approximately 750 GB of high-definition visible video imagery was collected at two different sites with up to four viewing locations at each site. Preliminary algorithms were developed and an initial field test using a laptop and a webcam was done. This field test confirmed the feasibility of creating these compact algorithms.

Background

Our national security organizations are collecting an increasing volume of full-motion video and imagery. While the applications of object recognition technology can be wide-reaching, there are immediate needs within the NNSA mission to automate the detection of known threats within video surveillance operations as a means to streamline alarming and response operations. This project investigated methods to extract meaningful data and condense it into very small packets that can be sent over low-bandwidth telecommunication paths. Although research in this area has been conducted by commercial entities, there is a continuing need for government agencies to aggressively develop compact, low-power algorithms that would benefit their applications. The low-power, compact nature of this algorithm set makes it useful to a number of NSTec sponsors including those in the tagging and tracking communities.

Project

The goal of this project was to determine the feasibility of extracting meaningful data from imagery and reducing it to a small byte count such that it can be transmitted via a very low-bandwidth telecommunication path. The project included three major tasks: (1) review current algorithm research, (2) perform new algorithm development based on our expected requirements, and (3) collect and organize data.

---

[1] oneillmd@nv.doe.gov, 805-681-2477

[a] Special Technologies Laboratory; [b] University of California, Santa Barbara

Algorithm Development

Prototype algorithms were developed to extract object (automobile) descriptions from a variety of cameras. These algorithms borrowed from the best of the wide variety of open source algorithms for object recognition. The key existing feature extraction algorithms were scale-invariant feature transform (SIFT) (Psounis, 2005) and speeded-up robust features (SURF) (Bay, 2008). SIFT and SURF both incorporate robust interest point detection and feature descriptor extraction, which are useful in object recognition and 3-D reconstruction. The Haar wavelet is part of SURF's image processing routine. The Haar wavelet is one of many possible wavelets that image and signal processing algorithm developers use to magnify the properties associated with the target of interest. A wavelet's shape determines what characteristics to magnify and what characteristics to attenuate. The implementation is a simple convolution of a wavelet kernel with the image of interest. Other wavelets may further enhance recognition of our targets of interest.

We also reviewed research by commercial companies and universities in the area of vehicle tracking, including:

- Quantum Signal, LLC: Vehicle tracking (Quantum, 2009)
- U.S. Patent 6,538,580: Method and device for registering the outer characteristics of a vehicle in a road toll unit (Bostrom, 1999)
- U.S. Patent 7,382,277: System for tracking suspicious vehicular activity (Ioli Trust, 2005)
- USC Institute for Robotics and Intelligent Systems: Research on location and tracking of objects (Yu, 2009)

This commercial research was helpful in selecting the algorithms that could be adapted for our project. Ultimately, we selected a feature extraction algorithm based on SURF, which is available for free within the Open Source Computer Vision (OpenCV) library. In addition to the image processing algorithms, the current algorithm research produced Java-based algorithms for word quantization (Li, 2009), database search, and structural and ranked matching (Nistér, 2006).

The final algorithms are expected to consider possible variations in imagery, use minimal processing power and time, and include descriptors based upon local image patches. Image variations may include illumination variation, partial occlusions (i.e., a portion of the vehicle blocked by another object in the image field of view), foreshortening of the vehicle due to aspect angle, and variation in apparent size due to distance to the vehicle. The algorithms were organized following the architecture in Figure 1.

Following the flow in Figure 1, still images and/or video are first processed with SURF, with an implementation provided by OpenCV. SURF converts local image patches to robust descriptors (keypoints) that are passed to the word quantization algorithm. The word quantization stage efficiently translates descriptors to simple word identifiers using a vocabulary tree. This list of word identifiers queries a database of identifiers based on known imagery of targets of interest. The structural matching function then verifies the structural layout of matching image descriptors. Then, based on structural matching scores, matches are ranked. Figure 2 shows an example car and the resultant word identifiers.

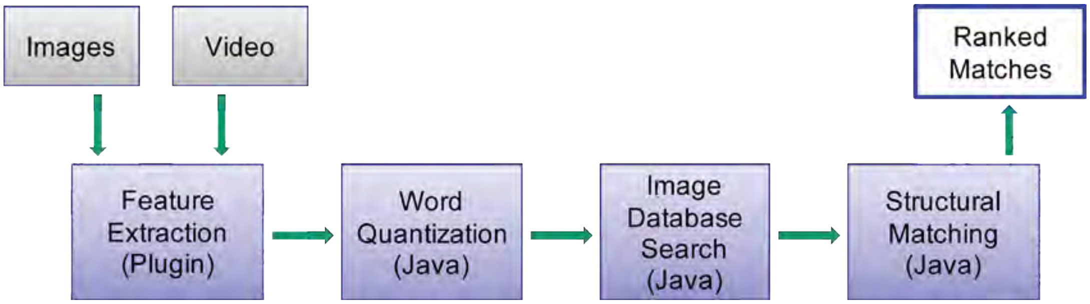

Figure 1. Modular algorithm architecture allows modifications and improvements to any software module. This prototype algorithm uses open-source software modules written in C and Java.

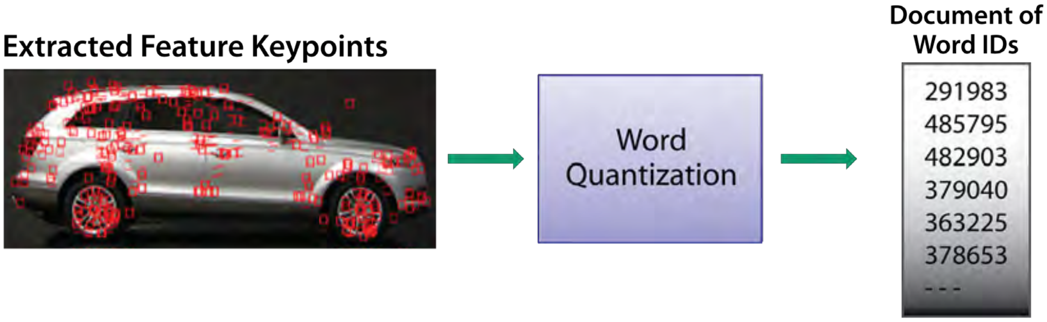

Figure 2. Extracting keypoints for low-bandwidth data transmission. Word quantization minimizes the amount of data needed to identify a vehicle type.

Data Collection and Algorithm Testing

In order to have a means to test these algorithms, we planned and executed two separate data collection exercises at two different test sites. To comply with Executive Order 12333, "United States Intelligence Activities," the data collection required approval from the Institutional Review Board. This approval was received on March 11, 2010. The data collection layout for test site #1 is shown in Figure 3, and the locations and cameras for test site #2 are given in Table 1.

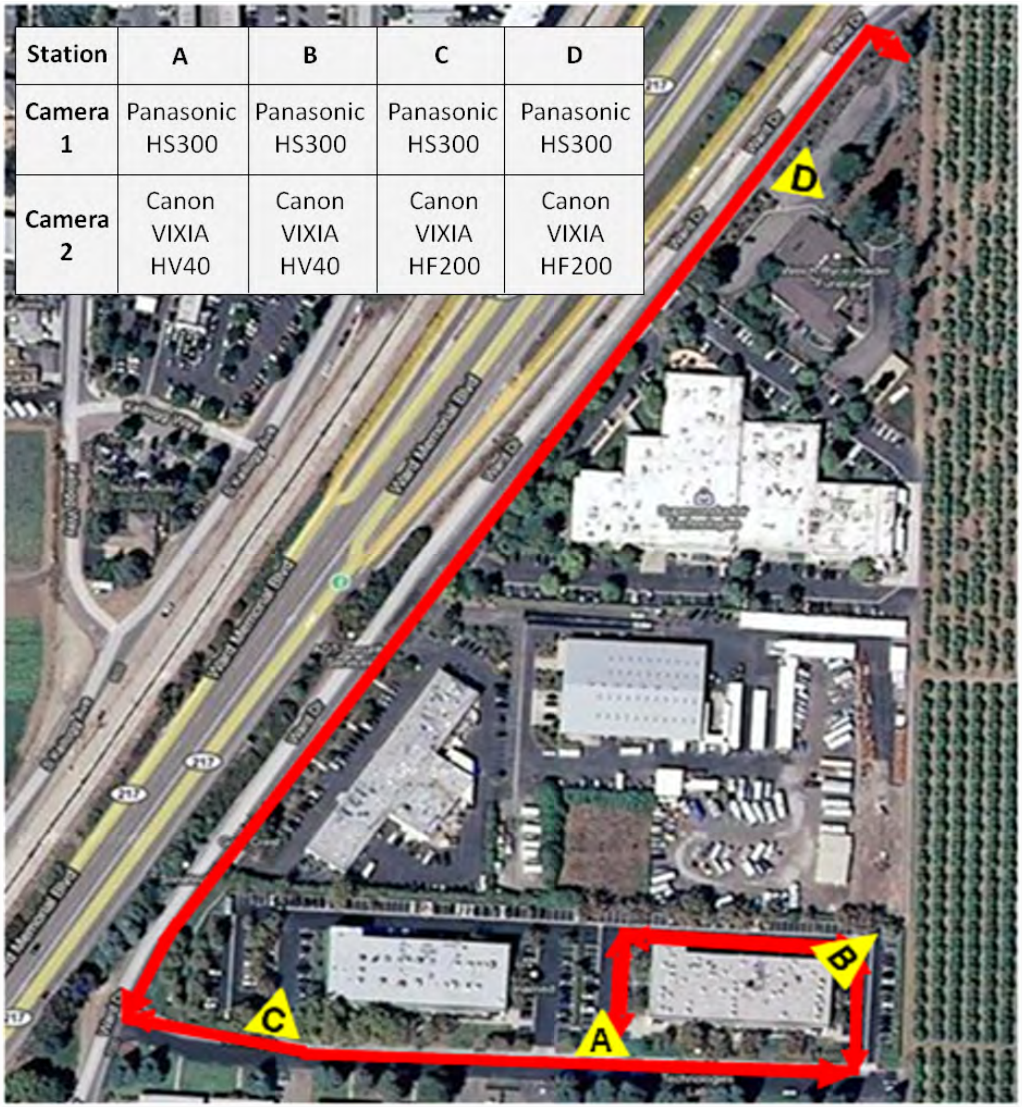

Station	A	B	C	D
Camera 1	Panasonic HS300	Panasonic HS300	Panasonic HS300	Panasonic HS300
Camera 2	Canon VIXIA HV40	Canon VIXIA HV40	Canon VIXIA HF200	Canon VIXIA HF200

Figure 3. Data collection layout for test site #1. Vehicles began at location A, travelled to location D and then returned, providing multiple views of all vehicles in the caravan.

Table 1. Data collection cameras and locations for test site #2

Station	A	B	C
Location	Lighthouse	Parking lot	Park
Camera 1	Panasonic HS300	Panasonic HS300	Panasonic HS300
Camera 2	Canon VIXIA HV40	Canon VIXIA HF200	Canon VIXIA HF200

Approximately 750 GB of high-definition visible video imagery were collected between April 19 and 30, 2010. Figure 4 shows the variability in the collected images based on time of day. Note that the near-zenith angle of the sun reduced the intensity of the visible light reflections at 1:00 p.m. and thus produced a darker image than at 8:00 a.m. and 4:00 p.m. This illumination variability must be considered in the algorithm development.

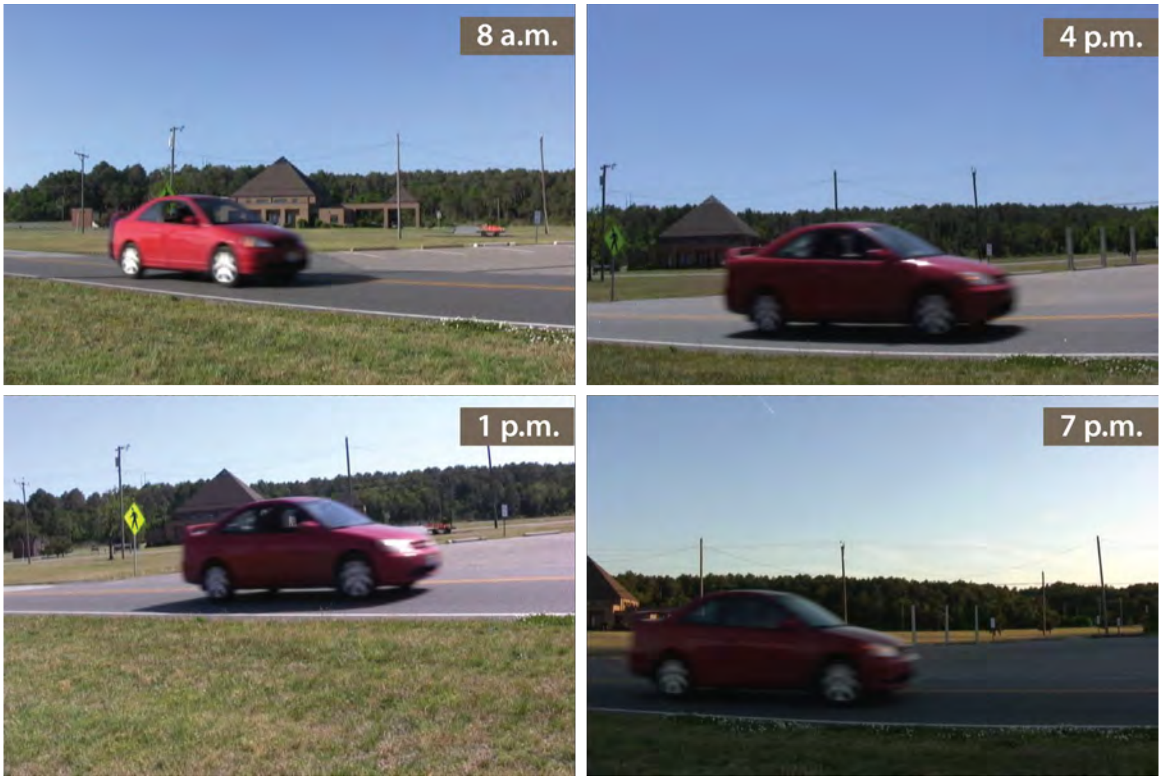

Figure 4. Sample images, test site #2, location A, four times of day. Note that the near-zenith angle of the sun reduced the intensity of the visible light reflections at 1:00 p.m. and thus produced a darker image than at 8:00 a.m. and 4:00 p.m.

Figure 5 shows a sample of the different camera views collected during these tests. The variation in the spatial dimension of the vehicle in each scene is apparent from the images in this figure. This extensive data set will provide a means to test the scale and aspect angle invariance of the improved algorithms.

Figure 5. Sample images, test site #2, four camera views at 1:00 p.m. This figure illustrates the foreshortening of the vehicle due to aspect angle and the variation in apparent vehicle size due to distance to the vehicle. The images in the top left and bottom right illustrate smearing variation due to shutter speed. This type of imagery will allow us to test the robustness of future algorithms.

Partial organization and categorization of the data were done during this phase of the project. This involved creating data sets for a given vehicle taken at different locations and different times of day. To do this efficiently we wrote a MATLAB script that creates a set of video clips based on the information in an MS-Excel spreadsheet. This effort will be completed in FY 2011, with creation of more data sets that can be used to further develop the algorithms.

As part of the test site #2 data collection effort, a field test of the algorithms was completed. Algorithms were tested using a single car at two observation points (locations A and B) using two field test setups. The field test hardware configuration is shown in Figure 6. The algorithm output was a simple alarm that a vehicle of interest was detected. This test identified areas for improvement. It was noted that the algorithms worked for the vehicle at a distance of between 2 and 4 meters. A number of improvements were implemented based on this test. A motion/change-detection algorithm was added that can automatically segment the moving car from a still background. This reduced mismatches due to extraneous background noise and increases detection speed by focusing on the most important features. An update that caches recently used database information in memory allowed the algorithms to exploit more recently seen cars that are more likely to be seen in the near future. This increased detection speed, as the most recent vehicle descriptors are in RAM, removing the need for a hard-disk search. The final improvement is in the data format associated with the feature data and vocabulary trees. By storing this data in XML formats, cross-platform development was more easily achieved.

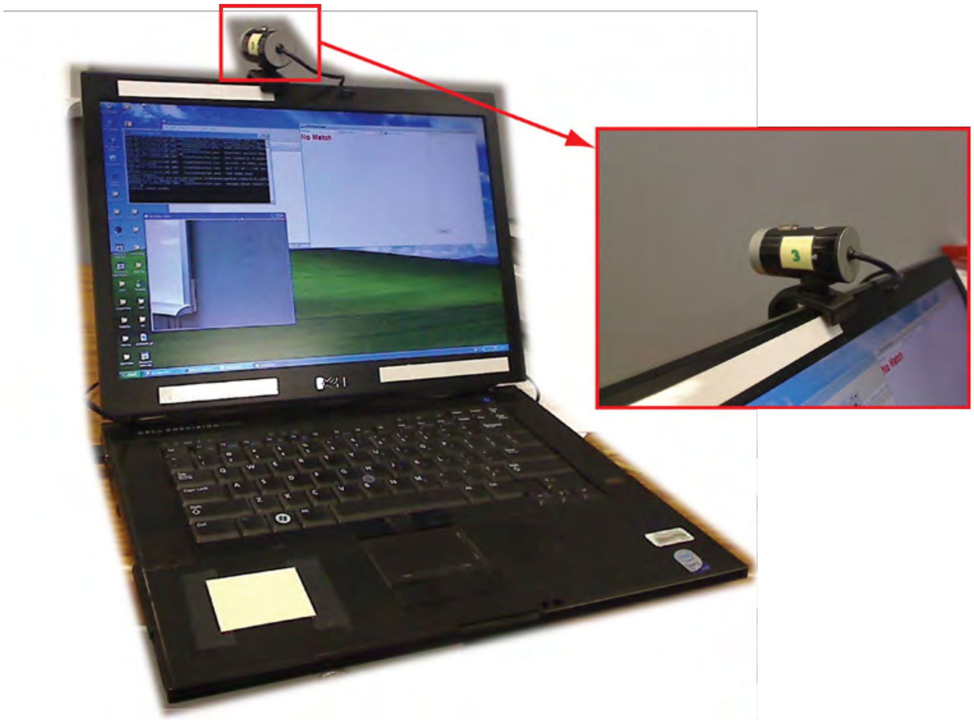

Figure 6. Field test hardware was compact and consisted of only a laptop and a low-cost webcam. Future work will investigate integration into an iPhone.

Conclusion

The team investigated methods to extract meaningful data and condense them into very small packets that can be sent over low-bandwidth telecommunication paths. As part of this SDRD project, we conducted a thorough review of current object recognition methods, collected a large quantity of video data, began categorizing and organizing these data, and developed preliminary algorithms for recognition of automobile types. An initial field test using a laptop and a webcam was performed. Improvements to the algorithms and a review of the algorithm architecture have been accomplished as a result of this first data collection effort.

In FY 2011, when this SDRD project continues, the algorithms will be improved. A learning system to automate the detection, indexing, and categorization of objects (vehicles) moving through a scene will increase the detection of targets of interest while reducing false positives. Geospatial and temporal-weighted matching techniques will also enhance the algorithms. We intend to explore optimization techniques for future implementation into graphics processing units using Computer Unified Device Architecture technology and object detection on handheld devices, including Android and iPhone cell phones. We will investigate a method to automatically detect when to capture the best image from a video stream in order to reduce power requirements, and we will also seek to investigate associated spectral (multiband) detection.

References

Bay, H., T. Tuytelaars, L. Van Gool, "Speeded-up robust features (SURF)," *Computer Vision and Image Understanding* **110**, 3 (2008) 346–359.

Bostrom, G., A. Liew, J. Frilund, "Method and device for registering the outer characteristics of a vehicle in a road toll unit," U.S. Patent 6,538,580, filed June 8, 1999 and issued March 25, 2003, http://www.freepatentsonline.com/y2002/0105440.html, accessed September 30, 2010.

Ioli Trust, E. D., "System for tracking suspicious vehicular activity," U.S. Patent 7,382,277, filed June 16, 2005 and issued June 3, 2008, http://www.freepatentsonline.com/7382277.html, accessed September 30, 2010.

Li, F., W. Tong, R. Jin, A. K. Jain, J.-E. Lee, "An efficient key point quantization algorithm for large scale image retrieval," *Proceedings of the First ACM Workshop on Large-scale Multimedia Retrieval and Mining* (2009) 89–96.

Nistér, D., H. Stewenius, "Scalable recognition with a vocabulary tree," *Computer Vision and Pattern Recognition*, *Proceedings of the 2006 IEEE Computer Society Conference* (October 2006) 2161–2168.

Psounis, K., A. Ghosh, B. Prabhakar, G. Wang, "SIFT: A simple algorithm for tracking elephant flows and taking advantage of power laws," *Proceedings of the 43rd Allerton Conference on Communication, Control and Computing* (September 2005) 10 pages (no pp. available).

Quantum Signal, LLC, Signal Processing Solutions, Vehicle Tracking/ID, http://www.quantumsignal.com/video_analytics/vehicle_tracking_id/, accessed December 1, 2009.

Yu, Qian., G. Medioni, "Motion pattern interpretation and detection for tracking moving vehicles in airborne video," *IEEE Xplore* (2009) 2671–2678, http://ieeexplore.ieee.org/xpl/freeabs_all.jsp?reload=true&arnumber=5206541, accessed September 30, 2010.

PHOTONICS

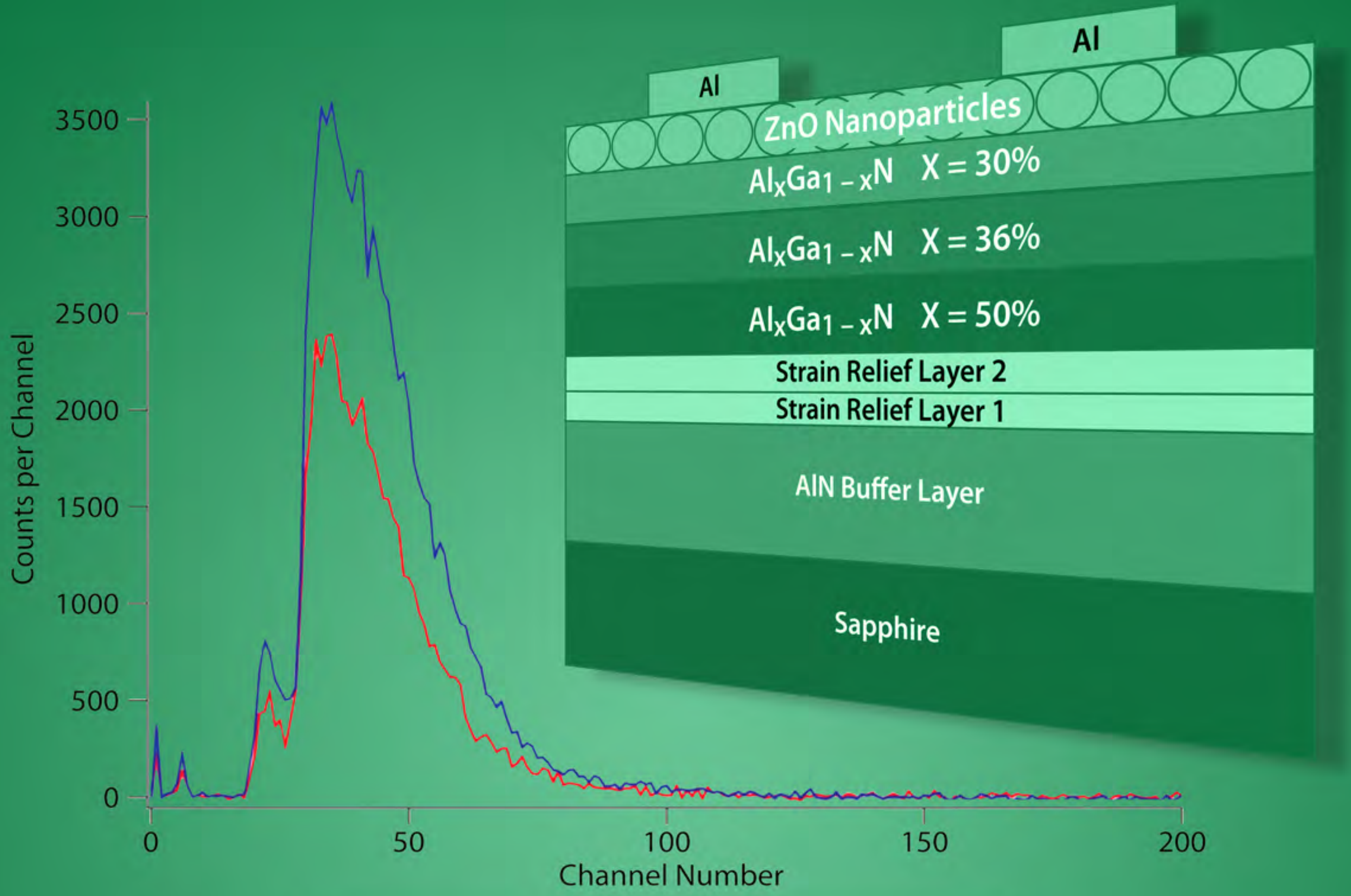
Counts per Channel
3500
3000
2500
2000
1500
1000
500
0
0
50
100
150
200
Channel Number
Al
Al
ZnO Nanoparticles
$Al_xGa_{1-x}N$ X = 30%
$Al_xGa_{1-x}N$ X = 36%
$Al_xGa_{1-x}N$ X = 50%
Strain Relief Layer 2
Strain Relief Layer 1
AlN Buffer Layer
Sapphire

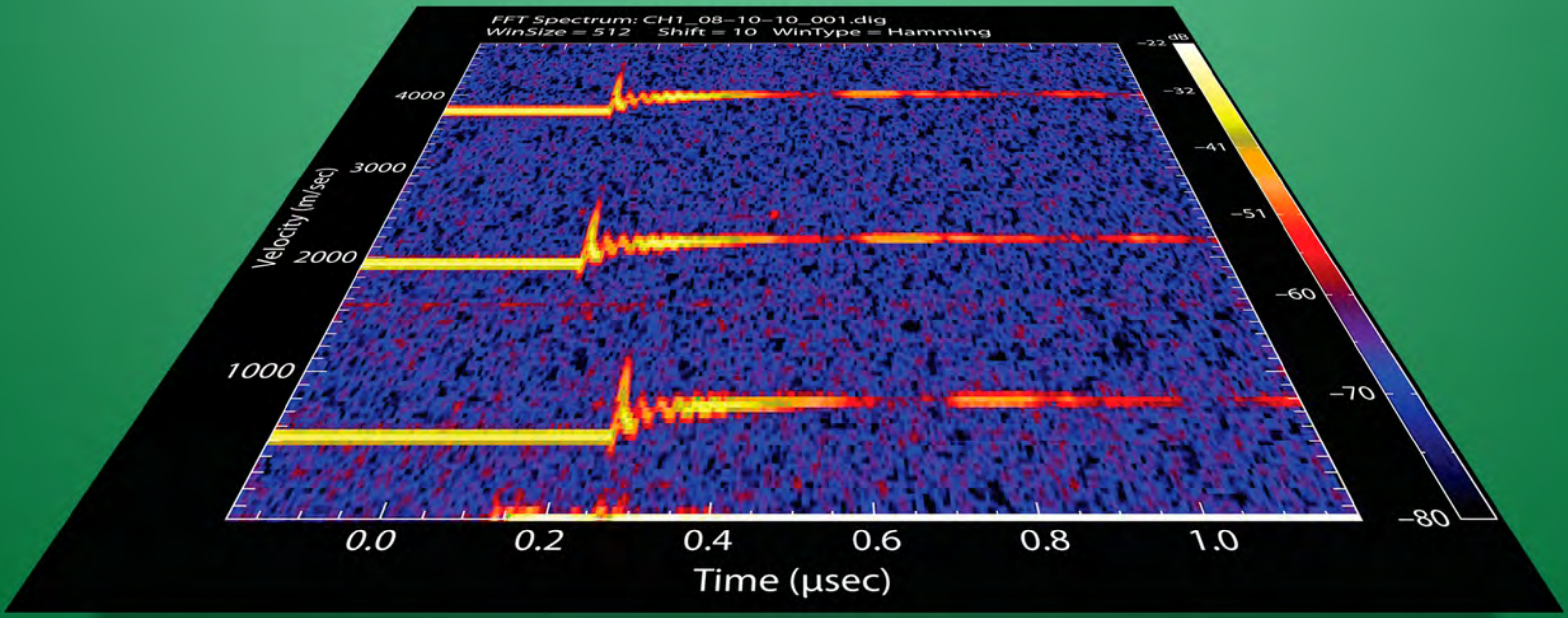
FFT Spectrum: CH1_08-10-10_001.dig
WinSize = 512 Shift = 10 WinType = Hamming
Velocity (m/sec)
4000
3000
2000
1000
0.0
0.2
0.4
0.6
0.8
1.0
Time (μsec)
dB
-22
-32
-41
-51
-60
-70
-80

ADVANCED PDV TECHNIQUES: EVALUATION OF PHOTONIC TECHNOLOGIES

Edward Daykin,[1,a] Carlos Perez,[a] Araceli Rutkowski,[b] and Cenobio Gallegos[b]

We evaluated commercially available technologies in combination with wavelength division multiplexing and optical heterodyning techniques to determine the feasibility of a frequency and time multiplexed PDV system. Commercial off-the-shelf technologies and vendors were selected for evaluation. Laboratory measurements of single-frequency lasers in combination with dense wavelength division multiplexing, optical amplification, and optical heterodyning have demonstrated performance suitable to a multiplexed system. A design for a multiplexed PDV architecture capable of frequency and time division multiplexing, user-adjustable optical heterodyning (up-shift or down-shift), and laser-safe (Class 1) operation was accomplished. The resulting system architecture has been named the multiplexed many-point PDV (MPDV). During the course of this project, the proposed architecture was shared with experts from the national weapons laboratories; they encouraged us to assemble a demonstration MPDV system. An expanded scope variance made this possible. Testing and application of the demonstration MPDV system will occur under FY 2011 programmatic efforts.

Background

The PDV (Strand, 2006) diagnostic measures surface velocity (m/s to km/s) on various dynamic experiments. PDV, used widely in dynamic compression research, is a relatively simple, portable, and robust diagnostic both in fielding and data fidelity (as compared to alternative methods such as VISAR [Barker, 1972]). In essence, PDV is a fiber-optic Michelson interferometer that combines Doppler-shifted light ($\lambda \approx 1550$ nm) from a moving reflector with a reference light source producing a complete interference fringe when the reflector moves $\lambda/2$. The reference source, referred to as a local oscillator in this report, is typically an unaffected portion of the source laser light; however, we have introduced a separate tunable laser source to allow for optical heterodyning. The time-dependent optical interference fringes are applied to a high-bandwidth photodetector, resulting in an electrical beat frequency that is then recorded onto a high-bandwidth (>12 GHz) digitizer.

The motivations for this SDRD were both practical and technical. For practical reasons—digitizer cost—we wished to multiplex data from several PDV probes onto a single digitizer channel. We accomplished this technically via frequency division multiplexing to take advantage of unused frequency space within a typical digitizer record. We also wished to replace the relatively expensive and potentially dangerous Class 4 laser system with less expensive, low-power (Class 1) lasers.

---

[1] daykinep@nv.doe.gov, 702-295-0681

[a] North Las Vegas; [b] Los Alamos Operations

Project

Overview

This investigation included (1) frequency division multiplexing to take advantage of the unused bandwidth typical for PDV recording systems, (2) heterodyne methods to provide user-adjustable beat frequency up-shifting or down-shifting, (3) wavelength division multiplexing to provide wavelength separation of multiplexed channels as well as methods for combining and separating optical signals, (4) optical pre-amplification of low-power signals ($<10\ \mu W$) to quantify signal-to-noise (S/N) performance and dynamic gain effects, and (5) time domain multiplexing. For the purpose of clarity, we refer to wavelength division multiplexing as the optical domain method for combining and separating lasers of differing wavelengths. Frequency multiplexing refers to the heterodyne beat frequency generated electrically by the photodiode and recorded onto a digitizer. Analysis of the beat frequency is typically accomplished by an FFT analysis. For our frequency multiplexed methodology, an FFT analysis is necessary in order to resolve the data—time domain analysis is not applicable!

Frequency division multiplexing of PDV data has two principal requirements. First, we require a method of optical heterodyning to generate a shift in the beat frequency for each data signal (probe) relative to the others, i.e., a separation in frequency space of the digitizer record. Second, we require each of the probes, which are to be combined onto a common digitizer channel, be at differing optical frequencies by an amount much greater than the recording system bandwidth so as to prevent probe-to-probe "cross-term" beat frequencies within the multiplexed data record. We reviewed three methods of optical heterodyning: acousto-optic frequency shifters, Mach-Zehnder frequency shifters, and use of multiple independent lasers. Previous work (Daykin, 2009) successfully demonstrated the use of acousto-optic modulators; however, their disadvantages include limited frequency shifting range, poor optical transmission efficiency, and large electrical current draw. Mach-Zehnder shifters have also been used previously but generate sidebands, which must be managed by additional hardware and/or techniques, adding an undesirable degree of complexity. Ultimately, we chose independent lasers to provide heterodyne frequency division multiplexing. This approach requires that each "probe" laser have a dedicated "local oscillator" laser in order to generate a heterodyne beat frequency. We refer to the probe laser as the source that illuminates the target and the local oscillator laser as the source that generates a beat frequency at the detector via heterodyne interference. The local oscillator optical frequency ν_{LO} is adjusted to differ slightly from that of the probe laser frequency υ_{probe} according to a user-determined beat frequency $\Delta\upsilon_{beat} = |\upsilon_{probe} - \nu_{LO}|$. This provides the flexibility to either up-shift ($\nu_{probe} > \nu_{LO}$) or down-shift ($\nu_{probe} < \nu_{LO}$) and also to separate the multiplexed signals within the data recording frequency domain by any amount appropriate to the experiment and the recording system.

We then pursued methods to optically combine (multiplex) or separate (demultiplex) optical signals from several probes at differing wavelengths. This process is a standard telecommunications methodology referred to as dense wavelength division multiplexing (DWDM). Several vendors and technologies were explored. A DWDM utilizing thin film coating technology with 200 GHz optical frequency separation was selected. The 200 GHz separation is an International Telecommunication Union (ITU) standard and is much greater than the recording system bandwidth. We took advantage of industry standardization and purchased both lasers and DWDM components on the following ITU channels: ITU29 (1554.13 nm, 192,900 GHz), ITU31 (1552.52 nm, 193,100 GHz), ITU33 (1550.92 nm, 193,300 GHz), and ITU35 (1549.32 nm, 193,500 GHz). The combination of lasers and DWDM components at these wavelengths allows frequency division multiplexing of four separate PDV probes, each probe on a different ITU channel, onto a common photodetector (i.e., 4X frequency multiplexing).

We also investigated the use of optical preamplification combined with relatively low-power lasers. A preamp is an optical amplifier located just prior to the photodetector that amplifies the Doppler-affected optical signals. We replaced the 100–1000 mW high-power laser with a 10 mW seed laser and then purchased an erbium-doped fiber amplifier (EDFA) preamp to boost the return signal to levels appropriate to the photodetector, i.e., 10–20 dB less laser light implied the need for equivalent optical preamplification. While the EDFA provided adequate signal levels at the photodetector, it also increased the detection noise floor due to amplified spontaneous emission (ASE). S/N degradation from the optical amplifier was investigated, as was time-dependent EDFA gain behavior.

Finally, we designed an MPDV architecture that allows for frequency and time division multiplexing as well as optical preamplification (laser-safe operations.) We conducted component evaluations and laboratory tests of subassemblies to quantify performance and test system validity. Laser and EDFA performance were measured on an optical spectrum analyzer and then subassemblies were dynamically tested with both electrically and laser-driven foils. System performance was quantified in terms of harmonic distortions, data cross-talk, and S/N ratio levels compared to a conventional PDV system. The principal components and MPDV demonstration system are shown in Figure 1.

Component Evaluation

We screened numerous vendors during a preliminary selection for components. The components of interest included lasers, optical amplifiers, DWDM multiplex and demultiplex (mux/demux), optical power monitors, and variable optical attenuators. Our evaluation of the three main components, laser, optical amplifier, and mux/demux, is given below.

Lasers

We tested low-power (Class 1, <10 mW) single-frequency planar external cavity lasers. Our laser requirements were optical line-width <50 kHz, optical power >5 mW, sideband suppression >40 dB, wavelength specified to an ITU channel number, and wavelength adjustable but stable (once set) to $\Delta\lambda < 0.001$ nm. Redfern Integrated Optics Inc. (RIO) was the only vendor who met the requirements. The RIO ORION seed laser module shown in Figure 1 is a plug-and-play unit with built-in software control and adjustable wavelength via temperature tuning. We purchased RIO ORION lasers on ITU channels 29, 31, 33, and 35 (as described above) and have found them to perform reliably and to specifications with very good vendor and software support.

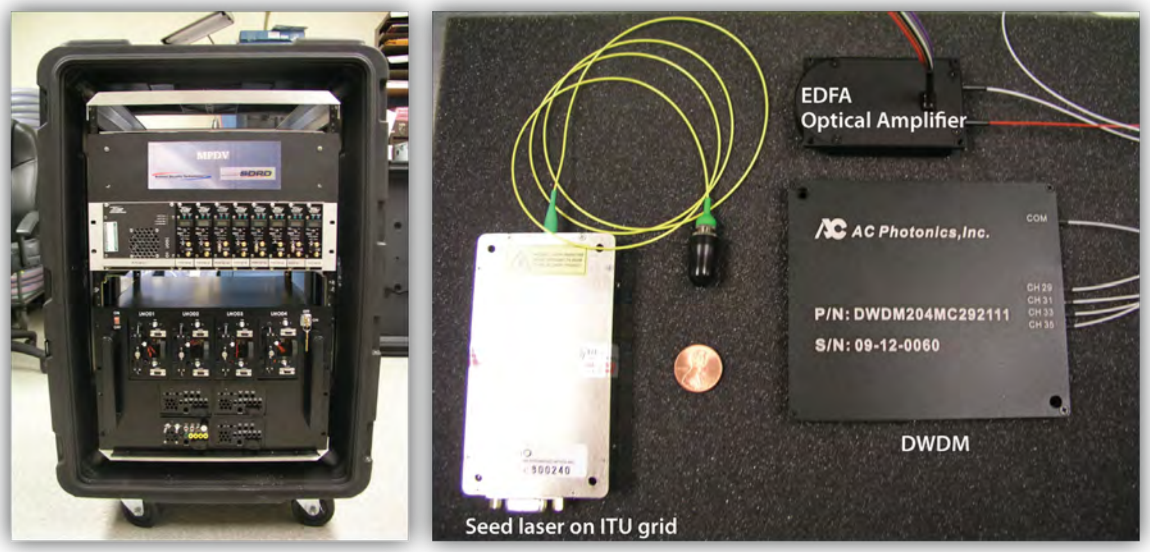

Figure 1. The MPDV demonstration system (not including digitizer) and principal components include the multiplexing chassis (upper unit), which provides up to 4X wavelength division multiplexing and 2X time division multiplexing (combined 8X multiplex) as well as optical amplification and photodetection. The laser chassis (lower unit) contains eight seed lasers (four probe lasers and four local oscillator lasers) and one high-power optical amplifier for light-starved experiments. Both chassis employ a modular architecture. *Note*: Four modules in the upper chassis are placeholders for "signal balancing" units not complete at the time of this photograph.

We demonstrated optical heterodyning with two ORION lasers on the same ITU channel. Laser wavelengths on the same ITU channel will, in general, not be identical but within tens of GHz of each other. We temperature tuned (via software control) one laser relative to its partner to achieve a desired beat frequency then measured beat frequency stability to be better than ~100 MHz over several hours of operation. Using this approach, we verified the ability to readily up-shift or down-shift the beat frequency within a range of approximately ±20 GHz.

DWDM Multiplexers

The performance and reliability of the thin film–based DWDM mux/demux available are regulated by Telcordia specifications. The performance measures we monitored were the mux/demux transmission efficiency, band-pass filter performance, and adjacent channel cross-talk extinction ratio. Products from the vendors we chose (AC Photonics due to their low cost and JDSU due to their high power rating of 2 W) performed to specification. The 200 GHz units are specified with a ~1 nm band pass; in addition to using them for both mux/demux, we used them to filter out ASE from the EDFAs (discussed below). We measured adjacent channel cross-talk isolation >45 dB on a sample of mux and demux units.

Optical Amplification

Two EDFA topics of interest to our application were optical noise (ASE) generation and time-dependent gain. We conducted laboratory tests on EDFAs from three vendors: Lightwaves2020 (Figure 1), Manlight, and JDSU. All units met specifications, but implementation (software control and hardware control) varied greatly.

ASE will degrade data fidelity by introducing a broadband optical spectrum into the signal that reduces S/N ratios in the optical domain and subsequently increases the photodetector noise floor. We mitigated the noise effects by optically filtering the ASE with 1 nm band-pass filters. The mux/demux units worked well for this purpose, serving double duty. Optical and electrical spectrum analyzer noise measurements were made, and performance among products was similar for comparable gain values. The Lightwaves2020 and Manlight preamps appear to be well suited to our applications; gain ≈ 23 dB and noise spectral density $S \approx -128$ dBm/Hz. This is approximately equal to the Miteq photodetector's electrical noise floor; thus, we expected minimal degradation in data fidelity.

EDFA gain is customarily specified for constant input power, whereas optical power returned from dynamic experiments is time dependent. When optical power at the EDFA increases beyond its maximum (saturated) level, then the EDFA gain will decrease to a saturation value. Literature (Desurvire, 2002) suggests that this occurs with a time constant of ~10–100 µs, which we confirmed for our candidate EDFAs under various gain and power conditions. We determined that dynamic gain saturation (or "hole burning") is unlikely to be a concern for the majority of our applications because the duration of transient power spikes within optical velocimetry experiments tends to be ~10 ns–1 µs and will have a negligible effect on the gain within that timeframe. Also, we chose to combine the local oscillator with the Doppler-shifted light after the EDFA gain stage to avoid gain saturation caused by the local oscillator. Gain saturation effects could be problematic for a PDV configuration that does not use an independent local oscillator but instead uses a probe to generate light for the local oscillator signal. In this case, when the Doppler-shifted return is weak but the probe generated local oscillator signal is relatively strong ($P \geq 100$ µW), then the local oscillator will saturate the EDFA gain, starving the weaker Doppler return of needed signal amplification.

System Laboratory Tests

We conducted numerous tests of subassemblies and components; however, we finished with two sets of dynamic laboratory measurements to demonstrate validity of heterodyne frequency multiplexing, and to establish benchmark measurements to quantify fidelity of laser-safe (preamp) methodology as compared to a conventional high-power laser used in PDV. These measurements were done with both electrically driven and laser-driven foils to generate realistic Doppler-shifted signals with fast transient behavior.

MPDV System Architecture Frequency Multiplexing Demonstration

We successfully demonstrated the validity of frequency multiplexing using the MPDV architecture shown in Figure 2. For these experiments we applied three sets of lasers (the fourth set was unavailable at the time.) We recombined the probe output channels into a single probe and onto the target foil. Raw and analyzed triplexed data from laser-driven foil experiments are shown in Figure 3. The composite beat waveform for three data channels, each at a different heterodyne up-shifted frequency, is well resolved by the FFT without the generation of undesirable harmonic "cross-terms."

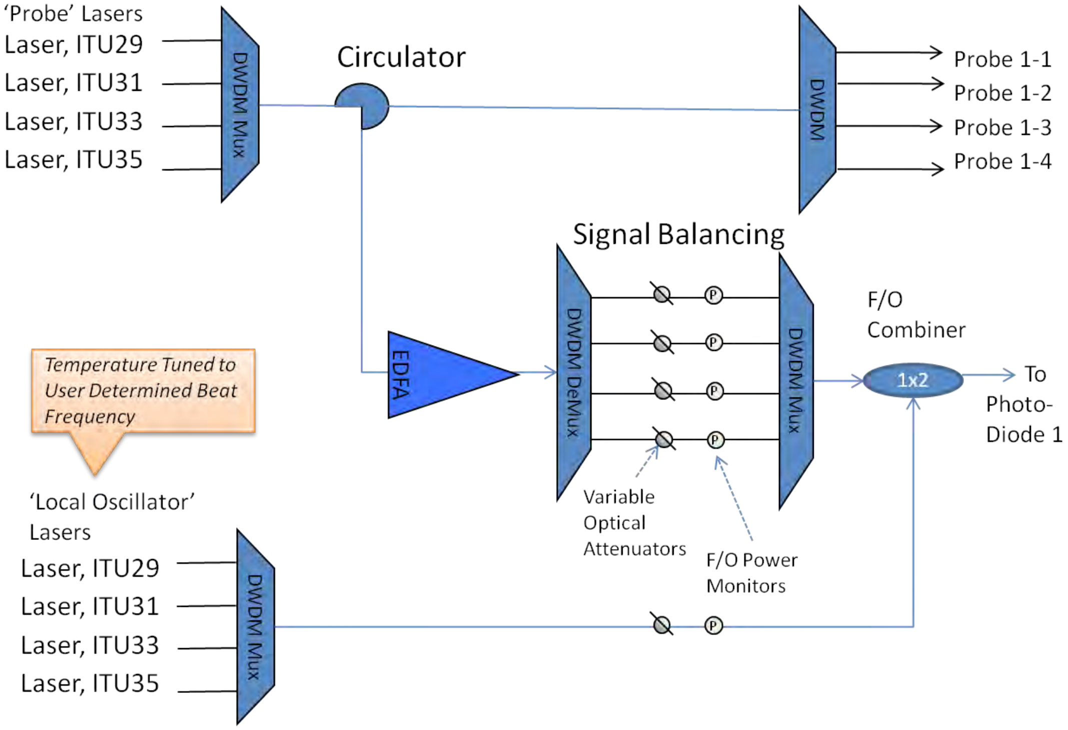

Figure 2. MPDV notional system architecture for 4X frequency multiplexing (F/O = fiber-optic)

Time division multiplexing was also tested within this configuration. We introduced fiber-optic time delays at two locations: a 25 µs delay following the circulator output (prior to the EDFA input) and also several relatively short ~100 ns delays within the "signal balancing" portion of this schematic. In both cases, there was no degradation in data fidelity. We believe time multiplexing is likely to be an essential tool in any multiplexing architecture that will help avoid ambiguity in the data.

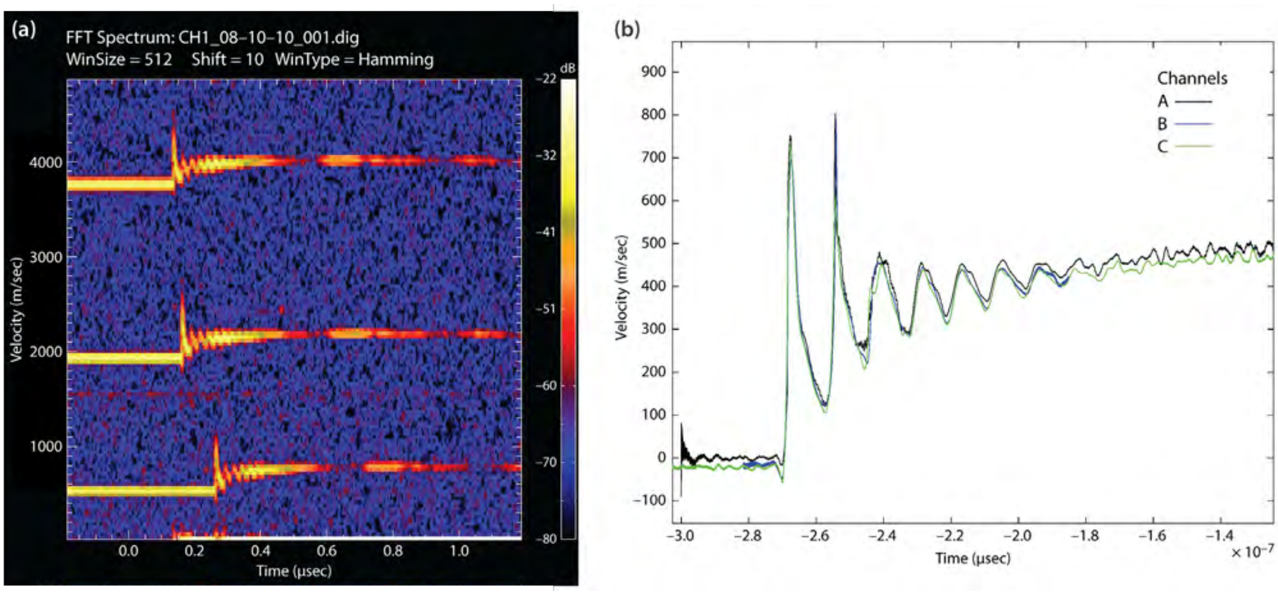

Figure 3. (a) Raw spectrogram and (b) analyzed data from triplexed laboratory measurement of laser-driven foil. Time shifts evident on raw data are a result of time-division multiplexing tested in combination with frequency multiplexing and were accounted for in analysis.

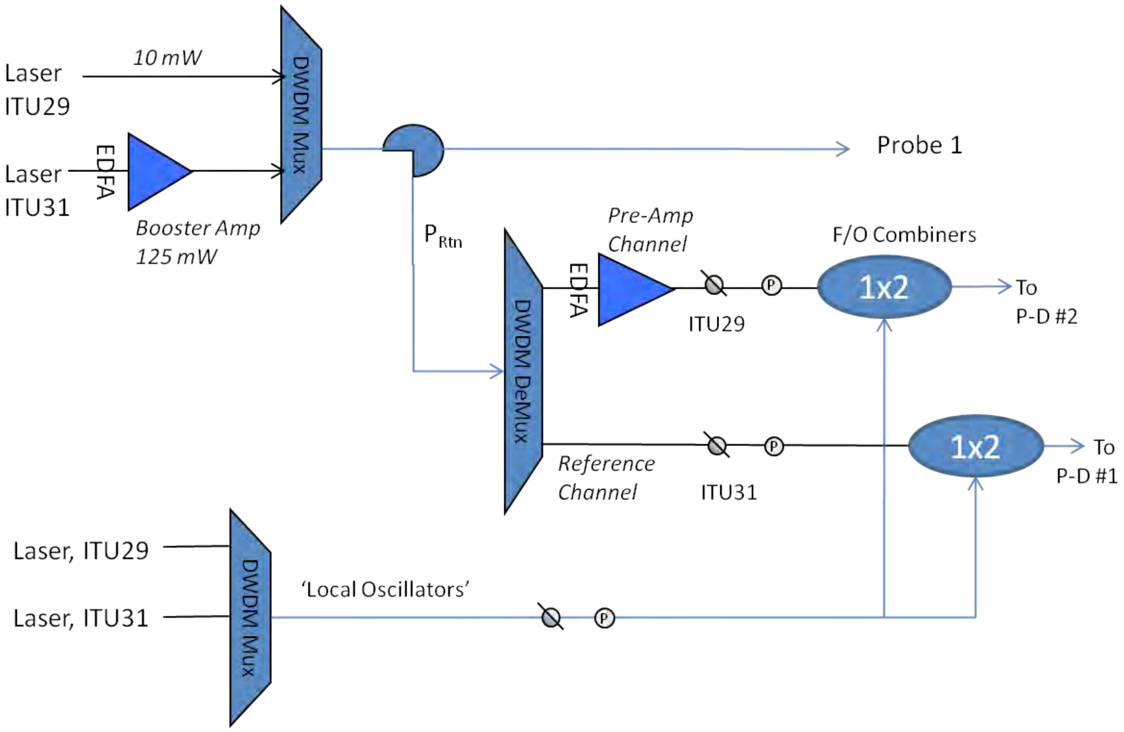

Figure 4. Test setup notional architecture for benchmark measurements

Benchmark Measurements

We compared "conventional" PDV to a laser-safe (seed laser + EDFA preamp) PDV to quantify variations in S/N ratio as well as boundary conditions for low-power operation. To investigate these questions, we used the configuration shown in Figure 4. This allowed for a head-to-head comparison of a high-power conventional PDV (125 mW without preamp) to a laser-safe PDV (10 mW with preamp) using a single probe imaged onto a common target spot of a laser-driven foil. Identical

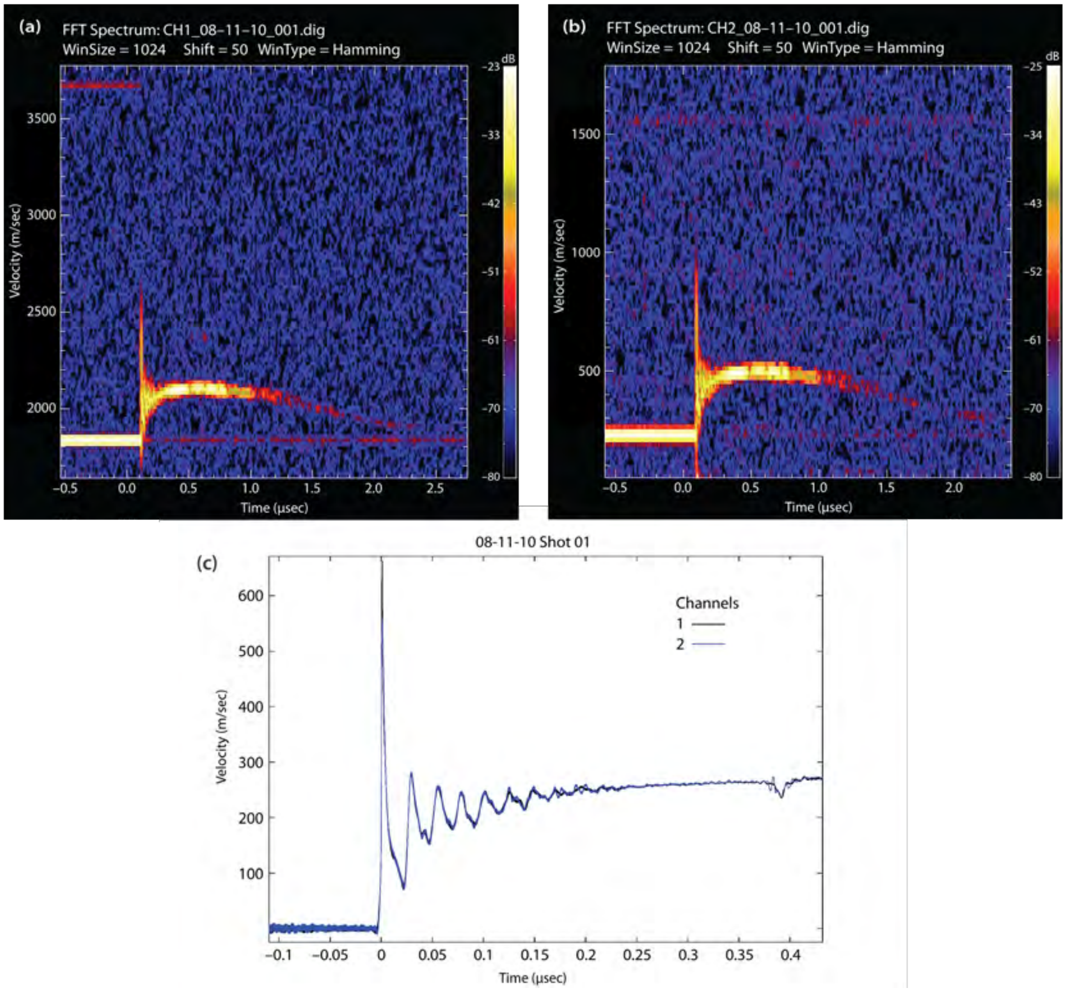

Figure 5. (a) and (b) Raw spectrograms and (c) analyzed data from benchmark measurements comparing laser-safe preamp PDV to conventional high-power "reference" PDV. Spectrogram (a) shows preamp data, (b) shows reference data, and (c) analyzed data is an overlay of both. Due to circulator light leakage, a small amount of non Doppler–shifted light mixed with the Doppler-shifted return and generated subtle artifacts in the spectrogram evident as (a) a non-heterodyne beat frequency and (b) an "extended baseline."

data were input to both systems. We maintained identical optical power from both channels at their respective photodetectors via variable optical attenuators as well as identical local oscillator powers to ensure an accurate comparison. Data were detected with two 13 GHz Miteq photodiodes and recorded onto a 12 GHz digitizer.

To investigate the limits of low-power operation, we attenuated the seed laser output. Our experiments compared the reference PDV channel to the low-power channel with optical return powers (at circulator output) of 500 μW, 10 μW, 1 μW, 100 nW, and 10 nW. To quantify the data, we generated and analyzed a spectrogram via an FFT analysis shown in Figure 5. For return power levels greater than 1 μW we measured no significant difference in S/N ratio, concluding that a seed laser/preamp combination is equivalent to a conventional high-power PDV. For powers ≤100 nW there was a degradation of approximately 8 dB relative to the reference PDV due to increased noise floor. Other laboratory data suggest that optical signal power ~1 nW will approach a S/N ratio limitation for use in a preamplified configuration.

Conclusion

Our investigations showed that frequency and time division multiplexing of PDV data is both a feasible and attractive diagnostic approach that may be economically and effectively accomplished with commercial off-the-shelf (COTS) telecommunications components. Our initial interests grew in scope beyond laboratory evaluations and resulted in the design and fabrication of an MPDV. Wavelength division multiplexing is a practical way to implement frequency multiplexing. Leveraging COTS DWDM components and industry standards provides the MPDV architecture with optically efficient fiber routing, data isolation from cross-talk, and band-pass filtering. Application of narrow line-width seed lasers in conjunction with EDFA preamps has demonstrated data fidelity performance comparable to a conventional PDV as well as laser-safe operations. Optical heterodyning allows flexibility to up-shift or down-shift. The combination of these components and techniques resulted in the design and construction of an MPDV demonstration system. This system is divided into two chassis: a laser chassis containing four laser pairs, and a multiplexing chassis containing DWDMs, fiber delays for time multiplexing, EDFA optical amplification, variable optical attenuators and power monitors, and 20 GHz photodiode detection. This system was designed in such a way as to provide both modularity and flexibility with selectable 2X, 3X, 4X, and 8X multiplexing, or without any multiplexing (conventional approach). We have also included a high laser power option for light-starved experimental applications. The MPDV demonstration system constructed as part of this project will provide a test platform to further investigate multiplexing methodology (topics such as optical gain clamping, polarization control, and system automation) and be a prototype from which to create a first-generation, production MPDV diagnostic system. Our research indicates that frequency and time division multiplexing of PDV is a very promising approach for both large channel count programmatic needs as well as applications outside of the DOE community.

Acknowledgments

We would like to thank David Holtkamp (Los Alamos National Laboratory) and Ted Strand (Lawrence Livermore National Laboratory) for their encouragement and material support.

References

Barker, L. M., "Laser interferometry in shock-wave research," *Exp. Mech.* **12**, 5 (1972) 209–215.

Daykin, E., "Many-point velocimetry using heterodyne techniques," *Nevada Test Site–Directed Research and Development,* FY 2008, National Security Technologies, LLC, Las Vegas, Nevada, 2009, 227–235.

Desurvire, E., *Erbium-Doped Fiber Amplifiers, Principles and Applications*, New York: Wiley-Interscience, 2002.

Strand, O. T., D. R. Goosman, C. Martinez, T. L. Whitworth, W. W. Kuhlow, "Compact system for high-speed velocimetry using heterodyne techniques," *Rev. Sci. Instrum.* **77**, 8 (2006) 083108–083108-8.

MULTILAYER HYBRID COLLOIDAL QUANTUM DOT ALGAN-BASED PHOTODETECTORS

Shayla Sawyer,[1,a,b] *Kevin R. Kyle,*[a] *Liqiao Qin,*[b] *Chris Shing,*[b] *and Stephan Weeks*[a]

Multiple layers of colloidal nanoparticles were used to make large-area, visible-blind, and wavelength-selective planar UV photodetectors. Layers of materials for detecting alpha radiation were also tested as a proof of concept. A specific deposition recipe was used to optimize the characteristics of the photodetectors. A photoconductor based on zinc oxide (ZnO) nanoparticles and aluminum has been fabricated with good UV responsivity due to an internal gain mechanism. Wavelength-selective photodetectors have been created with aluminum gallium nitride and gallium nitride epitaxially grown substrates. Metal-semiconductor-metal (MSM) photodetectors based on polyvinyl alcohol–coated ZnO nanoparticles with gold contacts were created through normal optical lithography and wet-etching. The MSM structure, using interdigitated finger design, achieved approximately three orders of magnitude higher responsivity than that of the fabricated photoconductors. Finally, proof-of-concept experiments were performed in systems requiring high sensitivity in UV wavelengths while blocking ambient light.

Background

The FY 2009 investigation (Sawyer, 2010) of colloidal quantum-dot (nanoparticle)–enhanced UV photodetectors introduced new challenges and expanded the potential for a hybrid material sensor. One particular challenge is in optimizing conductivity among dispersed colloidal nanoparticles (CNPs). There is a trade-off in performance between uniform deposition with low concentrations of nanoparticles and the current carrying capability of high concentrations. Multiple-layer deposition onto the substrate mitigates this trade-off. Our FY 2010 objective was to continue our investigation by using multiple layers of CNPs deposited on quartz and gallium nitride (GaN)–based materials. En route, new potential for layers of different materials emerged. The applications, therefore, broadened beyond light detection into alpha particle detection depending upon the nanoparticle material used. This detector should be visible-blind and could thus be used as part of an alpha-sensitive scintillator. This would eliminate the thin Mylar entrance windows currently used with photomultiplier tube (PMT)–based alpha detectors. The multilayer CNP design will result in a general purpose, UV-sensitive light sensor. Progress toward a rugged, lower-power, compact, multipurpose device array is enabled by this work.

UV detectors have a wide range of applications, such as plasma sensing, biological and chemical analysis, optical communications, astronomical studies, and missile launch detection (Monroy, 2003).

---

[1] sawyersm@nv.doe.gov, sawyes@rpi.edu, 518-276-2164

[a] Special Technologies Laboratory; [b] Rensselaer Polytechnic Institute

Specifically, the results of this project directly affect applications that require high sensitivity in specific UV and blue spectral ranges, namely, biological fluorescence detection and scintillator-based radiation detection. PMTs are commonly used for these applications for their high overall sensitivity across a broad spectral range. However, they are limited by high dark currents, susceptibility to environmental changes, sensitivity to ambient light, low quantum efficiency, large volume, high cost, and high power consumption. Semiconductor-based detectors provide an alternative to PMTs. And wide band-gap materials like zinc oxide (ZnO), GaN, and aluminum gallium nitride (AlGaN) are matched to detect light in the UV range.

Project

Multilayer ZnO Photodetector Performance

In an FY 2009 SDRD project, layers of polyvinyl alcohol (PVA)–coated ZnO nanoparticles (Sawyer, 2010) were deposited onto substrates with a spin-casting process using a Headway 8-inch spin coater in the clean room facility of Rensselaer Polytechnic Institute (RPI). The spin recipe was determined by much iteration followed by material characterization. The resulting best practice, also used in FY 2010, is shown in Table 1.

Table 1. Spin recipe for multilayer ZnO nanoparticles

Layer	RPM	Acceleration Between Steps	Time Per Step (seconds)	Recipe Number
1	0→100→500→1500→3000	100, 100, 200, 500	10, 5, 5, 5	1
2	0→100→500→1000→2000	100, 100, 200, 500	10, 5, 10, 5	2
Anneal in air for 5 minutes at 150°C following Layer 2				
3, 4 (3–6 if needed)	0→100→200→500→800→1000	100, 100, 100, 100, 100	10, 5, 5, 10, 5	3
Anneal in air for 5 minutes at 150°C following Layer 4 (6)				

Photoconductors were made by depositing two irregular 100 nm thick aluminum (Al) contacts, using E-beam via shadow mask, on top of the ZnO nanoparticle film formed as stated above. Point contact current-voltage (I-V) characteristics of samples were measured using an HP4155B semiconductor parameter analyzer under darkness and under illumination of a 340 nm UV LED with an intensity of 45.58 mW/cm^2. These measurements were performed at room temperature in air. Figure 1 is a typical I-V curve of the photoconductors. Figure 2 demonstrates the UV-generated current over dark-current ratios for PVA-coated and uncoated ZnO nanoparticles (Qin, "Ultraviolet photodetection," 2010). PVA-coated ZnO nanoparticles demonstrate a UV/dark current ratio up to 4×10^4.

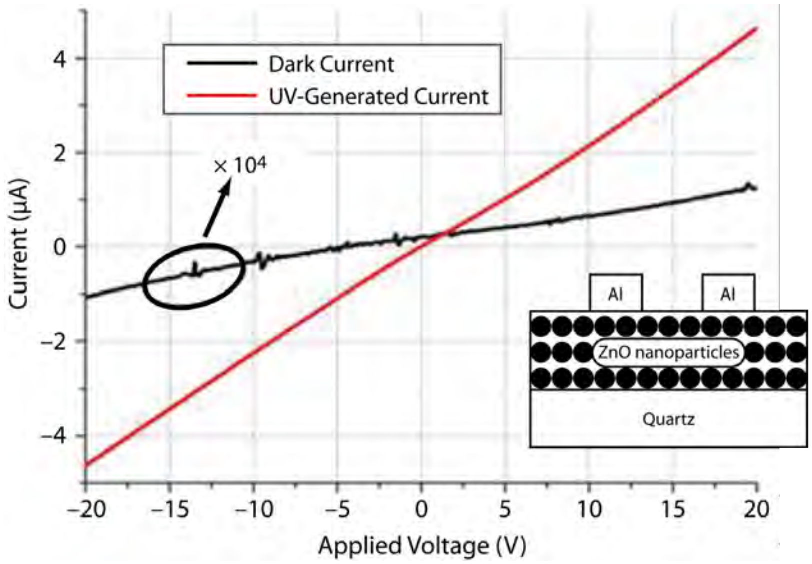

Figure 1. I-V plot of the photoconductor based on PVA–coated ZnO nanoparticles dispersed in ethanol and spin-cast onto quartz. The plot shows the expected linear I-V response and the UV-generated current to dark current ratio over four orders of magnitude. Inset: Schematic of device on quartz substrate (Qin, "Ultraviolet photodetection," 2010).

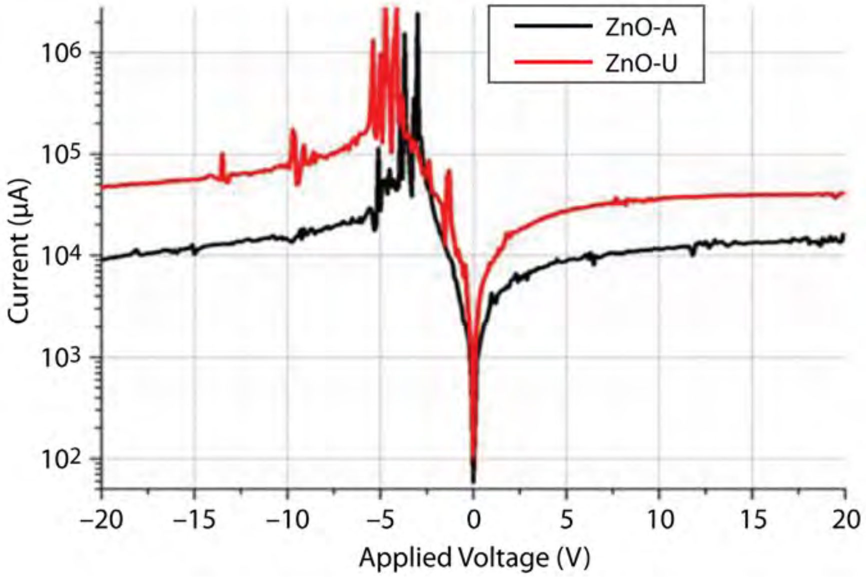

Figure 2. The ratio of UV-generated current to dark current of photoconductor based on uncoated ZnO nanoparticles (ZnO-A) and PVA–coated ZnO nanoparticles (ZnO-U) dispersed in ethanol and spin-cast onto quartz, respectively (Qin, "Ultraviolet photodetection," 2010).

Figure 3 demonstrates that the spectral response of the photoconductor on a quartz substrate biased at 20 V exhibits a low-pass response with two peak values at 260 nm and 375 nm. The peak at 375 nm corresponds to the band gap energy of ZnO.

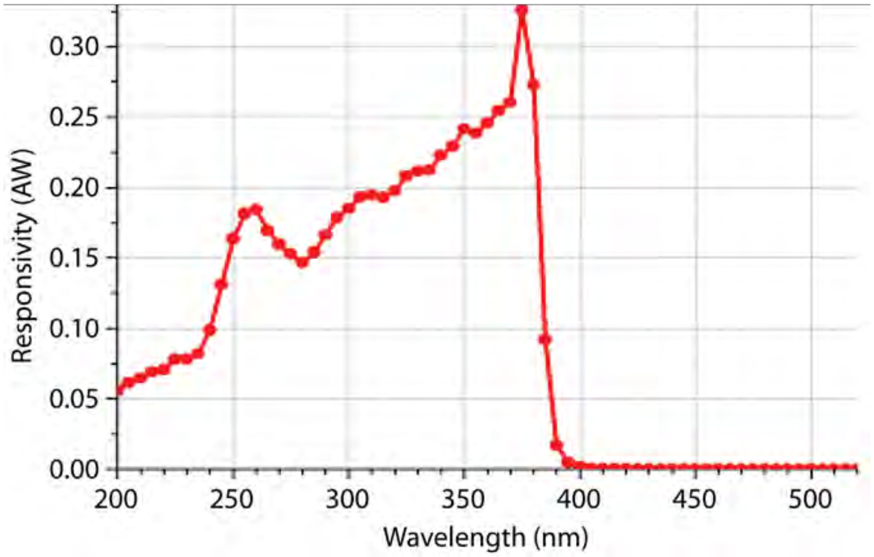

Figure 3. The spectral response of the photoconductor based on ZnO nanoparticles dispersed in ethanol and spin-cast onto quartz shows visible-blind low-pass performance

A similar fabrication process was used with multiple layers of spin-cast ZnO nanoparticles and Al contacts on AlGaN and GaN epitaxial substrates. The substrates were fabricated by SET, Inc. with targeted cut-off wavelengths of 300 nm and 360 nm, respectively. The schematic of the complete device on AlGaN is shown in Figure 4.

This wavelength-selective response is related to the absorption properties of the substrate and the ZnO nanoparticles when illuminated through the backside. When the wavelength of incident light is shorter than 300 nm, the absorption cut-off wavelength of AlGaN, the light is absorbed by AlGaN and electron-hole pairs are generated within the AlGaN alone (Figure 5). But these photo-generated carriers do not have a conduction path to the contacts that are deposited on top of ZnO nanoparticles; thus, there is no current generated. For incident light with wavelengths longer than 300 nm but shorter than 380 nm, the light penetrates the AlGaN and reaches the ZnO active layer to generate current. Incident light with wavelengths longer than the cut-off wavelength of ZnO penetrates the AlGaN but is not absorbed by the ZnO layer; therefore, no current is generated (i.e., visible-blind photodetection). This band-pass response can be applied for detecting specific wavelengths without the use of external filters, thus making the system simpler and further minimizing spectral noise in system applications requiring sensitivity to selected wavelengths. A similar response was

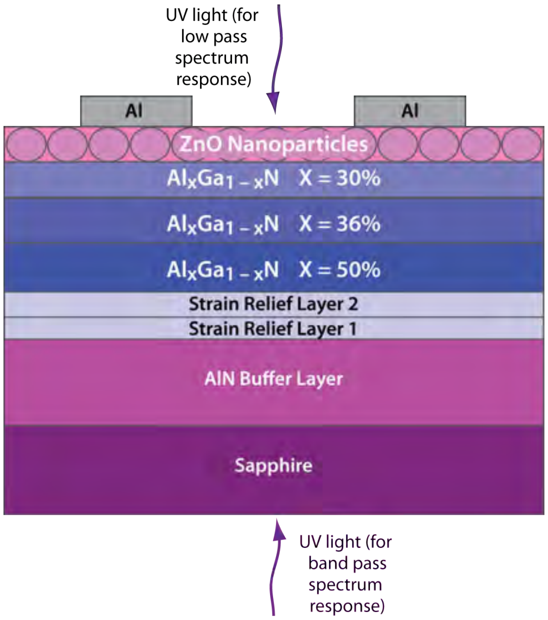

Figure 4. Schematic of photoconductor based on AlGaN (Qin, "Enhanced UV," 2010)

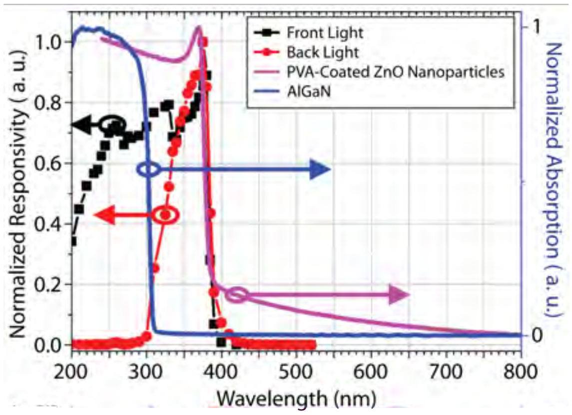

Figure 5. Front/back-illuminated photoconductors based on PVA-coated ZnO spin-cast on AlGaN substrate, exhibiting low-pass (black square) or band-pass (red circle: 300–380 nm) response as it relates to the absorption spectra of AlGaN (blue line) and ZnO (pink line) (Qin, "Enhanced UV," 2010)

demonstrated with a GaN substrate with a band-pass response from 360 to 380 nm. Therefore, wavelength selectivity can be tuned by altering the material of the substrate and the nanoparticles. The responsivity of the photoconductor with an AlGaN substrate in the UV range is twice that of a commercial UV-enhanced silicon photodiode when illuminated on the front side. The responsivity peak is as high as 0.8 A/W at 375 nm.

Metal-semiconductor-metal (MSM) photodetectors were created with the fabrication of gold Schottky contacts on the ZnO nanoparticle surface. Typically, MSM devices have shorter response times, smaller dark currents, and higher signal-to-noise (S/N) ratios than photoconductors. Schottky contacts, which require overcoming a potential barrier to conduct, are specified by the respective work functions of the contact and semiconductor material. However, fabrication of reproducible Schottky contacts, especially high-resolution interdigitated contacts on solution-processed ZnO nanoparticles, is often difficult to achieve. Surface defect states, residual surface contamination, and the interfacial gap between the metal and semiconductor dominate in nanoparticle devices, causing unpredictability in I-V characteristics (Jun, 2009). PVA-coated, ZnO-nanoparticle–based MSM photodetectors with different interdigitated electrodes created by traditional optical lithography and wet-etching were demonstrated on a quartz substrate. Figure 6a shows the device schematic, optical mask, and an image of the deposited contact on ZnO. Six device layouts with varying area, finger length, finger width, and finger spacing were characterized and compared for their UV/dark current ratio as summarized in Table 2.

Table 2. Parameters of each MSM device layout created

Device Number	Area	Finger Length	Finger Width	Finger Spacing	UV/Dark Current Ratio
A5	125 µm × 125 µm	117 µm	5 µm	5 µm	1.19×10^7
A6	125 µm × 125 µm	117 µm	5 µm	7 µm	3.85×10^6
A8	125 µm × 125 µm	117 µm	7 µm	5 µm	1.14×10^7
A7	125 µm × 125 µm	117 µm	7 µm	10 µm	4.51×10^6
A2	250 µm × 250 µm	242 µm	5 µm	7 µm	4.80×10^7
A3	250 µm × 250 µm	242 µm	7 µm	10 µm	1.34×10^8

Figure 6b is the typical nonlinear exponential response of the MSM devices. The UV/dark current ratio is significantly higher, at least three orders of magnitude, than that of the photoconductor. Similarly, the spectral response showed a marked improvement. A responsivity of 732 A/W with an incident light intensity of 216 nW/cm^2 at 345 nm was demonstrated. This high responsivity is attributed to internal photoconductive gain due to the presence of oxygen-related hole-trap states at the nanoparticle surface and the high-resolution interdigitated electrodes. The adsorbed oxygen molecules on the ZnO nanoparticle surface capture free electrons to form chemisorbed oxygen

$[O_2(g) + e^- \rightarrow O_2^-(ad)]$. When light is absorbed, electron-hole pairs are generated at the nanoparticle surface. The oxygen-related hole-trap states neutralize the chemisorbed oxygen $[h^+ + O_2^-(ad) \rightarrow O_2(g)]$ and prevent charge-carrier recombination, prolonging the lifetime of the photo-generated carrier (Soci, 2007). In addition, the reduced traveling distance of carriers to closely spaced finger contacts created by the optical lithography, in contrast to contacts via shadow mask, also decreases the recombination possibility of generated carriers. The results demonstrate that reproducible, high-sensitivity, visible-blind MSM UV photodetectors based on solution-processed ZnO nanoparticles can be fabricated by using traditional contact patterning and deposition techniques.

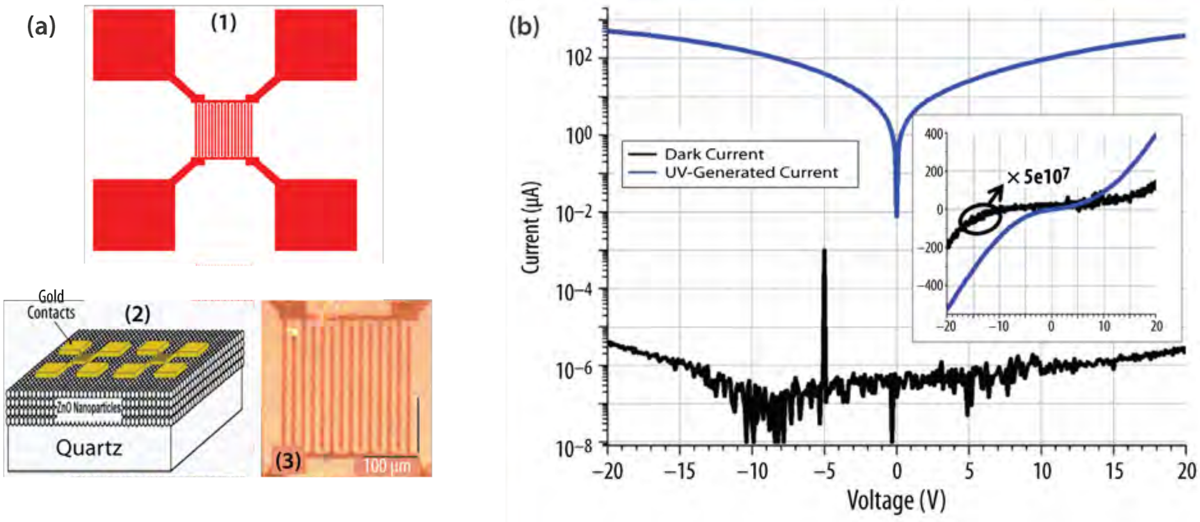

Figure 6. (a) (1) A pair of interdigitated fingers in the optical mask, (2) schematic of the MSM device, and (3) picture of deposited gold contact. (b) Typical nonlinear exponential I-V response of an MSM detector (Device #A3 in Table 2) showing a UV/dark current ratio as high as eight orders of magnitude (Qin, "Enhanced UV," 2010).

The ZnO multilayer device responsivity was compared to commercially available photodetectors with UV response. Figure 7 shows that both the AlGaN-based photoconductor and the MSM detector have better responsivity than a UV-enhanced photodiode but are far from the responsivity of a PMT. However, these detectors come with the advantage of a lack of response to ambient light. For some applications, such as biofluorescence detection, the S/N ratio is greatly enhanced by a filterless photodetector with a selective wavelength response.

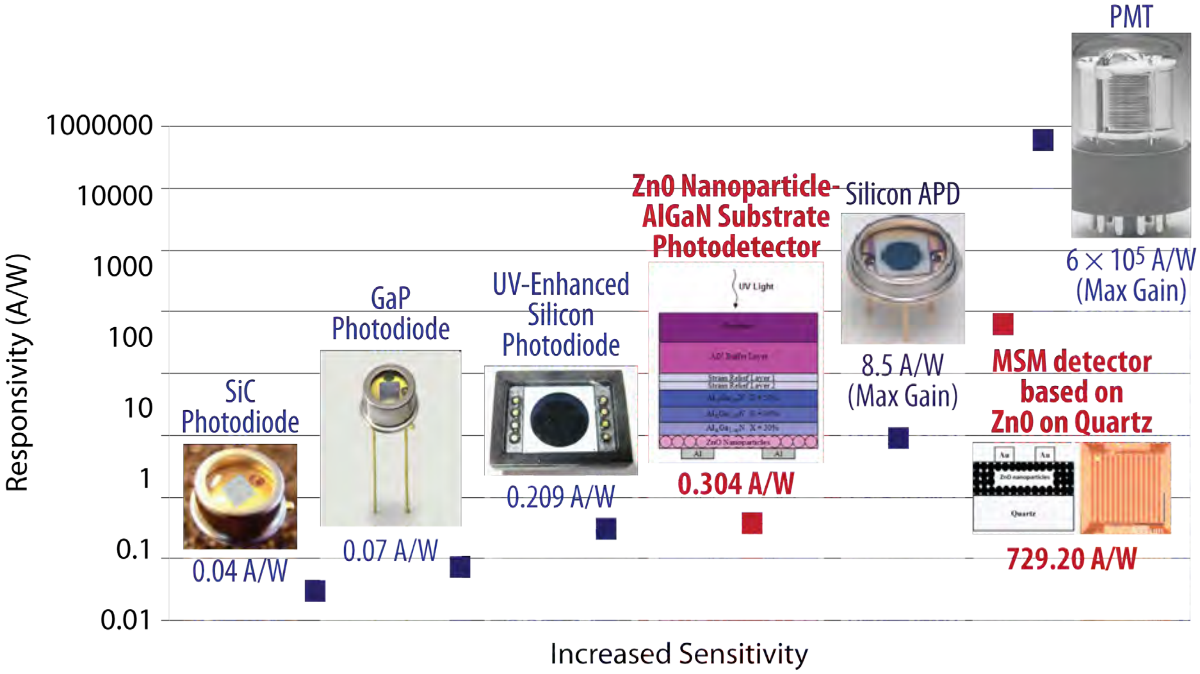

Figure 7. Responsivity of commercial photodetectors (data points shown in blue) compared to the ZnO nanoparticle-based photodetectors (under 20 V bias; data points shown in red) at 340 nm. The PMT detector has the greatest sensitivity. Other devices attempt to achieve this sensitivity while maintaining compact size and low power consumption. Added wavelength sensitivity in addition to this level of sensitivity for many applications would be ideal.

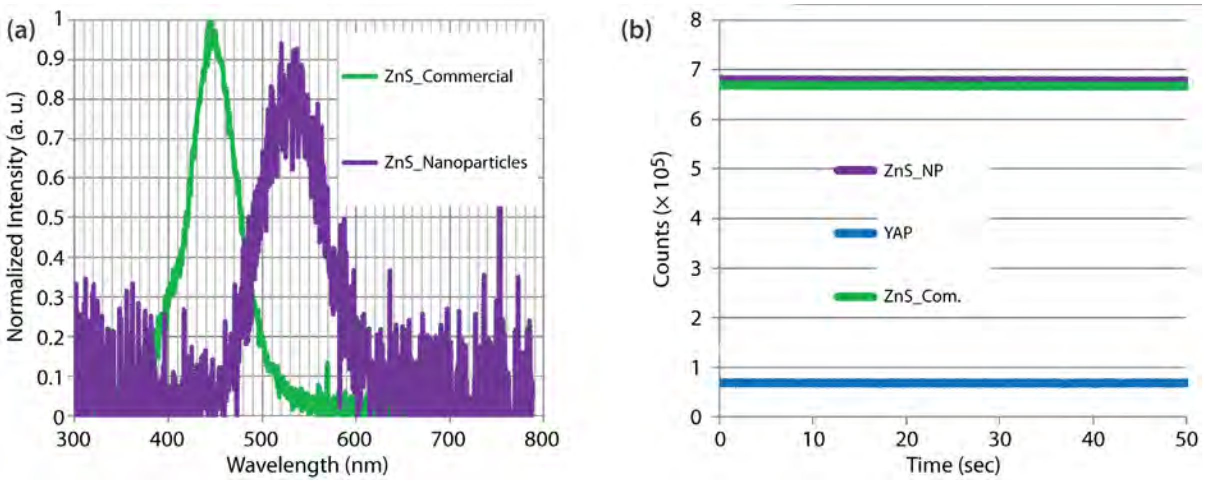

Figure 8. (a) Emission spectrum of ZnS:Ag scintillators excited by an alpha particle source (^{210}Po, 500 µCi); (b) light intensity of three scintillators excited by an alpha particle source measured by a counting PMT

Alpha Particle Scintillator Detection

The direct coupling of alpha particle scintillator material with a visible-blind nanoparticle photodetector was demonstrated. Initially, the brightest and most well-known scintillator material (ZnS:Ag) for alpha particles was obtained and nanoparticles were produced. After spectral analysis and characterization of its light output, it was compared with another UV-emitting scintillator, YAP:Ce. The results are shown in Figure 8. Finally, the YAP:Ce scintillator was coupled to the UV detector. A UV-generated current-to-dark-current ratio of about 4 at 30 V bias was observed, as shown in Figure 9. In future work, the ZnS:Ag scintillator material will be detected by a nanoparticle detector created for blue or green response by altering the material content from ZnO to CdZnO. Better light coupling to the photoconductor may increase the UV/dark current ratio.

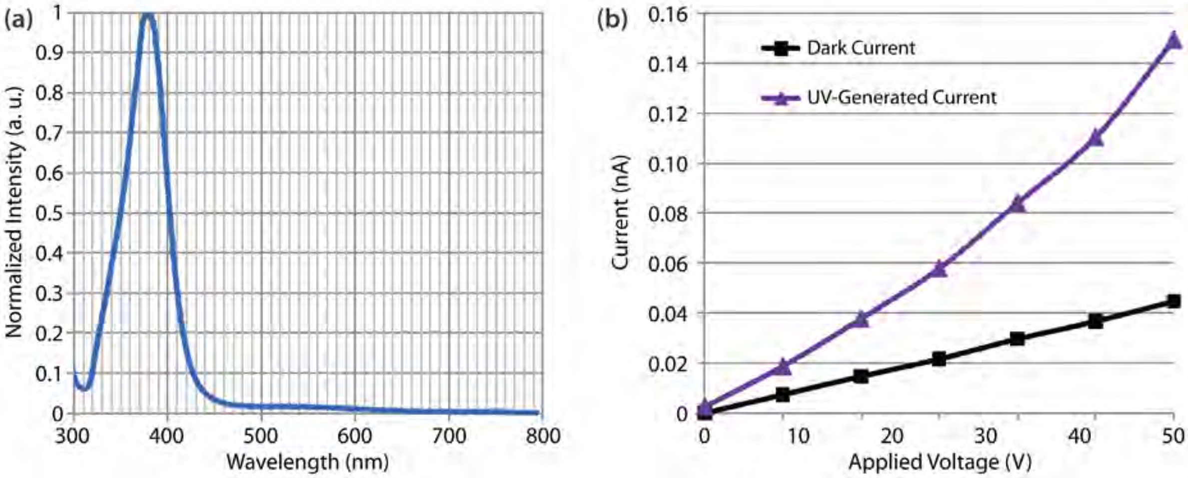

Figure 9. (a) Emission spectrum of YAP:Ce excited by a 280 nm LED. The emission light aligns with the spectral response of the ZnO nanoparticle-based photodetectors; (b) YAP:Ce light emission detected by the ZnO nanoparticle-based photoconductor (under 30 V bias) when the scintillator is excited by an alpha particle source (^{210}Po ~400 µCi).

Conclusion

The feasibility of large-area, visible-blind, and wavelength-selective planar UV photodetectors based on ZnO colloidal nanoparticles was studied. A specific spin-casting recipe has been investigated to create multilayer ZnO nanoparticles suitable for UV photodetection. Photoconductors based on ZnO nanoparticles and Al have been fabricated and characterized. Good UV responsivity was demonstrated due to the internal gain mechanism of nanoparticles. Low-pass and band-pass wavelength-selective alternative photodetectors with GaN-based substrates have been achieved by illuminating detectors through different directions. A normal lithography and wet-etching method has been well applied in fabricating finger contacts for MSM photodetectors based on PVA-coated

ZnO nanoparticles and gold. Approximately three orders of magnitude higher responsivity has been achieved over the photoconductors. The application of wavelength-selective photoconductors in a compact semiconductor-based detection system demonstrated the benchmark of detectors in a real system requiring a sensitive detector, even though the gain of the photoconductor is less than that of a PMT. The proof-of-concept experiment indicates the potential application of colloidal nanoparticle-based scintillator detectors. This work contributed to a total of three submitted peer-review journal papers (Qin, "Enhanced UV," 2010; "Ultraviolet photodetection," 2010; "Shortpass," in preparation), a conference proceedings paper (Qin, "MSM," 2010), and an invited paper to be included in a book (Sawyer, 2009). In addition, there were three conference abstracts submitted and five conference presentations.

Acknowledgments

We would like to thank Professor Partha Dutta of RPI for providing nanoparticle samples and advice, Dr. Max Shatalov of SET Inc. for the GaN and AlGaN substrates, and the Connection One National Science Foundation–funded Industry/University Cooperative Research Center.

References

Jun, J., H. Seong, K. Cho, B. Moon, S. Kim, "Ultraviolet photodetectors based on ZnO nanoparticles," *Ceramics International* **35**, 7 (September 2009) 2797–2801.

Monroy, E., F. Omnès, F. Calle, "Wide-bandgap semiconductor ultraviolet photodetectors," *Semiconductor Science and Technology* **18**, 4 (March 2003) R33–R51.

Qin, L., C. Shing, S. Sawyer, P. S. Dutta, "Enhanced UV sensitivity of ZnO nanoparticle photoconductor by surface passivation," *Optical Materials,* accepted (September 2010).

Qin, L., C. Shing, S. Sawyer, "MSM ultraviolet photodetectors based on ZnO colloidal nanoparticles," *IEEE Electron Device Letters,* submitted and in final review (September 2010).

Qin, L., C. Shing, S. Sawyer, "Shortpass and bandpass photodetectors on ZnO nanoparticle on AlGaN/GaN substrates," in preparation.

Qin, L., C. Shing, S. Sawyer, "Ultraviolet photodetection based on ZnO colloidal nanoparticles made by top-down wet-chemistry synthesis process," *2010 Symposium on Photonics and Optoelectronics (SOPO)*, Chengdu, China (June 2010).

Sawyer, S., K. Kyle, L. Qin, C. Shing, S. Weeks, "Hybrid colloidal quantum dot AlGaN–based photodetectors," *Nevada Test Site–Directed Research and Development,* FY 2009, National Security Technologies, LLC, Las Vegas, Nevada, 2010, 201–210.

Sawyer, S., L. Qin, C. Shing, "Zinc oxide (ZnO) nanoparticles for UV photodetection," *Special Issue of the International Journal of High Speed Electronics, Workshop on Frontiers in Electronics*, World Scientific, Ricon, Puerto Rico (December 14, 2009).

Soci, C., A. Zhang, B. Xiang, S. A. Dayeh, D. P. R. Aplin, J. Park, X. Y. Bao, Y. H. Lo, D. Wang, "ZnO nanowire UV photodetectors with high internal gain," *Nano Letters* **7**, 4 (March 2007) 1003–1009.

this page intentionally left blank

RADIATIVE DECAY ENGINEERING FOR IMPROVED SCINTILLATORS

Clare Kimblin,[1,a] *Larry Franks,*[b] *and James Tinsley*[a]

The goal of this project was to determine whether metal nanoparticles can be used to enhance emission from organic scintillators by a process known as metal-enhanced fluorescence. The focus has been on increasing the excitation/emission of commonly used scintillator solvents since transfer of energy from ionizing radiation to the bulk medium (solvent) is generally only ~2% to 3% efficient (Birks, 1964). Finite-difference time-domain simulations were performed to determine the most appropriate metal and nanoparticle (NP) size for optimal enhancement of toluene excitation/emission. Aluminum-NP (Al-NP) photo-induced fluorescence enhancement (up to 2-fold) was demonstrated using 265 nm excitation with Al-NPs of 14 to 21 nm in size. Ionizing radiation tests have subsequently been performed to determine if Al-NPs also enhance emission when ionizing radiation is used as the excitation source. With the Al-NP–coated substrates available to us, we did not observe evidence that Al-NPs increase scintillation. Experiments involving a suspension of colloidal metal NPs of a larger, more optimal size should be performed to address this question.

Background

Nuclear radiation detection and radiography would benefit from brighter and faster scintillators. For low-yield sources and pulsed-power experiments, short decay times are also required for positive identification by coincidence counting and for improved diagnostics. Better time resolution allows for better discernment of actual versus random coincidence because proportionally fewer random coincidences will contribute to signals received in a narrower time window. Generally speaking, inorganic scintillators, though bright, are not fast. Conversely, organic scintillators are fast, but not very bright. With inorganic scintillators, ionizing radiation transfers energy to the bulk medium fairly efficiently (on the order of 10% efficiency), whereas for organic scintillators only a small fraction (2%–3%) (Birks, 1964) excites the emissive solvent to the singlet excited state. Because liquid and plastic organic scintillators are suitable for large-area detection of radiation and are generally less expensive and easier to assemble than inorganic scintillators, improving their scintillation output, while maintaining or decreasing decay times, would be of great value.

It has been demonstrated by Geddes (2002; 2005) and others (e.g., Glass, 1980; Lakowicz, 2005; 2008) that suitably tuned metal nanoparticles (MNPs) can be used to increase emission and reduce the decay time of fluorophores that are in close proximity (<30 nm from the MNP) by a process analogous to surface-enhanced Raman scattering. The series of experiments performed in an FY 2009

---

[1] kimblicw@nv.doe.gov, 805-681-2257

[a] Special Technologies Laboratory; [b] Great Basin Technologies, Inc.

SDRD project (Kimblin, 2010) and those described in this report have sought to determine whether metal-enhanced fluorescence (MEF) (typically applied to biological assays [Aslan, 2005]) can also be used to enhance emission from scintillators by tuning the metal and nanoparticle (NP) size to match the solvent and excitation/emission wavelengths.

In FY 2009, finite-difference time-domain (FDTD) simulations were performed by our collaborators in the Geddes group at the University of Maryland Biotechnology Institute (UMBI) to determine metal and NP size for optimal enhancement of excitation/emission from toluene, a common scintillator solvent (Kimblin, 2010). Simulations indicated that indium (In) (180 nm diameter) and aluminum (Al) (~90 and 180 nm diameter) NPs are most suitable for enhancement of toluene emission. In- and Al-NP–coated slides were provided by the Geddes lab, and the ensuing FY 2009 experiments demonstrated fluorescence enhancement from toluene (~10-micron-thick toluene path length; see sample configuration in Figure 1) in contact with In (up to 1.4-fold reported by UMBI with toluene; however, negligible enhancement was observed at Special Technologies Laboratory [STL]) and Al-NP films (1.6- to ~2-fold observed repeatedly by STL and UMBI). A claim that 3.6-fold enhancement was observed with Al-NP substrates (15 nm “thickness,” based on the measured change in mass) at UMBI could not be substantiated at STL.

Project

After visiting the UMBI lab, it appears likely that differences in the preparation of control and NP slide samples may have led to the misleading 3.6-fold enhancement result, reported last year (Kimblin, 2010), for Al-NP substrates. We observed that slight differences in the volume of solvent sandwiched between two slides can significantly affect emission intensity. This is because MEF is reported as the ratio of fluorescence intensity in the presence of NPs to the fluorescence intensity in the absence of NPs (a blank slide), and solvent emission can be reabsorbed by the solvent (particularly in the absence of a Stokes-shifting solute). NSTec samples were generally prepared with either 20 or 25 µL of solvent or scintillator solution per 75 × 25 mm slide. Figure 1 shows a scintillator sandwiched between an Al-NP–coated slide (top) and a quartz slide (bottom, 1 mm thick). Even with carefully measured and prepared samples, air bubbles and some solvent/solution overflow sometimes appeared when the top slide was lowered onto the solvent/solution on the lower slide. Fluorescence measurements made on multiple samples were made to control for this.

Photo-Induced Fluorescence Studies

Particle surfaces were characterized by atomic force microscopy (AFM). AFM images obtained from Asylum Research (Santa Barbara, California) and the University of California, Santa Barbara (UCSB) demonstrated that the In-NP surface was uniformly coated with an array of ~20 nm diameter particles (Figure 2a), but that the Al-NP surfaces were composed of large clusters of ~15–20 nm diameter NPs (21 nm Al, 0.3 nm/sec deposition rate, Batch Y; Figure 2b). In an attempt to produce larger particle sizes, UMBI provided substrates made at a higher deposition rate (0.8 nm/sec). However, these

NP surfaces were less uniform, with *clusters* of particles ranging in size from 30 to 100 nm wide. In all cases, individual particle sizes were well below the optimal diameters determined by FDTD simulations. As part of the current work, UMBI also provided some Al-NP–coated (21 nm, 0.3 nm/sec) quartz microscope slides (1 mm thick) and quartz cover slips (~0.25 mm thick).

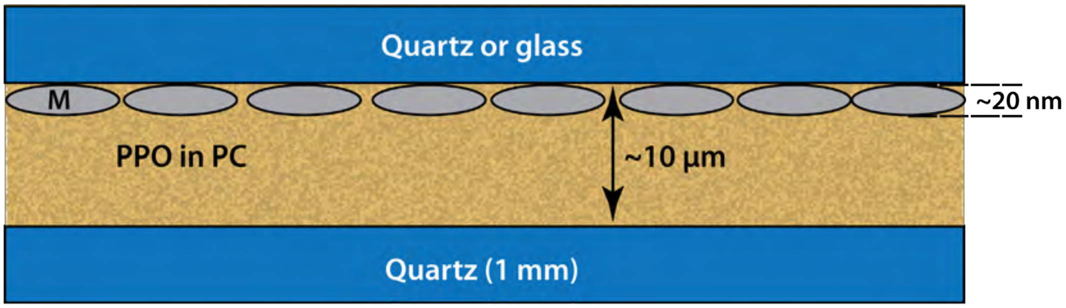

Figure 1. For fluorescence measurements, scintillator solvent (toluene, mesitylene, or pseudocumene [PC]), or a solution of 2,5-diphenyloxazole (PPO) in PC, was sandwiched between an Al-coated top slide (glass or quartz) or cover slip and a quartz base slide. Scintillator sandwiched between an uncoated slide (glass or quartz) or quartz cover slip and a quartz base was used as a control. Scintillation measurements employed a PPO in PC sandwich.

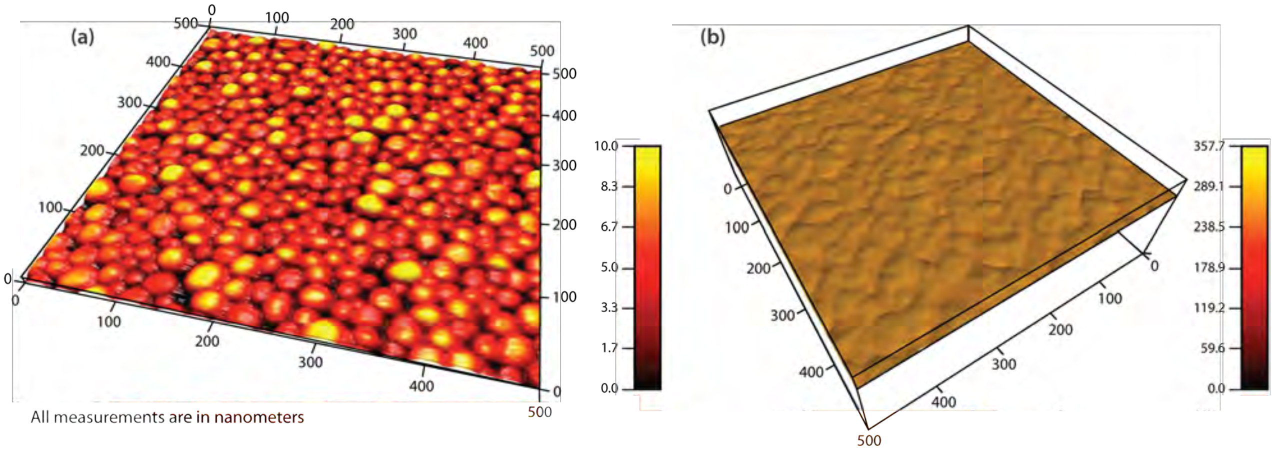

Figure 2. (a) AFM image of Batch 2 In (15 nm) (Asylum Research); cross section indicates ~20 nm diameter particles. (b) AFM image of Batch Y Al (21 nm, 0.3 nm/sec deposition rate) (UCSB). Clusters of 15 to 20 nm diameter particles were observed.

This year we also studied the scintillation of mesitylene (1,3,5-trimethylbenzene) and pseudocumene (PC; 1,2,4-trimethylbenzene) with and without 2,5-diphenyloxazole (PPO). These solvents were chosen over toluene due to their lower vapor pressure and, hence, their decreased propensity to evaporate during experimentation. (The solvents' refractive indices and absorbance and emission wavelengths are still very close to those of toluene; thus, FDTD simulations performed for toluene are still valid for mesitylene and PC.) MEF of up to 2-fold was observed with mesitylene and PC. Al-NPs deposited at faster rates tended to give better enhancement (2-fold); however, AFM images indicated that the NP size distribution varied greatly, and a more uniform size distribution was desired for this study. As a control for far-field reflectance, we also obtained Al mirror-coated slides from a commercial vendor (AccuCoat, Inc.). Slides were coated with Al (150 nm thick) and a protective layer of silicon oxide (SiO) (100 nm thick). The mirrored slides' nontransparent mirrored surface had the same dimensions as the Al-NP and control slides. The mirrored slides were more reflective than the Al-NP slides, and they provided MEF values on par with those observed with the Al-NPs. This suggests that the enhancement we observed with the Al-NPs was not simply a near-field effect and was also, in part, due to far-field reflectance. Generally near-field fluorescence is used to indicate distances much less than the wavelength of emitted radiation. Here, near-field and far-field are related to the distances between NP and fluorophore at which enhancement is observed. In this case, near-field fluorescence is ~50 nm from the surface of the NP, and far-field relates to distances >50 nm.

Because parameters for vapor deposition of optimally sized NPs were not known and recent observations show that greater metal-enhancement factors are recorded with increased power of the excitation source (Geddes, 2009), we elected to perform ionizing radiation studies with the available Al substrates. We had hoped to work with a colloidal suspension of ~180 nm Al-NPs, but the Geddes lab had not worked with Al colloids previously, and time and funding did not permit development of this capability at UMBI. (Note: It has since been found that suitably sized suspensions of Al-NPs may be available at Lawrence Berkeley National Laboratory [Gonzalez, 2007], giving us an alternative in the case of further studies.)

Ionizing Radiation Studies

These studies employed samples prepared using the same sample preparation techniques and sample cartridge used for the fluorimeter studies. However, whereas sufficient fluorescence signal could be obtained in the photo-induced fluorescence studies of neat solvents, PPO (1.5 g/L of PC) was added as a wavelength shifter to improve the detectability of ionizing radiation-induced signals. As with fluorescence studies, 25 μL of solution were generally sandwiched between a 75 mm long × 25 mm wide × 1 mm thick quartz (or glass) base slide, and a 75 × 25 × 1 mm top slide, which was either uncoated, coated with Al-NPs, or coated with 150 nm Al and a 100 nm layer of SiO (from AccuCoat, 2–3 nm/sec Al deposition rate). The latter slide provided a nontransparent mirrored surface. Because MEF is a near-field effect, ionizing radiation studies dictated that we study thin layers of scintillator as was done in the photo-induced fluorescence studies. While use of a greater volume of scintillator would have increased the signal overall by providing greater interaction between the ionizing radiation and the scintillator, it would have "diluted" the near-field effect we were attempting to observe. A ^{90}Sr beta source was selected for measurements. (A test run with a ^{133}Ba gamma source demonstrated that the ^{90}Sr betas interacted more with the thin layer of scintillator than did the gammas.)

Counting was performed using a side-on photomultiplier tube (PMT) (Hamamatsu 1P28) biased to −800 V, whose output was filtered and amplified with an ORTEC Model 570 shaping amplifier (2 µs shaping time, 150X gain). The signals were digitized and histogramed using the Health Physics Instruments "Rainbow" 10-bit multichannel analyzer. The sample, source, and PMT were set up in a light-tight box, which was also covered with black fabric to ensure that the exterior lighting did not affect the measurements. The PMT was held at bias in complete darkness for several days until the measured "dark current" reached a minimum. The beta source was collimated using a cylindrical Al shield that fit on top of the slide cartridge. The beta source could be raised and lowered within the shield, but was positioned such that the source was flush with the bottom of the collimator shield. Figure 3 shows a schematic of the experimental setup. Due to the constraint that only a thin layer of scintillator solution be studied (for which the emission was expected to be weak) data collection times of 16 to 75 minutes were used to acquire statistically significant numbers of events.

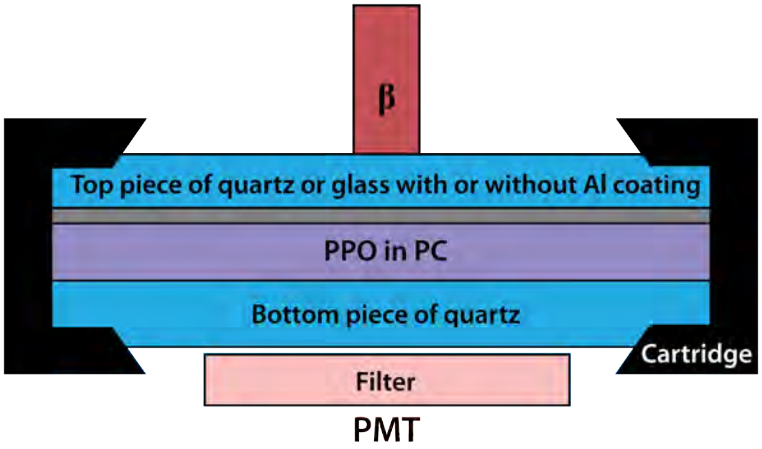

Figure 3. Schematic representing the setup used in ionizing radiation studies. A layer of PPO in PC is sandwiched between a top slide (or cover slip) and a bottom quartz slide. Al-NPs or a 150 nm thick layer of Al (coated with 100 nm SiO) are represented by the gray line. Control experiments were performed with a blank top slide or cover slip.

An initial study compared scintillator emission when the scintillator was in contact with blank quartz, Al-NP–coated quartz (Batch Y-U, 21 nm, 0.3 nm/sec), and Al mirror-coated quartz. We did not simply compare emission from the three different slide types with PPO solution. This is because a significant background signal was observed from interaction of the beta source with the slides alone, and the spectrum induced in PPO solution was determined to lie under the background signal peak, such that it could not be spectrally separated. Furthermore, the background (no PPO) signal was not the same for each slide type; it was greatest in the absence of Al, and smallest in the presence of the mirror-coated slide, as will be discussed. To account for the differences in background signals, the difference in signal obtained with the PPO solution and without the PPO solution was compared for each slide type. Difference plots for each substrate type with and without the PPO solution are shown in Figure 4.

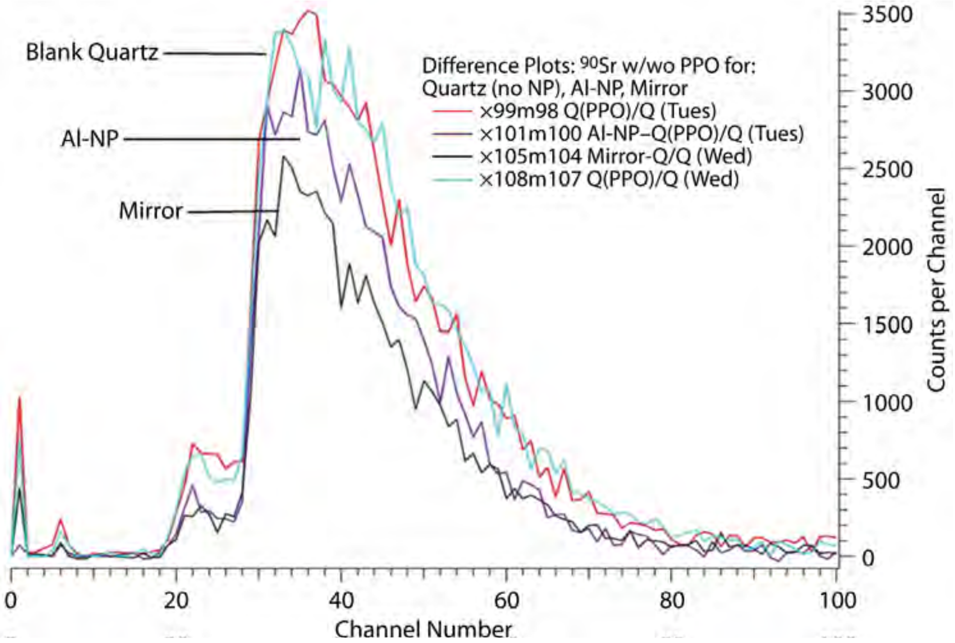

Figure 4. Comparison of difference plots for a blank quartz top slide, with and without the PPO solution (light blue and red), Al-NP–coated quartz with and without the PPO solution (purple), and Al mirror-coated quartz with and without the PPO solution (black). Runs were 60 minutes in duration.

The results shown in Figure 4 were not as expected. The signal is greatest in the absence of Al. If other factors were not at play, then it was expected that the mirror-coated slide would enhance the scintillation signal over the blank slide (in fact, mirror coatings are sometimes used to reflect scintillation signals toward the PMT). The fact that we did not observe this, and that the background signal (no scintillator) was greatest with the blank slide and least for the mirror-coated slide, indicated the presence of Cerenkov radiation. (It is possible that scintillation/fluorescence induced in the slides by beta particles also contributed to background signal.) We had anticipated the Cerenkov light background and, for the measurements shown in Figure 4, had used a filter to block light below 270 nm from entering the PMT. However, the filter (due to its placement directly in front of the PMT) could not prevent Cerenkov-induced fluorescence in the PPO solution. Because results with no solution present indicate that the Al-NPs and the Al mirror-blocked Cerenkov radiation from the top slide, with the mirror being most obstructive, we recognize that Cerenkov-induced fluorescence of the PPO solution would be least for the Al mirror-coated slide and also reduced for the Al-NP–coated slide. We therefore attempted to reduce the amount of Cerenkov fluorescence generated by (a) choosing a source with lower E_{max}, (b) using thin cover slips (blank and Al-NP coated) instead of microscope slides, and (c) using a longer wavelength filter. These results are described next.

Because the Cerenkov threshold in glass or quartz is ~180 keV for beta particles (and ~310 keV for gamma rays capable of generating electrons above the Cerenkov threshold by Compton scatter [Knoll, 2000]), a source with energy below this threshold was sought. ^{133}Ba, ^{241}Am, and ^{57}Co were available, and counts in the presence of the slide cartridge (in the absence of the scintillator) were recorded with these sources (Table 1). This signal was compared to the signal obtained from a PPO reference solution with a path length of 1 cm. As expected, Cerenkov radiation did not contribute to the signal observed with ^{57}Co (E_{max} = 122 keV), but the source was too weak to provide appreciable counts in the presence of the scintillator. With ^{241}Am, substantial scintillation (presumably generated by alpha interaction with impurities in the slides) was observed relative to the signal obtained from the reference PPO solution, so it was also deemed unsuitable. This signal was 10% higher when the top slide was glass versus quartz. Because standard glass is expected to fluoresce more than quartz,

Table 1. Comparison of scintillation counts with various sources for the PPO solution in a 1 cm path length cuvette, background signal (no PPO solution) observed with either a glass or quartz slide on top, and quartz at the base. In the absence of a source, the true background signal was ~3700 counts. Color coding indicates sources with energies above the Cerenkov threshold (orange) vs sources with energies below the Cerenkov threshold (green).

Source	Decay mode and E_{max} (keV) of particle(s)	Activity* (Curies)	Maximum counts with PPO (1 cm path length)	Maximum counts no PPO
^{133}Ba (γ)	γ (356 (65%), 384 (<35%))	8.76 E-5	48,000	5584 (glass)
^{90}Sr	β (546 (direct), 2284 (via Y-90))	6.22 E-5	31,000	9600 (quartz)
^{241}Am	γ (59.5), α (5485)	1 E-4	13,700	7561 (quartz) 8467 (glass)
^{57}Co (γ)	γ (136.5)	2.4 E-6	4300	3759 (quartz)

*Measured on May 7, 2009

this further suggests, in the case of ^{241}Am, that the slide itself was emitting (i.e., the signal was not just Cerenkov induced). ^{133}Ba produced lower background counts than ^{90}Sr, but interaction between gamma rays and a thin layer of scintillator solution was not significant enough to produce an observable scintillator signal (these results are not shown).

Thus, ^{90}Sr was deemed to be the best choice for the experiments. In an attempt to decrease the amount of Cerenkov radiation generated in the top slide, we used blank and Al-NP–coated quartz cover slips (~0.25 mm thick, 25 mm diameter, with 7 µL of PPO solution) on the top layer and implemented a longer wavelength filter (Melles Griot 03FCG125, blocking UV light <310 nm, and having just 10% transmission at 320 nm) to further limit any direct Cerenkov radiation from reaching the PMT. Figure 5 shows difference plots from the study employing a blank cover slip ("with PPO" minus "no PPO") or an Al-NP–coated cover slip (21 nm, 0.3 nm/sec) ("with PPO" minus "no PPO"). The results still indicate that emission in the presence of the Al-NPs is reduced relative to that in the absence of Al-NPs.

These results (using the thinner cover slips and a longer wavelength filter) also indicate that Cerenkov radiation from the top slide, and associated PPO fluorescence generated by the Cerenkov radiation, compete with direct beta-induced scintillation in the solution layer. Because the effect appears to be

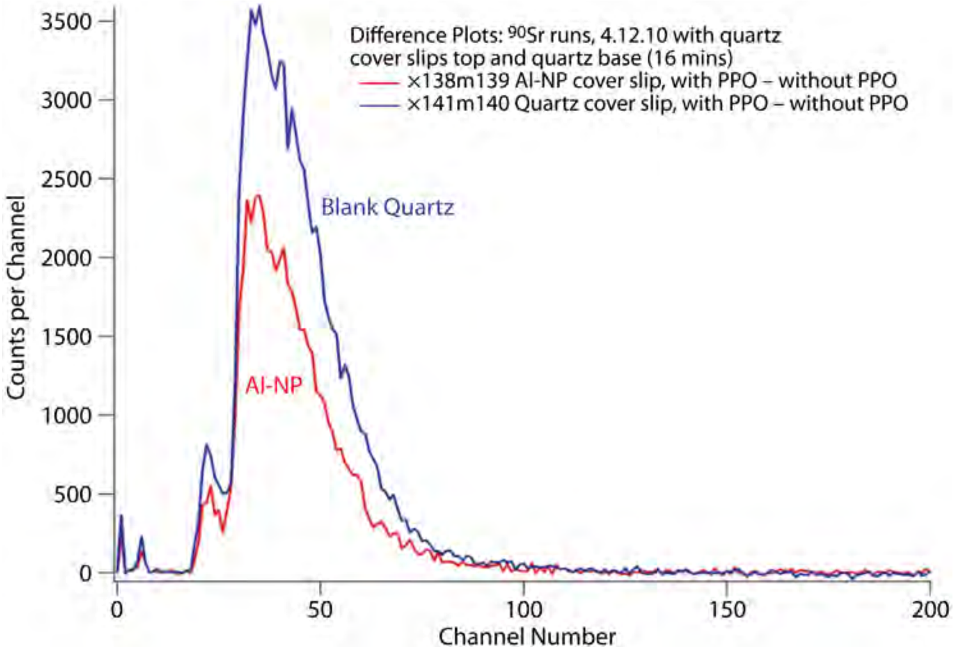

Figure 5. Difference plots using blank and Al-NP–coated quartz cover slips (top layer) and a longer wavelength filter. Results indicate that the amount of emission observed from the blank slide sandwich (blue trace) is still greater than that from the Al-NP sandwich (red trace).

of similar magnitude, it is not possible to determine whether the Al-NP substrate has an enhancing effect. It is clear from these tests that if the suboptimally sized Al-NPs do enhance emission, the effect is not very competitive with Cerenkov excitation of the PPO solution.

Conclusion

Based on measurements we made with NP "cluster-coated" slides, it is not apparent that MEF is induced by an ionizing radiation source. However, we were not able to perform tests with colloidal Al-NPs of the optimal size, and the ionizing radiation experiments were essentially two-dimensional, given the short (~10 micron) solution path length. To determine whether or not surface plasmon-induced scintillation enhancement is possible, a "three-dimensional" solution study, involving a larger cross section of scintillator consisting of colloidal NPs suspended in solution, is needed. One source of such Al-NPs is the Russo group at the Lawrence Berkeley National Laboratory (Gonzalez, 2007). Additionally, where scintillator strength is of concern, a beta source with E_{max} below the Cerenkov threshold for electrons in quartz/glass (~180 keV) and/or a stronger gamma source (with E_{max} below 310 keV) should be used. An end-on PMT would also help to collect signal generated from the solutions.

Acknowledgments

The authors would like to thank NSTec staff members Lisa Fukunaga for performing AFM measurements and for technical expertise in interpreting results, and Mike Grover for making metal film thickness measurements. We express our gratitude to Nicholas Geisse for providing AFM measurements of samples at Asylum Research (Goleta, California). We also thank the Engineering Materials Department at UCSB for providing training and access to the atomic force microscope in the Engineering Materials Department at UCSB.

References

Aslan, K., I. Gryczynski, J. Malicka, E. Matveeva, J. R. Lakowicz, C. D. Geddes, "Metal-enhanced fluorescence: An emerging tool in biotechnology," *Curr. Opinion in Biotechnology* **16**, 1 (2005) 55–62.

Birks, J. B., *The Theory and Practice of Scintillation Counting,* Pergamon Press, Oxford, Volume 27, 1964.

Geddes, C. D., J. R. Lakowicz, "Metal-enhanced fluorescence," *J. Fluoresc.* **12**, 2 (2002) 121–129.

Geddes, C. D., K. Aslan, I. Gryczynski, J. R. Lakowicz, "Metal-enhanced fluorescence sensing," in *Fluorescence Sensors and Biosensors,* ed. Thompson, R., Francis and Taylor Group, Boca Raton, Florida (2005) 121–181.

Geddes, C. D., Private communication, July 2009.

Glass, A. M., P. F. Liao, J. G. Bergman, D. H. Olson, "Interaction of metal particles with adsorbed dye molecules: Absorption and luminescence," *Optics Letters* **5**, 9 (1980) 368–370.

Gonzalez, J. J., S. Liu, S. Wen, X. Mao, R. E. Russo, "Metal particles produced by laser ablation for ICP-MS measurements," *Talanta* **73** (2007) 567–576.

Kimblin, C. K., C. D. Geddes, L. Franks, "Radiative decay engineering for improved scintillators," *Nevada Test Site–Directed Research and Development*, FY 2009, National Security Technologies, LLC, Las Vegas, Nevada, 2010, 191–198.

Knoll, G. F., *Radiation Detection and Measurement, 3rd Ed.*, John Wiley and Sons, Inc., New York, New York, 2000, 712.

Lakowicz, J. R., K. Ray, M. Chowdhury, H. Szmacinski, Y. Fu, J. Zhang, K. Nowaczyk, "Plasmon-controlled fluorescence: A new paradigm in fluorescence spectroscopy," *The Analyst* **133**, 10 (2008) 1308–1346.

Lakowicz, J. R., "Radiative decay engineering 5: Metal-enhanced fluorescence and plasmon emission," *Anal. Biochem.* **337**, 2 (2005) 171–194.

NNSA/Institutional and Joint Program Division

Lucille Gentry	(1)	Jamileh Mogin	(1)

NNSA/NA-123.2

Abdul Dasti	(1)	Lee Hamilton	(1)

NNSA/NSO

Charlotte Carter	(2)	Steve Mellington	(1)	Laura Tomlinson	(1)

NSTec

Dennis Barker	(1)	Howard Bender	(2)	Robert Buckles	(2)
Mike Butchko	(1)	Ken Cooke	(1)	Frank Cverna	(1)
Darryl Droemer	(1)	Jim Gatling	(1)	Steve Goldstein	(1)
Paul Guss	(2)	E. Chris Hagen	(1)	John Hollabaugh	(1)
A. C. Hollins	(1)	Jim Holt	(1)	Bill Kost	(1)
Ping Lee	(1)	Amy Lewis	(1)	Wil Lewis	(1)
Dana Lindsay	(1)	Michael Martinez	(1)	Rick Maurer	(1)
Tim Meehan	(2)	Dave Nichols	(1)	Robert Okagawa	(1)
Raffi Papazian	(1)	PIs	(1 ea)	Dave Post	(1)
Carson Riland	(1)	Gerald Stevens	(2)	Bob Summers	(1)
Tom Waltman	(1)	Alan Will	(1)	Steve Younger	(1)

Joint Nevada Program Office

Rick Higgs	(1)

LANL

Jeff Paisner	(1)
Bob Reinovsky	(1)
LDRD Office (ATTN: William Priedhorsky and Robert Kraus)	(2)

LLNL

Larry Wiley	(1)
LDRD Office (ATTN: Ken Jackson and John Knezovich)	(2)

SNL

Raymond Leeper	(1)
John Porter	(1)
LDRD Office (ATTN: Hank Westrich)	(1)

OSTI

Electronic copy	(1)

Resource Centers

Technical Library	(1)
Public Reading Center	(1)

Nevada National Security Site–Directed Research and Development
FY 2010 Report
DOE/NV/25946--1162
Report Date: April 2011

Site Directed R & D SDRD